Addressing structural uncertainty through seismic forward modelling

Simon John Oldfield

Submitted in accordance with the requirements for the degree of Doctor of Philosophy

The University of Leeds

School of Earth and Environment

August 2018

The candidate confirms that the work submitted is his own and that appropriate credit has been given where reference has been made to the work of others.

Abstract

Seismic reflection imaging provides one of the most widespread datasets for interpreting subsurface geometry. Subsequent interpretations are known to be uncertain and much remains to be done to understand and quantify that uncertainty.

Seismic forward modelling offers the ability to: investigate the accuracy of contemporary workflows through comparison with known truth-case models; understand imaging constraint in different settings by modelling wave propagation, and; compare potential interpretations directly to the original seismic image.

Combining contemporary approaches of reservoir modelling, structural restoration and seismic modelling, this thesis sets out to demonstrate a workflow to quickly generate detailed synthetic images. Generating example cases at various scales, I test contemporary analytical approaches to demonstrate the uncertainty introduced by seismic interpretation of structural geometries.

In doing so, I demonstrate that; in the case of an isolated normal fault, seismic attribute analysis may both over- and under-estimate fault length. Smoothing of structural geometries during seismic interpretation can increase the apparent cross-sectional areas available for fluid flow, increasing production forecasts by up to 40 %. Using synthetic data to support a multi-stochastic exploration assessment results in a 16 % difference in estimated resource compared a single case deterministic estimation.

In all of these cases, seismic forward modelling has assisted quantifying uncertainty and assisting interpretation. However, uncertainty in seismic images is spatially variable, and areas returning little energy to the surface will always challenge interpreters. To this end, mechanical modelling is trialled as a method to integrate geometric data from more certain aspects of an interpretation to produce a geologically feasible geometry.

These methods show great potential for testing at present and are likely to become more broadly applicable with increasing computational efficiency.

Acknowledgements

This body of work has been compiled at the University of Leeds during the period from September 2014 to August 2018. I would like to thank some of the many individuals who have offered assistance along the way.

For timely insight and discussion of many of the ideas presented in this thesis, my supervisors; Prof Douglas Paton, Dr Emma Bramham and Dr Taija Torvela.

For financial support; Ecopetrol, World Universities Network, PDS UK and the Tectonic Studies Group of the Geological Society of London.

For academic software licences; Midland Valley Exploration, Schlumberger, Norsar, Eliis, dGb Geoscience, TIBCO and Anaconda.

For their thoughts, imagination and support, my collaborators; Andrés Mora, Isabelle Lecomte, Emma Finch, Tom Lynch, Jamie Hilton, Viki O'Connor and Silje Skorve-Skarpeid. For insightful discussions; Richard Steele, Hannah Bentham, Estelle Mortimer, Paul Markwick, Mohammed Gouiza, Charlotte Botter and Alan Wood, and for practical support; Samantha Haynes, Richard Rigby, Rachael Spraggs and Penny Andrews.

For the many friends who have provided amusement and distraction along the way; H. Beaumont, M. Belhajam, S. Banning, L. Campbell, A. Campos-Candela, D. Cangelosi, N. Collins, F. Couperthwaite, T. Dalton, L. Everard, E. Fung, H. Goswell, R. Hebb, J. Lemon, J. Norcliffe, L. Oates, E. Pape, C. Prescott, D. Price, H. Rowlands, C. Smith, R. Stanca, R. Thomas, A. Traynor, J. Wallis and W. Young.

For the many questions, challenges and occasional hilarity provided by students of the MSc Structural Geology with Geophysics 2010 to 2018.

For their unwavering support and inspiring my curiosity and tenacity, my parents, John and Carol Oldfield.

Contents

List of figures

List of tables

Chapter 1

Introduction

Chapter structure:

1.1 Introduction

This thesis explores uncertainty in the interpretation of geological structures through application of seismic forward modelling. Advances in the efficiency of seismic image simulation (Lecomte et al., 2015) allow application at the scale of industry seismic acquisition (5-15 km^2), greatly exceeding recently published models at the 10's to 100's of metres focussed on individual stratigraphic elements.

Since the advent of reflection seismic surveying practitioners have been keenly aware of limitations and progressively acted to reduce them and minimise their affect (Dragoset, 2005). Expanding seismic modelling capabilities allows practical consideration of whole structural features, reservoirs and entire 3D seismic acquisitions, enabling investigation of the full range of associated uncertainty.

Contemporary workflows often apply seismic modelling to relate long recognised rock physics and petrophysical relationships (e.g. Wyllie et al., 1956), to observed variations in seismic response. Such approaches have been integrated with seismic modelling (e.g. Dvorkin and Nur, 1996; Nur et al., 1998), allowing correlation of observations to more data sparse areas throughout seismic volumes (e.g. Avseth et al., 2001) and building in a consideration of uncertainty and natural variation to further improve predictions (e.g. Bosch, 2004; Spikes et al., 2007; Grana, 2014).

However, equivalent approaches considering subsurface geometry, resulting from the development of geological structures are rare. Many advances in seismic imaging quality are principally driven by progress in surface acquisition geometry, providing additional dimensions, increased fold (Mayne, 1962) and subsequently full three-dimensional seismic surveys (Hilterman, 1970; O'Brien and Lercue, 1988; Cartwright and Huuse, 2005). Development of the physical changes to survey design has been accompanied by progress in data processing and significantly improvements in migration (Lecomte, 1999; Gray et al., 2001).

Early attempts to use seismic modelling to consider subsurface geometry focussed on

developing survey acquisition patterns that offered improved illumination of the target (Laurain et al., 2004). More complex, realistic, subsurface geometries were modelled using ray-tracing (e.g. Fagin, 1991, 1996) and later finite difference modelling (e.g. Alaei, 2005; Alaei and Petersen, 2007). These pioneering approaches successfully produced synthetic seismic, which has provided a means to improve data processing techniques (e.g. Versteeg, 1994). However, the iterative nature of seismic interpretation makes incorporation such approaches extremely time consuming, making such modelling impractical.

In this thesis, I use a recently developed 3D seismic image simulation approach (Lecomte et al., 2004), combined with contemporary reservoir modelling methods to rapidly build multiple structural models of varying complexity. This enables investigation of the uncertainty of structural interpretation in three ways: understanding the imaging constraint; validating the uncertainty of analytical approaches, and; comparing alternate potential interpretations.

These three approaches form the basis of my efforts to improve our understanding of uncertainty in subsurface estimates. The following section outlines the rationale and structure of this thesis. Applying various methodologies to facilitate these analyses has been achieved through interactions with various collaborators, acknowledged below:

Seismic forward modelling advise was generously given by Isabelle Lecomte (University of Bergen) and employees of NORSAR (Ch. 3, 4 and 6).

Reservoir simulation was enabled by use of initiation files supplied with advice by Tom Lynch (University of Leeds), with further discussions with Jamie Hilton (Premier Oil) and Silje Skarpeid-Skorve (Shell) (Ch. 5).

Structural framework modelling and related customisation of the workflows to allow application at much larger than typical scales was enabled by discussions with Stuart Smith and Steve Freeman (Schlumberger) (Ch. 3 & 6).

Balanced sections from Colombia were provided by Diego Constantino (University of Leeds) and Andrés Mora (Ecopetrol) (Ch. 6).

Mechanical modelling scripts, advice and guidance were provided by Emma Finch (University of Manchester) for discrete element modelling (Ch. 7).

1.2 Rationale

Interpreting complex geological structures in seismic images presents a key challenge in applied geoscience. Rapid lateral velocity contrasts and steeply dipping strata lead to reduced resolution and detectability, adversely affecting image quality. Generating synthetic seismic images of potential interpretations offers a means to investigate the relationship between the subsurface and resulting seismic images.

This project was originally conceived by Prof. Douglas Paton and Dr. Andrés Mora in response to challenges faced by Ecopetrol in the frontal ranges of the Eastern Cordillera, Colombia. In the frontal ranges of this compressional orogen seismic imaging quality is dramatically reduced (Fig. 1.1), leading to increased reliance on drilling data and regular side-tracking of wells. As a result it was suggested that forward modelling the seismic response of alternate interpretations could provide additional insight.

On this basis, the author identified three manners in which synthetic seismic was likely to contribute in improving our understanding of the uncertainty related to seismic interpretation of geological structures:

Understanding image constraint: mapping the distribution of survey illumination and noise provides insight on the effectiveness of imaging features of different contrasts and orientations.

Validating analytical methods: to understand the manner in which structural features may present themselves, our limitations of identification and the strengths and weaknesses of different attributes applied to interpretation.

Comparing alternate interpretations: understanding the constraint of different geometric interpretation cases provides an indication of their relative likelihood of occurrence.

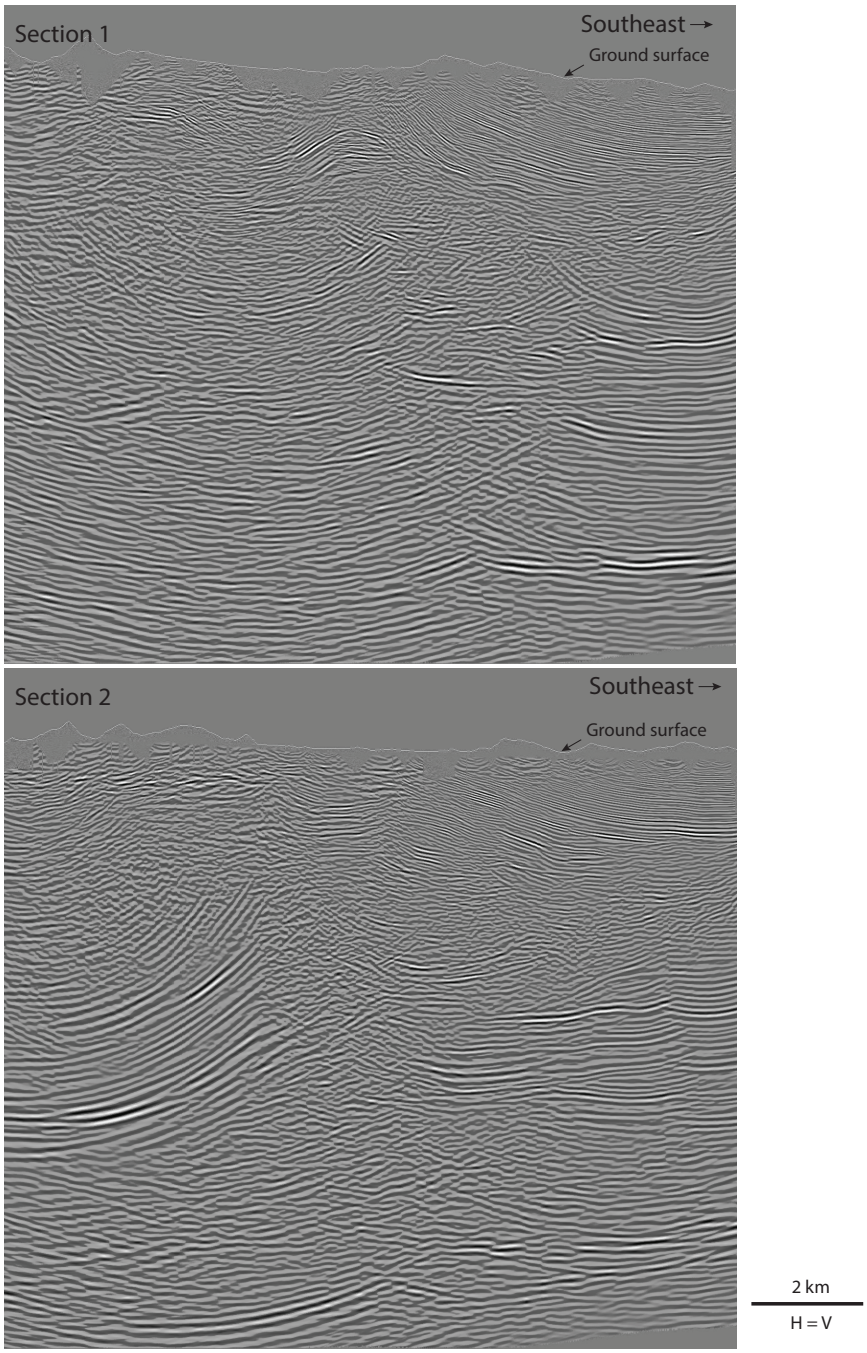

Figure 1.1: Two two-dimensional pre-stack depth migrated (PSDM) sections from the foothills of the Eastern Cordillera, Colombia. Poor seismic imaging quality leads to reliance on well data for subsurface interpretations. Sidetrack wells are typically utilised to provide multiple well penetrations to define the target.

Seismic reflections represent changes in subsurface acoustic properties resulting from changes in; composition, geometry and acquisition parameters. As a wave propagates it is continually modified by filtering and attenuation, in this way the overburden of any location contributes to its seismic response. As a result, not only are seismic interpretations non-unique solutions as to the nature of the subsurface, but the seismic data upon which they are based may also vary significantly dependent on acquisition and processing decisions.

In areas of geological complexity, interpretation becomes more reliant on the availability of multiple data sources and application of multiple analytical methods (e.g. Zamora-Valcarce and Zapata, 2015). Such an approach allows for cross-validation, utilising the strengths of certain analytical methods to compensate for the weaknesses of others. In many cases one of the key issues of seismic interpretation is interpreting the strengths and weaknesses of a dataset and the analytical processes applied to it. Rapid seismic forward modelling of multiple alternate interpretation cases under the same acquisition models presents a means to investigate this further.

Analysis of synthetic seismic data provides insights as to the illumination directions at which structures may be more or less likely to be detected (Gjøystdal et al., 2002). Knowledge of the input geology provides a key constraint on understanding the accuracy of our geometric estimates from equivalent data, and use of multiple known geometries provides a means to investigate the elements of a geometry that are better imaged and thus illustrate better spatial constraint.

Common to all of these applications is the attempt to delineate the likely range of potential outcomes in light of a given observation. Depending on the aim of the analysis the sensitivity to a given factor is likely to vary. As such, any meaningful consideration of uncertainty requires definition of an objective function against which performance may be measured through optimisation to maximise or minimise a value (Saltelli et al., 2008).

In this thesis, the main application is considered to be hydrocarbon exploration, appraisal and extraction. In this application time and value parameters dominate decision-making,

though they themselves summarise the affect of more specific subsurface parameters (Suslick et al., 2009).

For example, once hydrocarbon presence is proven, the volume in-place and production rate become the critical factors for economic viability and surface facility requirements. Failure to appreciate the range of potential outcomes may cause significant time delay through mistaken specification of equipment, incurring significant cost and delaying project delivery (Merrow et al., 1988).

To this end, this thesis selects a series of key interpretation elements that may be tested by seismic forward modelling and investigates the use of synthetic seismic in addressing aspects of the relevant uncertainty. No attempt is made to scale the results to formal business decisions, instead the aim is to act as a proof of concept to reveal applications of seismic forward modelling to investigate scientific accuracy.

1.3 Thesis structure

This thesis is structured to represent the underlying work, initially developing a workflow, and then proving application and relevance at progressively larger spatial scales.

Chapter 1: Introduction introduces the rationale thesis and layout.

Chapter 2: Literature review provides a broader discussion of introductory material related to both the challenges faced and the workflow that has been developed. In particular, attention will be given to prior work using seismic forward modelling and other validation techniques to address these challenges.

Chapter 3: Workflow development & testing describes the seismic forward modelling approach used in this work. Discussing the integration of reservoir modelling and seismic modelling, this chapter outlines the steps taken to ensure that the final workflow is robust and reproducible. This will be referred to repeatedly throughout the remaining thesis to minimise necessary repetition.

Chapter 4: Fault interpretation uncertainty applies forward modelling at the scale of simple individual features. Models of a single simple normal fault are used to investigate the accuracy of analytical methods in identifying fault presence. Initially this is achieved through manual analysis of samples across the faulted area. Building on observations from this work a machines learning algorithm is developed by the author and used to analyse along-fault attribute extractions. These reveal previously unidentified trace attribute responses that may explain broader observations made in the literature. Significantly, they also provide a means to identify across-fault juxtaposition patterns offering new information on likely uncertainties during flow modelling.

Chapter 5: Reservoir interpretation uncertainty expands the spatial scale of consideration to reservoir scale. These models also propagate interpretation uncertainty common in earlier stages of work into development and production workflows. Reservoir flow simulation is used to quantify the degree of geometric control on subsequent estimates of reservoir flow, likely production rates and the timing of water breakthrough. This demonstrates that estimates of both volume in-place and production rates are sensitive to the geometries derived from seismic interpretation.

Chapter 6: Prospect interpretation uncertainty expands the scale of focus to an entire prospect, forward modelling the seismic response of a volume equivalent to contemporary acquisitions. Modelling large complex compressional geometries provides a proof of concept that it is possible to adapt new reservoir modelling processes for these purposes and generate multiple models in a reasonable timescale for iteration in comparison of alternate interpretations and original seismic data.

The potential volume of resources in places for each of theses alternate models is then used as a metric to quantify the significance of the potential variation in perceived risked volumes. This provides an additional analysis of the merit and sensitivity of the resource estimation to the strategy applied to integrate a consideration of risking for multiple potential interpretation scenarios, as is encouraged by the utilisation of seismic forward modelling workflows.

Chapter 7: Mechanically constrained interpretation is investigated as a means of providing additional interpretation in areas of low data constraint. Recognising variation in the spatial constraint of data, it is proposed that mechanical modelling may be used with interpretation elements of greater certainty to provide an alternative means of constraining potential geometries. Using a strong basement reflector that is considered to be of greater certainty than reflections observed in the interval of interest for exploration, this geometry is captured. Using this basal surface and knowledge of the local geology constrained by nearby field and surface data, mechanical modelling is utilised to provide alternate interpretation scenarios.

Chapter 8: Discussion & concluding remarks draw together the presented work into a coherent set of observations on the overall subject, prior to suggestions for future work themes.

1.4 Contributions

Various elements of this work have previously been contributed at scientific and industrial conferences, as detailed below.

- Oldfield, S.J., Paton, D.A., Bramham, E.K., and Torvela, T. 2018. Spatially variant uncertainty in the geological interpretation of reflection seismic data, EGU General Assembly.
- Oldfield, S.J., Paton, D.A., Bramham, E.K., and Torvela, T. 2018. Fault related frequency anomalies: geometric controls from seismic forward modelling, EGU General Assembly.
- Oldfield, S.J., Paton, D.A., Bramham, E.K., and Torvela, T. 2018. Reservoir compartmentalisation and seismic interpretation uncertainty: Insights from seismic forward modelling, Tectonic Studies Group Annual General Meeting.
- Oldfield, S.J., Lynch, T.O., Hilton, J., Lecomte, I., Paton, D.A. and Fisher, Q. 2017. Reservoir modelling strategies for intra-reservoir faulting, Handling Fault Seals,

Baffles, Barriers and Conduits Conference.

- Oldfield, S.J., Finch, E., Paton, D.A., Bramham, E.K., and Torvela, T. 2017. Structural inheritance of fault displacement profiles from continental rifting to thrust fault propagation – from observations to mechanics. Fold and Thrust Belts: Structural Style, Evolution and Exploration Conference.
- Oldfield, S.J., Paton, D.A., Bramham, E.K., and Torvela, T. 2017. Fault length, connectivity and reservoir compartmentalisation – Testing workflows with seismic forward modelling. AAPG Annual Conference and Exhibition, Houston, USA.
- Oldfield, S.J., Paton, D.A., Bramham, E.K., and Torvela, T. 2017. Elucidating structural uncertainty using seismic forward modelling. Joint Assembly TSG-VMSG-BGA 2017, Liverpool, UK.
- Oldfield, S.J., Paton, D.A., Constantino, D., Bramham, E.K., Torvela, T., and Mora, A. 2016. Using seismic forward modelling to risk sub-thrust plays. AAPG Annual Conference & Exhibition, Calgary, Canada.
- Oldfield, S.J., Paton, D.A., Bramham, E.K., Torvela, T., Mora, A. and Alzate, J.C. 2015. Reducing uncertainty in the geological interpretation of complex structural geometries through seismic forward modelling: application to frontal ranges of the Llanos Basin, Colombia. AAPG Annual Conference & Exhibition, Denver, USA.

The author has also chaired and co-chaired the following sessions for AAPG:

- AAPG ACE 2017 - Reviewer and session chair for the Crustal architecture & rifting poster session.
- AAPG ACE 2017 - Reviewer and session chair for the Structure, geomechanics and tectonics theme poster session.
- AAPG ACE 2016 - Reviewer and session chair for the Structure and tectonics of unconventionals poster session.
- AAPG ACE 2015 - Session chair for Structure and tectonics of unconventionals oral session.

Further work by the author may be associated with the following Orcid ID:

https://orcid.org/0000-0002-7947-9901

Knowledge is an unending adventure at the edge of uncertainty.

Jacob Bronowski

Chapter 2

Literature review

Chapter structure:

2.1 Introduction

This chapter outlines some of the necessary background information to develop a robust basis for discussions throughout the thesis. It is structured to progressively focus onto the issue at hand progressing from a broad consideration of geological interpretation and uncertainty, general controls on the seismic response to geology and how this may be simulated using seismic forward modelling.

While this forms the basis of work presented throughout the thesis, where possible repetition will be avoided. In particular, some background regarding development of the workflow will be presented separately, in Chapter 3: Workflow development & testing. Discussion of the workflow in this chapter will be limited to that which sets the context of workflow development.

2.2 Geological interpretation of seismic data

Geological interpretation is the process of determining the structure and composition of the subsurface, typically by understanding the mechanisms of causation and the likely relationships between what can and cannot be seen. That understanding and representations of it form a geological model.

Common between most geological models is a need to integrate the known and unknown across time and space. Early constructs represented this in the observed form of cross-sections and maps (Smith, 1815) or interpreted form of the time-stratigraphic plots of Grabau (1906) (Stark et al., 2013).

The advent of seismic data revolutionised this by providing significantly greater constraint on the geometry of geological bodies over larger areas than can be easily observed in outcrop. This additional data, allowed better constrained maps of the subsurface, Wheeler diagrams (Wheeler, 1959; Qayyum et al., 2017), directly integrating structural and stratigraphic constraints.

As seismic imaging technology improved, recognition of the compositional data contained in a seismic signal grew. In convolutional modelling, reflections are interpreted to represent a convolution of the source wavelet and contrasts in acoustic properties (Ziolkowski, 1991), revealing an association between reflections and chronostratigraphic surfaces (Vail et al., 1984). Though later disproved by seismic forward modelling (Zeng et al., 1998a), these approaches marked significant maturation of the technology from the early depth profiling tool of the 1920s (Dragoset, 2005) into a true subsurface imaging tool (Cartwright and Huuse, 2005).

2.2.1 Seismic data analysis

Seismic data analysis begins with significant processing to generate images of reflections representing acoustic contrasts in the subsurface (Yilmaz, 2001). This processing is often completed independently of the seismic interpretation process.

While large three-dimensional seismic volumes are now commonplace, initial interpretation procedures remain rooted in two-dimensional interpretation workflows (Brown, 2011). Two-dimensional slices across the volumes in each direction and horizontally across a timeslice (Stark, 1996) are visually inspected, with key reflections marked and correlated from one section to another. The introduction of randomly oriented lines and picking of non-planar surfaces and volumes has modernised approaches.

It is now common to extract data along geologically significant surfaces forming stratal slices (Zeng et al., 1998b; Stark, 2004). Using grids to sample the seismic volume and derived attributes in this manner means that data along the slice originate from more comparable strata. This links variations in attribute response more directly with potential variations in geological properties as fluid or rock composition or deformation. Interpreting methods continue to evolve with the application of geobodies to extract volumes representing entire geological bodies (de Groot et al., 2016).

As interpretation becomes more automated, new methods have begun to use

cost minimisation approaches during auto-tracking to generate full volume horizon interpretations. These are volumes in which all reflections have been automatically picked and associated with neighbouring picks so long the cost of linking two points does not exceed a cost minimisation function (Wu and Hale, 2015). This results in a volume that is essentially picked in both acquisition time and depositional time through Wheeler transforms (Lomask et al., 2006).

Currently these approaches target stratigraphic applications, recent work suggests that mapping volumes of poor signal quality associated with deformation may also be of structural value (Iacopini et al., 2016), despite a range fo potential interpretation pitfalls (Hardage, 2015; Ferrill et al., 2016).

2.2.2 Interpretation validation

Interpreting structurally complex areas is challenging, reflections are often discontinuous with varying amplitude responses, often resulting in miss-correlation of response across structural features. Validating interpretations confirm that fundamental geological principles are not breached, this is a considerable step short of verifying a model against reality. The latter may only be achieved through a priori knowledge of the true situation in a synthetic dataset or through additional subsurface data.

Existing validation methods make analytical comparisons of a given situation to broadly accepted trends in geometries for equivalent categorical situations (Brandes and Tanner, 2014), such as detachment faults (Poblet and McClay, 1996; Suppe, 2011), fault-bend (Suppe, 1983) or fault-propagation folds (Erslev, 1991).

Recent development of validation techniques have focussed on physical principles, such as mass preservation, approximated by minimising change in line-length (Chamberlin, 1910; Dahlstrom, 1970; Hossack, 1979) or area (Gibbs, 1983; Epard and Groshong, 1995; Groshong and Epard, 1994) during section balancing. However, volume changes associated with deformation have long been recognised (Ramsay and Wood, 1973).

Efforts to address this are currently focussed on application of more rigorous mechanical modelling (e.g. Moretti et al., 2006) to better consider energy balance (Elliott, 1976; Dahlen, 1988) and fault zone processes (Savage and Cooke, 2010; Boneh and Reches, 2017).

2.2.3 Uncertainty and decision-making

Frodeman (1995) described geological sciences as both interpretative and historical, in the sense that conclusions are based on contemporary observations that are spatially sparse and temporally instantaneous. To predict occurrence, the order of historic events must be considered. As such the reductionist approach (Bacon, 1878), is typically inappropriate. Instead our focus should be to decrease the delay between interpretation and practitioner feedback to increase the strength of inference (Platt, 1964).

The terminology of uncertainty varies widely, dependent on the field of application and scale of observation (Samson et al., 2009). Some consider uncertainty as an umbrella term (Pshenichny, 2004), while others divide it into elements that may be treated as mutually exclusive or co-dependent. One such classification scheme considers uncertainty as aleatory or epistemic in origin, where aleatory may be considered as variation of a result around an expected outcome caused by a natural variability or limitations observation. Meanwhile, epistemic uncertainty is related to incomplete knowledge, often associated with misinterpretation of a situation leading to application of an inappropriate categorical descriptor.

These alternate 'types of uncertainty' have been criticised due to their implication of mutual exclusivity (Winkler, 1996), however in application they are useful in determining the method used to address the uncertainty (Begg et al., 2014). Aleatory uncertainty may be modelled using probabilistic modelling such as Monte Carlo approaches (e.g. Fig 2.1). Epistemic uncertainty may not be addressed in this manner as categorical analyses are considered in terms of their singular, independent likelihood of occurrence (Aven, 2010).

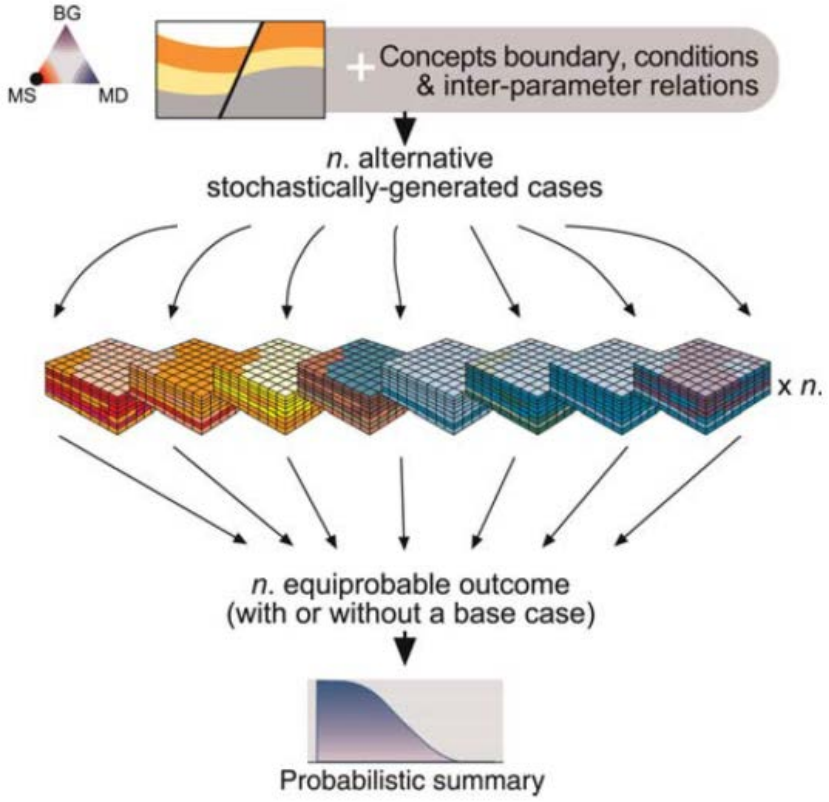

Figure 2.1: Illustration of multiple stochastic models, Bentley and Smith (2008)

As a result uncertainty of categories must be addressed by consideration of alternate interpretation scenarios (Van der Heijden, 1997, 2011; Corre et al., 2000) and any subsequent variation of dependent aleatory uncertainties (Chamberlin, 1965; Nilsen and Aven, 2003). In this manner, the variability expected within each model is dependent on the scenario within which it sits (e.g. Fig. 2.2). This fundamentally changes the natures of errors expected (Lever et al., 2016).

Beyond scientific rigour, it is important to understand the uncertainty space of geological interpretations in order to understand subsequent implications. In industrial settings, subtle variations in subsurface interpretation may lead to a requirement to modify project specifications, this can quickly cause delays increasing costs (Merrow et al., 1988). In the long term, under-specification of facilities can lead to their overuse and increased risk of failure (Ruffo et al., 2006).

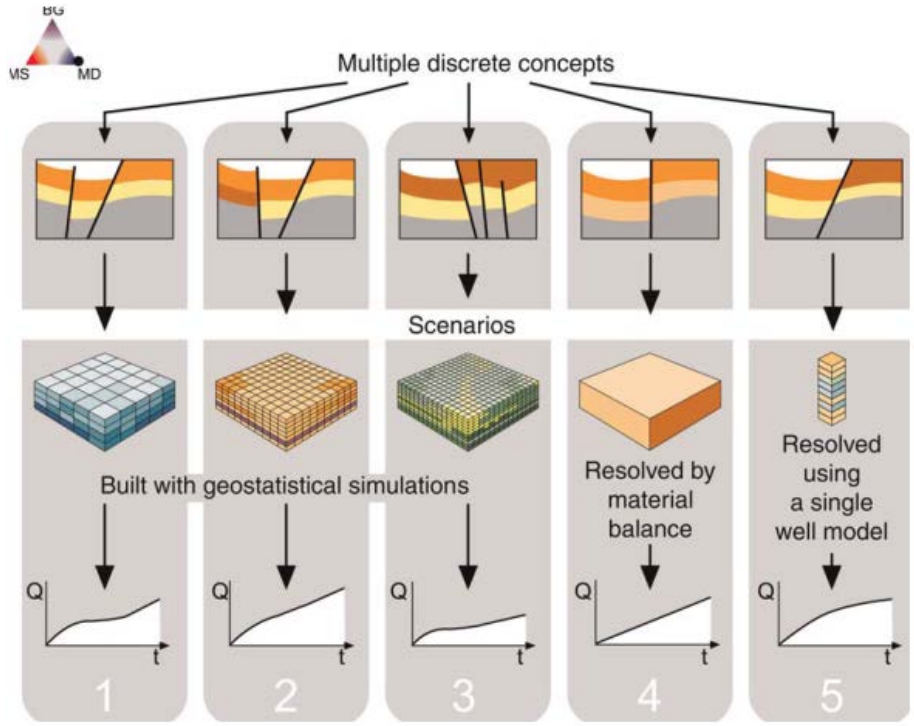

Figure 2.2: Illustration of multiple deterministic models, Bentley and Smith (2008)

Structural geology impacts subsurface uncertainty in various ways, at reservoir scale it may influence fluid flow (Rotevatn et al., 2009) and at larger scale it is likely to impact estimates of trapped volumes (Bond et al., 2008; Bond, 2015). This uncertainty space is heavily influenced by a number of other factors, including; horizon picking, fault picking, migration, velocity modelling and depth conversion (Thore et al., 2002).

Of these uncertainties, the interpretation error may be most difficult to resolve, requiring elicitation of opinion from multiple interpreters, which in itself introduces a significant source of potential uncertainty and bias (Aspinall, 2010; Usher and Strachan, 2013; Morgan, 2014; Curtis, 2012). While elements of research presented in this thesis address methods to overcome these issues, details are beyond the scope of this project. Instead, the reader is directed to: Kahneman and Tversky (1972); Tversky and Kahneman (1974); Arkes (2001); Kahneman and Klein (2009); Bond et al. (2008, 2015); Chellingsworth et al. (2015).

Interdependence of parameters is highly influential on the overall sensitivity of a system

(Egeland et al., 1992). For example, at a business scale decision, multiple relatively minor risks can quickly lead to significant time delays. In large projects it has been estimated that this may increase costs by up to 88 % (Merrow et al., 1988).

2.3 Controls on seismic response

Seismic reflection surveying relies on the reflection of energy emitted from a source to a receiver. In industry, sources are typically active, using an airgun, dynamite or vibroseis to emit a signal that will be reflected towards a receiver array. Seismic response will be determined by the composition and geometry of the subsurface, and properties of the survey.

At surface, the response is primarily determined by the size of the source used and sensitivity of the receiver array. Where the latter is impacted by many variables including receiver ground coupling, array distribution and spacing. The nature of the survey and the subsurface combine to affect the overall response.

During transmission the intensity of energy passing through a given location is expected to decrease with travel time due to spherical divergence and attenuation. Spherical divergence is the spreading of energy away from the source and subsequent points of diffraction or reflection (Aki and Richards, 2002). Attenuation is principally a function of subsurface composition and is particularly prominent in the presence of low viscosity fluids such as gas (Beckwith et al., 2017), due to dampening and conversion of particle motion from kinetic energy to other forms.

The direction of energy propagation as it passes from source to receiver is determined by Snell's Law (equation 2.1). As an incident ray of energy interacts with a reflector energy will be reflected, refracted and transmitted. The proportion of energy used in this is determined by the angle of incidence and the reflectivity of the surface.

$$\frac{\sin\theta_1}{\sin\theta_2} = \frac{v_1}{v_2} \tag{2.1}$$

Where; θ_1 is the angle of incidence, θ_2 is the angle of reflection, v_1 and v_2 are the velocities of layer 1 and 2.

$$AI = \rho_b.V_p \tag{2.2}$$

$$R = \frac{AI_1 - AI_2}{AI_1 + AI_2} \tag{2.3}$$

Where AI is acoustic impedance, derived from bulk density, ρ_b , and compressional wave velocity, V_p. From this the reflectivity coefficient is defined as the contrast in acoustic impedance from one layer to another (AI_1 to AI_2).

The amplitude of the signal at a given interface is determined by both the physical properties and the angle of incidence, leading to variance in amplitude with angle, discussed further in § 3.4.3.

Once reflected energy has been acquired, undergone initial processing and stacking (Yilmaz, 2001), the seismic image is formed by migration of reflected energy to image the points of origin through supposition of energy from the available receivers (Bee Bednar, 2005; Gray, 2013; Jones, 2014)). Issues are known to exist with regards to the existence of overlying velocity contrasts from faulting (Fagin, 1996), salt (Jones and Davison, 2014) or gas bodies (Arntsen et al., 2007).

2.3.1 Seismic imaging quality

Seismic imaging quality may be thought of as the accuracy with which an interpretation can be made using a given seismic dataset. This may be perceived in different ways, during processing, extensive parameter testing is undertaken aiming to optimise the apparent focussing, however aesthetics may come before accuracy. Experience of seismic data in more structurally complex compressional areas suggests that overzealous smoothing, or filtering, may remove useful data despite resulting in an image that looks easier to interpret due to sweeping, smooth continuous reflections.

Imaging quality is often treated interchangeably with resolution in the interpretation literature. However, as discussed below, resolution has a strict definition. Furthermore,

the convolutional model suggests that even below resolution geometries are expected to impact the passing seismic signal.

As resolution is specific to a wavelet and the velocity of the media through which it is passing, it also fails to consider the reflectivity element of imaging. Should an impedance contrast be insignificant or an area lie within the shadow of an area of high attenuation, it is unlikely to be detected (Hall, 2006b).

Resolution

In physics resolution specifically refers to the ability to discriminate between the peaks of two wavelets. This was initially demonstrated by Rayleigh (1879), during investigations focussed on the resolution of light. While some work suggests that his use of $\lambda/8$ (where, λ = wavelength) may be pessimistic in physical terms (Ram et al., 2006). However application in seismic imaging suggests that this is a reasonable approximation of vertical resolution.

Building on Rayleigh's work, Ricker (1953a,b) defines the vertical resolution as being the time between the peak of a zero-phase wavelets response and the sidelobe, which is equal to the tuning thickness. This decreases the separation required between two wavelets for them to be resolvable by considering a broadened flat top between two wavelets, identified using the second derivative, to indicate the presence of more than one response (Fig. 2.3).

Widess (1973) instead focussed on the resolution of thin beds, and so impedance contrasts with opposite polarity. Using wedge shaped models to simulate the thin beds, amplitude variations were observed related to the presence of the thin bed until the bed thickness was approximately one eighth of the wavelets wavelength.

It is important to note that the Ricker and Rayleigh criterions are based on examples using zero-phase wavelets with insignificant noise and equal polarity impedance contrasts. Building on this Widess (1973) considered the presence of beds with acoustic impedances that are equal in magnitude but of opposite polarity. This work agreed that wavelets could

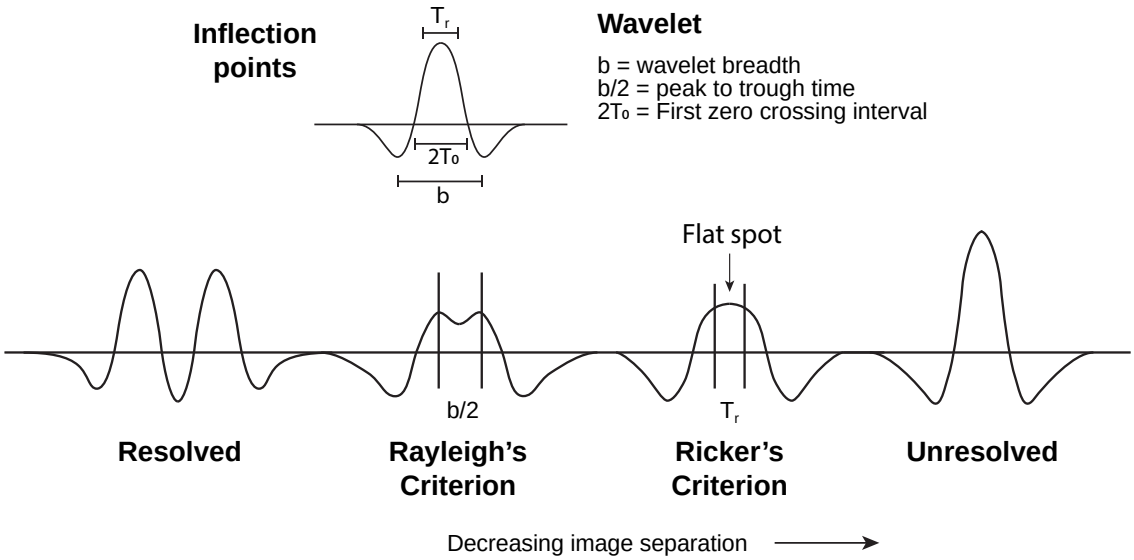

Figure 2.3: Comparison of resolution criterion, after Kallweit and Wood (1982).

be discriminated between at approximately $\lambda/8$.

Analysing the above work, Kallweit and Wood (1982) convolved a series wavelets with a reflectivity series taken from a sonic well log, concluding that in $\lambda/4$ provides a realistic measure of resolution. Utilising solely amplitude limits potential detection of seismic data, as complex trace analysis (Taner, 1979; Robertson and Nogami, 1984) often reveals more subtle details. Narrow frequency band extractions allow improved interpretation of thin beds (Marfurt and Kirlin, 2001) and can reveal removal of frequency content from the source signal, representing the filtering effect of the subsurface (Okaya, 1995; Hall, 2006b).

These studies illustrate the vertical resolution, discriminating between reflections along a vertical axis. Interpreting faults and structures in three dimensions however requires consideration of lateral resolution, determined from the Fresnel zone. This may be considered as the area of a surface within a quarter of a wave period across the arc of a propagating wave (Sheriff, 1977; Lindsey, 1989).

Adopting the Fresnel zone as the limit of lateral resolution assumes that diffracted energy from a range of different source and receiver couplings may be perfectly collapsed to their

point of origin (Deregowski et al., 1997). This is unlikely to be the case, considering the reflector as a line of points acting as a diffractive grating (Huygens Principle), a non-planar, undulating reflector would be expected to scatter incoming signals. Lateral resolution is therefore dependent on the configuration of both the acquisition survey and the subsurface, requiring case-by-case modelling for accurate of post-migration image resolution (Chen and Schuster, 1999; Tabti et al., 2001).

Detection & illumination

Detection is the act of identifying the presence of an object, in the case of seismic imaging this is likely to be the detection of a specific geometry or feature. In order for an object to be fully identified it must be resolvable, however in the presence of noise or in scenarios where an area is poorly illuminated an object greater in size than the limit of resolution may not be detected.

Noise may be coherent or incoherent, dependent on the relationship of its source to the acquisition (Sheriff and Geldart, 1995). Coherent noise can often be modelled and filtered effectively, however incoherent noise can only be suppressed. Using larger sources, or increasing the fold of a seismic survey may be used to boost the signal and cancel out random noise. Broadening the frequency content of source wavelet may also boost propagation of the source (Yilmaz, 2001).

The energy incident on a surface significantly impacts the likelihood of detection of returned signal from that location. This may be in part quantified by the term fold of coverage, that is the number of source and receiver pairs that contribute energy from a given location in the stacked dataset. As a result, variation in the fold of coverage on a surface may vary with the illumination with dip and curvature (Fig. 2.4). Additionally, subsurface features such as gas chimneys and salt diapirs (Drottning and Branston, 2009; Jones and Davison, 2014) may obscure underlying strata, similar effects are been observed related to faulting (Sigernes and Morton, 2002; Sigernes, 2004).

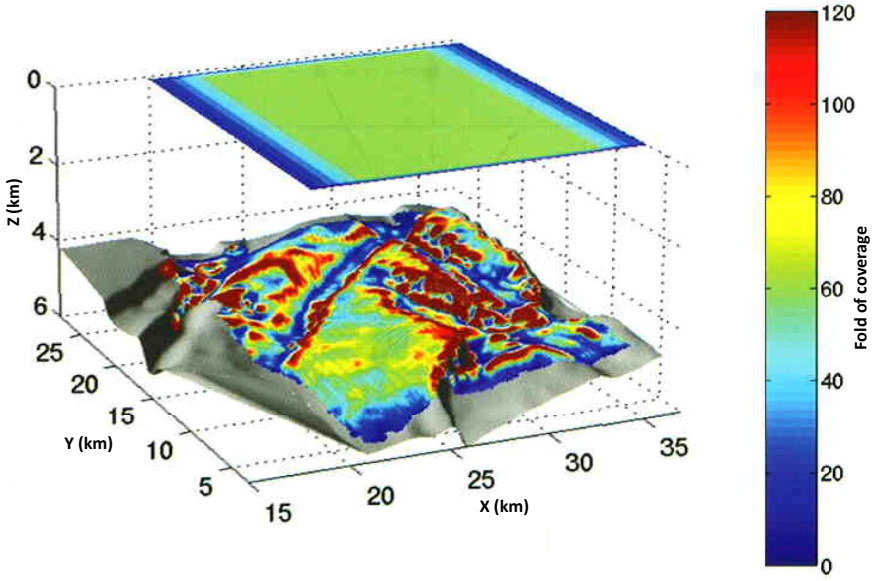

Figure 2.4: Common mid-point fold of coverage mapped to a geological surface. Note the shallower horizontal surface illustration the uniform nature of survey illumination, from Laurain et al. (2004).

2.3.2 Seismic expression of geological structures

All seismic interpretation of geological structures should be aware of potential pitfalls (Marfurt and Alves, 2015) and limitations such as survey illumination (Anell et al., 2016; Lecomte, 2008), resolution (Long and Imber, 2010) and detection limits (Kallweit and Wood, 1982). To understand the representation of these issues and their interaction with even simple subsurface geometries, seismic modelling is required (Carcione et al., 2002; Lecomte et al., 2015; Anell et al., 2016).

Faults are observed in seismic data as offsets along reflections, representing fault displacements (Hesthammer and Henden, 2000). As displacement varies along the length of a fault, approaching zero at the fault tip, such offsets will fall below seismic resolution, becoming undetectable. This has significant implications for fault network connectivity and topology, as small differences in the fault length can commonly contribute to compartmentalisation in reservoirs (Wood, 2013). This is also interpreted to be one of

the key drivers for loss of detail during interpretation of areas of more complex faulting (e.g. Wood et al., 2015).

Analysis of amplitude on reflections approaching faults are observed to vary. Recent work has demonstrated that the in internal structure of faults may be detectable using industry surveys in low noise settings (Botter et al., 2017; Kolyukhin et al., 2017). Extraction along horizons have become common element of fault interpretation workflows (§ 2.2), using rapid changes in response of a given attribute to indicate fault location. Attempts at such finer scale interpretation may be achieved using seismic attributes.

2.3.3 Seismic attribute analysis

Complex trace analysis enables extraction of trace attributes such as envelope, phase and frequency from individual stacked traces (Taner, 1979; Barnes, 1996). Use of trace attributes has been widely adopted for use in work oriented towards understanding subsurface composition and tuning anomalies; such as fluid contents (Wang, 2001; Bredesen et al., 2015), stratigraphic sequences (Hart, 2008) and onlap geometries (Partyka et al., 1999; Widess, 1973).

There are limited attributes that may be derived from a single seismic trace (Barnes, 2006), however there has been an accumulation of attributes based on varying implementations of calculation. As illustrated in Figure 2.5, some attributes are effectively equivalent (e.g. total absolute amplitude versus reflection strength), others are strongly correlated but emphases different aspects of data (e.g. average energy versus RMS amplitude), while others that at first may appear equivalent actually reveal underlying differences in seismic character (e.g. maximum trough amplitude versus maximum peak amplitude).

Trace analysis limits consideration of variance to a single dimension along the, typically vertical, seismic trace. Geometric attributes compare trends between neighbouring traces, enabling consideration in two- or three-dimensions. For example dip attributes correlate local features in each amplitude trace (e.g. peaks, troughs or zero-crossings) and calculate

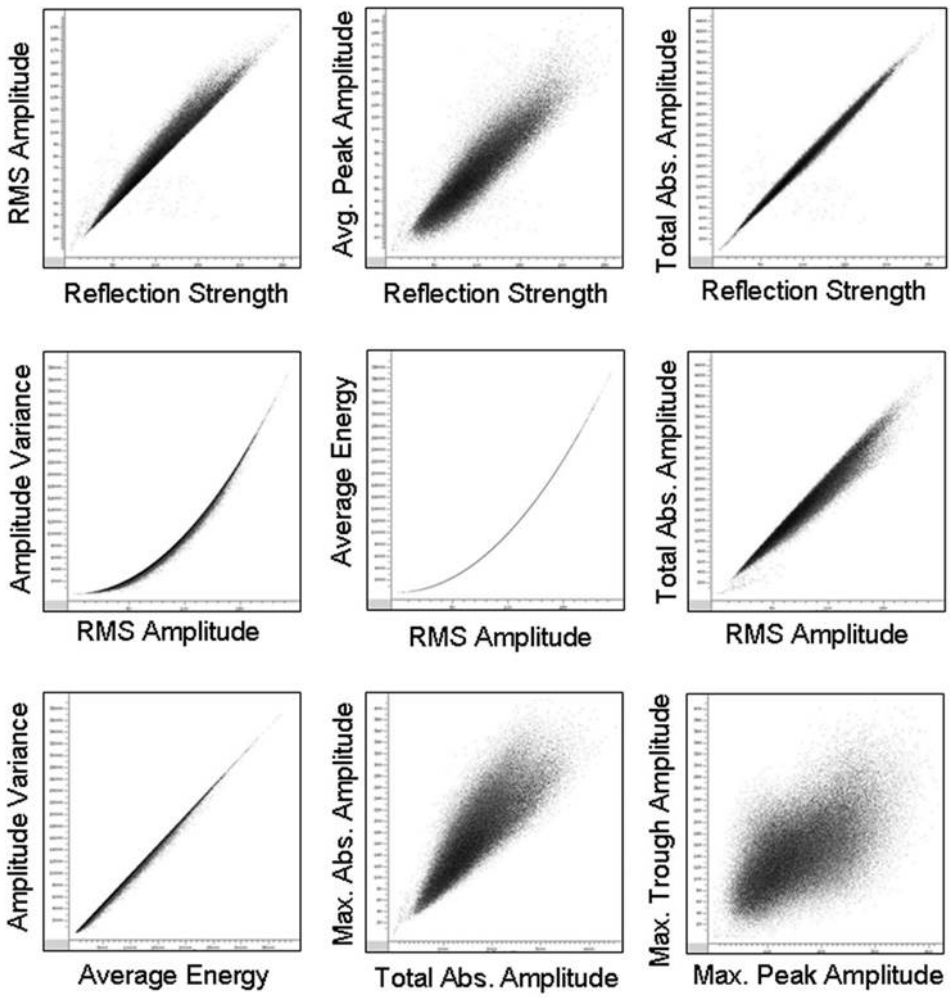

Figure 2.5: Cross-plots of various derived seismic trace attributes, illustrating the similarity of many, from Barnes (2006).

the dip between them, broadening the search area and considering dip variations a similar approach allows for the calculation of curvature (e.g. Jones and Knipe, 1996; Hesthammer and Fossen, 1997a; Townsend et al., 1998). Similarity or coherency attributes analyse the spatial variance in magnitude of another attribute (e.g. amplitude) identifying changes in seismic character (Marfurt et al., 1999, 1998).

Adoption of spectral decomposition (Castagna and Sun, 2006), the transformation of data to the frequency domain for analysis, has increased the application of trace attributes further. Typically these methods isolated selected frequencies of interest for tuning

analysis or particular geological bodies or trends and present them individually or blended together into a multi-attribute visualisation (Marfurt, 2015). Part based on the idea that frequencies sample spatial scales differently, there are attempts to use this data to infer the missing frequency content through estimating the equivalent content from field examples, spectral re-composition (Tomasso et al., 2010).

Despite recognition of trace attributes anomalies associated with faulting in amplitude (Townsend et al., 1998) and frequency (Iacopini and Butler, 2011), relatively little work has been undertaken to improve their incorporation into quantitative interpretative techniques for structural geology. As with any method aimed at extracting more information from data, seismic attributes are sensitive to the presence of noise and artefacts (Hesthammer and Fossen, 1997b; Hall, 2006b; Marfurt and Alves, 2015). This may be one of the limiting factors in structural analysis of seismic attributes data at lower scales.

2.4 Seismic forward modelling

Seismic modelling has long been used to guide our understanding and interpretation of seismic surveys. Prior to growth of computing power required to process numerical models of the type used in the thesis, Hilterman (1970) used physical analogue models to understand the effect of out of plane reflectors by simulating a three dimensional seismic acquisition.

Growth of computer power now allows for seismic modelling at all scales, whether to consider the mechanisms behind seismic wave induced fluid movement at the pore scale (Saenger et al., 2007; Wenzlau and Müller, 2009) or margin scale structural styles (Reston, 2009). In this section I outline elements generic background elements to seismic forward modelling that provide the basis for continued discussion in this thesis.

2.4.1 Modelling approaches

Modelling is performed for many reasons, subtly guiding the approach taken. Calculation of wave propagation through a subsurface media or analogue may be considered as seismic modelling, however in this thesis, I am primarily concerned with the simulation of images subsequently used for seismic interpretation.

For this purpose, two primary modelling methods exist; full-wavefield approaches including finite difference, and; ray-tracing approaches (Lecomte et al., 2015). Finite difference approaches allow for complete simulation of a propagating wavefield in two- or three-dimensions, however the approach is prohibitively expensive in terms of computational requirements for most applications related to seismic image interpretation. Carcione et al. (2002) provides a useful summary of seismic modelling approaches.

Ray-tracing can be applied in various manners. In its simplest form, image tracing, a one-dimensional vertical lines are drawn from a hypothetical receiver location to depth. Each time an impedance contrast is encountered the impulse, or reflectivity, is calculated and convolved with a defined wavelet to provide an amplitude response in a similar way to a well tie (White and Simm, 2003).

Normal incidence ray-tracing operates in a similar manner, however each time an impedance contrast is encountered, Snells Law is applied to refract the ray-path, resulting in more realistic ray-paths. At this point implementations may simply propagate the ray to observe its path, providing information on likely patterns of illumination in the models, or they may also convolve a wavelet in order to simulate an image.

These approaches are essentially one-dimensional, as contrasts are calculated along individual raypaths. Three dimensional seismic modelling has long been attempted (Hilterman, 1970), however processing times have presented a critical challenge to their applicability and as a result they are commonly only applied for individual shots and receivers.

The simulated prestack local imaging approach (Lecomte, 2008) applied in this thesis,

provides a computationally efficient three-dimensional convolutional approach. Rather than convolving a one-dimensional wavelet with the reflectivity series, a point-spread function (PSF) is calculated, using a background velocity model to calculate illumination vectors that may be convolved with a wavelet and assembled in the frequency domain as a PSDM filter, which once converted back into spatial dimensions forms the PSF (Fig. 2.6).

The PSF provides a three dimensional prestack depth migrated response that would be expected from a point diffractor. This may then be directly convolved with a reflectivity model to simulate imaging. An interesting property of PSFs is that coupled with the PSDM filter they provide direct insight to the optimal orientation of reflectors for detection.

2.4.2 Previous applications

Utilisation of seismic forward modelling for the purpose of image simulation is relatively new. Although, the potential for forward modelling to influence interpretation has long been recognised (Fagin, 1991), the requirement of computational power has limited usage. This has limited application to a small number of studies investigating specific phenomena. However, increased computing power and efficiency now facilitates application to larger field analogues more easily.

Outcrop analogues have been modelled to investigate the impact on the seismic signal of individual stratigraphic geometries (Hodgetts and Howell, 2000; Bakke et al., 2011; Janson and Fomel, 2011; Sæther, 2013; Anell et al., 2016), overlying intrusives (Eide et al., 2018), gas chimneys (Arntsen et al., 2007) and salt diapirs (Jones and Davison, 2014). At a much larger scales, simplified models have been used to test regional interpretation concepts (McDermott and Reston, 2015).

Sigernes (2004) rather innovatively, combined field measurement of physical properties from around a fault zones, which were then calibrated using samples taken for mechanical testing and used to the seismic forward model the response to faulting.

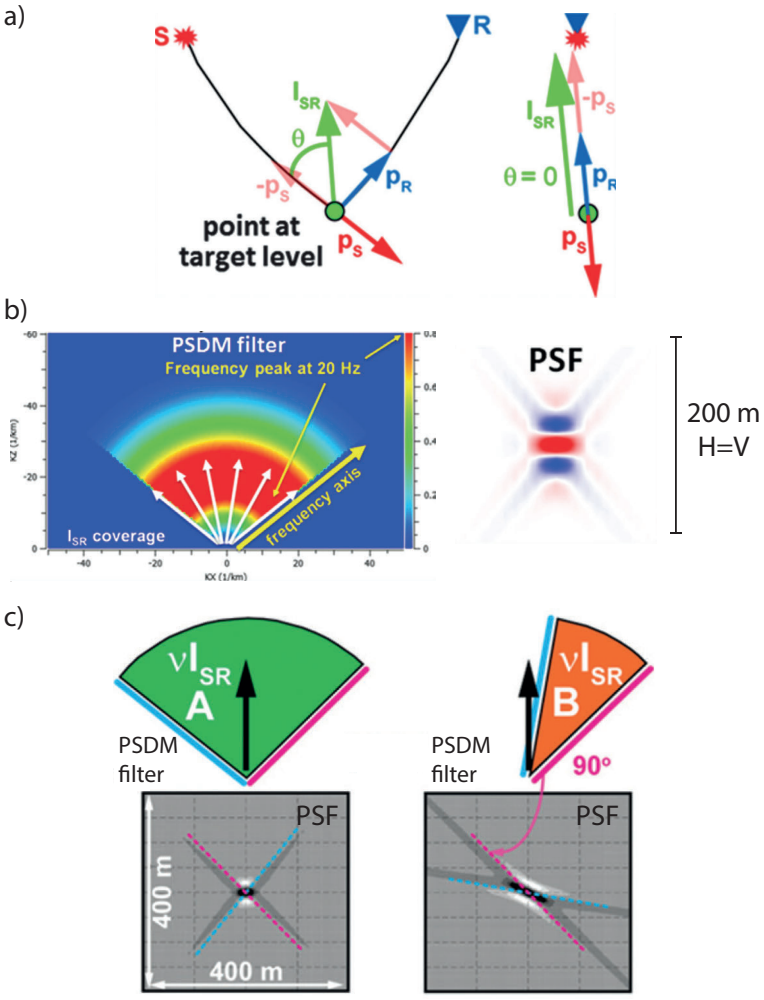

Figure 2.6: Illustration of key elements of the simulated pre-stack local imaging method (after Lecomte et al., 2015). Illumination vectors are calculated as a (a) vector subtraction of the slowness of the incoming and outgoing wave, (b) using a distribution the incoming frequency spectra along an illumination path the PSDM filter may be generated and converted from frequency to space for application as a point spread function. These functions provide additional information (c) on the optimal orientation of reflectors for illumination.

A standardised synthetic model has long been used in the seismic processing industry to understand how to address key challenges in processing such as lateral velocity contrasts and complex geometries (Brougois et al., 1990; Versteeg, 1994), and more recently attributes anomalies such as amplitude versus angle (Martin et al., 2006).

Models such as these are evidently useful, however it is suggested the present use of a very limited number of complex geometries that are not necessarily geologically likely, may be better achieved through the use of a set of geologically realistic situations that are challenging to processing.

The hand is the cutting edge of the mind.

Jacob Bronowski

Chapter 3

Workflow development & testing

Chapter structure:

3.1 Introduction

Seismic forward modelling requires consideration of a broad range of parameters. Robust application requires standardisation of the process that will be discussed in this chapter. Here, I outline the overall framework of modelling to be used throughout the thesis. Subsequently, individual chapters describe deviations from this generic workflow as required. To facilitate this, a workflow diagram has been developed that will be referred to in each chapter to provide a consistent point of reference for comparison (Fig. 3.1).

Dividing the process into three parts facilitates discussion in the three fundamental elements that define the modelling process; geometry definition, compositional modelling and seismic imaging. Geometry definition provides the structural geometry within which compositional parameters may be distributed. Compositional modelling is used to define the rock properties that will come to define the reflectivity series. Seismic imaging parameters then define aspects of the geophysical process of acquisition and simulation of imaging.

3.2 Geometry definition

Geometry definition provides the framework within which compositional information and elastic properties are distributed. Figure 3.2 illustrates geometric data may be captured through delineation of interfaces across which elastic properties vary. These variations may be captured in two manners, by defining the interfaces as surfaces labelled with details of the contrast, or by representing elastic properties as a regularly sampled grid throughout the volume.

Using either approach requires definition of geometry in Euclidean space as structured grids of quadrilaterals or cuboids; or, unstructured grids of triangles or tetrahedra. In structured grids the design of the data table is inherently representative of the underlying spatial relationships, simplifying some computational aspects of analysis. Meanwhile

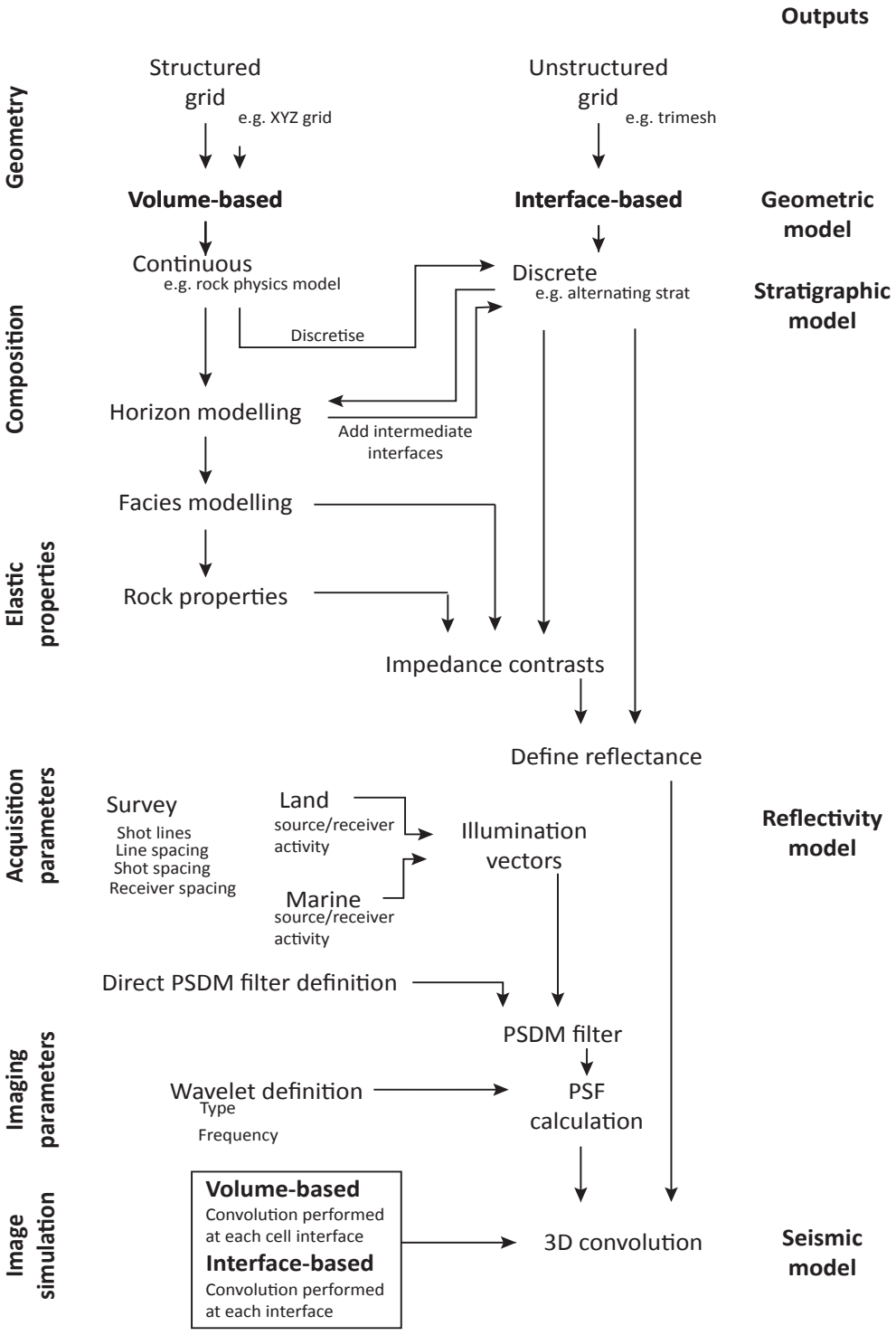

Figure 3.1: Workflow diagram illustrating the relationships between the six principle areas of work for a seismic forward model and their outputs.

unstructured grids, often referred to as meshes, store spatial data and attributes separately, using look-up tables to relate the two (Farrashkhalvat and Miles, 2003).

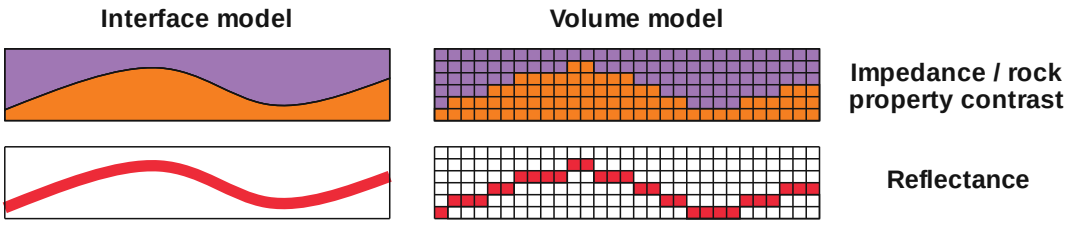

Figure 3.2: Illustration of difference in the style of subsurface representation offered by the interface- and volume-based modelling methods. Note that representation of a surface as a single interface allows application of a single impedance contrast.

3.2.1 Interface-based modelling

An interface-based modelling (IBM) defines the subsurface as a set of interfaces representing the boundaries between each area of differing elastic properties. Each interface is limited to representation of a single impedance contrast, as a structured or unstructured grid.

Structured grids, in subsurface applications, are typically two-dimensional grids, divided into grid cells regularly spaced along each dimensional axes (e.g. volume model of Fig. 3.2). Any topographic variation may be captured as an elevation attribute allocated to each grid cell. As a result cells may be represented in a table within which the spatial relationship of cells is emulated by the table structures, cells neighbouring each other in a table view will also be spatial neighbours.

This allows efficient spatial calculations to be applied a matrices directly to the table formatted data. However, consideration of elevation as a cell attribute rather than a geometric attribute implies that only a single elevation point (z) may be used for a given lateral location (x,y). This presents a key challenge in application to areas of overlying or overturned horizons.

The data structure may also cause a memory issue as neighbouring cells with identical values take up memory allocation. This results in efficient data access, but increases data storage requirements.

Unstructured grids allow multiple elevation values (z) for a given set of lateral coordinates (x,y) enabling models of more complex structures. Their unstructured nature requires use of look-up tables as the geometric attributes are stored in three-dimensions, with other attributes (e.g. elastic parameters) stored separately. This allows for irregular sampling across and area, with increased mesh spacing in areas of low attribute variance and the association of a single attribute measurement with multiple areas of a mesh (Mavriplis, 1996).

In geoscience, unstructured grids commonly take the form of triangular meshes generated using Delaunay triangulation (Delaunay, 1934). This approach allows for efficient representation of data in a format suitable for modelling and subsequent visualisation (Zehner et al., 2015; Görz et al., 2017).

3.2.2 Volume-based modelling

Volume based modelling (VBM) stores elastic properties as a three-dimensional structured grid, in the same format as structured corner point grids applied in reservoir modelling (Ringrose and Bentley, 2015). Each cell contains the value representing an elastic property for that space. During seismic modelling the contrast between elastic properties of each neighbouring cell boundary must be calculated to provide reflectivity, significantly increasing the runtime compared to the interface based method.

Sampling of these grids must be small enough to avoid introducing artefacts, increasing storage and processing requirements. However, the approach facilitates the generation of structurally complex models as cells may be allocated any property, allowing modelling of overturned and overlapping horizons.

The size of these property grids necessitates their storage in binary format, requiring

custom programming for interaction and visualisation.

3.2.3 Comparison of methods

A key difference in the modelling approach of these two methods is their handling of faults. Volume based models consider faults as a composite of across-grid cell boundary contacts, making a stair-step like fault. Interface based models do not directly model faults, they model only the deformation of strata around them. To model faults directly using IBM would require discrete interfaces to be generated for every impedance contrast formed by across-fault juxtaposition. This proved to be impractical to achieve using open source software to edit triangular mesh surfaces.

Using a simple fault model, fully introduced in Chapter 4 (Fig. 4.1), both approaches were applied to the full workflow, testing various parameters and allowing direct comparison of results of the IBM and VBM approaches. A histogram of the amplitude composition (Fig. 3.3) and compilation of the frequency extractions from across the fault plane (Fig. 3.4) for these two approaches are used to consider differences.

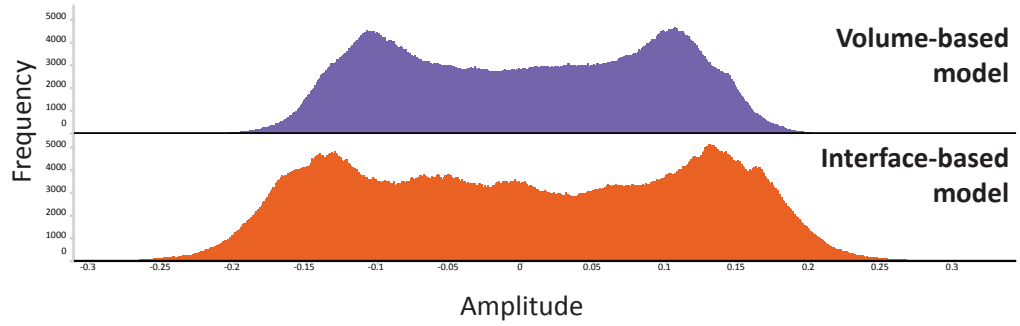

Figure 3.3: Histogram of amplitude response from interface- and volume-based methods as applied to a single geometry.

Amplitude responses using VBM appear slightly smoother, possibly due to increased noise related to orthogonally oriented cell boundaries, while IBM feature some subtle deviations from a similar overall geometry. It is suggested that these may be due to more direct observation of asperities in geometry, providing a stronger response from offsets

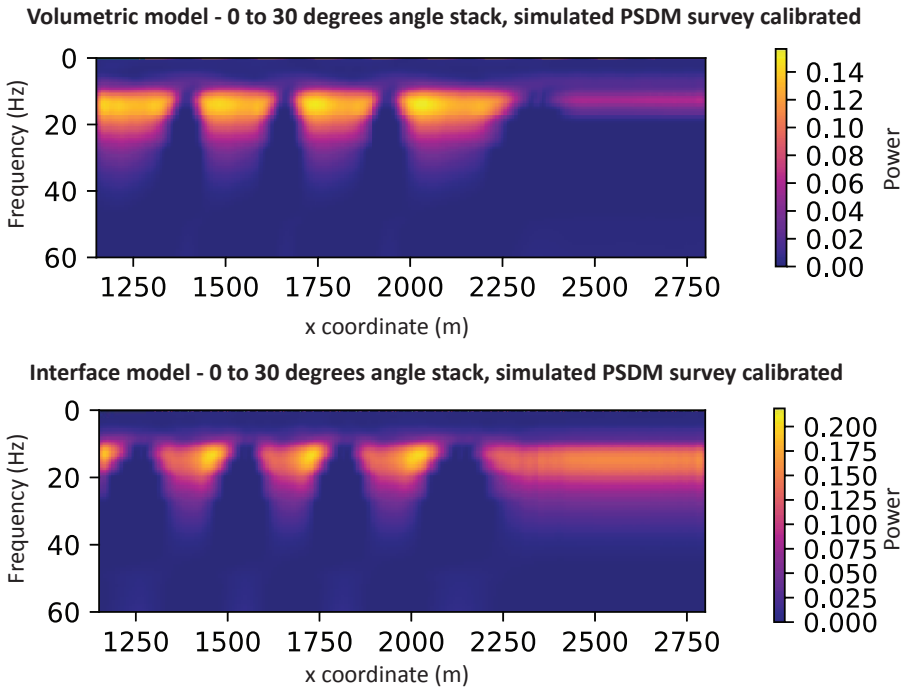

Figure 3.4: Frequency extraction from a volume- and horizon-based methods applied to a single geometry.

associated with faulting. Frequency anomalies indicate a similar overall pattern of tuning anomalies, though with subtle variations in the distribution of the highest power signal.

3.3 Compositional modelling

To calculate reflectivity the impedance contrast must be known, either directly or through knowledge of the contrasting elastic properties across a boundary. Two approaches are employed in these models; firstly, use of a simple alternating stratigraphy with velocities representing average rock properties for sand and shale, or; secondly using a simple rock physics model to introduce depth dependence, representing variation of velocities for different lithologies with representative compaction trends.

3.3.1 Alternating stratigraphy model

A simple alternating stratigraphy has been applied in most modelling presented in this thesis. Representative values for elastic properties have been selected from data presented in Mavko et al. (1998) (Table 3.1). These data represent water saturated sandstone measured using a sonic tool at an effective pressure of 30 to 40 MPa (Han et al., 1986). Median values are taken of compressional- and shear-wave velocities (V_p & V_s) and density (ρ).

Rock	Sandstone	Shale	Shale2	Basement
V_p (kms^{-1})	3.2	2.4	2.8	4.3
V_p/V_s	1.7321	1.7321	1.7321	1.7321
ρ_b (kgm^{-3})	2.3	2.15	2.22	2.65

Table 3.1: Rock properties used for seismic forward modelling throughout the thesis (after Mavko et al., 1998).

In application, geometries are subdivided into different elements and populated with these properties. In addition to affecting the seismic reflectivity of normal incidence reflections, they will also impact the nature of amplitude variation with angle (and therefore amplitude versus offset), as illustrated in Figure 3.5.

3.3.2 Depth dependent rock physics model

A more advanced model has also been generated, using simple rock physics relations to model the variation of porosity and bulk density with depth for a typical sand and shale (Fig. 3.6). The depth curve is modelled to a depth of 4 km with exponential porosity decline, equation (3.1) (Athy, 1930; Hedberg, 1936). Parameters used here from Sclater and Christie (1980) are observed in the North Sea. This method has been chosen for consistency with other work in lieu of some more recent methods, e.g. Martin and Wood (2017).

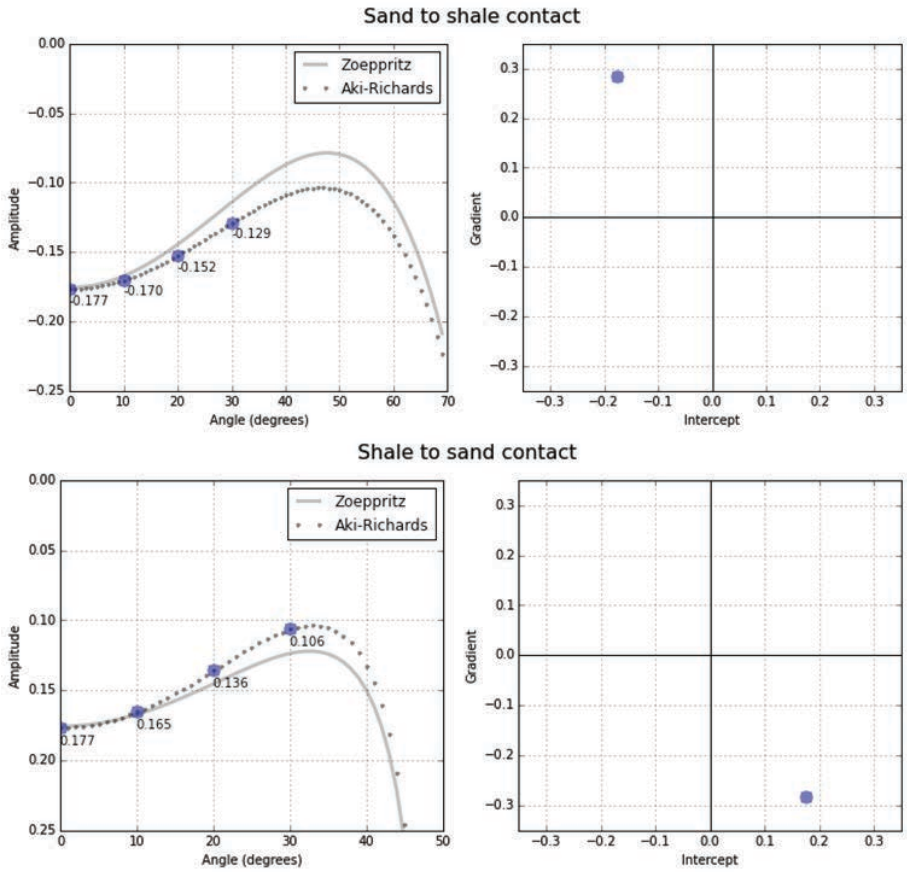

Figure 3.5: Amplitude versus angle response for sand to shale, and shale to sand, impedance contrasts.

$$\phi_z = \phi_0 e^{-cz} \tag{3.1}$$

Where; ϕ_z is the porosity at a given depth and ϕ_0 is the initial porosity. Table 3.2 details parameters used to calculate compaction curves. Knowledge of these curves combined with idealised densities for the solid and fluid components of rock provide input for calculation of bulk density, equation (3.2), and application of mixing models to calculate representative elastic moduli. Rock density is calculated for the solid components using representative densities from the literature assuming a typical composition of quartz and clay. Clay volumes were assumed to be 45% for shales and 10% for sandstone.

$$\rho_b = (1 - \phi)\rho_{gr} + \phi\rho_{fl} \tag{3.2}$$

Where; ρ_b is bulk density, ϕ is porosity and ρ_{fl} is fluid density.

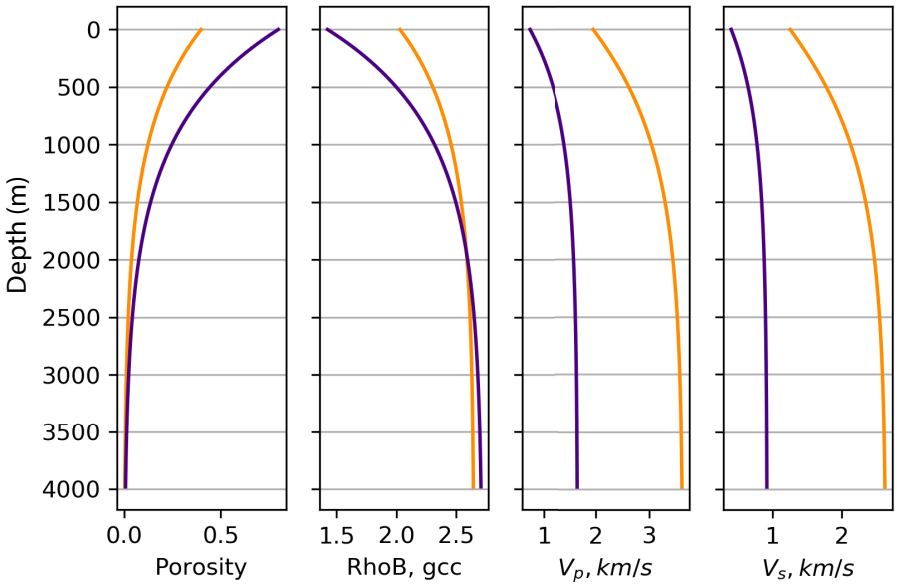

Figure 3.6: Synthetic porosity (ϕ), bulk density (ρ_b), p-wave (V_p) and s-wave (V_s) velocities for sand and shale (orange and purple, respectively).

Parameter	Symbol	Sand	Shale
Compaction factor	c	0.51	0.51
Initial porosity	ϕ_0	0.4	0.8
Grain density	ρ_{gr}	2.65	2.72

Table 3.2: Properties used for compaction modelling from Sclater and Christie (1980) and Avseth et al. (2005).

Elastic moduli for the mixed rock are based on mixing of representative elastic moduli for each mineral component (Table 3.3). The elastic moduli of a composite rock is determined by textural characteristics in addition to the moduli of its component elements. As a result calculation of moduli from compositional parameters provides bounds to the moduli rather than an individual value (Mavko et al., 1998; Avseth et al., 2005).

The Voigt bound, M_v, provides an upper limit by taking the arithmetic average of the moduli of material phases, equation (3.3). This assumes that textural changes cannot lead to a material being stiffer than the average of its constituents. As this forms the ratio of

Material	Bulk modulus	Shear Modulus	Units
Quartz	38	44	GPa
Clay	20.9	6.85	GPa
Pore water	2.15	-	GPa

Table 3.3: Mineral elastic properties used for calculation of the mixed mineral rock properties.

the average stress to the average strain it is sometimes referred to as the isostrain average (Voigt, 1890). The Reuss bound, M_r, provides a lower bound (Reuss, 1929) by taking the harmonic average of all constituents, equation (3.4). This provides the ratio of the average stress to the average strain assuming all constituents have the same stress (the isostress average).

$$M_v = \sum_{i=1}^{N} f_i M_i \tag{3.3}$$

Where, f_i is the volume fraction of the i^{th} constituent, and M_i elastic modulus of the i^{th} constituent.

$$M_r = \sum_{i=1}^{N} \frac{f_i}{M_i} \tag{3.4}$$

Due to the simplicity of their calculation and underlying assumptions, these bounds may be applied in the same manner to any elastic moduli. Here they are used to calculate both the bulk and shear moduli (K $[kgm^{-1}s^{-2}]$ and μ $[kgm^{-1}s^{-2}]$, respectively). An average taken to provide a simple but realistic estimate of moduli, as in equation (3.5) (Hill, 1952), referred to as the Voigt-Reuss-Hill average (Mavko et al., 1998).

$$M_{vrh} = \frac{M_v + M_r}{2} \tag{3.5}$$

The Voigt-Ruess-Hill average provides a the mixed moduli of a multi-mineral rock, that when used with equations (3.6) and (3.7) provide representative seismic velocities for compressional (V_p $[ms^{-1}]$) and shear (V_s $[ms^{-1}]$) waves.

$$V_p = \sqrt{\frac{K + 4/3\mu}{\rho}} \tag{3.6}$$

$$V_s = \sqrt{\frac{\mu}{\rho}} \tag{3.7}$$

Where K is the bulk modulus, μ the shear modulus and ρ_b the bulk density of the rock the wave is passing through.

These velocities may be used with the bulk density as input elastic properties for seismic forward modelling. In IBM they may be used to calculate the impedance across an interface or in VBM they may be applied directly as uniform rock properties for a cell.

3.4 Acquisition simulation & imaging parameters

Acquisition simulation is not absolutely necessary for seismic forward modelling, in many published examples. Rather than simulating the complexity of acquisition, a wavelet may be used to generate a three-dimensional point spread function (Lecomte et al., 2015), that represents the energy likely to be incoming from an overlying survey.

This analytical filter approach allows consideration of the level of detail that a seismic response is likely to represent, providing an improved understanding of resolution effects and tuning anomalies. However, it will not consider the impact of the overburden in guiding and filtering incoming and returning energy.

In this thesis, all modelling simulates a survey acquisition, considering acquisition geometry, compositional and geometric effects on illumination. This section outlines details of custom derived wavelets, survey geometry and amplitude calculation.

3.4.1 Source wavelets

Imaging the subsurface is dependent on the convolution of a source wavelet with a impedance contrast (Simm and White, 2002). In reality the source wavelet would be determined by the mechanism of source generation, however in modelling it is also dependent on data processing. Optimally the source wavelet would be recorded during

acquisition, used during processing (Ziolkowski, 1991; Ziolkowski et al., 1998) and transformed so that the post-processing wavelet is known; unfortunately this is not practised. Instead wavelets are typically derived as an analytical signal defined by a small number of parameters or through statistical wavelet extraction from processed data.

Analytical wavelets such as those defined by Ricker, Ormsby, Berlage and Butterworth are commonly used in seismic modelling (Ryan, 1994; Simm and Bacon, 2014). They offer repeatability and definition by a small number of simple parameters to produce wavelets broadly representative of those observed.

Wavelet estimation approaches utilise either statistical correlation within a seismic volume or comparison to well data in the time (Walden and White, 1984; White and Simm, 2003) or frequency (Walden and White, 1998) domains. Unfortunately, comparison of data observed at different scales introduces a number of potential pitfalls, such as use of inappropriate smoothing (Duchesne and Gaillot, 2011) or the 'leakage' of spatial geological data into the wavelet (Skauvold et al., 2016; Edgar and van der Baan, 2011).

Recent work, suggests a hybrid solution between the two could be most appropriate, fitting simple parametric signal to observed extracted waves. This maintains repeatability and uniformity between experiments, while better fitting the observed data (Skauvold et al., 2016).

Analytical wavelets are used throughout this body of work to maintain relevance to the broadest range of potential applications. There are many analytical signals to choose from (Cerveny and Brown, 2003), in this study I focus on the Ricker, Berlage, Ormsby and Butterworth wavelets (Fig. 3.7, 3.8 and 3.9). These wavelets have been produced using custom scripts by the author, based on published equations from the literature and compared to equivalent wavelets produced from the propriety software SeisRoX (NORSAR) and Petrel (Schlumberger).

The Ricker wavelet (Ricker, 1943, 1953a) has been broadly applied, partly due to its simplicity of calculation. Some argue that despite the wavelets prevalence, it fails to

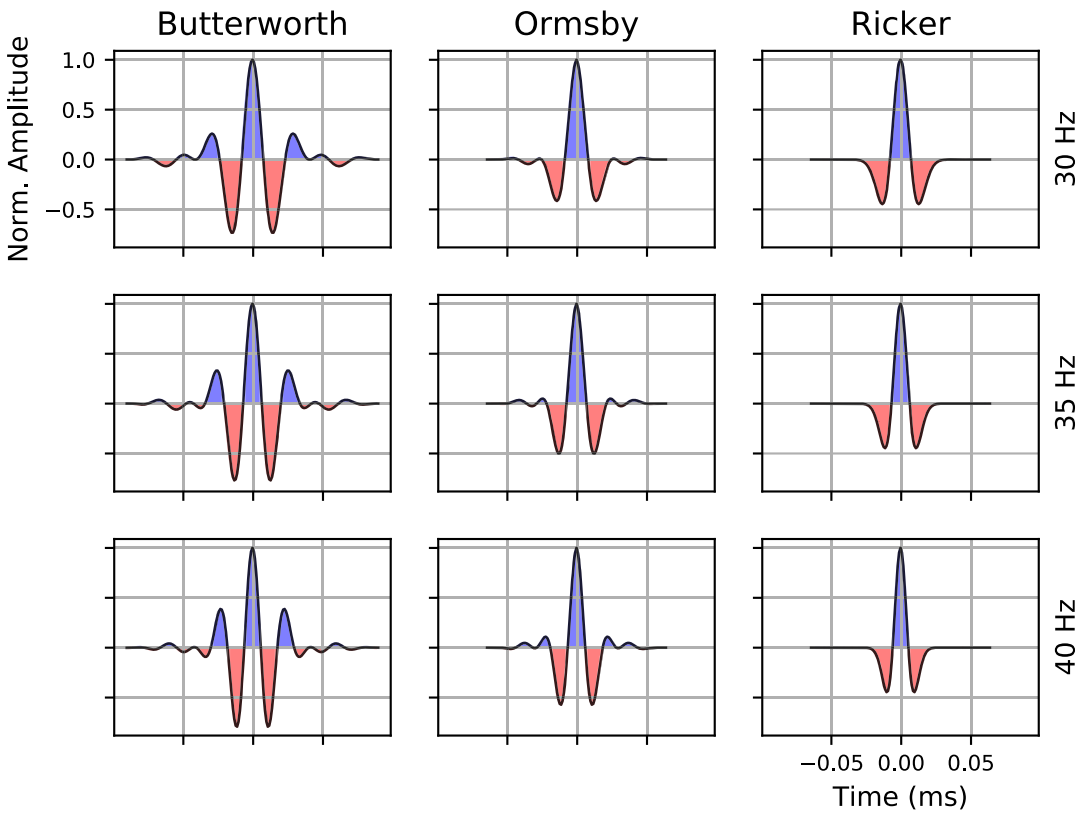

Figure 3.7: Ricker, Ormsby and Butterworth wavelets at frequencies of 30, 35 and 40 Hz, as used in simulations. Graphs represent normalised amplitude (unitless) against time (ms).

emulate naturally occurring wavelets (Hosken, 1988). While this may be valid, the nature of this simulation requires a wavelet that emulates the processed waveform, rather than the source waveform. In this, the Ricker wavelet offers perhaps the simplest method of robust estimation (Gholamy and Kreinovich, 2014).

The Ricker wavelet has a fixed relationship between wavelength and amplitude and hence is simply approximated with only the frequency, f, defined to provide the amplitude as a function of time, $a_{(t)}$, equation (3.8) and Table 3.4.

$$a_{(t)} = (1 - 2\pi^2 f^2 t^2) e^{-\pi^2 f^2 t^2} \tag{3.8}$$

The Berlage wavelet defined in equation 3.9 (Berlage, 1932), is a non-zero-phase wavelet

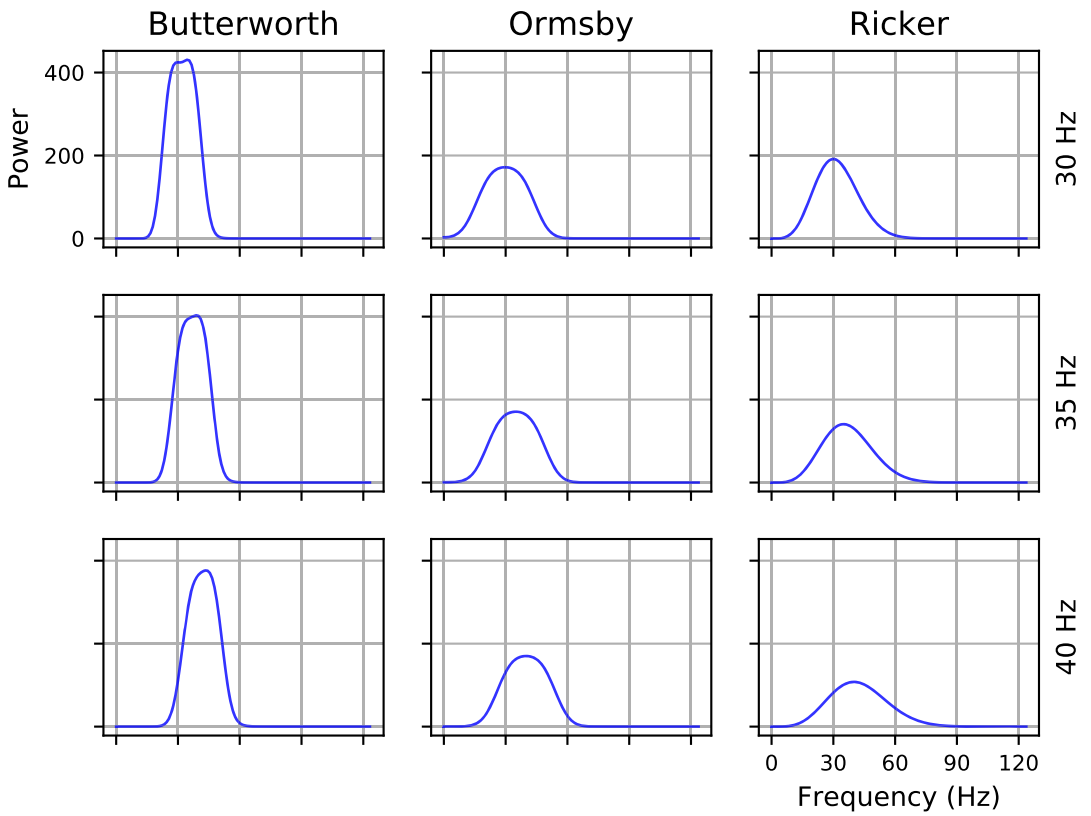

Figure 3.8: Frequency spectrum for Ricker, Ormsby and Butterworth wavelets, illustrated at frequencies of 30, 35 and 40 Hz. Wavelets are generated, transformed and presented in the Fourier domain.

applied by some authors in forward modelling (Gjøystdal et al., 2002; Lecomte, 2004) to simulate a shot source (Aldridge, 1990). In this study the Berlage wavelet is rotated to zero-phase to simulate a post-processing wavelet. Subsequent discussion with software developers suggested that customised wavelets such as the other discussed here should be used instead (Lecomte, I., 2015, pers. comm.), to better emulate the nature of a post-processing wavelet.

$$w_{(t)} = AH(t)t^n e^{-\alpha t} cos(2\pi f_0 t + \phi_0) \tag{3.9}$$

Where; H(t) is the heavy-side step function of time, t (seconds), where $H(t) = 0$ for $t =< 0$ and $H(t) = 1$ for $t > 0$. A amplitude scalar, n time exponent, α decay factor (radians per second), f_0 frequency and ϕ_0 initial phase angle (radians). The Berlage

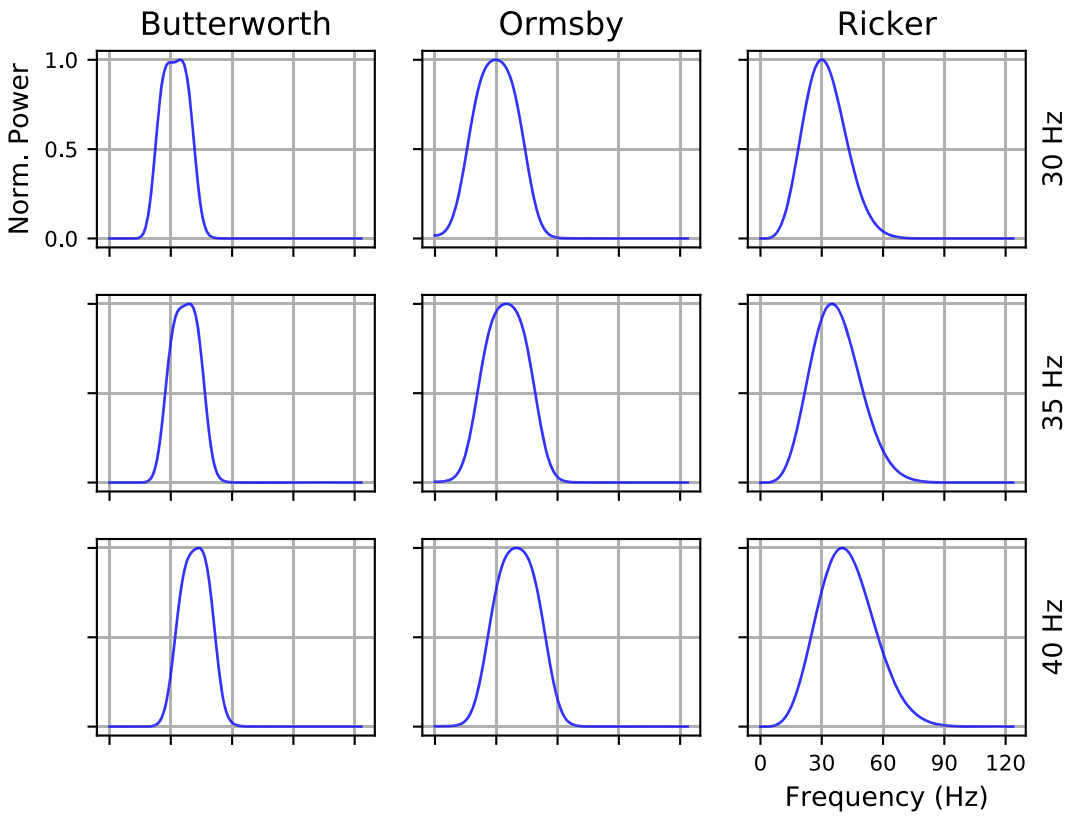

Figure 3.9: Frequency spectrum for Ricker, Ormsby and Butterworth wavelets, illustrated at frequencies of 30, 35 and 40 Hz. Wavelets are generated, transformed and presented in the Fourier domain.

wavelet is typically generated in the frequency domain and then converted by Fourier transform to the time domain.

The Ormsby wavelet (Ryan, 1994), is a zero-phase wavelet, defined by a series of frequency filters, the low-cut, f_{lc}, below which frequencies are excluded, the low-pass, f_{lp}, above which frequencies are included, the high-pass, f_{hp} and the high-cut, f_{hc} (equation (3.10)).

$$\begin{aligned} a_{(t)} = &\left[\frac{(\pi f_{hc})^2}{\pi f_{hc} - \pi f_{hp}} sinc^2(\pi f_{hc} t) - \frac{(\pi f_{hp})^2}{\pi f_{hc} - \pi f_{hp}} sinc^2(\pi f_{hp} t)\right] \\ &- \left[\frac{(\pi f_{lp})^2}{\pi f_{hc} - \pi f_{hp}} sinc^2(\pi f_{lp} t) - \frac{(\pi f_{lc})^2}{\pi f_{lp} - \pi f_{lc}} sinc^2(\pi f_{lc} t)\right] \end{aligned} \tag{3.10}$$

Wavelet	Peak frequency (Hz)
Ricker 30 Hz	30
Ricker 35 Hz	35
Ricker 40 Hz	40

Table 3.4: Definition of terms used in calculation of Ricker wavelets.

In this study, these frequencies has been related to a central frequency, f_c, to allow comparison to wavelets defined in other manners. Using the relationships derived from the equations (3.11), the wavelet parameters were set as listed in Table 3.5.

$$\begin{aligned} f_{lc} &= f_c - 15 \\ f_{lp} &= f_c - 10 \\ f_{hp} &= f_c + 10 \\ f_{hc} &= f_c + 15 \end{aligned} \tag{3.11}$$

Wavelet	f_{lc}	f_{lp}	f_{hp}	f_{hc}
Ormsby 30 Hz	5	20	40	55
Ormsby 35 Hz	10	25	45	60
Ormsby 40 Hz	15	30	50	65

Table 3.5: Definition of terms used in calculation of Ormsby wavelets.

Modelling the Butterworth wavelet is achieved by applying a Butterworth filter to an impulse in the frequency domain. This is then translated into a time domain impulse via the Fourier transform. The Butterworth wavelet used in this work have been derived from the implementation of Schlumberger in the Petrel software package. A full treatment of the wavelets derivation is discussed in detail by Curtis (1975).

As with the Ormsby wavelet, the Butterworth is defined by frequency filters, however rather than defining and pass and cut filters only cut filters are defined, with associated

cut-off slopes (typically described in decibels per octave). Again the frequency values have been defined in relation to a central frequency f_c for comparison as in equations (3.12). The parameters used to define these are described by equations in (3.6).

$$\begin{aligned} f_{ls} &= 20 \\ f_{lc} &= f_c - 10 \\ f_{hc} &= f_c + 10 \\ f_{hs} &= 40 \end{aligned} \tag{3.12}$$

	Low		High	
Wavelet	**Slope (dB/octave)**	**Cut (Hz)**	**Cut (Hz)**	**Slope (dB/octave)**
Butterworth 30 Hz	20	20	40	40
Butterworth 35 Hz	20	25	45	40
Butterworth 40 Hz	20	30	50	40

Table 3.6: Definition of terms used in calculation of Butterworth wavelets.

Comparison of these waveforms (Fig. 3.7), illustrates the simplicity of the Ricker wavelet, with a single set of side lobes. This forms a narrow band spike in the frequency domain, illustrated using a Fast Fourier Transform (FFT) (Cooley and Tukey, 1965) implemented in SciPy (Oliphant, 2007; van der Walt et al., 2011; Hunter, 2007) (Fig. 3.8). Power was calculated using equation (3.13). The Ormsby wavelet offers greater complexity with undulation of the sidelobes and a subsequent broadening of the frequency bandwidth. Similarly the Butterworth further broadens the frequency spectrum increasing the length of the pulse and introducing a flatter peak at the central frequency.

$$Power = |F(m)|^2 \tag{3.13}$$

3.4.2 Survey geometry

Acquisition surveys are typically of land or marine type, with the operational environment of each determining key aspects of the surveying strategy. In land surveys, access is often limited, leading to increases in the spacing between lines and use of irregularly spaced receiver locations. Marine surveys on the other hand are typically shot using streamers and airguns, leading to a uniform distribution of receivers relative to the shot, but constant illumination counter to the direction of ship movement.

Simulation presented in this thesis use a blend of the two, regular acquisition geometries are employed, using footprints from industry reports. All source locations are recorded as active channels throughout the whole acquisition. This set-up has been chosen in order to simulate the effect of a true acquisition geometry, while also maintaining constant elements to allow more direct comparison between models.

Unless otherwise stated surveys applied in this work feature a receiver spacing of 20 m, source spacing of 60 m, in 6 to 12 lines with 200 m line separation.

3.4.3 Amplitude calculation

As discussed in Chapter 3 this ray-based technique calculates a filter representing the illumination vectors of source to receiver ray paths within the background velocity model (Lecomte et al., 2003). An inverse Fourier transform is then used to transform this PSDM filter from the frequency domain to the spatial domain, forming a 3D point spread function that may be convolved with a 3D reflectivity model to form the synthetic seismic volume (Lecomte et al., 2015).

Reflectivity is calculated using the Zoeppritz equations, providing an angle dependent stack, representative of a range of offsets. A model is run at every 5° from 0 to 30°, each is then calibrated to the reflectivity of a single horizontal impedance contrast across the centre of the volume with a reflectivity coefficient of one and intercept gradient of zero.

Samples are then taken for each angle-stack interval before applying these as coefficients to each reflectivity volume using Promax (Table 4.3). Following calibration all volumes are added together and the mean response taken (see § 3.4.3). This emulates the process of angle-stacking, providing a multi-angle common-mid-point gather (Yilmaz, 2001).

Using a 3D point spread function estimates a 3D seismic response, however the reflectivity is calculated based on one dimensional vertical sampling. This causes a sampling issue for steeply dipping beds, limiting lateral sampling rate to the seismic bin size.

Zoeppritz approach

Applying the Zoeppritz equations requires direct input of the compressional and shear wave velocities (V_p and V_s) and the bulk density (ρ). Here, an approximation to the Zoeppritz equations, assuming weak-contrast of physical properties (Aki and Richards, 2002) is used to estimate p-wave reflectivity with varying incidence angle ($R_{PP}(\theta)$), equation (3.14).

$$R_{PP}(\theta) \approx \frac{1}{2}(1 - 4\rho^2 V_s^2)\frac{\Delta\rho}{\rho} + \frac{1}{2\cos^2\theta}\frac{\Delta V_p}{V_p} - 4p^2 V_s^2 \frac{\Delta V_s}{V_s} \tag{3.14}$$

Implementation of the Zoeppritz equation in Norsar Software Suite calculates the impedance contrast using one-dimensional vertical samples, sampled with the bin size. Using this approach, surfaces are sampled continuously laterally with respect to the lateral bin size, however in the case of steeply dipping surfaces, this is likely to result in discontinuous vertical sampling, resulting in reflectivity being captured as a series of point diffraction responses located along the inclined surface.

R_0-G approach

In order to avoid the vertical sampling issue described above some models featuring steeply dipping reflectors have been ran using the R_0-G approach, Aki-Richards approach

(Equation 3.15). Using this approach p-wave reflectivity for a given angle ($R_{PP}(\theta)$) may be directly applied to a surface.

$$R_{PP}(\theta) \approx R_{\theta=0} + G\sin^2\theta \approx R_0 + G\sin^2\theta \tag{3.15}$$

Direct input of reflectivity allows the user to calculate reflectivity outside of the software environment, allowing custom calculation of the reflectivity volume, avoiding one-dimensional sampling problems. To this end custom scripts were used to edit property volumes, calculating impedance directly from compressional wave velocity and density ($I = V_p\rho$). The two-dimensional first derivative is then taken to be reflectivity ($R = (I_1 - I_2)/(I_1 + I_2)$). This is calculated by taking the first derivative in each axis direction, squaring each, summing the two and taking the root, equation (3.16).

$$R_{xy} = \sqrt{R_x^2 + R_y^2} \tag{3.16}$$

This approach provides more robust representation of the seismic response of steeply dipping strata. This provides a good example of how the algorithmic implementation of standard equations can lead to difficulty in representing geometry accurately.

Amplitude calibration

Using the Zoeppritz equations or an Aki-Richards approximation, calculates an amplitude response that is dependent on fold of coverage and various imaging parameters (Yilmaz, 2001), requiring calibration. These consider variation of amplitude with the angle of incidence from and to a source and receiver. Stacked data, incorporating energy from various ray path routes, must therefore me calibrated for the amplitudes to be considered relative to geometric controls.

To address these issues, each angle-stack of a model is calibrated individually, before merging the results to form the final simulated PSDM volume (e.g. Table 3.7). Calibration is achieved by simulating the response of a horizontal plane placed in the centre of the model, using otherwise identical modelling parameters.

	Observed		Multipliers	
Angle	**Filter**	**Acquired**	**Filter**	**Acquired**
0	0.0556	0.0271	17.986	36.900
10	0.0547	0.0362	18.282	27.624
20	0.0522	0.0394	19.157	25.381
30	0.0481	0.0375	20.790	26.667

Table 3.7: Parameters used for amplitude calibration. Amplitudes are observed along a horizontal plane at the mid-depth of the model and allocated a uniform reflectivity of one and intercept gradient of zero. Multipliers are calculated to scale amplitudes observed from the geometric model runs.

The plane is allocated a reflectivity coefficient of 1 with an intercept gradient of 0. The simulated amplitude of this horizon provides a calibration point for the survey in use. This idealised reflectivity may be used to normalise results from the true model. To ensure that all angle-stacks are weighted evenly, each volume is divided by the ideal response from this reflector at that given angle, thus scaling values to a maximum response given a reflectivity contrast of 1.

Though not possible in the case of real acquisitions, this step essentially emulates the process of using well data to balance amplitudes through calculation of an impedance series and amplitude balancing with respect to convolution on a derived wavelet.

3.5 Sensitivity testing

This section discusses three sets of sensitivity testing that have been applied using the workflow described above. The images presented are used to explore the nature of simulated seismic images, using them to consider their limitations in the work to be conducted and sensitivity of the seismic method to different geometric aspects.

The methodology presented here is now tested on a set of basic geometries, before

considering more realistic fault-propagation fold geometries and subsequently an industry example applied to a real interpretation problem.

3.5.1 Basic geometries

Three basic geometric elements are generated using custom scripts in order to test the seismic forward modelling process. These geometries are each varied incrementally to form a set of spheres, monoclines and antiforms. Each of these sets are then forward modelled as interface based models to test the nature of seismic image simulation response to known geometric controls, including; dip, curvature and thinning (Yilmaz, 2001).

Monoclines

Simple monoclines (Fig. 3.10) are used to isolate the effect of dip on response. Varying dip angle from 0 to 60°. These results demonstrate sensitivity of the method up to approximately 50°, with a gradual decline in response from 20° to 50°. Above this level of dip, steeply dipping reflectors are poorly sampled and so not properly represented in the modelling output.

Although three-dimensional ray tracing is applied, the software employed calculates reflectivity from one-dimensional vertical sampling (§ 3.4.3). Using reasonable lateral cell sizes this means that a steeply dipping reflector may only be captured as an intermittent change in reflectivity. I spent considerable time attempting to resolve this issue through coding a new custom workflow to calculate reflectivity. This approach used a volume based modelling input in binary format, calculating one-dimensional reflectivity along two or three axes, depending on the dimensionality of the dataset. Using these, the root mean square response was calculated from the available dimensions.

This method was partly successful as the new calculation would include the lateral reflectivity as sampled by the lateral one-dimensional sampling intersections. Firstly, the polarity of the amplitude response in modelling is singular, should an incident

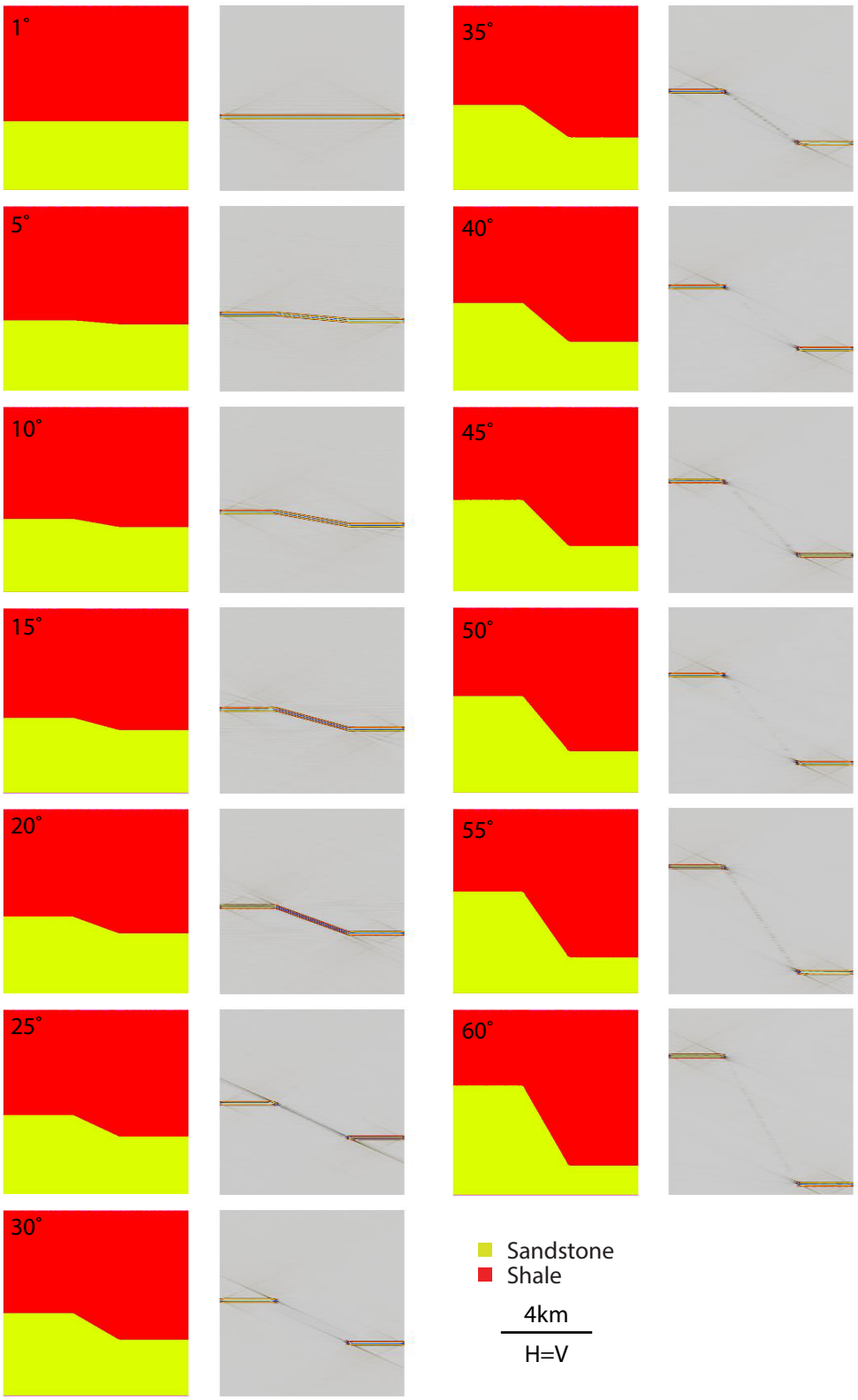

Figure 3.10: Sensitivity test of monoclines dipping between 0 and 60°, representing a shale to sand impedance contrast.

ray be travelling in the opposite direction to the calculated reflectivity, this will result in application of an inconsistent polarity to that element of the signal. Attempts to resolve this issues resulted in the decision that the most appropriate solution would be to calculate the impedance contrast during ray-tracing, rather than as a separate reflectivity calculation. This approach however would significantly increase processing time and require a level of programming skill beyond those available to the author.

Stratigraphic pinch-out

A single geometry is developed to test thinning, curvature and survey geometry. Three horizontal planes are placed with two sinusoidal antiforms between the second and third horizontal plane (Fig. 3.11). Between the second horizontal plane and the first antiform, intermediary layers are spaced proportionally between the two, forming a pinch-out geometry. The space between the two sinusoids is then also filled with a stack equally spaced sinusoids.

These results appear to indicate that dip is a more significant control on imaging quality than curvature or possibly survey spacing. Variance between models with different source and receiver spacing appears to be minimal, with the most significant effect being an increase in the noise generated by the simulator in area of no contrasts for models with larger receiver offsets (e.g. 100 s, 100 r).

In the thinned strata approaching the top of the antiform, tuning anomalies are observed coalescing to form a curved, bright responses approaching onlap. In lower strata, the opposite effect is observed to either side of the apex of the antiform as the limits of imaged reflectors are approached.

Spheres

To test the detectability of the survey, a simple resolution test is conducted using 27 spheres of varying size laid out in three rows on a horizontal plane. The first and second

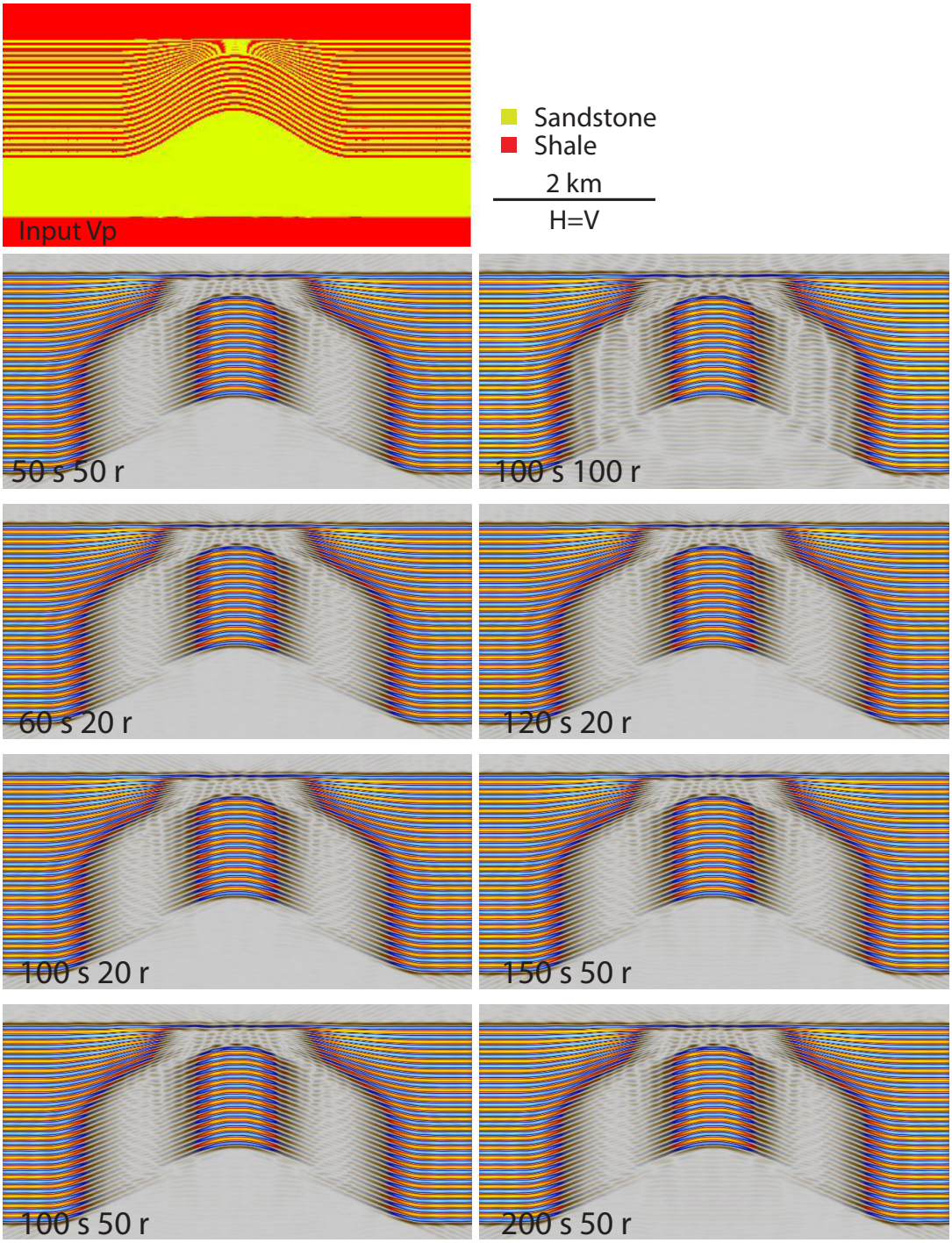

Figure 3.11: Sensitivity test of synthetic seismic image using a simple stratigraphic pinch out model. Models are labelled by their source (s) and receiver (r) spacing in metres.

row feature 10 spheres sized with a diameter each meter from 10 to 19 m and 20 to 29 m diameter. The third row features spheres of 10, 20, 30, 40, 60, 80 and 100 m diameter. A three-dimensional survey with a 30 Hz wavelet was then simulated having applied a sand to shale impedance contrast to the outer edge of all spheres (Fig. 3.12).

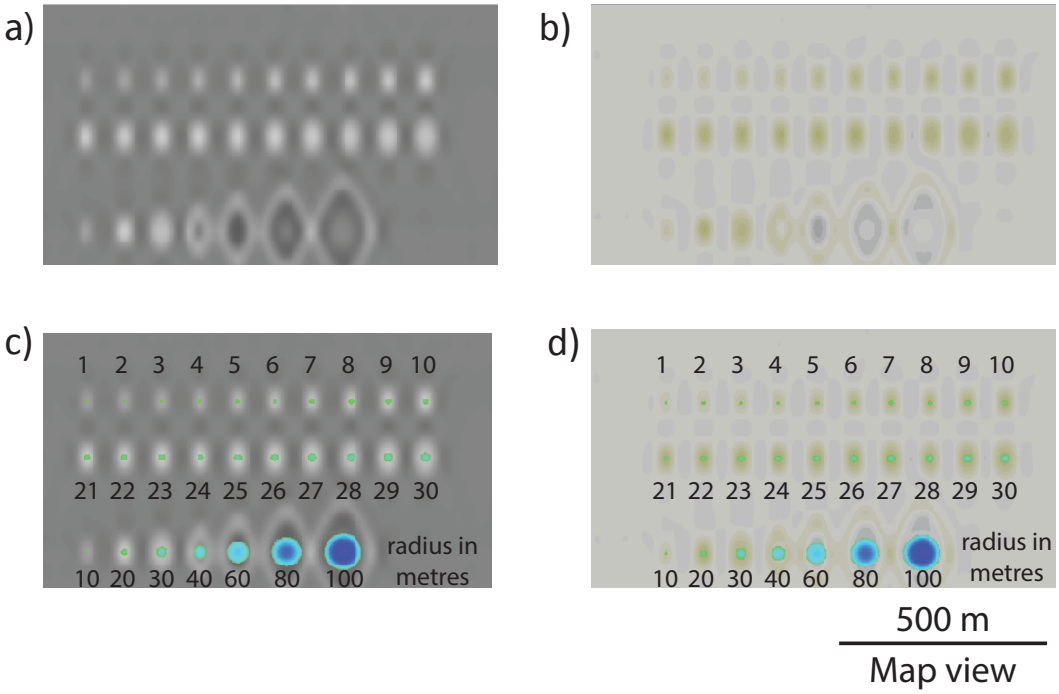

Figure 3.12: Resolution test of synthetic data using spherical reflectors.

The resultant image detects the presence of all spheres, illustrating that even below the limits of resolution the seismic signal interacts with impedance contrasts capturing their influence (Widess, 1973). In a zero noise sample such as this experiment, this suggests that detectability is far greater than would be expected in a real seismic acquisition.

3.5.2 2D thrust models

Prior to adoption of the simulated prestack local imaging method (SIMPLI), simple two dimensional ray-tracing was used to model the seismic response of a range of models. Although, these results are now largely redundant, some warrant brief discussion with

respect to their indications for the sensitivity of the seismic method in application to complex structures.

Two-dimensional ray-tracing models the propagation of energy as ray-paths through a model of elastic properties. Imagining a point source, such as dynamite or a air-gun pulse, energy will propagate away from that point as an approximately spherical wave. Ray paths provide a description of this propagation as lines drawn perpendicular to the wavefront, parallel to the waves direction of propagation.

The reduction in volume of the model in this approach increases computationally efficiency compared to direct simulation methods such as finite-difference modelling. While the approach does not capture all potential wave types, such as diffraction points or body waves, the method does provide a good approximation of the coherent signal.

Here, using basic fault-propagation fold geometries around a thrust ramp, modelled using a trishear algorithm implemented in Midland Valley's Move software, I simulate the seismic response of basic compressional geometries (Fig. 3.13).

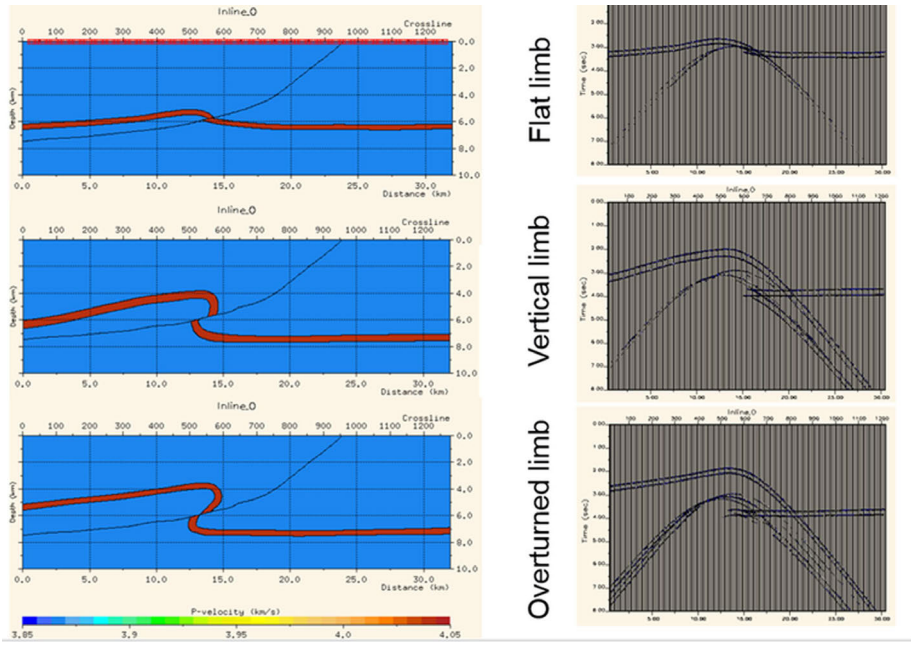

Figure 3.13: Comparison of synthetic data of different forelimb geometries.

Using normal incidence ray-tracing, these models provide an insight into the likely

post-stack time response. These produce significant characteristic refraction hyperbole, providing some indication of how significant this energy is prior to processing. Although the output is dated, one advantage of this form of modelling is the possibility to generate a spikeogram (Fig. 3.14).

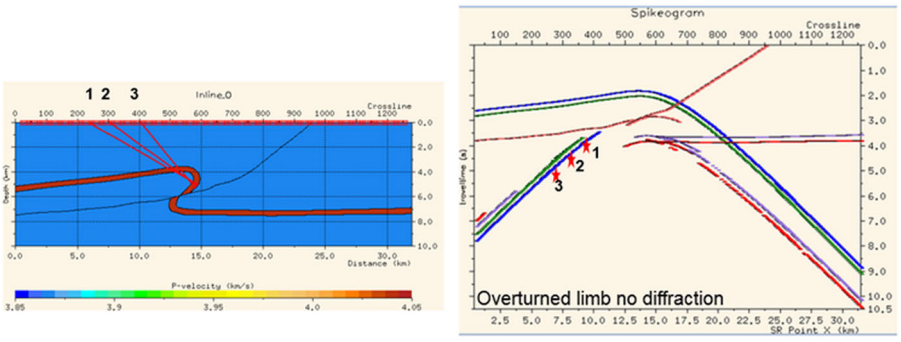

Figure 3.14: Spikeogram illustrating ray paths contributing to stacked signal.

These plots allow highlighting of the ray paths contributing energy to the seismic response at a given location. Here, the selected ray paths correspond to responses in the displayed post stack time data. This indicates that responses from the overturned limb of the fault-propagation fold are indicated in the seismic section as dipping strata in the opposite direction due to erroneous location during migration.

Considering this observation is notable that the primary discriminator between the three fault propagation models becomes not seismic but geometric as the vertical spacing between the coherent reflection in the hanging wall relative to that in the footwall becomes a diagnostic feature.

In addition to these simple geometries nine global analogues were also modelled using this approach, including:

- Sierra Barrosa, Neuquen Basin
- Puri Anticline, Papua New Guinea
- East Painter, Idaho-Wyoming-Utah Fold Belt
- Atwater Valley, Mississippi Fan Fold Belt

- Lenghu 5 Fault, Qaidam Basin, China
- Sant Cornelli Anticline, Spanish Pyrenees

These models illustrated that the difficulty in discriminating between different realistic geometries due to increased background noise and reduced coherency of reflections. Although not presented in this thesis, the principle conclusion from this work was that this form of modelling (2D ray tracing) is insufficient for informative discrimination between alternate interpretation cases for realistic geometries.

3.5.3 Illumination factors

Combining the 2D and 3D ray-tracing approaches allows further investigation of the effect of illumination in controlling the resultant image from a survey. This approach has been used to analyse the relative likelihood of two potential interpretations provided by industry partner, Ecopetrol.

The examples represent two interpretations from a common seismic section, validated by line-length balancing. As the original data is not available to the author, the results presented here (Fig. 3.15) are used for discussion of the sensitivity of the seismic response to differing geometric controls.

The sections are forward modelled using an interface model with impedance representing a shale to sand contrast. The alternate models incorporate identical overburden models, with either a duplex stack or a buckle fold towards the base, forming the economic target. As illustrated, the input models are compared and then the synthetic seismic generated with the model and then cross-referenced from one model to the other. In the comparative images a thin black line is used to illustrate the amplitude anomaly associated with the original input model.

Comparing the two models to each other illustrates the differences in amplitude responses between them. The duplex model results in a localised area of increased amplitude responses, forming a single fairly high amplitude anomaly, whereas the box-fold model

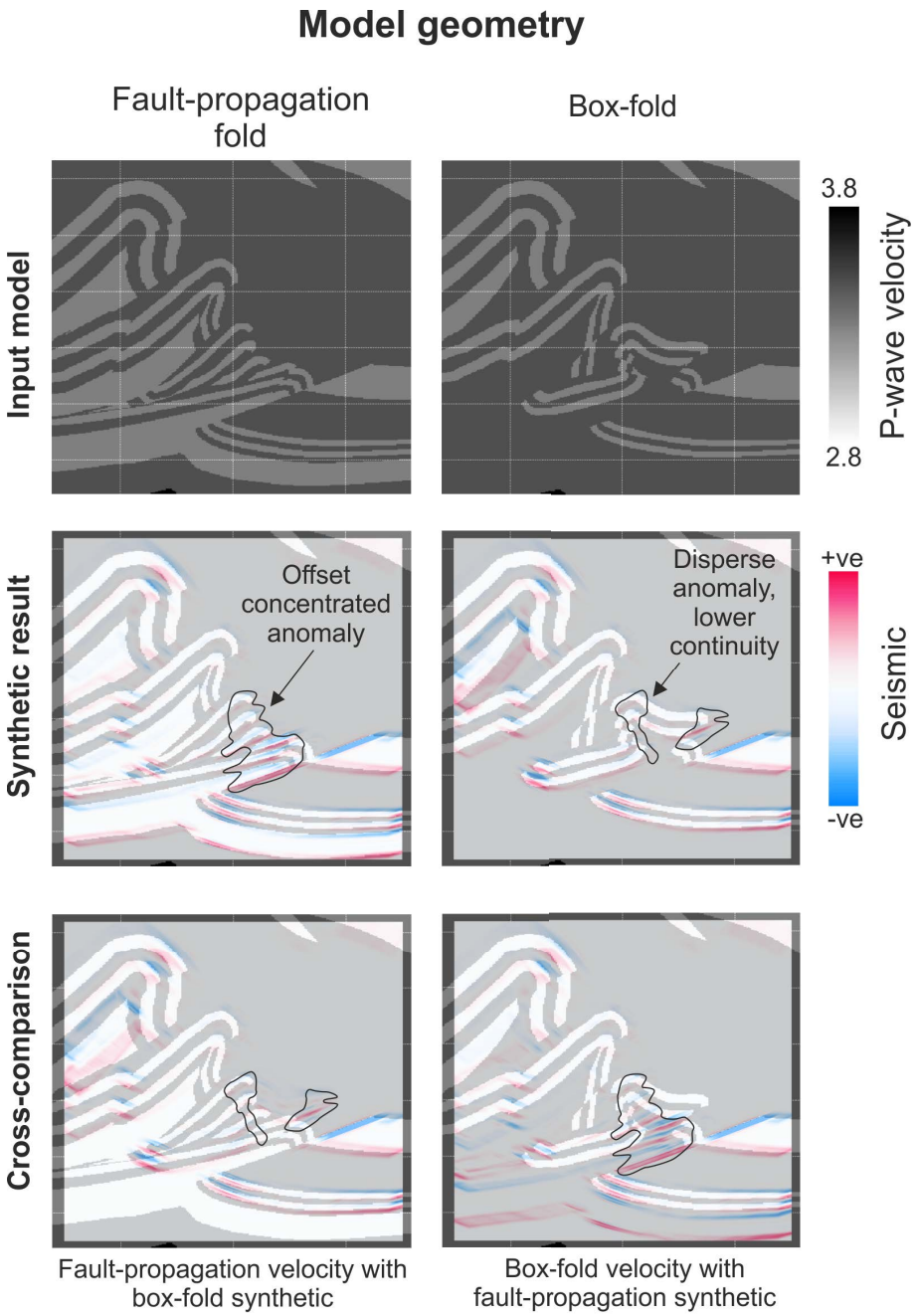

Figure 3.15: Two subsurface models and synthetic seismic based on them are used to illustrate the variation of peak amplitude anomalies. It is suggested that the difference in the nature of these anomalies may be used to aid interpretative efforts comparing the two models.

results in two separate anomalies of more moderate amplitude.

Without access to the original data it is not possible to complete quantitative analysis, however it is suggested that assuming a similar level of noise to Figure 1.1, an averaging filter passed over the amplitude, e.g. root-mean squared amplitude attribute, may provide a smoothed amplitude response to enable identification of the elevated background levels of amplitude even in the presence of significant noise and incoherent signal.

One of the primary causes of poor imaging in these scenarios is believed to be inconsistent illumination. Figure 3.16 illustrates a simple experiment considering this for the duplex scenario. Placing three artificial shot locations at constant depth in sequential locations across the model (Fig. 3.16b, c & d) a normal incidence ray-tracing experiment can be conducted, firing rays at an equal angular interval from the shot point.

These rays propagate obeying Snells law to form the normal incidence path that defines the specular reflection (Hubral et al., 1996). To have perfect illumination of the location of the experiments shot point, a source and receiver would needed at the end of each of these ray paths. Simply observing the geometry of the spread of ray paths in these images it is possible to see that this is not possible, both due to practicality of placing instrumentation and due to a need for prior knowledge of the geometry.

Using these images to consider a typical acquisition geometry featuring a regularly spaced surface array of sources and receivers, one would not expect to observe specular reflections in receivers located between 0 and -4 km for point (c), whereas reflections from points (b) and (d) would be expected (Fig. 3.16). The opposite would be true for receivers located between 1 and 6 km.

Capturing these ray paths along each shot to receiver ray path enables mapping of the expected energy loss., defining the filtering effect imposed by the subsurface (Lecomte et al., 2015). The innermost portion of this pattern forms a point spread function (PSF) mapping the frequency filter expected from incoming rays according to their angle of incidence (Fig. 3.17).

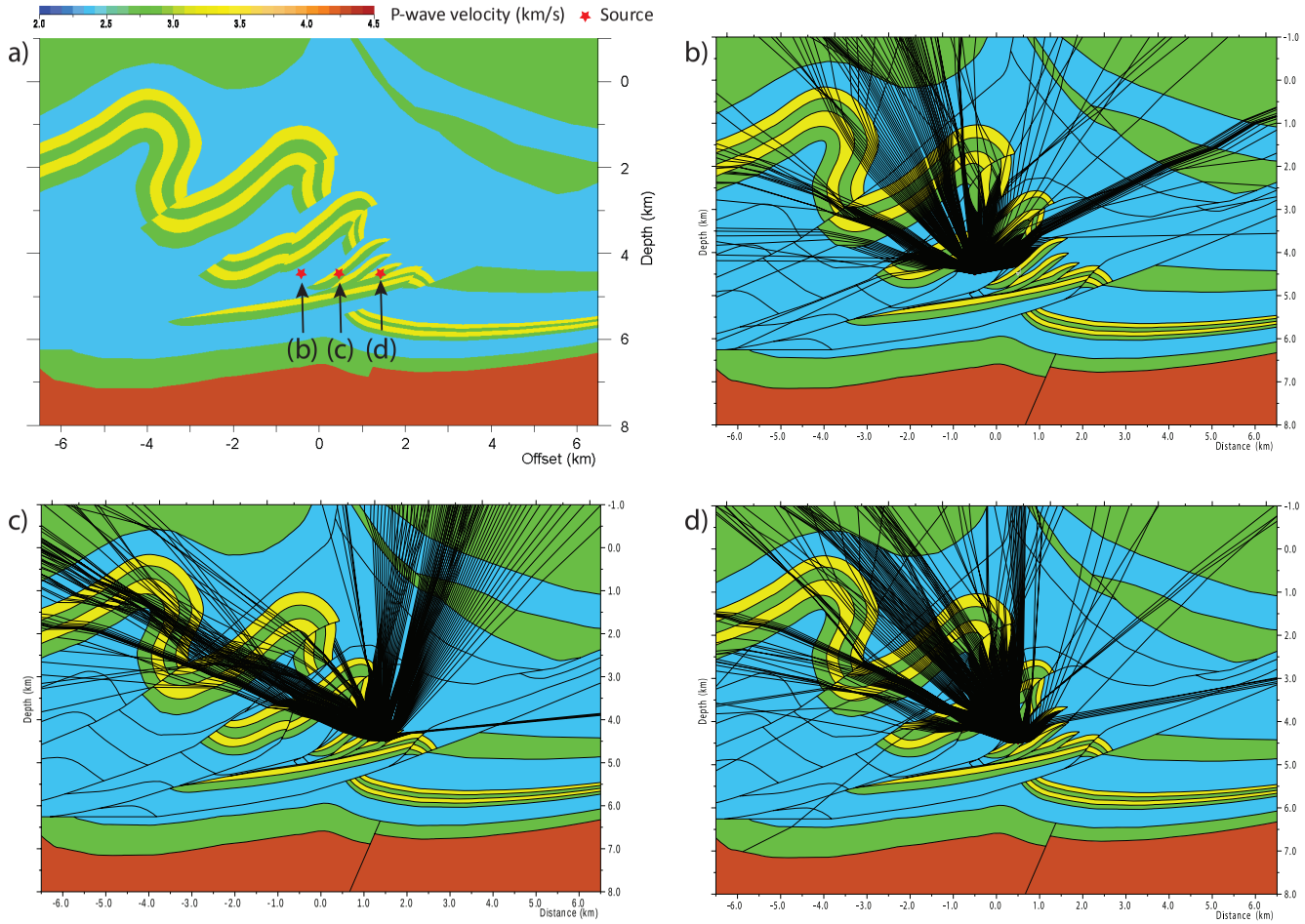

Figure 3.16: Illustration of variation in illumination dependent on overburden geometry. Three shots (a) are located beneath a stack of folds with a spacing of 500 metres. Normal incidence ray paths are projected from each shot locality (b-d) every half of a degree. A source and receiver pair placed at the end of each ray path would receiver the specular reflection.

For most models this filtering effect will be calculated for the entire model, however in larger models or models in which the overburden is expected to cause variation in anticipated illumination, the PSF can be calculated separately for different areas of the model. This allows spatially variable filtering of the ray paths (Fig. 3.18).

Reviewing the nature of the responses presented (Fig. 3.16), in consideration of the controls on seismic responses discussed in the literature review (§ 2.3), key controls on the spatial variation of amplitude response in this model are described below:

Curvature controls focussing of the signal response from source to receiver. Antiforms provide a consistent reflector across a wide range of receiver offsets, providing a consistent reflector. Synforms may focus energy over a specific interval of receivers depending on precise alignment. As the alignment required to generate a strong signal is limited, the significance of this response may be partly lost in the stacking process.

Dip direction and magnitude in places direct source energy away from receivers leading to a decreased response in fold limbs.

Overburden containing high amplitude reflectors decreases the energy transmitted to deeper reflectors, decreasing their potential amplitude before consideration of attenuation.

Depth alone does not affect signal amplitude in this model as no attenuation has been applied.

Noise is absent from the modelled sections. As such they represent the highest image quality that could be expected of this simplified stratigraphy.

Travel time is a factor in most of the above aspects, as ray-paths become more lengthily or tortuous, the energy carried by the ray will decrease.

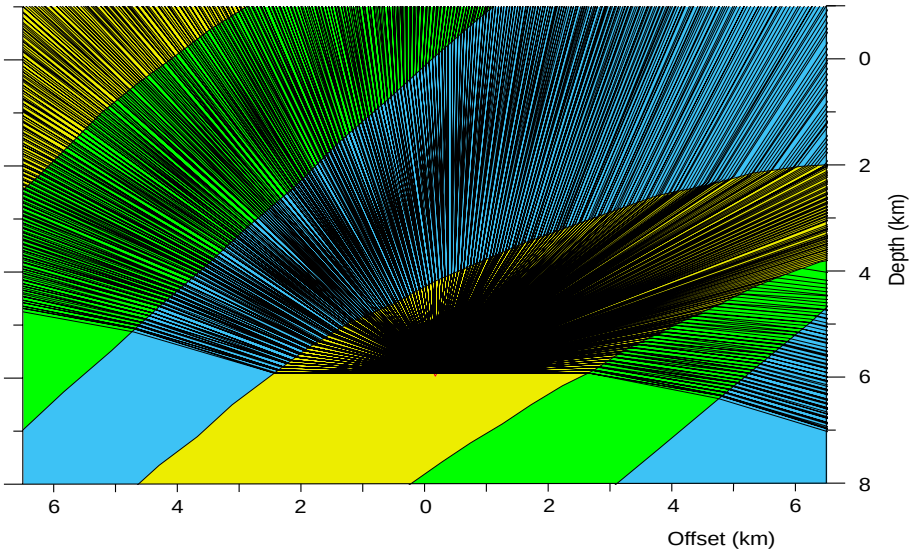

Figure 3.17: Close-up of the spreading of ray-paths from the placed shot. Note that rays are visualised from 90° to -90°, every 0.2°.

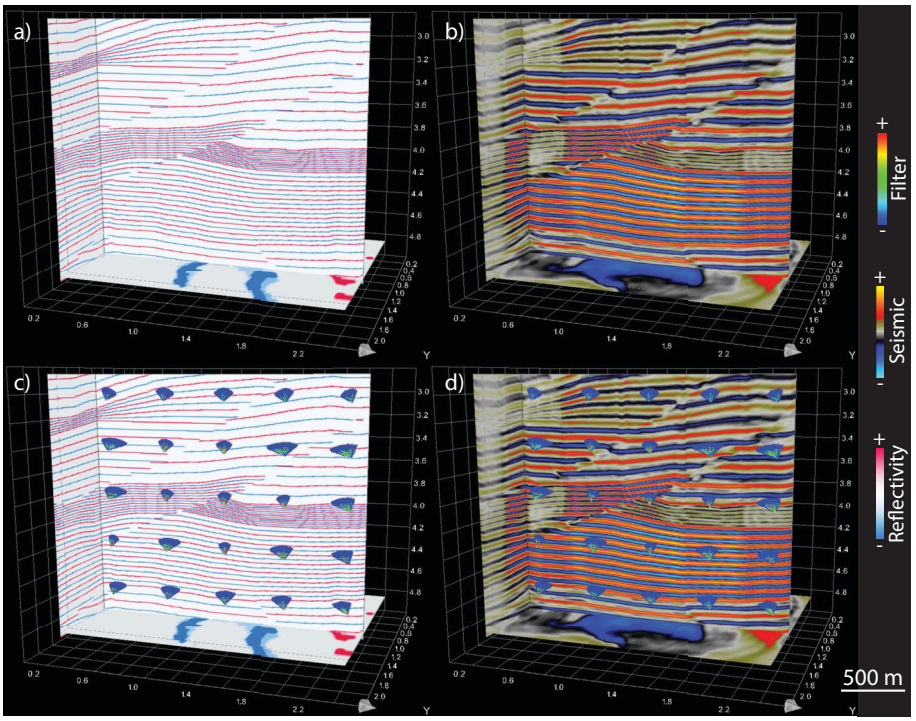

Figure 3.18: Point spread functions shown over a reflectivity series (a, c) and a synthetic seismic image (b, d) for a prospect scale model (Ch. 6).

The obscure we see eventually. The completely obvious, it seems,
takes longer.
Edward Murrow

Chapter 4

Fault interpretation uncertainty

Chapter structure:

4.1 Abstract

Faulting is observed in seismic images as offsets, discontinuities or subtle variations in seismic reflections. Using a synthetic model of a single, isolated, normal fault, this chapter investigates the manner in which faults are expressed and may be recognised in seismic data.

Seismic attribute analysis for the purpose of fault interpretation often seeks anomalies representing fault presence along their length. This work demonstrates that responses are variable along length, dependent on the nature of across-fault juxtapositions of materials with contrasting elastic properties. As such approaches founded on the principle of single attribute fault detection are flawed.

I use a machine learning approach to identify and measure the fault length recognised by different attributes within a synthetic dataset, featuring a fault of known length. This provides a means to investigate the relative efficacy of attributes in making such estimates.

It has long been assumed that estimates of fault length from seismic data will under-estimate fault length. This dataset suggests that for high signal-to-noise examples, both under- and over-estimates are possible.

Trace attributes, long applied in stratigraphic analyses are demonstrated to offer valuable structural information. In particular, seismic frequency anomalies are demonstrated to form along the fault plane around the intersections at which hangingwall and footwall horizon to fault juxtapositions cross each other.

Recognition of this causative mechanism of commonly observed anomalies is consistent with published sightings in the literature. This challenges interpretations that such anomalies must result from compositional change, indicating along fault fluid or fault zone complexity.

4.2 Introduction

In this chapter I investigate the efficacy of seismic attribute interpretation in identifying the presence and extent of a single isolated normal fault. Reducing the issue of fault interpretation to this level allows investigation of the seismic response to faulting in various seismic attributes. This progresses the focus of the thesis to application of the integrated seismic and geological modelling approach discussed in Chapters 2 and 3.

Prior work provides a thorough analysis of interpretation using acquired data (e.g. Hesthammer and Fossen, 1997a; Hesthammer, 1998), guiding modern fault interpretation practices (§ 2.3.2). However, improvements in the quality of seismic imaging lead to the recognition of more subtle interpretation problems (Dragoset, 2005).

Many existing fault interpretation workflows initially consider offsets in the amplitude of reflections and then geometric attributes (§ 2.3.3). However, it has long been known that trace attributes such as amplitude also respond to the presence of faulting (Badley, 1985; Townsend et al., 1998; Botter et al., 2014) and more analysis has focussed on attribute extractions from the immediate vicinity of faulting, demonstrating anomalies in frequency (Iacopini and Butler, 2011) and envelope (Iacopini et al., 2016).

Using synthetic seismic data, I investigate the spatial relationship between subsurface geometries and their simulated responses. This contributes an improved understanding of interpretation constraint on simple fault geometries, providing insight for application to more complex arrangements. Initially one-dimensional extractions across the fault provide insights into the presence of faulting. These are then used with image and along-fault extractions to investigate variation along trend, associated with geometric change.

A machine learning algorithm is developed to utilise these along-fault extractions to consistently pick the fault tip, providing insight as to the seismic attributes that provide most accurate constraint. Building upon observations from this work, my focus then shifts to concentrate on the use of trace attributes and particularly frequency in determining the nature of faulting.

4.3 Synthetic modelling

4.3.1 Geometric modelling

Two fault geometries are modelled, each featuring forty horizons, displaced by a single isolated normal fault. The models are named Dmax5 and Dmax10, representing the variation in their maximum displacement to length ratios, described below. This difference allows comparison of the seismic response between two models for which geometry is the only variant.

Forty horizons are initially generated as horizontal triangular mesh layers using Delaunay triangulation (Delaunay, 1934), forming a rectilinear volume of 2 km x 1 km x 0.64 km (Figure 4.1). These are tilted 1° towards the South (parallel to fault dip direction, in the YZ-plane). This rotation, moves the planar horizon surfaces away from the horizontal imposing a trend on their dip. While minor, this decreases variations in dip direction measurements as dip approaches zero. Dip in the XZ-plane of the footwall remains 0°, while in the XZ plane dip in the hanging-wall varies with modelled fault displacement.

A single planar fault inclined at 60° towards the south forms a dislocation of the surfaces, simulating horizons displaced along the fault. Displacement is modelled using the trishear algorithm (Erslev, 1991; Pei et al., 2014), with the along fault distribution of strain forming a Gaussian fault length to displacement profile. This algorithm changes the geometry of a horizon to simulate the geometric effect of deformation (Pei et al., 2014).

The fault placed with maximum displacement located at the edge of the geometric model, with the point of zero displacement, the fault tip, located three-quarters (1.5 km) of the way across the model (Fig. 4.1c). Applying the maximum displacement to fault length ratios mentioned earlier gives maximum displacements of 150 m and 300 m for the 5% and 10% models respectively (D_{max}/L), simulating a total fault length of 3km. This broad geometry is consistent with global datasets with a maximum displacement to fault length ratio of 5% (Kim and Sanderson, 2005).

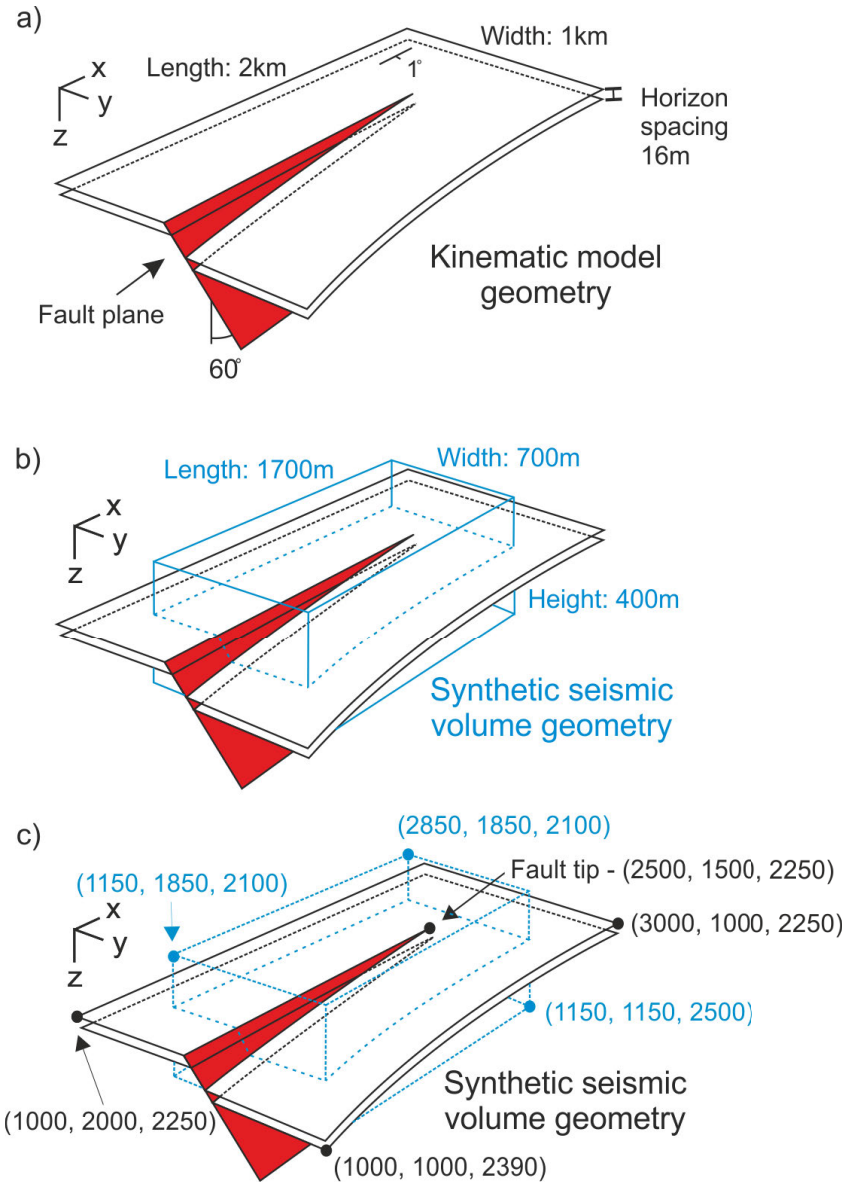

Figure 4.1: Illustration of the isolated normal fault geometry with (a) measurement dimensions used for generation, (b) the outline of the synthetic seismic volume subsequently generated from the model shown in blue, and (c) coordinates of the model edges for reference.

4.3.2 Elastic property modelling

To facilitate seismic forward modelling the geometric models must be populated with elastic properties. This is accomplished by building a three-dimensional structured grid around the horizons generated above. As the principle area of interest is structural influence on seismic response, the stratigraphic model is simplified as an alternating sequence of water saturated, low porosity, sands and shales.

Each modelled grid cell is allocated compressional and shear wave velocities with bulk densities representative of their modelled facies as described in Chapter 3 (§ 3.3). Compressional wave velocity (V_p) and bulk density (ρ_b) are selected from published datasets (Mavko et al., 1998), while shear wave velocity (V_s) are defined as a fixed ratio of compressional wave velocity ($V_s = V_p/1.73$), consistent with low porosity sand and shale lithofacies with similar pore texture (Tatham, 1982), presented in Table 4.1.

These properties are distributed as an alternating sequence of sand and shale intervals, with a bedding thickness of 16 m (Figure 4.1a). Using the definition of Widess (1973), wavelength, λ, may be used to estimate the thickness at which thin beds may be expected to cause tuning anomalies as $\lambda/8$. In this case average p-wave velocity, $\bar{v}_p = 2800ms^{-1}$ and frequency, $f = 30$ Hz, therefore $\lambda = v/f = 93.3$ and $\lambda/8 = 11.7m$. As such, the model's reflector spacing provides sufficient juxtapositions for repeated analysis, while maintaining the thickness above the level of tuning.

Property	**Sand**	**Shale**
P-wave velocity, V_p (km/s)	3.2	2.4
S-wave velocity, V_s (km/s)	$V_p/1.73$	$V_p/1.73$
Bulk density, ρ (kg/m^3)	2.3	2.15

Table 4.1: Elastic properties used in seismic forward modelling. Values for V_p, V_s and ρ taken from a sandstone with porosity of 13% Mavko et al. (1998).

Both interface and volume based models were developed for simulation of these geometries and compositions (see § 3.2). Although amplitude and frequency spectra

for outputs from the two models are equivalent (Figures 3.3 and 3.4), a volume based model is used for further modelling. This selection was made on the basis of the spatial representation of the model at the fault. An interface model by definition only models the horizons that a signal may respond from. A volume model however populates properties at every location within the model, meaning that any lateral impedance changes across the fault are explicitly modelled.

Using reservoir models to build elastic property cubes complicates the geometric expression of faulting due to the use of stair-stepped faults. This method represents faults by demarcating cell boundaries along the trend of a fault as faulted, allowing application of a flow tensor. As such, rather than a smooth planar feature, the fault is represented as a rough assemblage of approximately orthogonal cell edges. Given the increased level of effective detectability in these models (see § 2.3), this becomes a critical issue in imaging.

In response, models were built with reduced cell size, such that the dimensions would be significantly below the level of seismic resolution. This approach significantly increases processing difficulties, resulting in each of the three property cubes approaching 100 GB in file size. This increases both run times and the rate of runtime error occurrences, that prevent completion of modelling to unacceptable levels.

An intermediate approach was adopted, whereby the geological model is built at a fine cell size, passed over with a median filter and then resampled at a coarser cell size. This reduces the complexity of the model, smoothing fault plane responses, while maintaining a steep enough gradient across impedance contrasts to ensure representation of the model at an appropriate resolution.

Using this workflow, the initial sampling rate is 0.5 m vertically and 2 m laterally, parallel to in-line and cross-lines. Before down sampling, a smoothing filter is applied, having testing Hanning, Hamming and Gaussian filters, the Hanning filter is applied. This filter provides the best result balancing runtime and effective localised smoothing. Using OpenDtect 6, smoothing was applied across a window of 4 m lateral and 2 m vertically.

Achieving the same with the more computationally efficient interface-based approach

would be preferential due to the ability to use triangular mesh surfaces directly in the seismic modelling, rather than as an input for geometry building. However, only a single impedance contrast may be coded to each interface; a fault surface featuring multiple across-fault juxtapositions and therefore multiple lateral impedance contrasts across its surface would require generation of a trimesh surface for each juxtaposition interval. This may be a preferable method for future development of the work, however in this case was deemed to be overly complicated for implementation.

4.3.3 Acquisition and imaging parameters

The simulated acquisition survey is based on a proprietary industry design providing realistic illumination of the target. Shot and receiver lines are oriented parallel to, and centred on the fault, 3 km long and 2.4 km wide (Table 2). Individual shots and receivers are located coincidentally and all receiver channels are active throughout the acquisition.

Parameter	**Shot**	**Receiver**
Shot lines (units)	12	12
Shot line length (m)	3000	3000
Shot line separation (m)	200	200
Shot spacing (m)	60	60
Shot depth (m)	5	5
Target depth (m)	2300	2300

Table 4.2: Seismic acquisition survey parameters.

In comparison to real surveys this blends the nature of marine and land surveys. Typically during marine surveys the use of streamers would prevent all receiver locations being active throughout the survey, similarly on land it would be impractical to locate shots coincidently with the receiver array. As such the simulated acquisition may be expected to provide more evenly distributed illumination.

Significant illumination issues are expected even in the case of perfectly evenly distributed

illumination due to variation in wave propagation introduced by subsurface structure (Fig. 3.16). As such, this modelling approach is believed to move towards isolating the impact of illumination introduced by the subsurface rather than the survey.

Seismic image simulation is completed as described in Chapter 3, using Zoeppritz equations to calculate reflectivity, providing an angle dependent stack representative of a range of offsets. Using a 30 Hz Ricker wavelet (Ricker, 1953b; Hosken, 1988) to represent the post-processing wavelet at 2.5 km depth (Hauge, 1981), once convolved with the reflectivity profiles, this outputs a PSDM image (§ 3.4.1).

Models were run at every 5° from 0 to 30° with each subsequently calibrated to the reflectivity of a single horizontal impedance contrast across the centre of the volume with a reflectivity coefficient of one and intercept gradient of zero (Table 4.3). Following individual calibration, the mean is taken for all volumes (§ 3.4.3), emulating the process of angle-stacking to provide a multi-angle common-mid-point gather (Yilmaz, 2001). The resultant synthetic volume is used in all subsequent analysis within this chapter.

Angle gather	Filter	Acquisition geometry
0°	0.0098	0.0048
10°	0.0091	0.006
20°	0.0076	0.0057
30°	0.0059	0.0046

Table 4.3: Maximum amplitudes observed from a single horizontal plane with a known reflectivity of 1, located at the mid-depth of the synthetic model using the same acquisition survey. This process is repeated for each of the analytic filter and local-target PSDM simulators.

4.4 Seismic attribute response to faulting

From the simulated seismic volume, various attributes are calculated for comparison against the input geometry. Precise knowledge of the location and displacement along the fault then allows for investigation of the exact response of seismic data and consideration of the causation of different observations.

Four sampling geometries are used to extract data from volumes (Fig. 4.2). Horizontal and vertical intersection planes capture spatial variation in attributes assuming no a priori knowledge of the geological structure, in a similar manner to interpretation of real data. Extraction along the known dipping plane of the fault assumes knowledge of the fault location, but provides an insight to the exact nature of response along the fault surface itself. One-dimensional extractions along-fault (parallel to fault strike) or across-fault (parallel to fault dip) provide may be used with or without a priori knowledge of faulting.

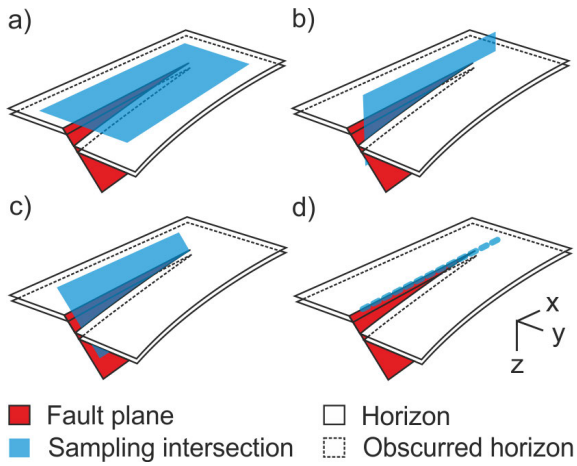

Figure 4.2: Sampling plane geometries defined with respect to the model geometry. (a) horizontal intersection plane, (b) vertical intersection plane, (c) along-fault intersection plane and (d) along fault intersection line.

I have calculated a comprehensive suite of seismic attribute volumes, including both geometric and trace attributes. These include geometric attributes; curvature, dip, and; trace attributes; amplitude, phase, dominant frequency and isolated frequency components. For dip-based geometric attributes, event, tensor and principal component

analyses have been applied.

4.4.1 Variation with fault displacement

Using a combination of horizontal intersection planes and across-fault one-dimensional extractions the attribute volumes are sampled and analysed without a priori knowledge of the structure. As discussed in § 2.3.2, faults may be expressed in seismic data in various forms.

A series of figures are used to illustrate the seismic attribute response to fault displacement. All follow the form of Figure 4.3, where an intersection is shown on the upper half of the plot, overlain with a series of regularly spaced sample lines coloured by a sequential index number. These lines are displayed again in the same colours in the lower half of the plot, showing a plot of the attribute response versus the position along the x-axis (parallel to fault strike).

To provide an intuitive example, depth to horizon is illustrated in this format in Figure 4.3. Colouring of the horizontal extraction illustrates deepening of the depth to horizon across the location of the fault. This is further represented in the lower half of the plot which takes the form of a structural cross-section.

Figures 4.4 to 4.6, illustrate the responses observed from selected geometric and trace attributes, as labelled, while Figures 4.7 to 4.9 represent selected responses from isolated frequency components, extracted as part of spectral deconvolution.

Attribute responses to fault presence may be described as broadly falling into two categories, those in which the attributes responds locally around the fault presence and those in which the fault presence is inferred by a change in the background values of the attribute across the location of faulting. These responses may take the form of changes in magnitude or variance.

Table 4.4 summarises the nature of attribute responses to faulting for the attributes illustrated in the previous figures. Notably, most geometric attributes represent the fault

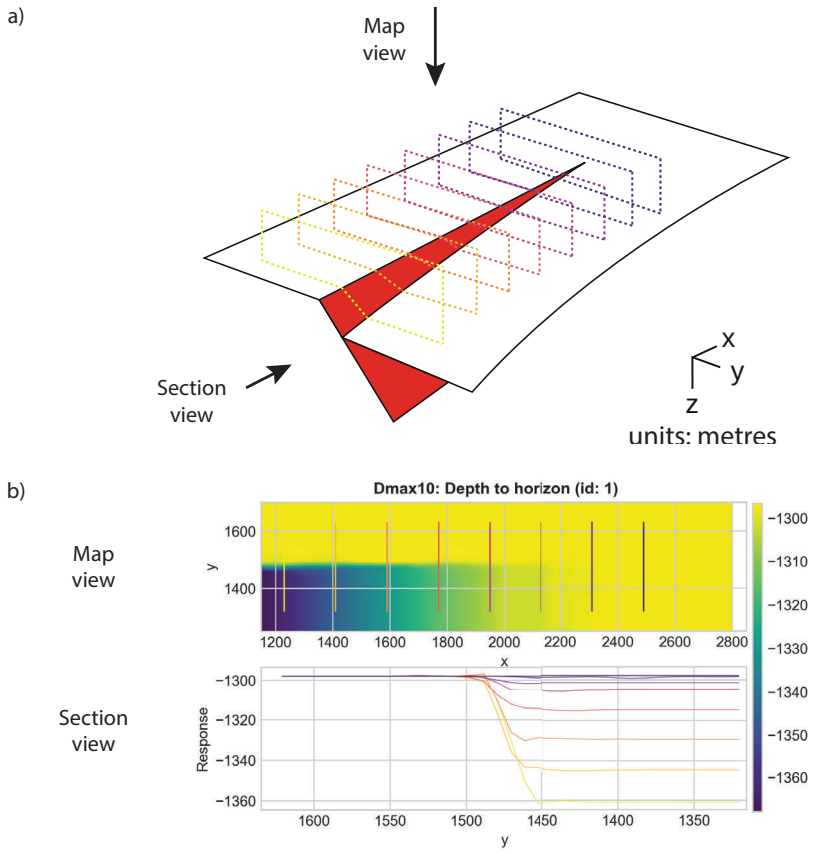

Figure 4.3: Attribute display of depth to the faulted horizon for the Dmax10 model geometry; (a) relationship between 3D model and cross-section locations, and; (b) attribute display used for each subsequent attribute. This combine a horizontal extraction from the attribute volume overlain with profile locations and a section view plotting the one-dimensional attribute extractions, colour-coded for comparison.

primarily as a local response, while trace attribute responses are more varied. None feature a simple relationship between along fault location and attribute response.

Geometric attributes are observed to feature local responses highlighting the location of the fault (y = 1480 m). In the horizontal plane extractions, this can be observed as a line extending across the image maps. In most cases, the linear pattern of response is punctuated by local maxima and minima.

Dip attributes have been calculated using the event (Dip), gradient (Dip Grad) and principal component (Dip PC) algorithms. Notably, only the gradient calculation provides

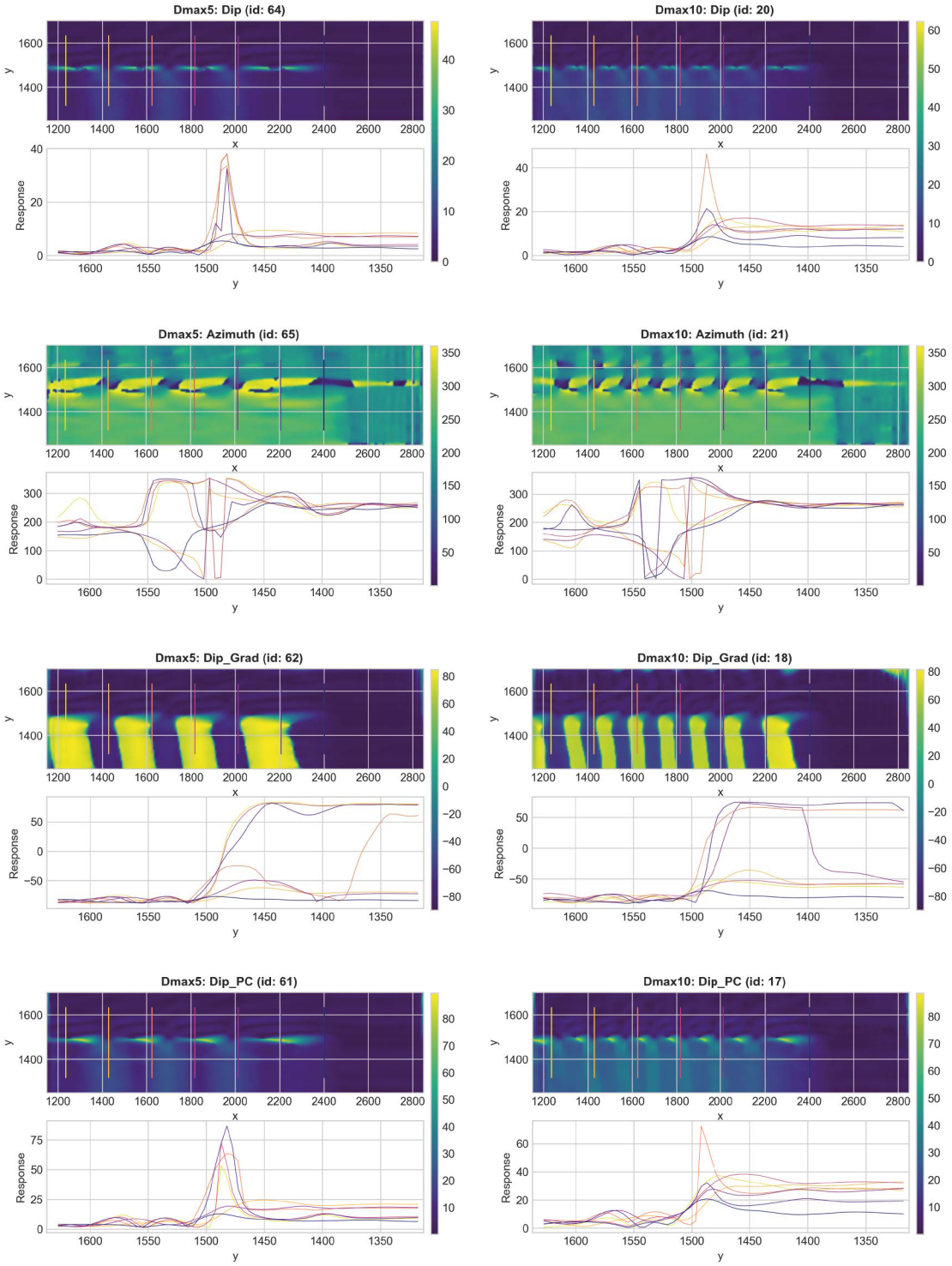

Figure 4.4: Dip and azimuth attributes from Dmax5 and Dmax10 models. See Figure 4.3 for description of layout.

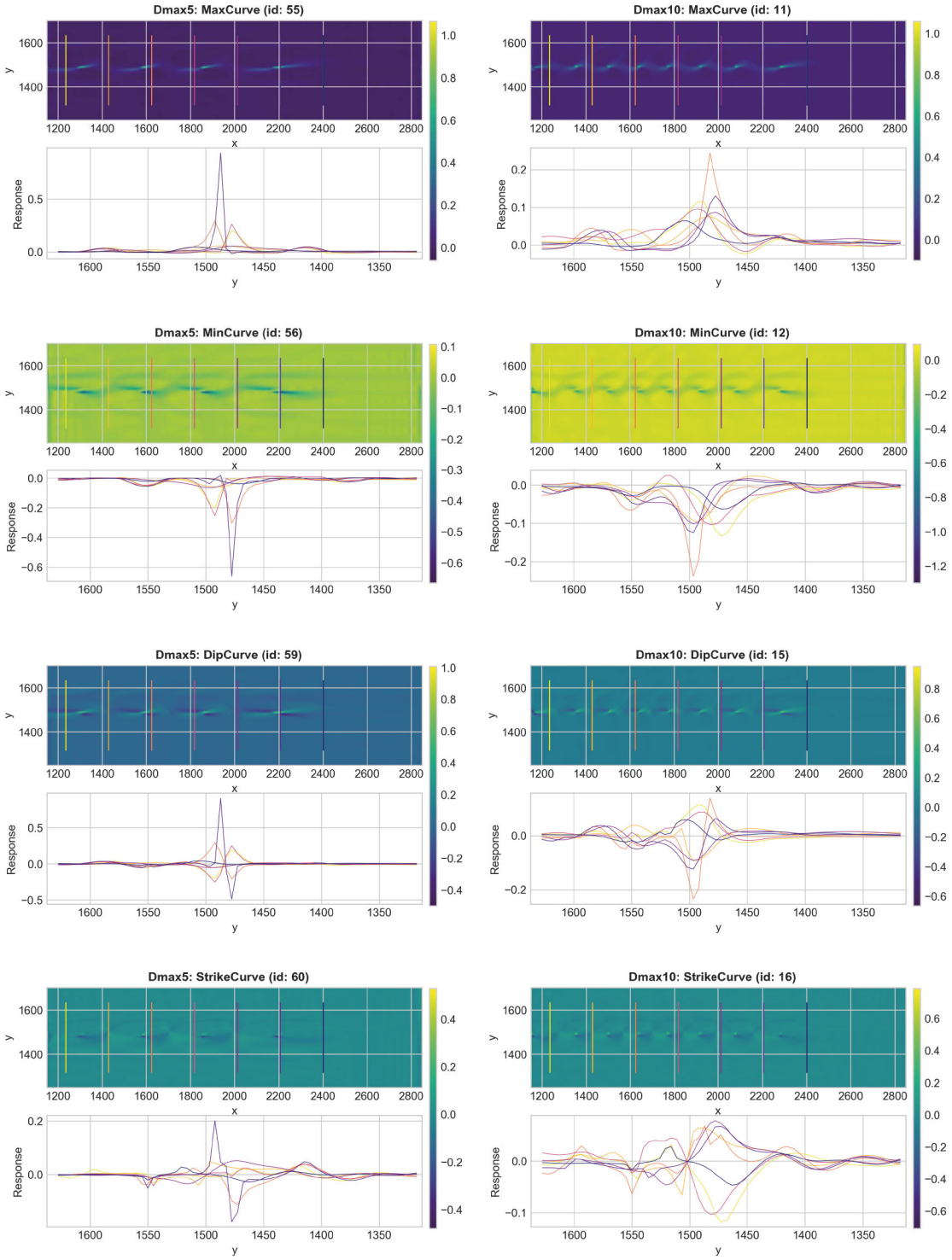

Figure 4.5: Curvature attributes from Dmax5 and Dmax10 models. See Figure 4.3 for description of layout.

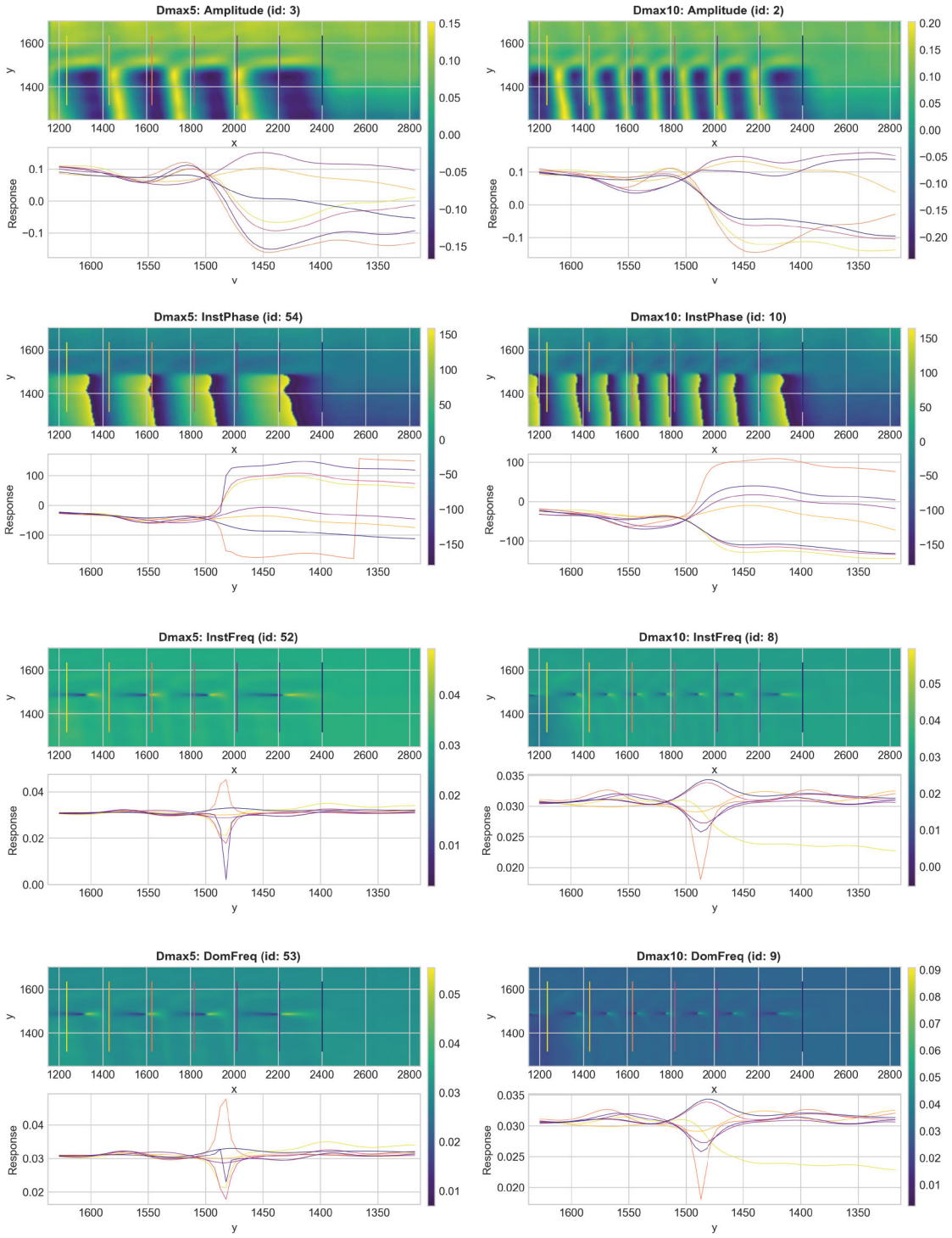

Figure 4.6: Instantaneous and trace attributes from Dmax5 and Dmax10 models. See Figure 4.3 for description of layout.

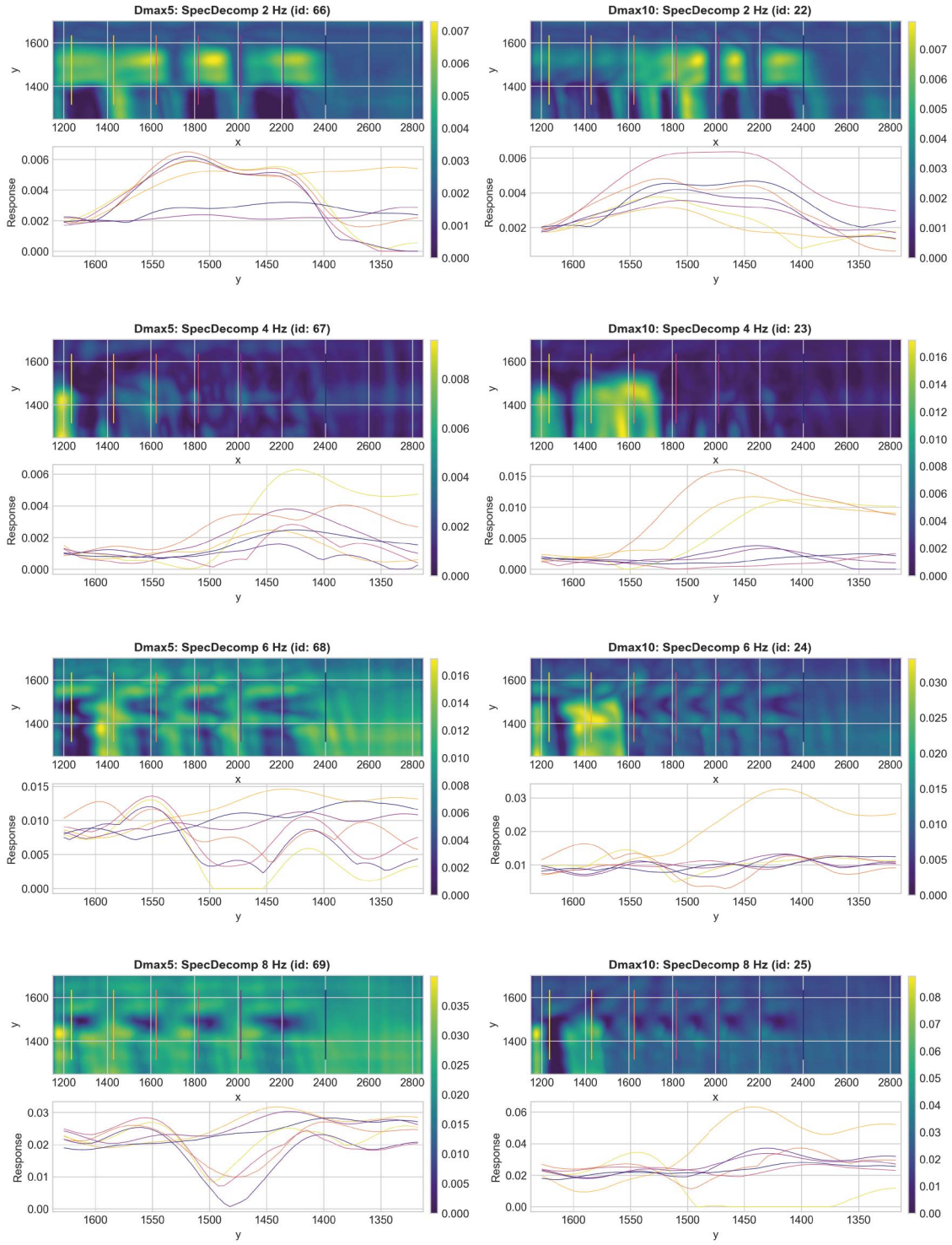

Figure 4.7: Spectral frequency extractions at 2, 4, 6 & 8 Hz from Dmax5 and Dmax10 models. See Figure 4.3 for description of layout.

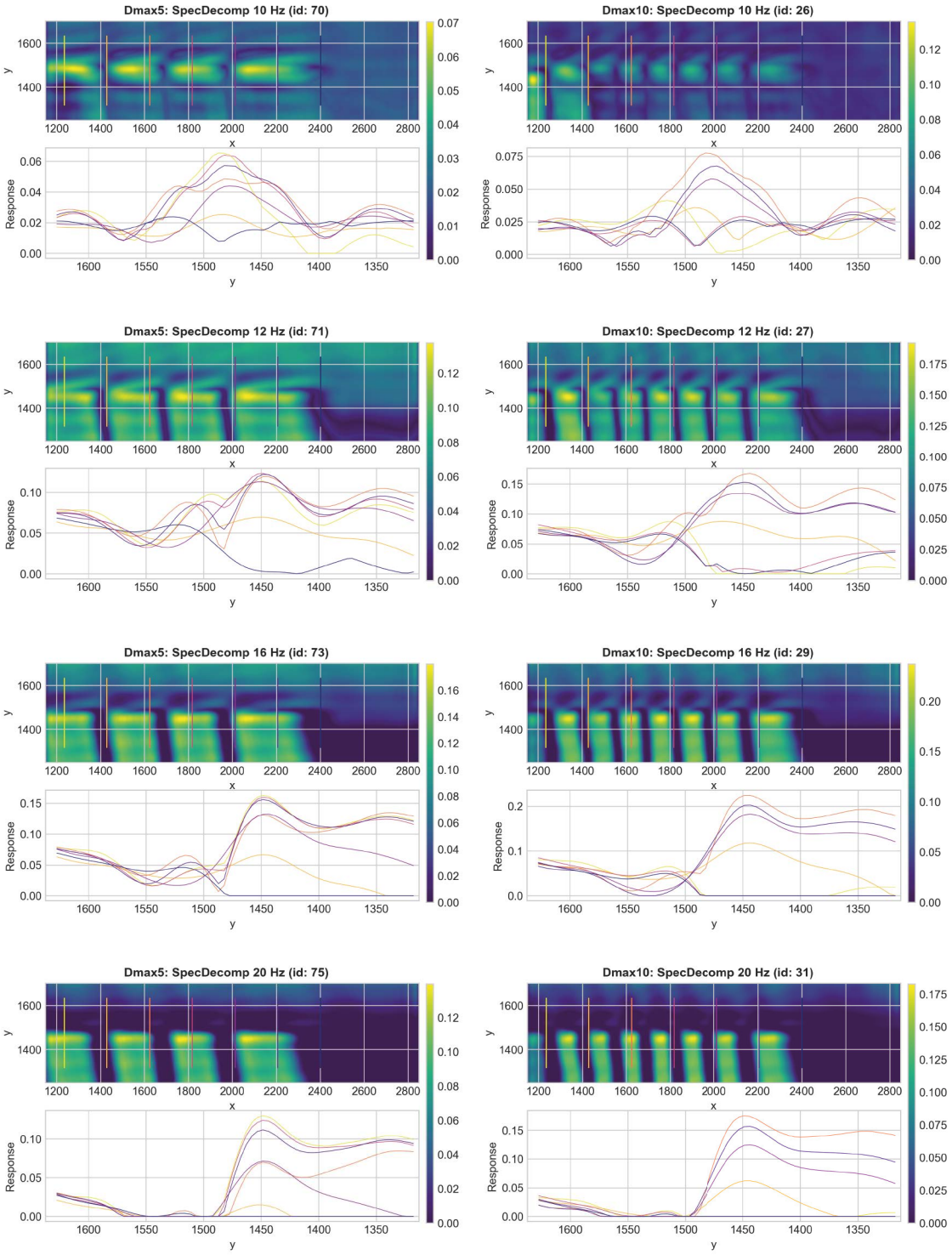

Figure 4.8: Spectral frequency extractions from Dmax5 and Dmax10 models at 10, 12, 16 & 20 Hz. See Figure 4.3 for description of layout.

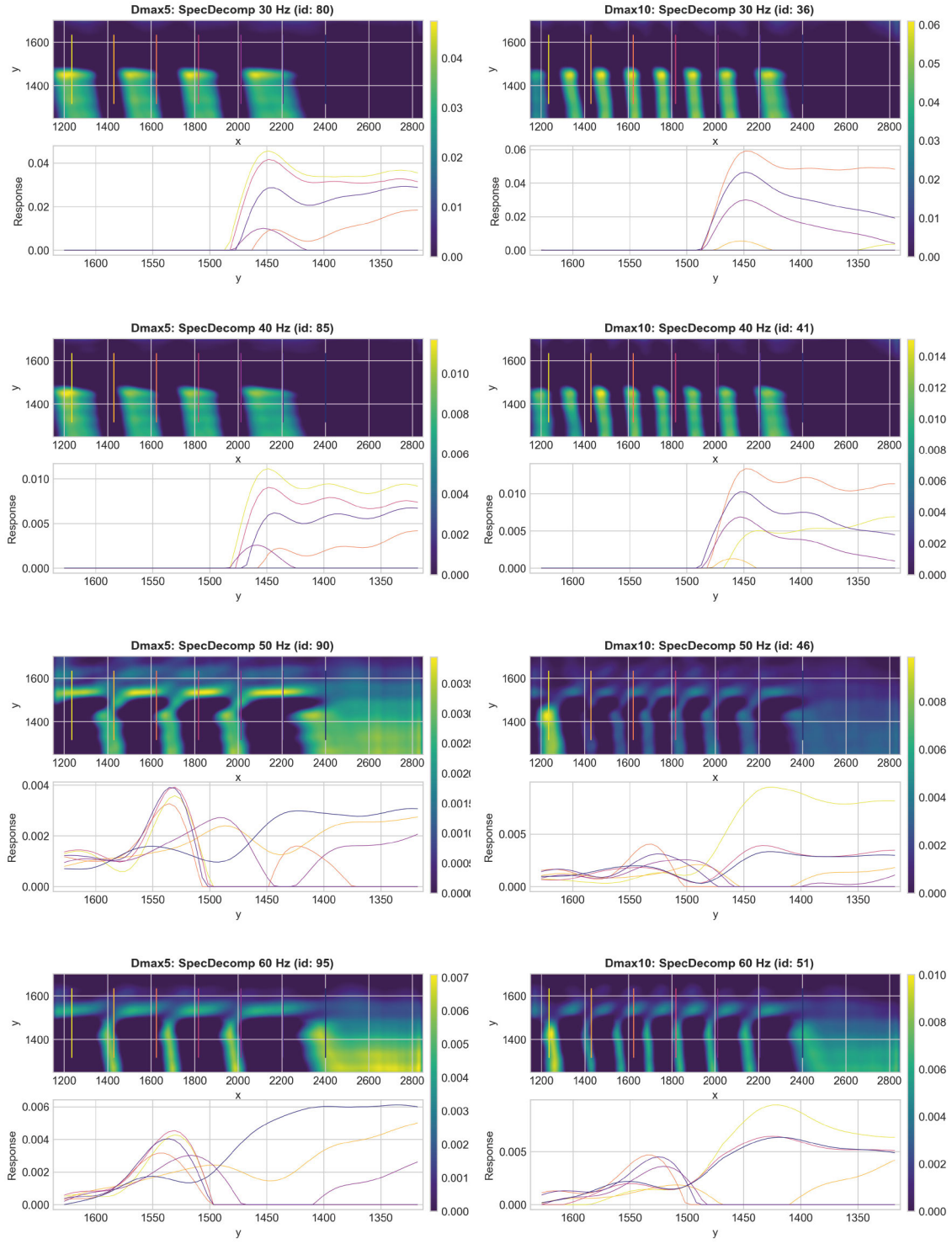

Figure 4.9: Spectral frequency extractions from Dmax5 and Dmax10 models at 30, 40, 50 & 60 Hz. See Figure 4.3 for description of layout.

Attribute	Fault zone		Background	
	Mag	Var	Mag	Var
Depth	-	-	H	L
Dip (Event)	H	H	M	L
Dip Azimuth (Event)	M	H	M	H
Dip Gradient	-	-	L	L
Dip (PC)	H	H	M	M
Max curvature	H	H	L	M
Min curvature	H	M	-	L
Dip curvature	H	H	-	-
Strike curvature	H	H	L	L
Amplitude	-	-	H	H
Inst. Phase	-	-	H	L
Inst Frequency	H	H	-	-
Dom Frequency	H	H	-	-

Table 4.4: Seismic attribute response characterisation in the presence of faulting. H/M/L indicate qualitative judgement of high, medium or low response in terms of variance at the described location of the model.

an indication of structural dip representing the dip of horizons themselves. However, it also appears to have a more smoothed response to faulting. Curvature attributes illustrate local response to fault presence, maximum and minimum curvature occur to one side of the fault, while anomalies in dip and strike curvature change polarity across the fault.

Azimuthal attributes are generally poor, investigation shows that this is due to the relative flatness of horizons, meaning subtle variations in dip when dip is approaching zero may cause large swings in the azimuthal attribute.

Trace attributes also respond with respect to the location of the fault. Amplitude and instantaneous frequency feature a step change in the magnitude of response across the

fault's location. Comparison to the trend of fault displacement (increasing towards the left), shows an inconsistent relationship.

In the horizontal extractions, thick bands oriented parallel to fault dip are formed, following the trend of intersections of the dipping horizons of the hanging wall. Correlation of the one-dimensional extractions with these anomalies illustrate that the change in magnitude across the fault is controlled by the point of intersection with the hanging-wall and the relative position of that intersection to the different facies represented in the hanging-wall.

Analysis of different elements of the frequency spectrum illustrate an interesting pattern, whereby the lowest frequencies, $\leqslant 4$ Hz, reveal an incoherent signal, probably related to the acquisition. Other low frequencies, $5 - 10$ Hz, show a broad response to the local presence of faulting, while at other frequencies, $\geqslant 12$ Hz, both a local response and a change in the background magnitude across the location of the fault is visible.

4.4.2 Identifying fault tip locations

As discussed in the Literature Review, picking of fault tips in seismic data is a key challenge in interpretation due to the influence of fault network connectivity (§ 2.3.2). Typically this challenge is addressed through application of seismic attributes supported interpretation. Many case studies exist of the application of attributes, however there is relatively restricted quantitative analysis of the relative merits across the variety of attributes available, and very little consideration of trace attributes for contributing to this type of analysis.

In this section, I compare the efficacy of different individual seismic attributes for identifying the location of fault tips. Using synthetic data allows validation of the fault tip picked from attribute analysis against the true location. To do this, a one-dimensional extraction is taken parallel and coincident with the location of the fault (Fig. 4.10).

The response along that extraction is expected to feature decreased variance as the fault tip

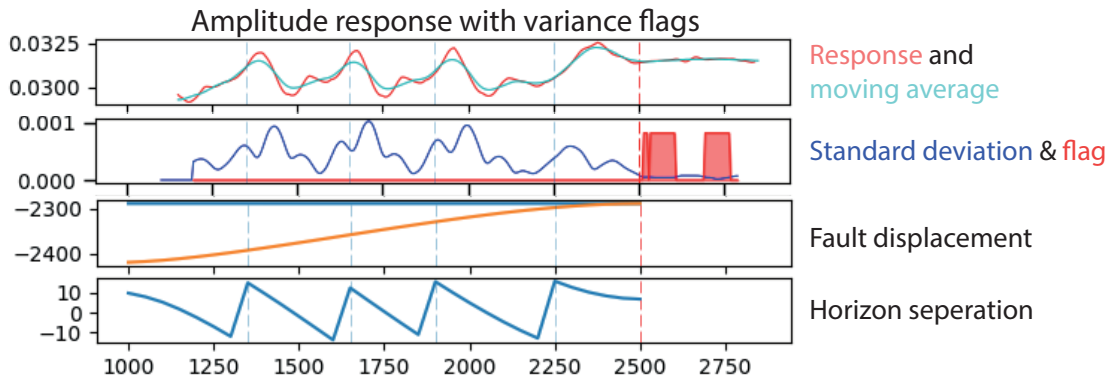

Figure 4.10: Output from machine learning script used to identify the location of fault tips on the basis of minima in standard deviation of seismic attributes.

approaches zero-displacement or below seismic detectability. The degree of background variance is expected to change in different attributes, making it challenging to directly compare their accuracy in determining the location of faulting.

During interpretation a geoscientist would develop an understanding of such trends and use them to guide their analysis. Here, this aspect is simulated using machine learning to attempt fault tip identification at increasing levels of standard deviation, raising a flag each time the attribute breaches that level. The script trials various levels, and minimises the number of flag raises, until a clear prediction of the fault tip is identified, in a similar way to a human interpreter.

Using this approach removes interpreter bias, ensuring that all attributes are tested equally and so allowing direct comparison of their results. Additionally the level of variance that is used in identifying fault tips provides a measure of the clarity of signal, proving an additional measure of accuracy.

The script plots each attribute, considering the magnitude of response, moving average and the standard deviation across a rolling window. Calculates a flag value, that is a categorical, true or false, signal dependent on whether the data stream exceeds a defined percentile cut-off of the overall population of variance in the data. The script applies a range of cut-offs automating parameter testing for selection of the standard deviation that

best separates signal from noise. A range of potential cut-offs are applied, from 0.25 to 20.5, while counting how many flags were raised at each level of sensitivity. The model then selects the run with the highest standard deviation that activates a single flag close to the position of the known fault tip.

Results for various attributes were visually inspected to ensure appropriate selection of parameters (see appendices). Once a percentile has been set for each attribute flag series, the standard deviation and location of raised flags may be extracted. The standard deviation measures variation around the central tendency for the dataset, therefore this provides and indication of signal quality.

Considering the the standard deviation as an indicator of the clarity of signal from the fault tip, it may be used with the difference between the predicted and actual fault tip location to understand the reliability of the signal (Fig. 4.11 & 4.12).

Most attributes overestimate the fault length for both the Dmax5 and Dmax10 geometries, with the latter being a slightly worse estimation. Azimuth attributes appear to be most variable, poorly constraining the fault tip in both models. All dip magnitude attributes appear to gather closely with regards to predicting the fault tip location, over-estimating fault length by a similar amount in each case.

Curvature attributes show the greatest variability between different types in both cases. This should be expected due to the nature of the curvature calculation, whereby minimum and maximum curvature would be expected to highlight opposing sides of the fault. As illustrated, the maximum curvature underestimates the fault length in each case, while the minimum overestimates in each case.

Contrary to contemporary workflows, the best estimate of fault tip location appears to arise from analysis of frequency attributes rather than the geometric attributes typically employed in modern workflows.

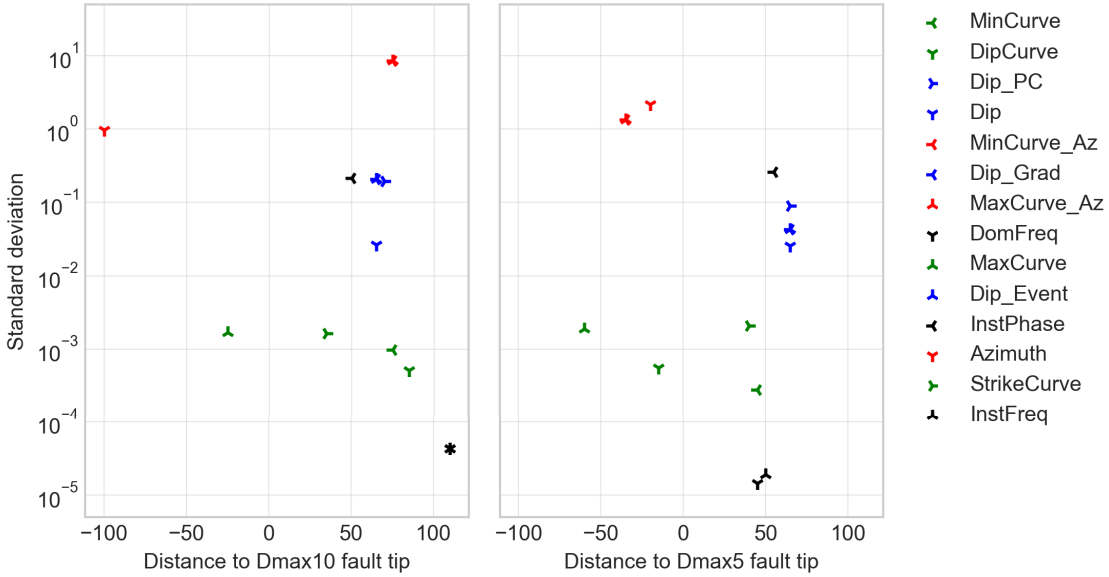

Figure 4.11: Cross-plot of distance between predicted and known fault tip location with value of standard deviation used to flag the location for each geometric model (Dmax10 (left) and Dmax5 (right)). Attributes are coloured by type of attribute.

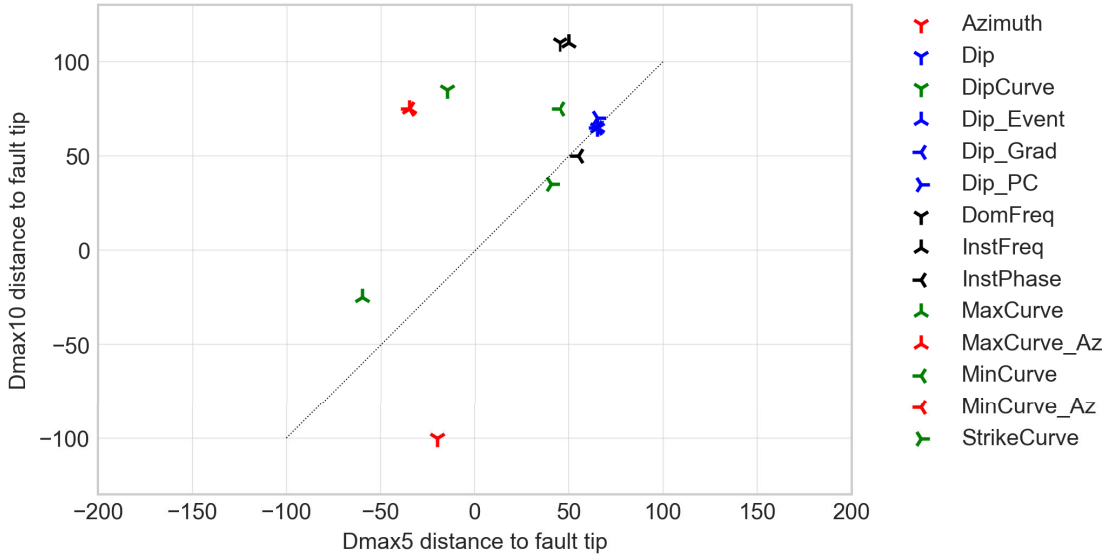

Figure 4.12: Cross plot of fault tip identification for like-to-like attributes for the two geometric models. Dotted black line indicate parity, highlighting the comparability of different attributes.

4.5 Frequency fault response

As identified above, trace attributes and in particular frequency attribute appear to offer greater potential for fault interpretation than has been widely discussed. Reviewing the data above, there does not appear to be a simple correlation between fault displacement and attribute responses. However, targeted frequency extractions show differences in response locally around faulting relative to background values (e.g. Fig. 4.13).

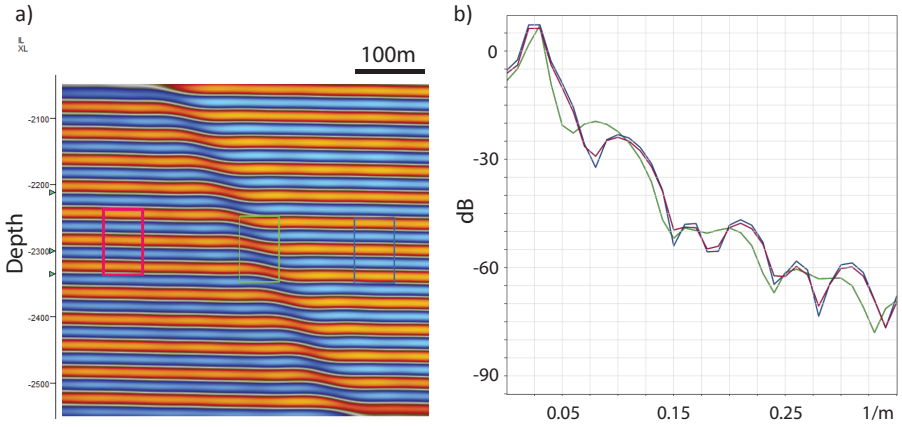

Figure 4.13: Spectral depth analysis (a) sampling areas used for extraction of (b) spectral analysis from the hangwall (blue), footwall (red) and fault zones (green). Note that spectral notches for the fault zone are not aligned with those of the wallrock.

Frequency analyses are commonly utilised in the interpretation of stratigraphic geometries likely to result in tuning anomalies, such as pinch-outs and thin beds (Robertson and Nogami, 1984; Zeng and Marfurt, 2015; Widess, 1973; Kallweit and Wood, 1982). Some authors have identified the presence of frequency anomalies associated with faulting (Iacopini and Butler, 2011), however, perhaps due to a lack of understanding as to the causative mechanism, these attributes have not yet been included in typical structural interpretation workflows (Marfurt and Alves, 2015).

Considering these results (Fig. 4.13) in the context of thin bed analysis, a series of local minima are observed in the immediate vicinity of the fault that occur at a different rate to those in the background signal. These could be interpreted as spectral notches, the spacing

of which would be expected to correlate to the spacing of reflectors (Hall, 2006a).

Comparison of one-dimensional frequency extractions show direct correlation between frequency variations and the juxtaposition pattern along the fault surface (Fig. 4.14). Power spectrum analysis, using a discrete Fourier transform (Castagna and Sun, 2006), illustrates that this response varies with spectral component, typical of tuning related anomalies (Widess, 1973). A calculated geometric attribute representing the vertical distance from the sample intersection to the closest sand to shale impedance contrast, forms a direct correlation with changes in instantaneous phase and minima across all spectral components.

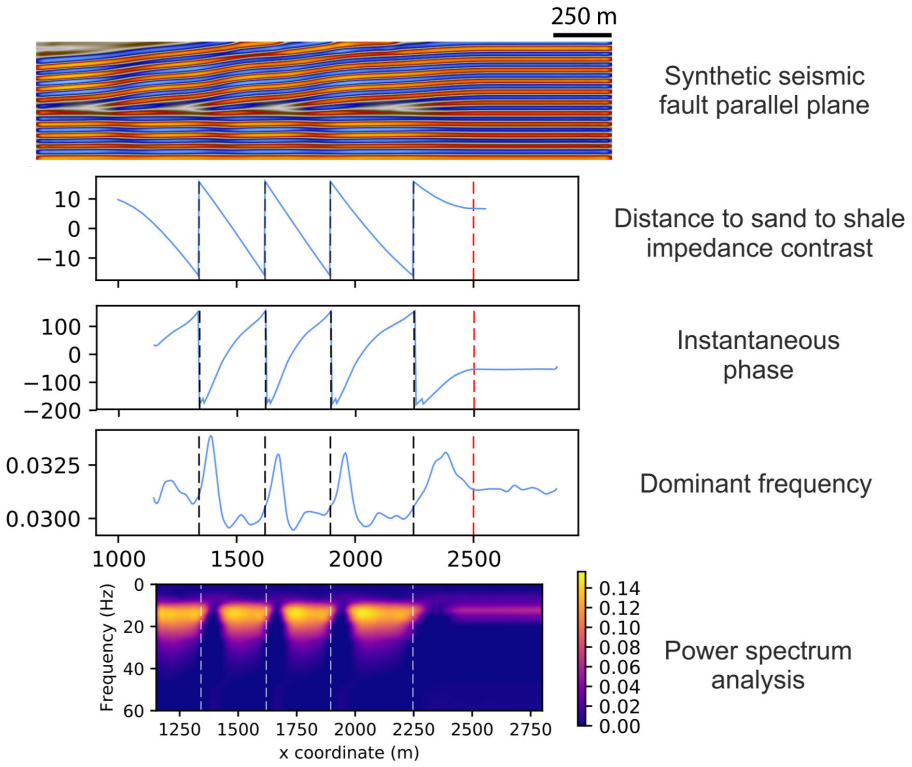

Figure 4.14: Analysis of seismic trace attribute response to juxtaposition styles. Plotting the distance to sand to shale impedance contrast along with seismic extractions illustrates the relationship between phase, frequency and fault juxtaposition. A power spectrum analysis highlights an asymmetric tuning anomaly associated with fault-horizon intersection crossovers.

Seismic attribute anomalies are noted to vary along the fault, but feature a broadly

repeated pattern, punctuated by polarity changes coincident with changes in the distance to the closest impedance contrast to the sample line. Anomalies appear to be slightly offset from this change, also the two central anomalies appear to feature a shorter wavelength than the outer two. It is noted that the dipping horizons of the hanging-wall would also be steeper at these points.

By extracting the dominant frequency attribute along an inclined plane coincident with the modelled fault plane, the anomalies identified in one-dimension are observed to form a set of approximately linear intersections parallel to fault dip (Fig. 4.15). Correlation to the input model geometry shows that these are coincident with elements of the pattern of across-fault juxtaposition.

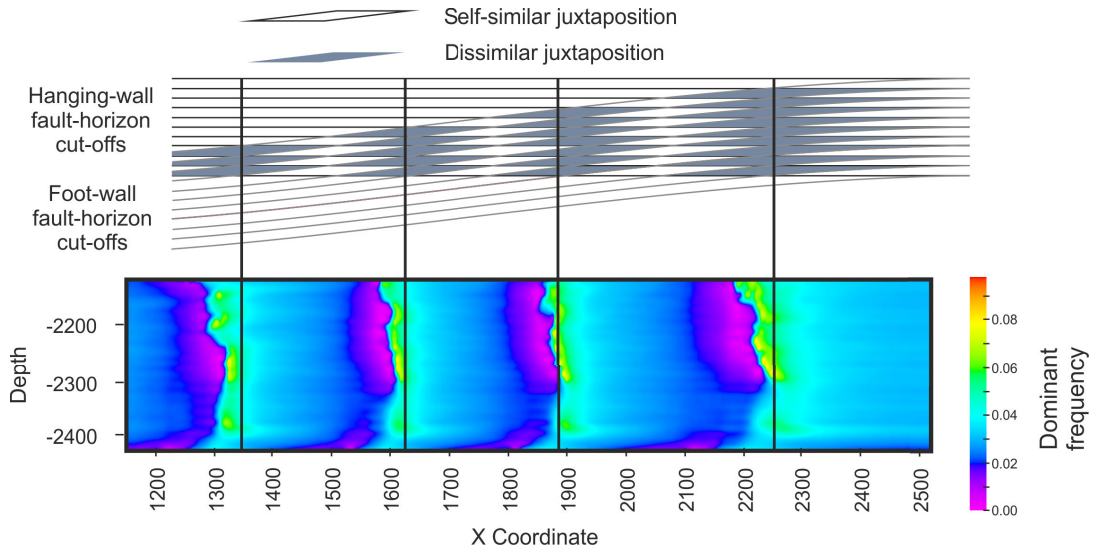

Figure 4.15: Correlation of juxtaposition styles with frequency anomalies, highlighting correlation between frequency wrap-around and a polarity change in impedance across the fault.

The dominant frequency signal switches polarity from maxima to minima coincident with the centre of areas of across-fault juxtaposition of dissimilar material. To analyse this further, three-dimensional extractions were made of the dominant frequency attribute anomalies (Fig. 4.16). The imaged isometric surfaces delineate volumes defined by surfaces of equal value of dominant frequency.

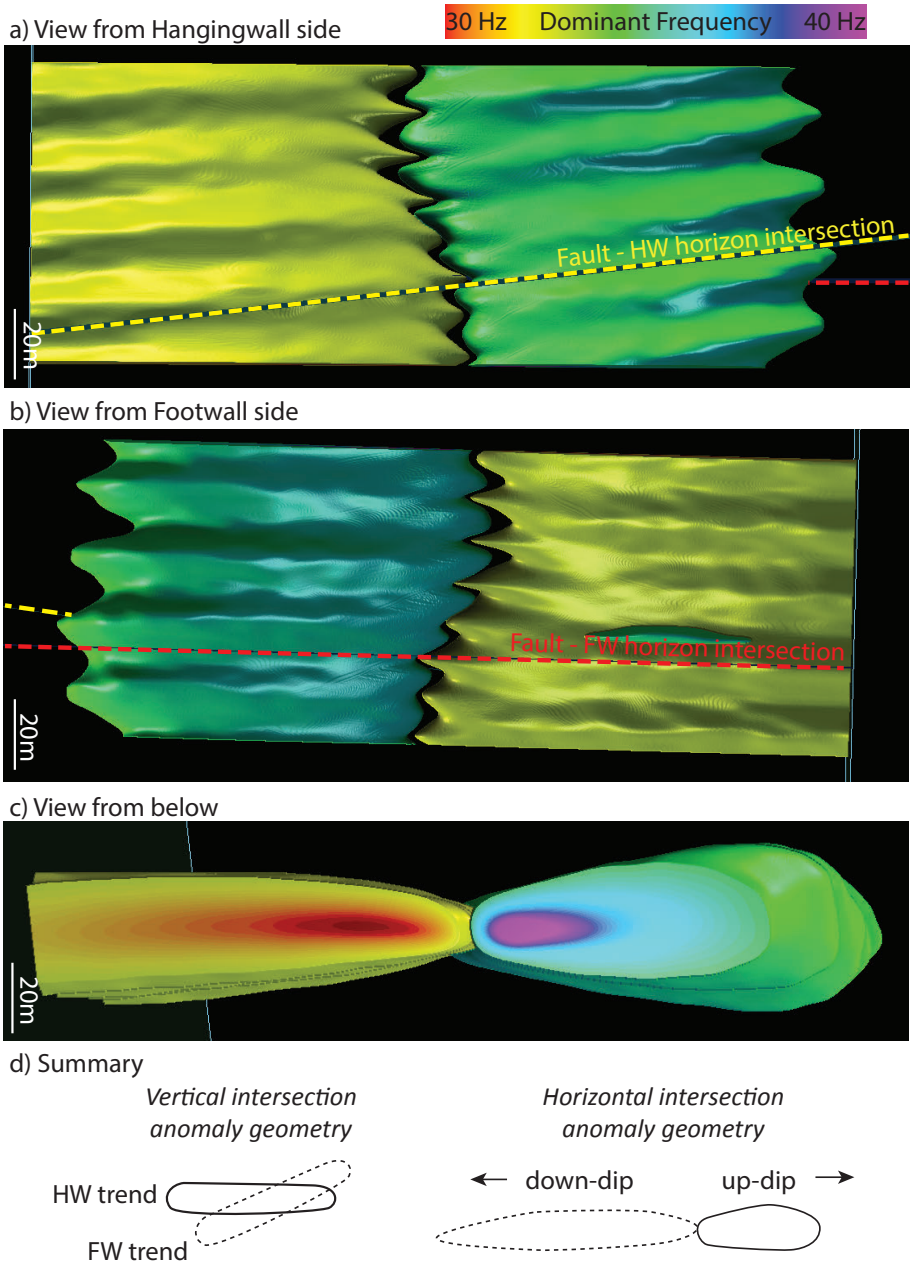

Figure 4.16: Three-dimensional geometry of frequency anomalies. Note that the anomalies are assymetrical about both the fault plane and the fault-horizon intersection crossovers (also inferred in Fig. 4.15)

These continue to illustrate an association between the location and nature of frequency anomalies with the across-fault juxtaposition pattern. Viewing the anomalies from the foot-wall and hanging-wall sides illustrate that trends in the dominant frequency follow the trends of the horizons to each side. In-line with observations from the one-dimensional extraction an notable up-dip to down-dip asymmetry is also observed (Fig. 4.16d).

In cross-section, perpendicular to the fault plane, the frequency anomalies are concentrically zoned around the fault-horizon intersections. On each of the hanging-wall and foot-wall sides the anomalous zone follows the horizon away from the fault intersection. As such frequency anomalies follow the edge of each horizon as defined by a fault-horizon intersection line, and reach a maxima at the intersection of fault-horizon intersections lines from different horizon tops (fault-horizon intersection cross-overs, Fig. 4.17).

4.5.1 Frequency anomaly causation

Identification of the correlation between cross-over points of the foot-wall and hanging-wall fault-horizon intersections and frequency anomalies appear to indicate a potential cause for the observed frequency anomalies. Displacing strata along the fault results in across-fault juxtaposition of differing facies. This lateral change in acoustic properties represents either self-similar or dissimilar juxtaposition across the fault (Fig. 4.17).

In this simplified model, with changing displacement along the length of the fault and constant bedding thickness, trends in juxtaposition form linear intersections that trend vertically through the model. For the purpose of discussion, I will refer to elements of this as fault horizon intersection cross-overs.

For a package uniform thickness beds, this is the sub-vertical line formed by the lateral edge forming the boundary between similar and dissimilar juxtaposition. In reality these conditions are unlikely to be met, however, the term provides a theoretical point of reference for discussion.

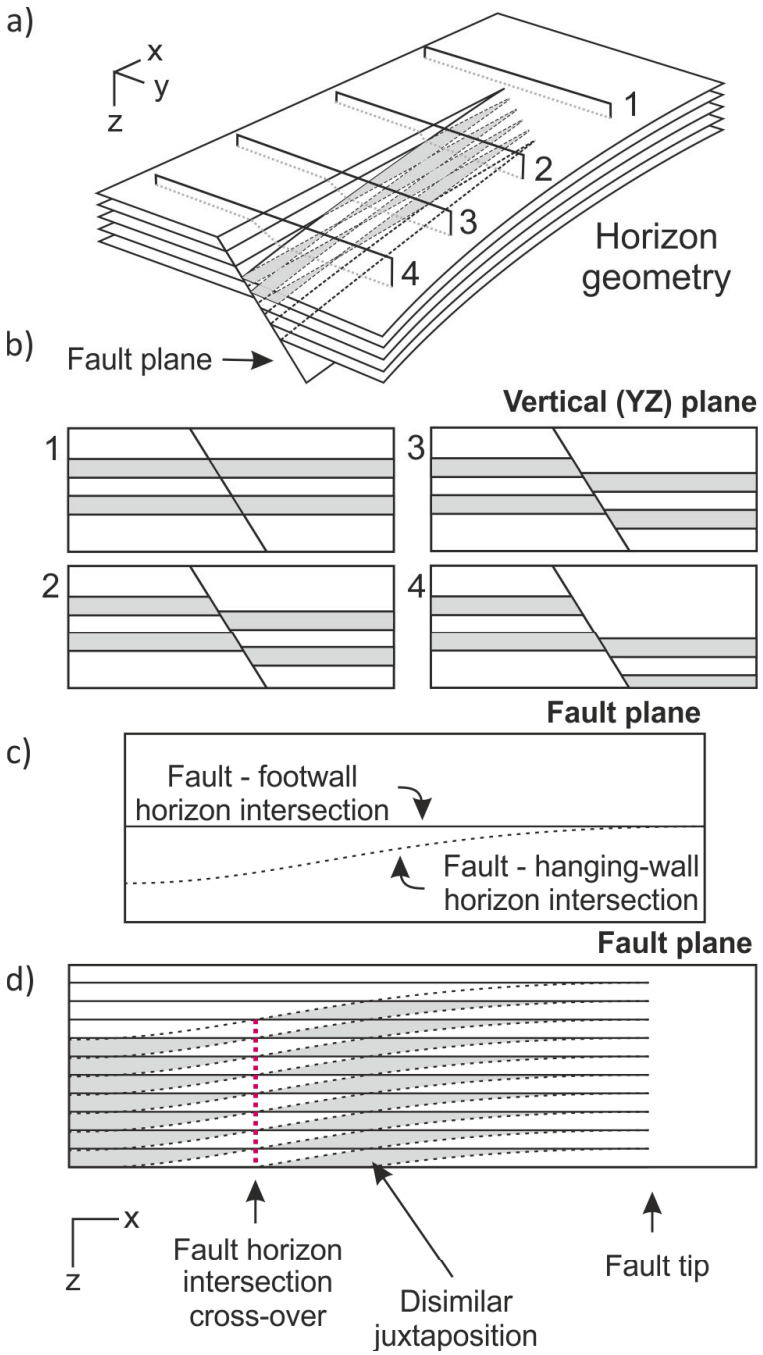

Figure 4.17: Illustration of terms regarding the geometry of fault juxtaposition. The displacement geometry along the fault (a) leads to juxtaposition of the hangwall and footwall (b), mapping of the fault-horizon intersections for each of the hangingwall and footwall side of the fault (c) forms a pattern of fault-horizon intersection cross-overs across the fault bound areas of self-similar and dissimilar juxtaposition (d).

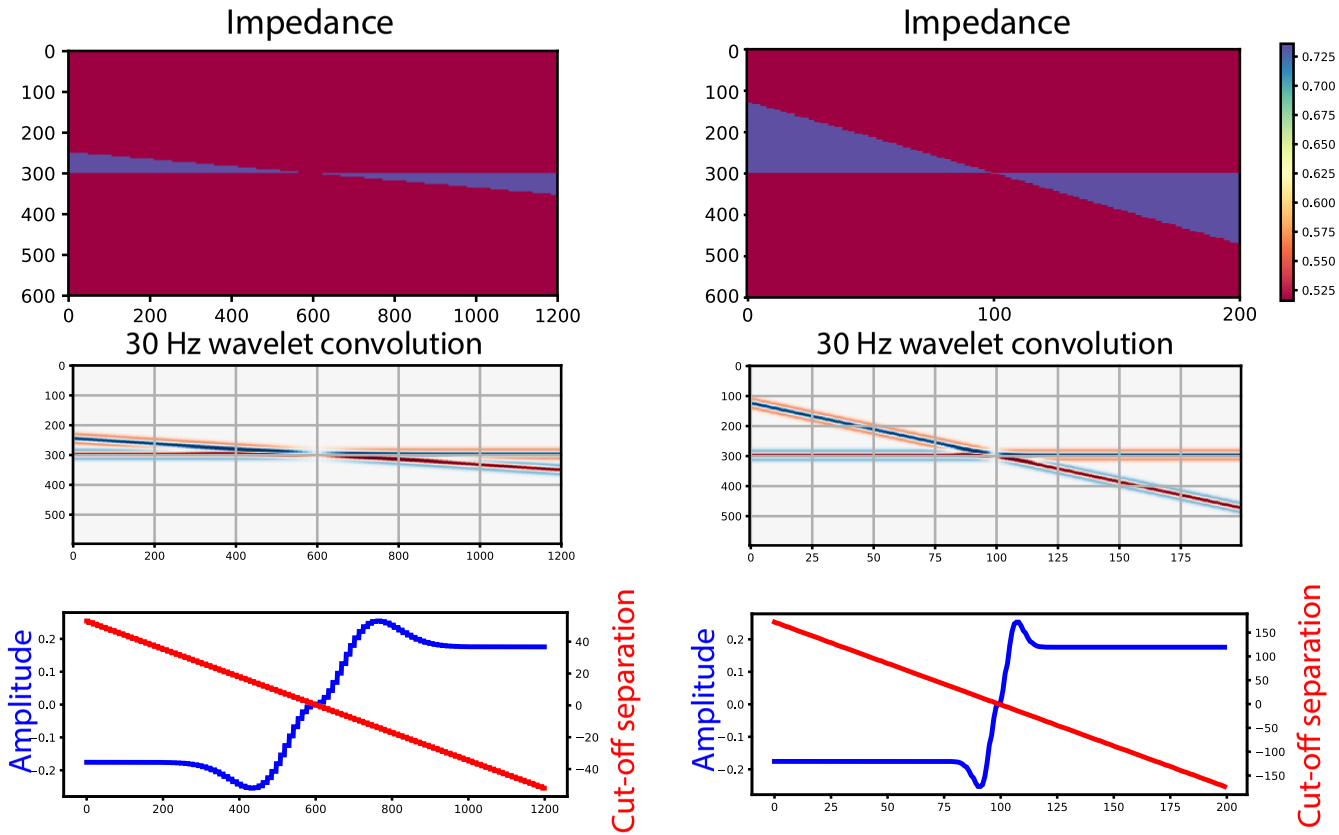

Figure 4.18: Adaptation of a convolutionary tuning wedge model to consider the two-dimensional geometries created by a fault (a) parallel and (b) perpendicular section.

Considering the vertical impedance change across the fault at the location of the fault-intersection cross-overs, these represent a polarity change from a sand to shale transition to a shale to sand transition. Dip on the fault results in a three-dimensional wedge geometry, resulting in across-fault and along-fault wedge geometries.

Tuning wedges are a long established tool for investigation of the seismic response of triangular geometries, often applied in stratigraphic analysis to investigate resolution (Kallweit and Wood, 1982) and tuning anomalies (Robertson and Nogami, 1984). Modifying an existing script for modelling tuning wedges to allow modelling of a 'double tuning wedge', allows for the use of two of these simple models to test the likely geometry of such responses (Fig. 4.18).

In both the along- and across-fault cases, the anticipated seismic response features a zero-crossing at the point of intersection, with local amplitude extrema immediately adjacent. These models suggest an amplitude anomaly that is approximately 600m long (fault parallel) and 40m wide (fault perpendicular). The aspect ratio of these geometries are broadly consistent with those observed from the extraction of three-dimensional isometric surfaces (Fig. 4.16).

4.5.2 Cross-over proximity analysis

Results are displayed using this presentation for the Dmax5 and Dmax10 models in Figures 4.20 to 4.23. In each plot, each point represents a single point of extraction, these points form trends that are coloured by throw, revealing their continuity with sampling order. Points tend to form continuous lines that represent different crossovers along the fault-horizon intersection. Typically the cross-overs from the minimum and maximum zones of throw are grouped together, and those featuring throws approaching the average diverge from them. It is noted that the minimum horizon structural dip correlates to the more extreme values of throw, while maximum structural dip is coincident with average mean throw values.

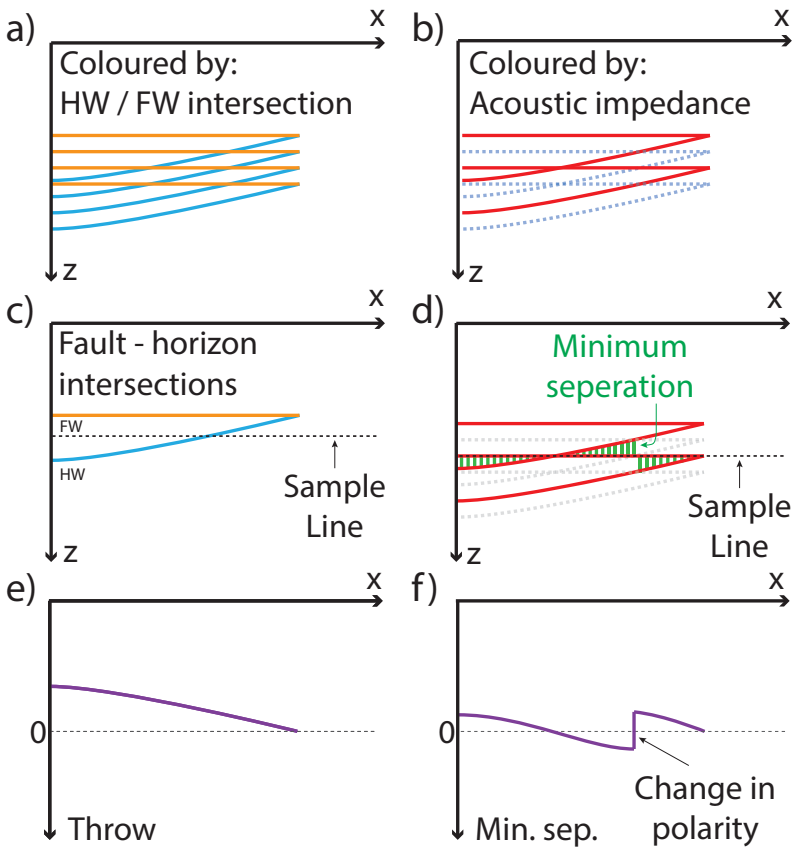

Figure 4.19: Schematic description of the juxtaposition extraction technique. Schematic of along fault profiles, defining along-fault minimum separation as applied in subsequent plots. Minimum separation is the minimum vertical separation from the sampling plane to a reflection above or below of a given acoustic impedance polarity, considering both the the foot-wall and hanging-wall fault-horizon intersections.

On all plots samples from minimum throw, that is those closest to the fault tip diverge from the trend of results. With this exception in each plot the attribute responds consistently for each cross-over. Geometric attributes feature either a peak or polarity change at the point of zero horizon separation. Trace attributes show a more complex response. Dominant and instantaneous frequency have an asymmetric response, as previously observed.

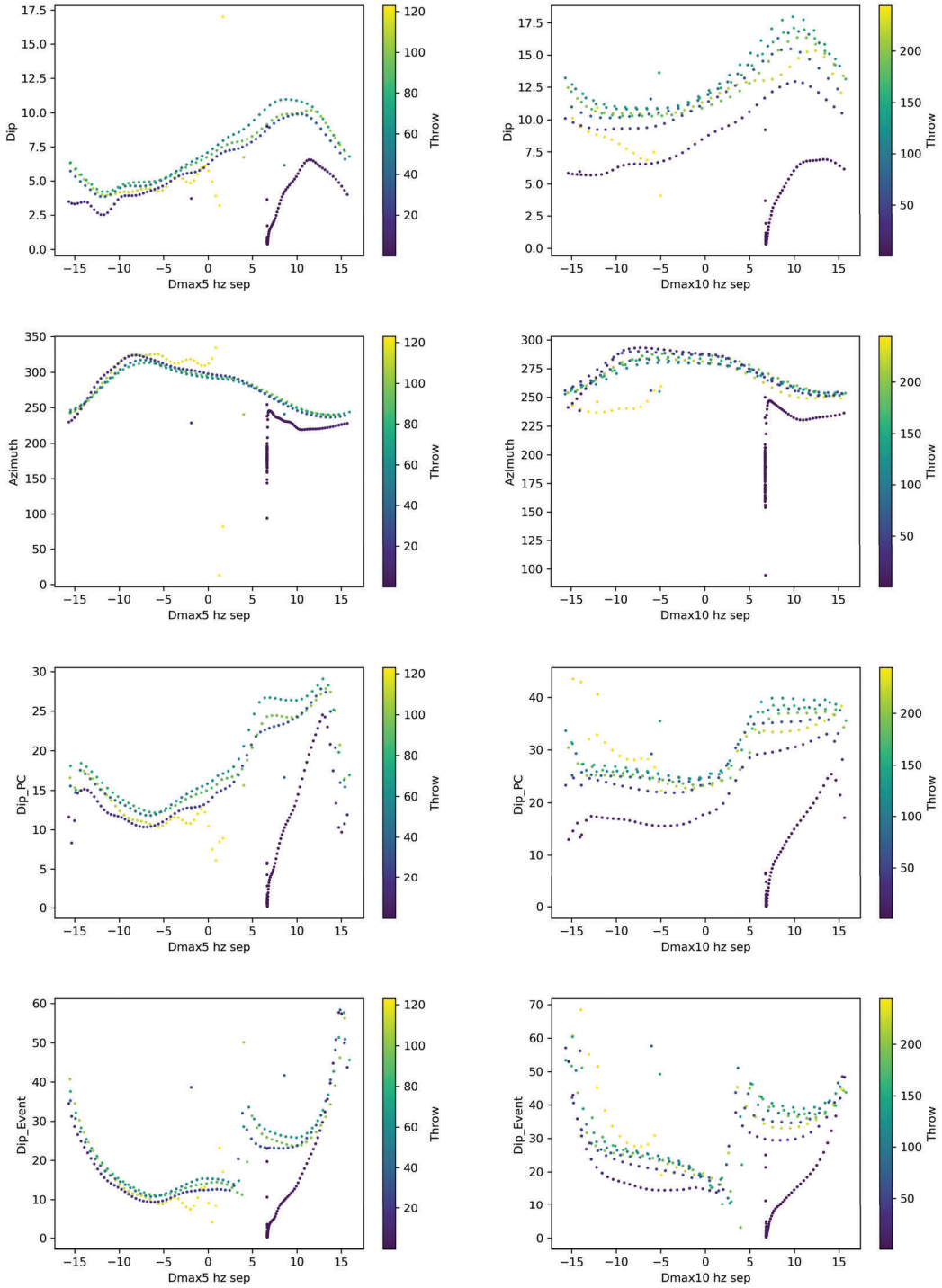

Figure 4.20: Various geometric seismic attributes (indicated by y-axis label) plotted against horizon separation for the Dmax5 geometry.

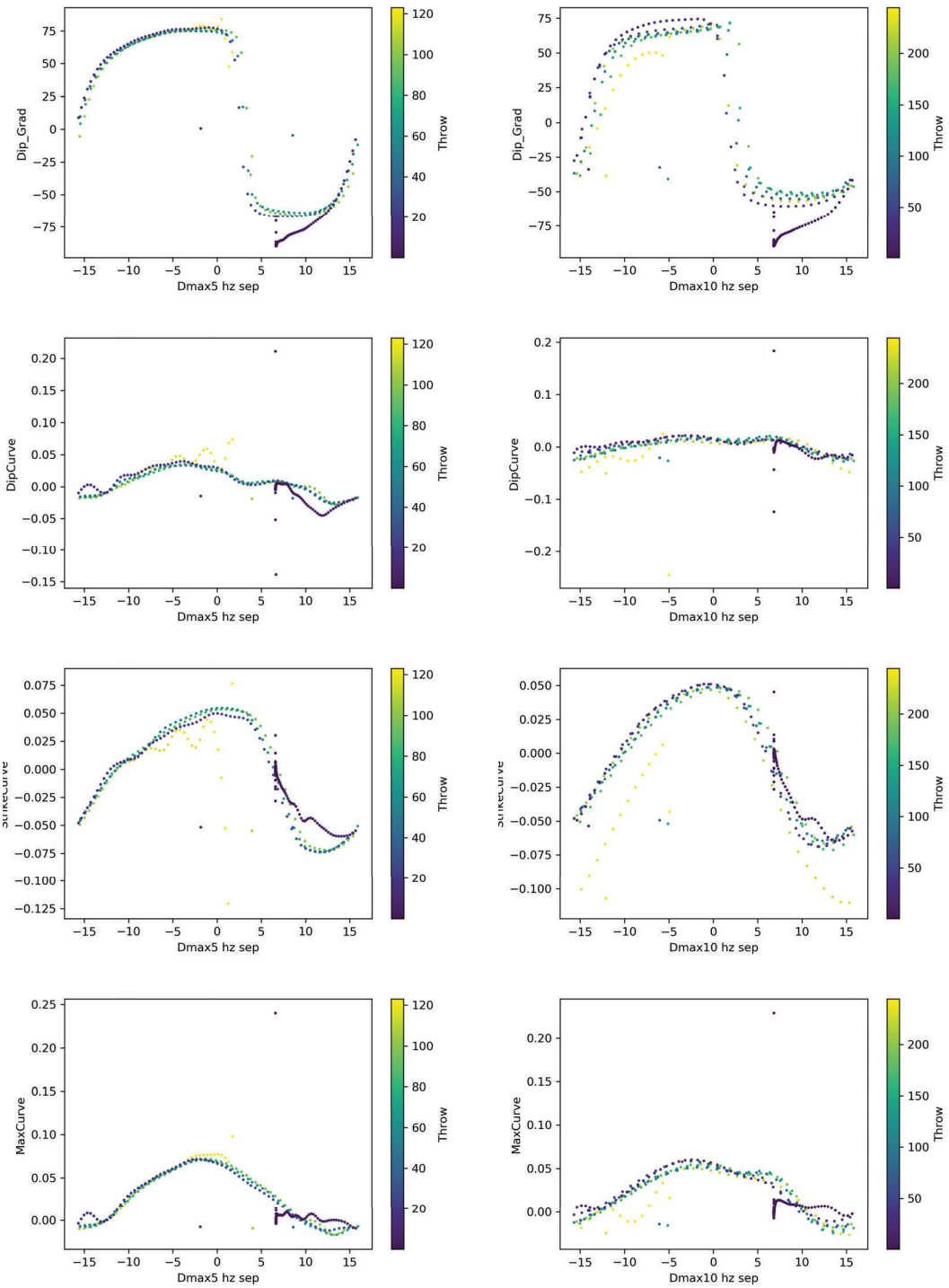

Figure 4.21: Various geometric seismic attributes (indicated by y-axis label) plotted against horizon separation for the Dmax10 geometry.

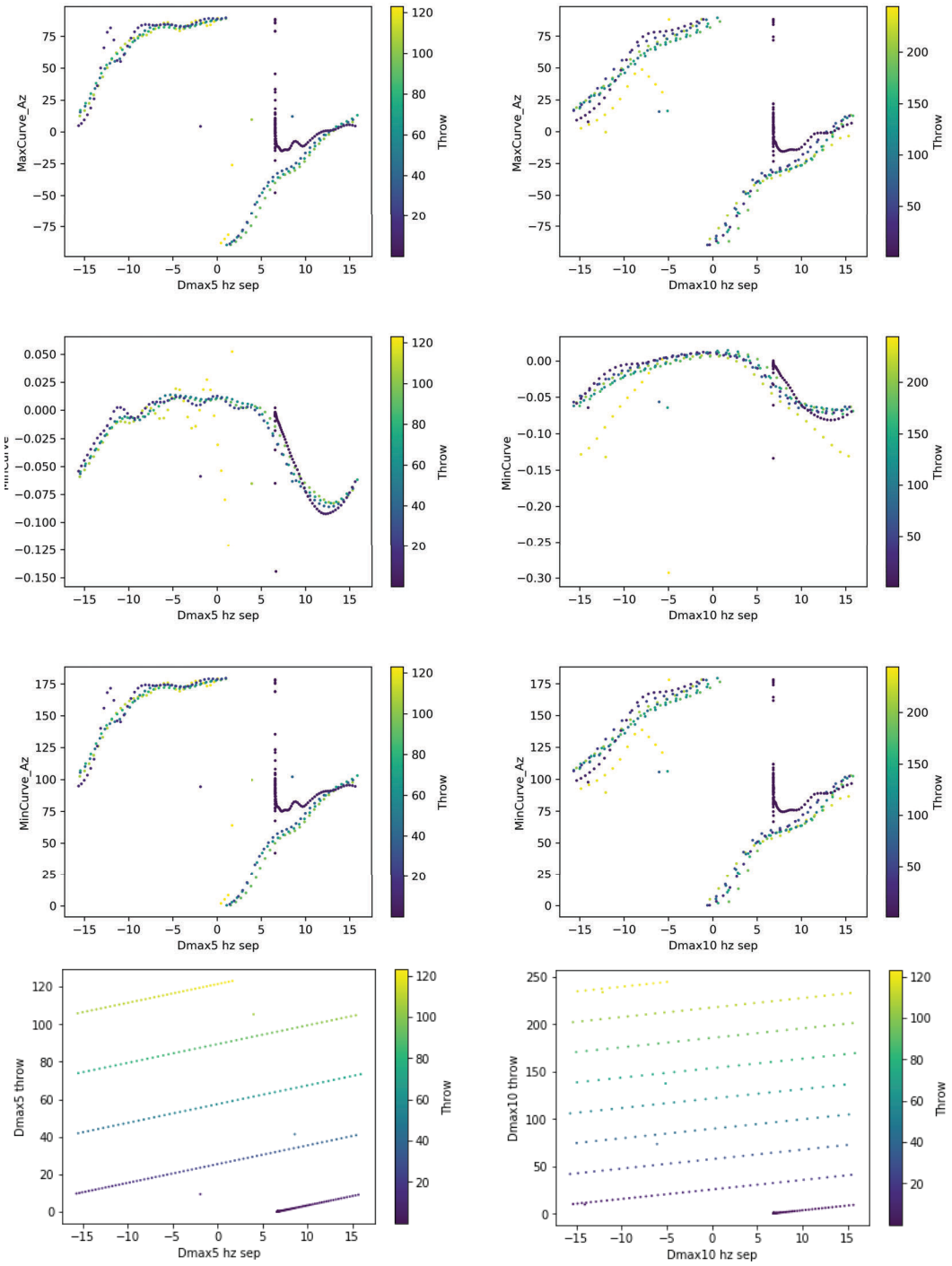

Figure 4.22: Various geometric seismic attributes (indicated by y-axis label) plotted against horizon separation for the Dmax5 geometry.

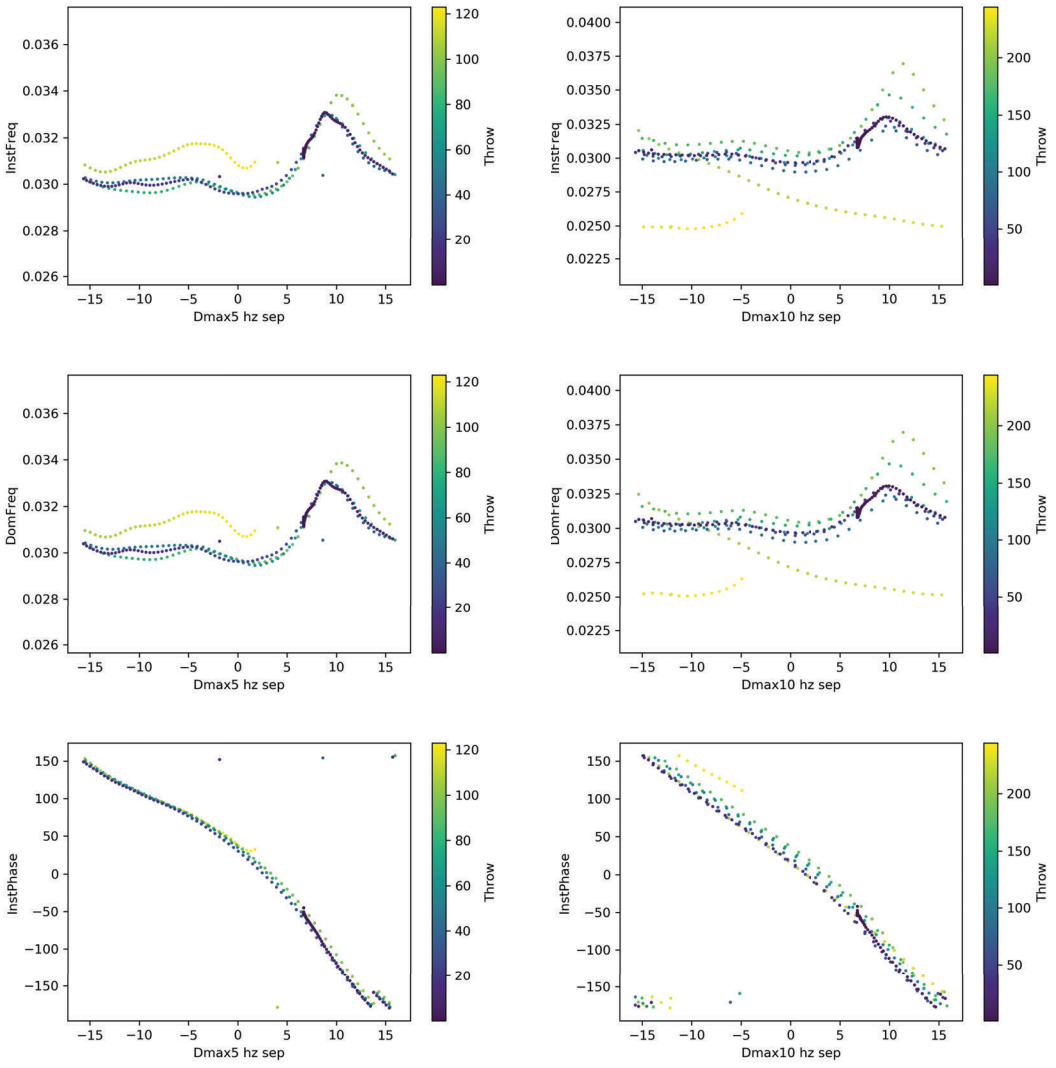

Figure 4.23: Various geometric seismic attributes (indicated by y-axis label) plotted against horizon separation for the Dmax10 geometry.

4.6 Discussion & concluding remarks

Analysis of seismic attribute responses to faulting illustrate that faults are detected by either recognition of a change of properties across the fault or by a response local to the fault itself related to localised deformation. If present local fault structures are likely to be minimal in their expression, as illustrated in numerical models (Guo and Morgan, 2008; Botter et al., 2014), field studies (Torabi and Berg, 2011) and seismic observations (Couples et al., 2007). Faults are more typically interpreted based on lateral changes in the properties of the surrounding rock, through juxtaposition of differing lithologies.

Interpretation tools such as coherency and similarity, may identify lateral compositional change as a local response due to the calculation looking for local differences (Marfurt et al., 1998, 1999). The suite of illustrations provided here highlight this variance in how faults are portrayed by different seismic attributes. Along-fault attributes have been extracted in an unrealistic manner, as the location and shape of the fault are known. This allows direct extraction of data and comparison between attributes and the known geometry.

Literature discussions of fault interpretation uncertainty typically consider the amount of fault that is not seen (e.g. Wood et al., 2015), inferring longer faults than are directly observed. My results suggest that in fact fault lengths may be both under- and over-estimated by a similar order of magnitude. Furthermore, this discrepancy or 100-120 m, is broadly equivalent to the expected Fresnel zone.

This is unexpected, as it would be expected that as the throw of a fault reduces below the vertical resolution of seismic data, it would become undetectable. Also of significance, is that if in fact the limitation on imaging is the Fresnel zone, this would imply that the limitation is essentially within measurement error. Such uncertainties may be effectively modelled using Monte Carlo type approaches. In a reservoir modelling setting, this may be significantly easier to consider than more geological causations.

Comparison between the accuracy of different attributes in determining fault tip location

on the two geometries indicates that the accuracy ranking of attributes varies (Fig. 4.12). This suggests that it would not be possible to select a single attribute that is most accurate, as any such selection would not be cross-applicable to other examples.

Real seismic data commonly illustrates discontinuous frequency anomalies associated with faulting (e.g. Fig. 4.24). At a larger scale, even in poorly imaged fault zones, recent work has extracted associated frequency anomalies (Iacopini and Butler, 2011). Commonly the literature ascribes such fault-related seismic anomalies to pore fluid content (Wiprut and Zoback, 2002), local stress fields (Price et al., 2017), fault damage zones (Kolyukhin et al., 2017) or fault-related deformation (Yousef and Angus, 2016).

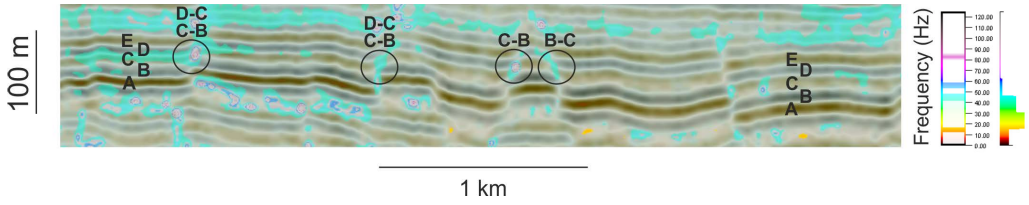

Figure 4.24: Example of fault-related frequency anomalies. On the left each seismic signal peak is labelled A-E, this nomenclature is used to label each across-fault juxtaposition, illustrating commonality in the nature of frequency anomalies between examples featuring juxtaposition of the same units.

Using synthetic models, I have demonstrated a spatial association between frequency anomalies and across-fault juxtaposition patterns (Fig. 4.16). Using customised forward modelling, this was further confirmed by estimating the tuning anomalies likely to be related to geometries in the immediate vicinity of faulting (Fig. 4.18). Isolation and analysis of multiple fault-horizon intersection crossovers indicates a strong correlation between all observed attribute responses and the fault juxtaposition (Figs. 4.20 to 4.23).

This association (Fig. 4.25) does not appear to have been previously identified in the literature. The level of anomalies observed in these experiments are difficult to compare to real data due to a lack of noise. Adding realistic noise to such datasets remains an outstanding challenge for seismic forward modelling (Eichert, 2006). As such it is uncertain how clear or detectable any anomalies if present would be in real data.

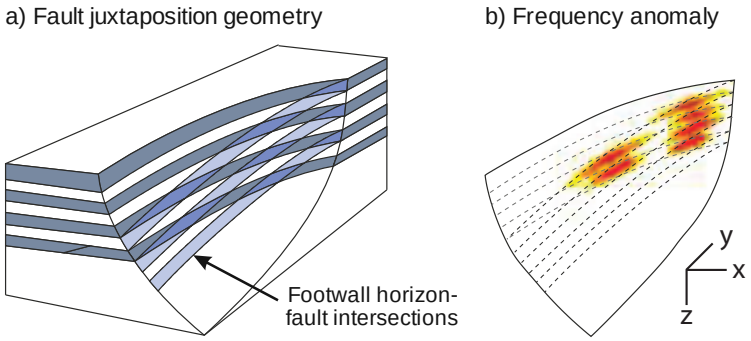

Figure 4.25: Association between frequency anomalies and fault juxtaposition patterns.

Furthermore, as the anomalies are associated with juxtaposition patterns, they are dependent on local stratigraphy. Models of alternating stratigraphy with low levels of noise are ideal for detection of such anomalies. Sequences with more gradual change of composition are likely to feature less abrupt juxtapositions of materials of differing physical properties.

However, if anomalies such as those identified in real data, such as Figure 4.24, can be associated with this mechanism, it may demonstrate that such anomalies do not require the presence of pore fluids, complex fault fill or other scenarios. This could impact the perceived risk of leakage from underlying reservoirs.

The one-dimensional forward modelling conducted above may suggest that the impedance contrast across the fault may affect the response. If such anomalies can be related to the physical properties of the rock, fault juxtaposition patterns could be a useful source of additional compositional constraint in seismic volumes with limited well data.

All models are wrong but some are useful

George Box, 1978

Chapter 5

Reservoir interpretation uncertainty

Chapter structure:

5.1 Abstract

During reservoir development the first arrival of dynamic data often leads to recognition of small-scale faulting and other previously uninterpreted geological features. Resulting in a requirement to refine reservoir modelling in an effort to achieve greater accuracy in production forecasting. This chapter utilises a seismic forward model of a known geometry to test the relative impact of different strategies to making such refinements and investigates the impact of this choice on forecast accuracy.

Faulting can impact flow by modifying reservoir permeability; acting as a barrier or baffle to flow across the fault; and, increasing tortuosity through displacement and juxtaposition of different flow units.

Reservoirs are typically represented in numerical models as geocellular grids, capturing details of both the geometry and flow properties of the subsurface in a numerical table. Spatial information is stored as Cartesian coordinates of the corner points of rectilinear grid cells. Property information is stored as a table of data that emulates the geometry of the grid with data from neighbouring cells also stored as neighbouring table entries.

Three strategies may be applied to consider the impact of faulting on a reservoir; a faulted model may feature the geometry of the fault as a grid offset with transmissibility multipliers applied to cell boundaries to emulate across-fault flow controls; an unfaulted model, where the grid geometry may be unmodified, but transmissibility multipliers applied along cell boundaries to model faults; or, by assuming an isotropic affect of faults on fluid flow and applying bulk permeability multipliers.

Choice between these strategies significantly impacts the time-cost of application. This work indicates that the production forecasts are sensitive to this control, with modelling strategy selection resulting in as much as 60 % variation in predicted production rate. This suggests sensitivity testing should be undertaken to justify the selection reservoir modelling strategies.

5.2 Introduction

In this chapter, I use a synthetic seismic image to demonstrate the degree of uncertainty that may be introduced into flow simulation by structural interpretations. The aim of exploration and appraisal workflows is to constrain the range of likely volume of recoverable hydrocarbons in-place to inform investment decisions (Jones et al., 2016). The purpose of this work is to constrain the degree of uncertainty introduced by reservoir modelling strategy selection.

The influence of structural interpretation in determining trapped and connected volumes is clear. However, there is also significant scope for geometric interpretations to affect flow simulation and therefore estimations of recoverability.

As a hydrocarbon project matures from exploration, to development and production, progressively more data become available to interpreters. This is particularly the case with regards reservoir flow performance, for which data constraint is only available from natural analogues prior to drilling.

The arrival of drilling results, particularly dynamic data, often leads to reassessment of existing interpretations and the data upon which they are based. The following work explores uncertainty derived from seismic interpretation in this process.

5.3 Interpretation

Initial seismic interpretation is typically completed in the context of a broader scale sub-regional interpretation of a large seismic volume, reviewing the volumes for prospect leads. Once prospects are identified, they may be graded into different levels of priority and highly graded leads are likely to be considered further as prospects.

At early stages the most influential element of a potential prospect leads success is perceived to be the prospect's trapped volume. A coarse interpretation grid, provides

a reasonable indication of likely success on this metric. Figure 5.1a illustrates such an example, where a horst block has been interpreted and part of a potential reservoir interval highlighted in the red box.

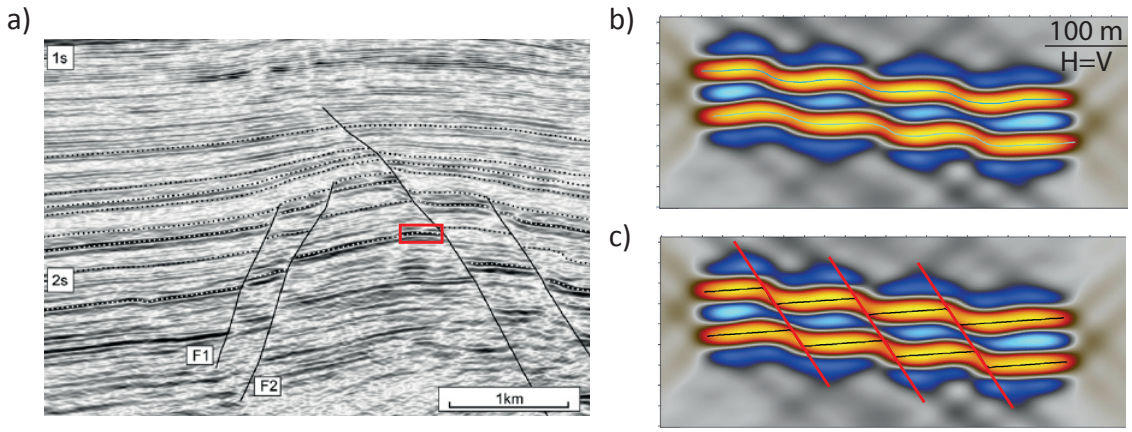

Figure 5.1: Synthetic, small-scale deformation is presented at the scale of a seismic section used for exploration; (a) illustration of exploration stage seismic data from the literature (Long and Imber, 2010), (b) synthetic models representing alternate interpretations at the appraisal, and (c) synthetic model superimposed by sketch of the input geometry.

The published regional interpretation (Long and Imber, 2010) provides suitable input at an exploration stage, however more may be required subsequently. The synthetic seismic image in Figures 5.1b & c illustrates how subtle undulations at this scale may be interpreted as two different geometries.

5.3.1 Synthetic seismic modelling

The two geometries interpreted above have been based on the same synthetic seismic image. The geometric model behind this synthetic consists of ten equally spaced horizons displaced by three normal faults, dipping at 60° towards the right, delineating four fault blocks.

To generate this model, a stack of horizontal planes is generated in a rectilinear volume of 500 x 50 x 50 metres (X, Y and Z, respectively). These planes are split and displaced

using kinematic modelling to simulate an offset of 25 m along each fault (Figure 5.1c). The entire model is then rotated anti-clockwise by 5° to provide a more realistic tilted fault block geometry.

The uppermost and lowermost horizons are then used to generate an interface based model (Fig. 3.1). Acoustic impedance contrasts equivalent to a shale to sand transition are applied to both surfaces (Table 3.1). At this scale, this avoids destructive interference of the primary reflections providing a best case scenario for imaging quality.

The model itself is then simulated at a depth of 3km. The simulated acquisition uses a 30 Hz Ormsby wavelet (§ 3.4.1). The survey design is based on an industry acquisition for which sources and receivers are located at a spacing of 60 m and 20 m, respectively (§ 3.4.2). along survey lines that are located 200 m apart, oriented parallel to faulting. During acquisition, all receivers are active throughout the entire survey, this provides for a more symmetrical survey illumination meaning that any observed illumination issues are as a result of the input geometry rather than the simulated acquisition.

Zoeppritz equations are used to calculate reflectivity along interfaces, providing an angle dependent response (§ 3.4.3). These amplitudes are again calibrated as previously discussed (§ 3.4.3).

5.3.2 Alternate interpretations

Seismic interpretation is an inverse problem providing a non-unique solution. Considering the synthetic seismic presented here (Fig.5.1b & c), the geometry may be reasonably interpreted as noise, subtle folding or small-scale faulting.

As described above, it is likely that in early stages of work the regional scale of interpretation will lead to an assumption of relatively simple geometry. In this case the inset synthetic model displayed would be likely to be picked by auto-tracking with some subtleties lost and faulting picked indirectly. Should the data be revisited in more detail, particularly if an interpreter is looking for causes of reduced reservoir performance, it

seems likely that these faults may be picked as discrete features.

As a result two geometries may be picked from this image, one with smoothed horizons draped across the faults (Fig.5.1b) and one with angular fault-horizon intersections illustrating fault offsets (Fig.5.1c). In either case an interpreter may consider the presence of faulting, as a key element of converting interpretations to subsurface models is selecting features that are of appropriate scale and affect to be discretely modelled.

These two models offer two principle differences with regards to fluid flow. In a single reservoir interval, the folded model allows lateral flow from one side of the model to the other, without the need to move vertically between different stratigraphic units. Secondly, the juxtaposition across faults in the faulted model causes a slightly reduced cross-sectional area across the area of the fault compared to the folded geometry.

It should be noted that at this point only geometric differences have been considered. If faulting is interpreted, a decision must also be made on the manner of inclusion in reservoir models.

5.4 Reservoir modelling & simulation

5.4.1 Modelling strategies

Once potential faulting has been identified there are a variety of options to incorporate these observations into the existing subsurface model. Three are methods are commonly employed:

Interpret faults – build their geometry into a new grid, honouring new observations, explicitly modelling faults with transmissibility multipliers (Fig. 5.2a);

Simulate faults – label existing cell boundaries as faulted, applying transmissibility multiplers to cell edges without regridding the model (Fig. 5.2b); or,

Ignore faults – using the existing grid, applying permeability multipliers as required

model isotropic or anisotropic flow (Fig. 5.2c).

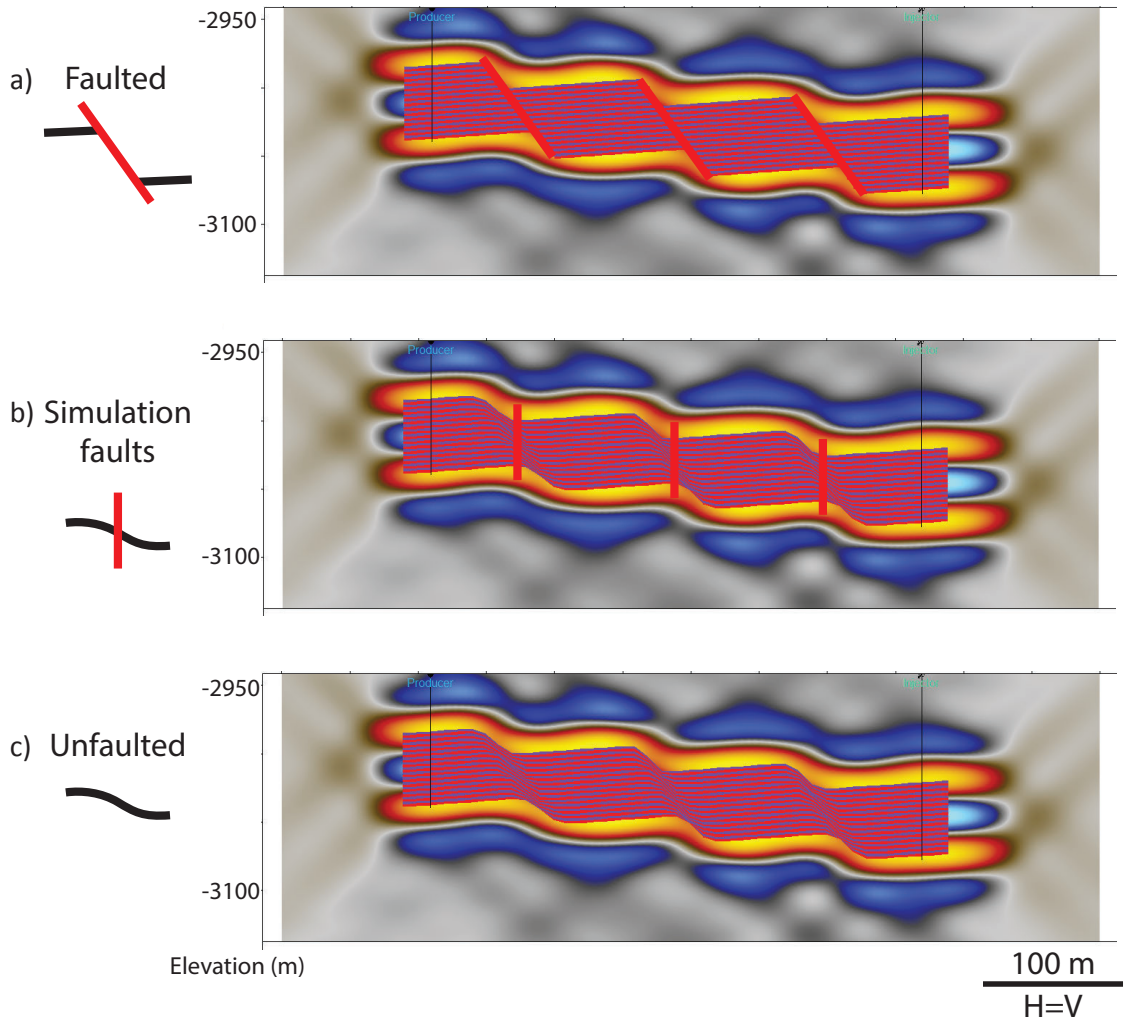

Figure 5.2: Three strategies for incorporating newly interpreted small-scale faults into an existing reservoir model: (a) faulted, (b) simulated faults and (c) unfaulted.

In this scenario, both the unfaulted option and simulated fault options may be implemented using the original interpretation with smoothed steps across faults. As a result existing simulation geometry grids may be used without any need to update. Avoiding such a grid update can be used to maintain the existing pore space volume preventing a complete rebuild of the static modelling components of a simulation.

Using the simulated faults approach, transmissibility multipliers may be used to add consideration of the fault effects on fluid flow. Applying the faulted model allows direct

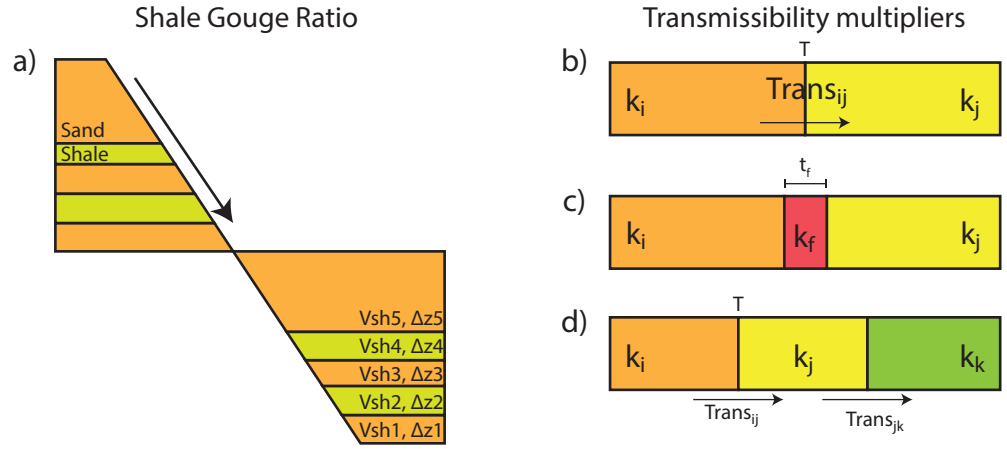

Figure 5.3: Illustration of the input variables for the calculation of shale gauge ratio and transmissibility multipliers; (a) Input variables for shale gouge ratio (after Fisher and Jolley, 2007), (b) transmissibilty multilier, T acts on the transmissibility from i to j, (c) the fault thickness, t_f, and associated altered permeability, k_f is considered. (d) a transmissibility multilier only affects flow across the specified boundary $\overrightarrow{ij}$ or $\overleftarrow{ij}$ (after Manzocchi et al., 1999)

modelling of the faults, including both their transmissibility and any related geometric effects.

To better understand the implications these strategies some background is required. Faults may promote, inhibit or prohibit flow in the subsurface dependent on their physical properties. In reservoir models this is parameterised through a simplified model consisting of fault zone thickness, fault zone permeability, reservoir permeability and fault throw (Fig. 5.3). These parameters are used to calculate shale gauge ratio (Yielding et al., 2010), equation (5.1) and transmissibility multipliers (Manzocchi et al., 1999; Fisher and Jolley, 2007), equation (5.2).

$$SGR = \frac{\sum(V_{cl} * \Delta z)}{t} * 100\% \tag{5.1}$$

Where; SGR = shale gauge ratio, V_{cl} = volume of clay by volume, Δz = vertical thickness and t = thickness of total unit.

Model	Parameter	Comments
Faulted	Juxt., TM & $\bar{k}$	Explicitly considers geometric effects, fault zone permeability and averaged affects on reservoir permeability.
Simulation faulted	TM & $\bar{k}$	Explicitly consideration fault zone permeability and averaged reservoir permeability affects, but not geometric effects.
Unfaulted	$\bar{k}$	No explicit consideration of faulting, but averaged reservoir permeability may be tuned to reflect some degree of fault-related anisotropy.

Table 5.1: Descriptive parameters for fault representation in reservoir simulation; $\bar{k}$ = bulk reservoir average permeability, juxt. = juxtaposition; and TM= transmissibility multipliers.

$$T = \left[1 + t_f * \frac{(2/k_f - 1/k_i - 1/k_j)}{L_i/k_i + L_j/k_j}\right]^{-1} \tag{5.2}$$

Where; T = transmissibility multiplier , L = length, k = permeability, $_i$ or $_j$ related to hanging wall or foot wall side of the fault, $_f$ related to the fault itself.

In addition, to the explicit modelling of faults either as discrete features or cell boundary conditions as transmissibility multipliers, the overall reservoir permeability tensor may also represent fault controlled fluid flow. In a case whereby the fault effect on fluid flow is isotropic and non-pressure dependent, a simple multiplier applied to permeability may also be sufficient to numerically model the faults effect. However, such an approach would require extensive parameter testing and evidence of non-anisotropic flow. As such, the geological control on fluid movement may be captured within these models in a variety of manners, as summarised in Table 5.1.

One final implication of modelling strategy is controlled by the selection of the underlying geometric model. Once the model has been populated with layered surfaces, the

smoothed geometry features layers that drape across the location of faulting, with lateral connection from one side of the model to the other. Whereas the faulted geometry features juxtaposition of horizons against the fault plane. As such, in order for a fluid to migrate upwards through the stratigraphy in simulation, it will be limited by the vertical permeability, defined by a horizontal versus vertical permeability ratio, K_v/K_h.

5.4.2 Modelling & simulation

Three reservoir models are made representing each of the above modelling strategies. Originally two models were generated for each of these scenarios, one with homogeneous pack and one with alternating layers of properties representing sand and shaley-sand. Only the layered model will be further discussed here for brevity.

Once the geometry is defined, the model is divided into thirty layers and alternating facies of sand and shaley-sand are populated throughout allocated with properties representing porosity (22 & 14 %, respectively) and permeability (23.5 & 3.3 mD, respectively) values (Ringrose and Bentley, 2015). For each layer properties are laterally uniform, in addition to a permeability difference, a vertical to horizontal permeability ratio (K_v/K_h) of 0.1 is introduced in line with industry practice (Pickup et al., 1994). Static model properties are summarised in Table 5.2.

The initial building of the static reservoir model highlights a change in the total pore volume between the two geometric models, whereby the total volume of the simulated fault and unfaulted models are both 435 m^3 larger than the faulted model. Investigation shows that this difference can be attributed to changes in the ceiling and base reservoir geometries related to the angle of cut-off and degree of smoothing of horizons around the fault-horizon intersections.

A transmissibility multiplier of 0.4 is applied to all faults in both the simulated faults and the faulted cases. In the faulted case, additional calculations are made in the Petrel implementation that accounts for cell to cell area contacts and coordinates non-neighbour

Parameter, Units	Faults	Simulated Faults	No Faults
Total pore volume, Rm^3	180134	180569	180569
Av. pressure, BarSA	369.82	369.82	369.82
Median permeability, mD	13.4	13.4	13.4
K_v/K_h, fraction	0.1	0.1	0.1
Permeability isotropy	Isotropic	Isotropic	Isotropic
Average porosity, %	18.5	18.5	18.5
Dissolved gas, fraction	0	0	0

Table 5.2: Static properties applied for reservoir modelling of tilted fault blocks model.

connections across discretely modelled faults in the faulted case. This transmissibility multiplier represents a fault that is 0.09 m wide, with a grid cell width of 10m and fault rock permeability of 0.0799 mD. this is broadly consistent with the scale of deformation represented by a throw of 15m (Walsh et al., 1998; Childs et al., 2009). No TMs are applied to the unfaulted case.

Dynamic modelling is accomplished using the Eclipse 100 Black Oil Reservoir Simulator (Schlumberger), assuming the dynamic properties described above (Table 5.2) and relative permeability curves and capillary entry pressures are presented in Figure 5.4. The model is ran for 15 years, reporting at monthly intervals. This duration has been selected based on the common usage of 6 and 12 years as key cut-offs in calculating estimated ultimate recovery (EUR).

Production is simulated using a waterflood production strategy with an injector and producer pair. For each model the producer is located in the most up-dip fault block and the injector in the most down-dip block (right hand side of Fig. 5.2). All wells are completed by perforation throughout the penetrated reservoir interval and skin effects are assumed to be negligible.

During production wells are typically choked to maintain sustainable production rates balancing the increased value of production volumes in the short-term, with that

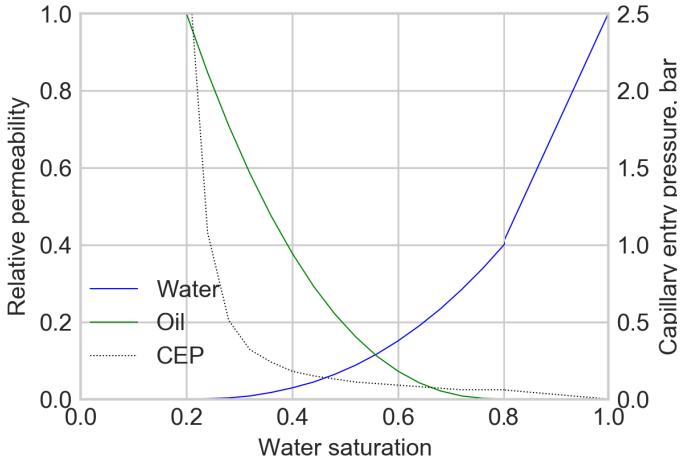

Figure 5.4: Modelled water saturation and capillary entry pressure.

of increased ultimate recovery (Archer and Wall, 1986). Injection of fluid allows maintenance of reservoir pressure over the long term, increasing recovery, however as Darcy flow is part determined by pressure gradient any variation will influence the nature of subsurface fluid flow. As such, the implementation in these models is significant as to the manner of observations that may be made subsequently.

Two water flood strategies are applied in this work; revealing different aspects of intra-reservoir fluid flow while sharing basic properties (Table 5.3). The pressure-controlled strategy regulates the rate at which water is injected into the reservoir, maintaining a constant bottom-hole pressure at the injector well. The volume-controlled strategy maintains a constant water injection rate so long as pressure remains below a threshold that could cause damage to the reservoir. No dissolved gas is modelled to maintain simplicity.

Using the pressure controlled strategy, water injection is regulated to maintain a near constant average reservoir pressure. This maintains a constant drive for flow to the surface and is representative of common industry extraction strategies utilising choked production wells and variable water injection rate. In this case, decreased permeability or baffles to flow will result in less efficient flow of fluid away from the injection site, reducing pressure

Dynamic parameter	Value
Water injector BHP target	400 psi
Water injection rate limit	20 rm^3/d
Producer BHP limit	250 psi
Initial average reservoir pressure	325 psi
Model duration	15 years
Report frequency	monthly

Table 5.3: Details of the production strategy employed for reservoir simulations

dissipation. Therefore geological reductions in flow capacity will result in a reduction in the rate of water injection.

The volume controlled strategy provides greater insight into the interaction of fluid pressure and faults, as the motion of the waterfront would be more continuous under otherwise stationery conditions. As production rates are more constant the reservoir pressure may be used to better understand the effect of the fault presence on the waterflood as it propagates across the reservoir, providing a means to investigate effect of fault presence on pressure transience (e.g. Whittle and Gringarten, 2008).

5.4.3 Results & analysis

The three reservoir models have all undergone flow simulation using both the pressure- and volume-controlled production strategies (Fig. 5.5). Results using the pressure control strategy illustrate significantly different initial production rates, with the unfaulted model performing best, followed by the simulation faulted model and then the faulted model. For the first 2000 days of production the three models share a similar decline curve maintaining approximately the same differences in production rate (Q).

Between 1500 and 2000 days the first derivative of production rate (dQ/dt) illustrates a divergence that forms the forerunner to water breakthrough. At this point oil production

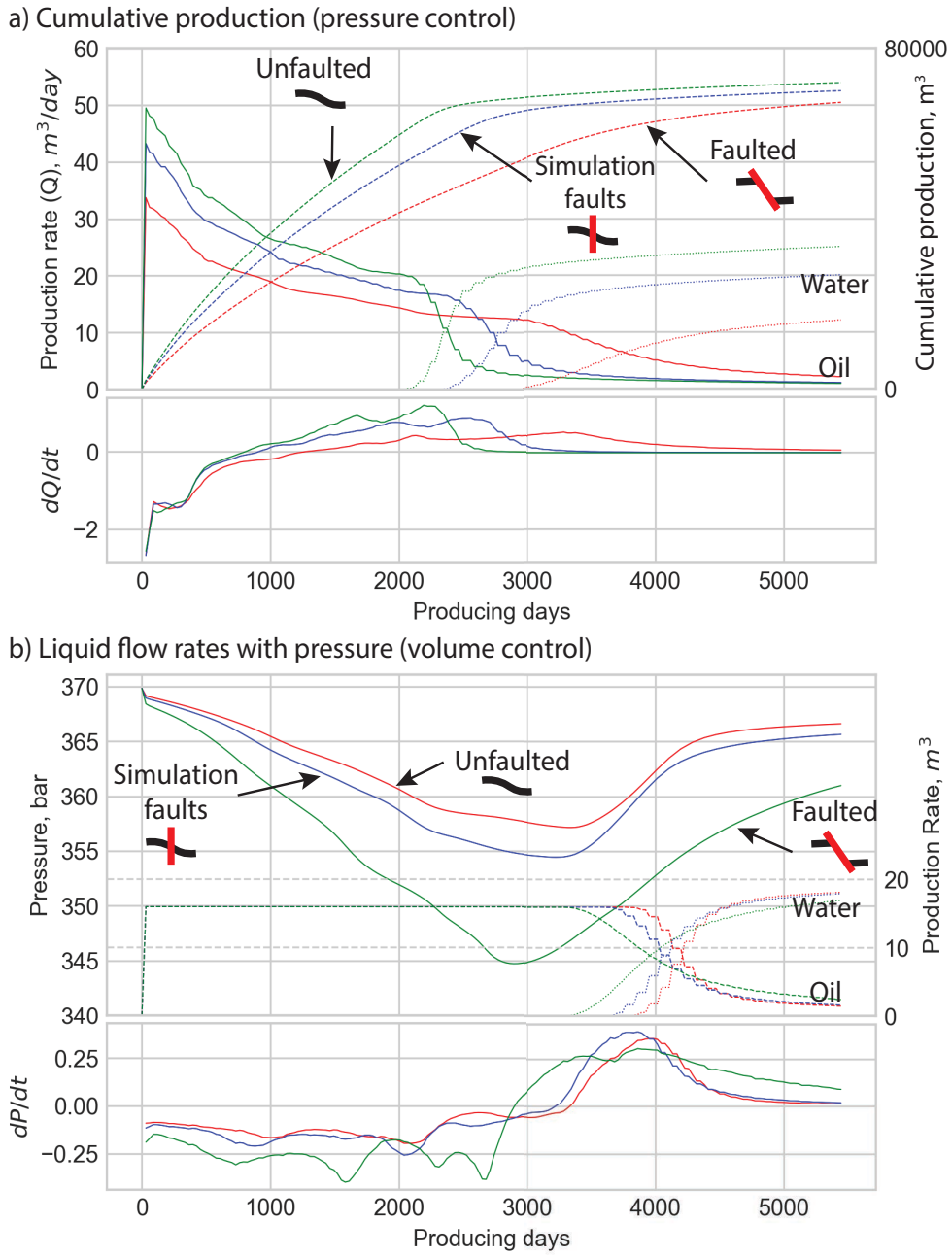

Figure 5.5: Simulated production data for different fault modelling strategies. (a) Cumulative oil production for different fault geometry modelling styles using pressure control. (b) Liquid flowrate for oil (solid lines) and water (dashed) using production volume control. Average reservoir pressure (bar) (dotted lines).

Model	Inflection 1	Inflection 2	Inflection 3
Faulted	2019/01	2023/03	2026/01
Sim fault	2019/06	2023/01	2025/11
Unfaulted	2019/04	2023/04	2023/01

Table 5.4: Graphical estimate of timing of pressure inflections observed in volume controlled flow simulation for each of the modelling scenarios.

rates from the faster flowing models rapidly reduce as water breakthrough takes its place. Despite convergence in the cumulative production volumes, there remains a significant difference in the ultimate recovered volumes at 5000 days.

In the case of the volume controlled production strategy, the rate of production is fixed exacerbating the pressure response observed as the waterfront progresses through the reservoir. In each of the modelling scenarios there is an overall trend of decreasing pressure until shortly before water breakthrough, when pressure is rapidly increased to levels approaching initial conditions. Notably during the initial pressure decline there are a series of pressure inflections, highlighted by the first derivative of pressure (Table 5.4).

Water saturation is extracted at various timesteps throughout each of the simulations, for both the volume controlled (Figs. 5.6 to 5.8) and pressure controlled models (Figs. 5.9 to 5.11). Using the water saturation to understand the progress of the water front with respect to the inflection points observed in the press-controlled cases, some correlation is observed. The significance of these inflections appears to be greatest in the faulted model and least in the unfaulted model.

These timestep images also provide an insight into the nature of fluid flow in the reservoir. The faulted case is observed to have a longer oil-water interface indicating a broader water flood front. In the simulated fault cases, the waterfront is divided into an upper and lower front by the sixth year. In the unfaulted cases the front is shorter and more coherent, forming a steady sweep across the reservoir.

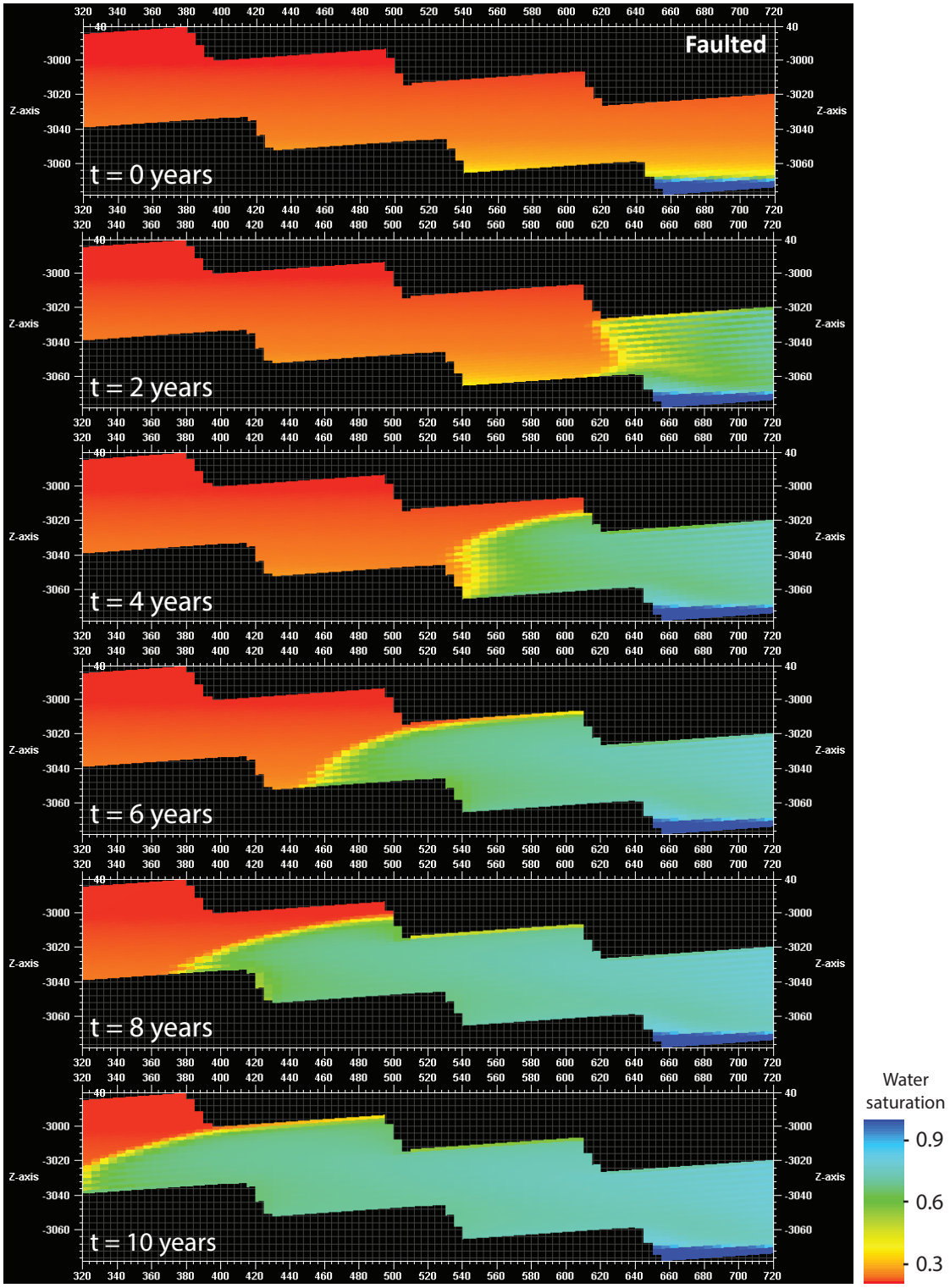

Figure 5.6: Simulated water saturation for the faulted model through time at 0, 2, 4, 6, 8 and 10 years of the 15 year long simulation, using the volume control production strategy.

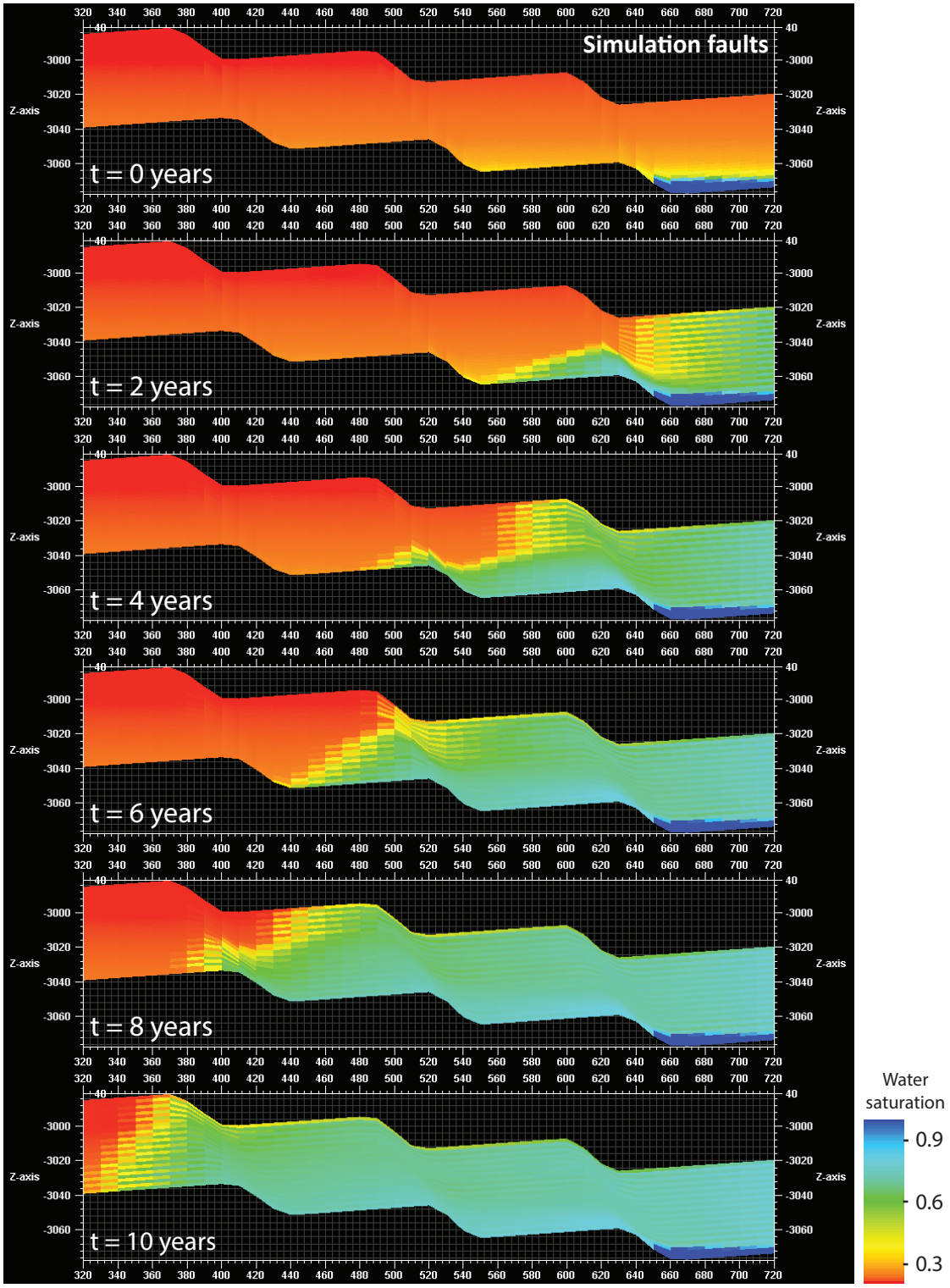

Figure 5.7: Simulated water saturation for the simulated fault model through time at 0, 2, 4, 6, 8 and 10 years of the 15 year long simulation, using the volume control production strategy.

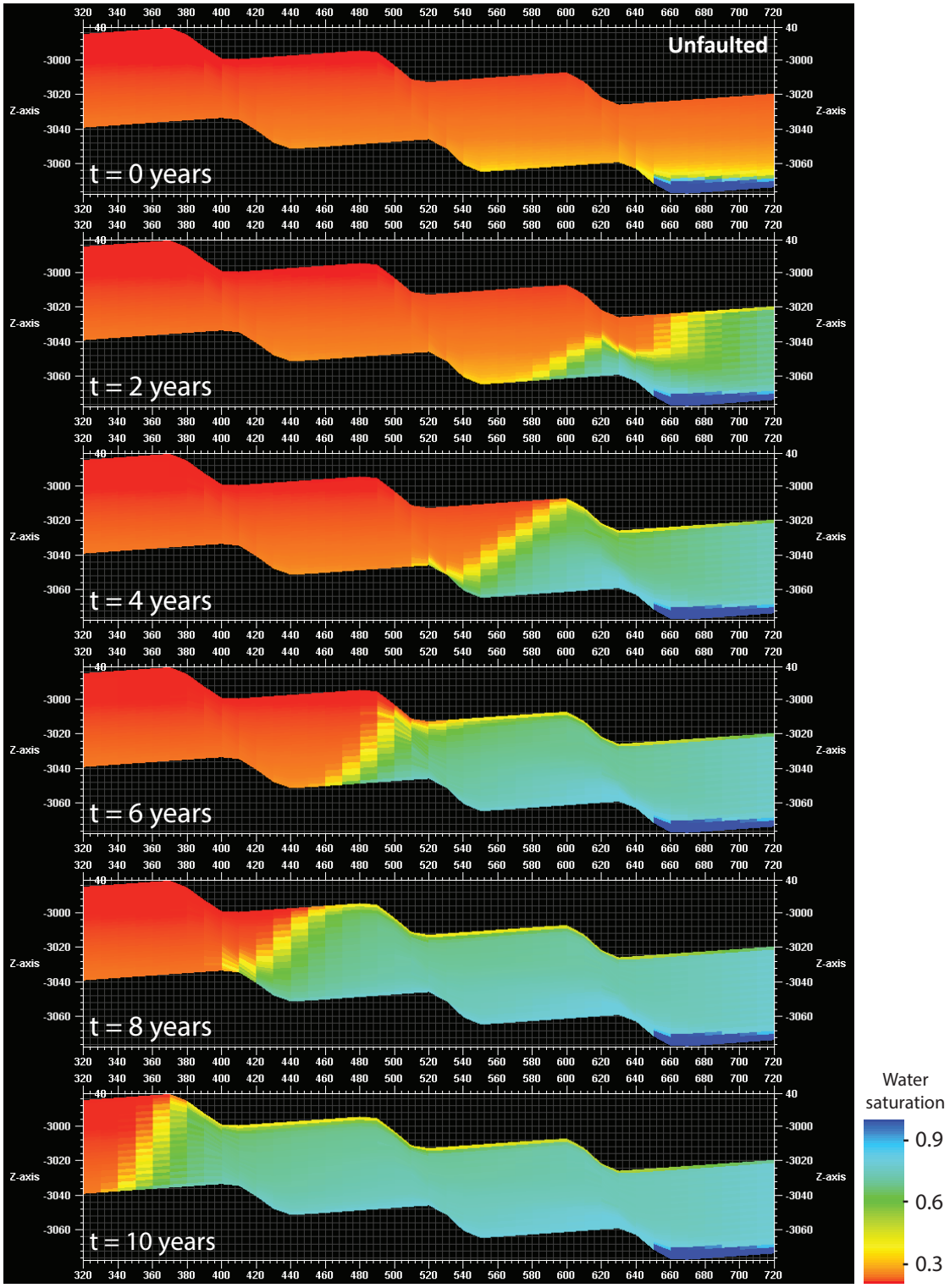

Figure 5.8: Simulated water saturation for the unfaulted model through time at 0, 2, 4, 6, 8 and 10 years of the 15 year long simulation, using the volume control production strategy.

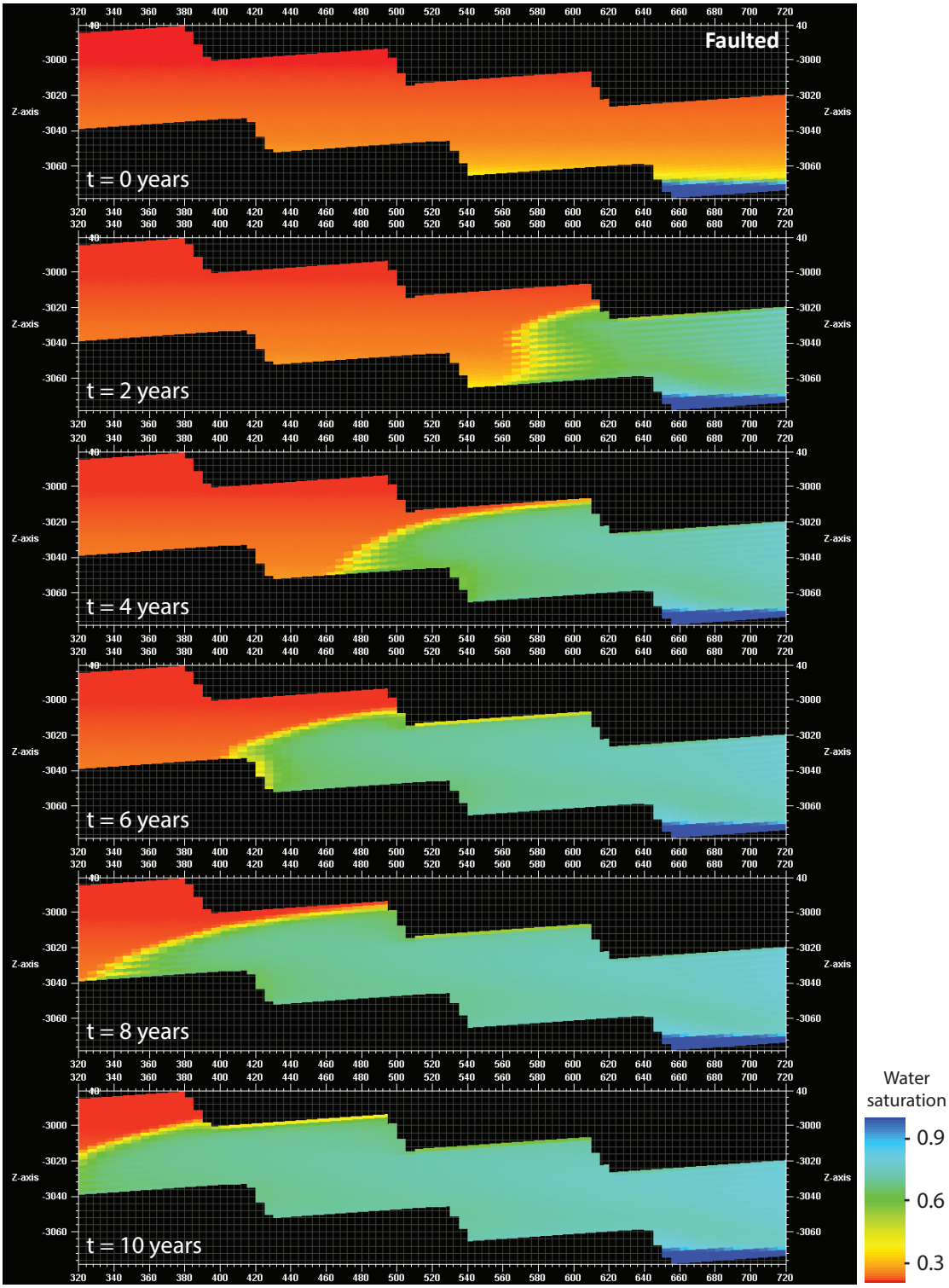

Figure 5.9: Simulated water saturation for the faulted model through time at 0, 2, 4, 6, 8 and 10 years of the 15 year long simulation, using the pressure control production strategy.

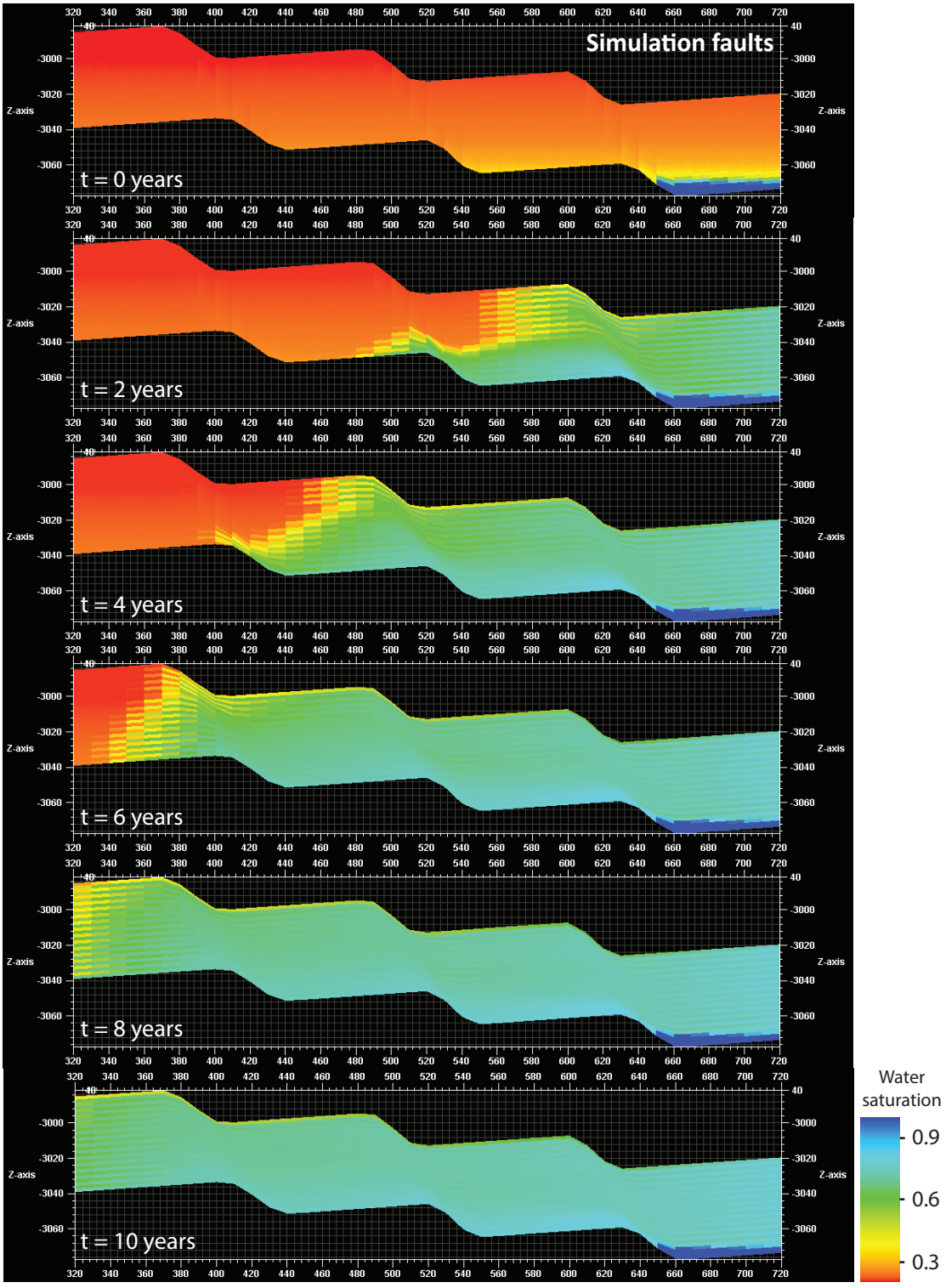

Figure 5.10: Simulated water saturation for the simulated fault model through time at 0, 2, 4, 6, 8 and 10 years of the 15 year long simulation, using the pressure control production strategy.

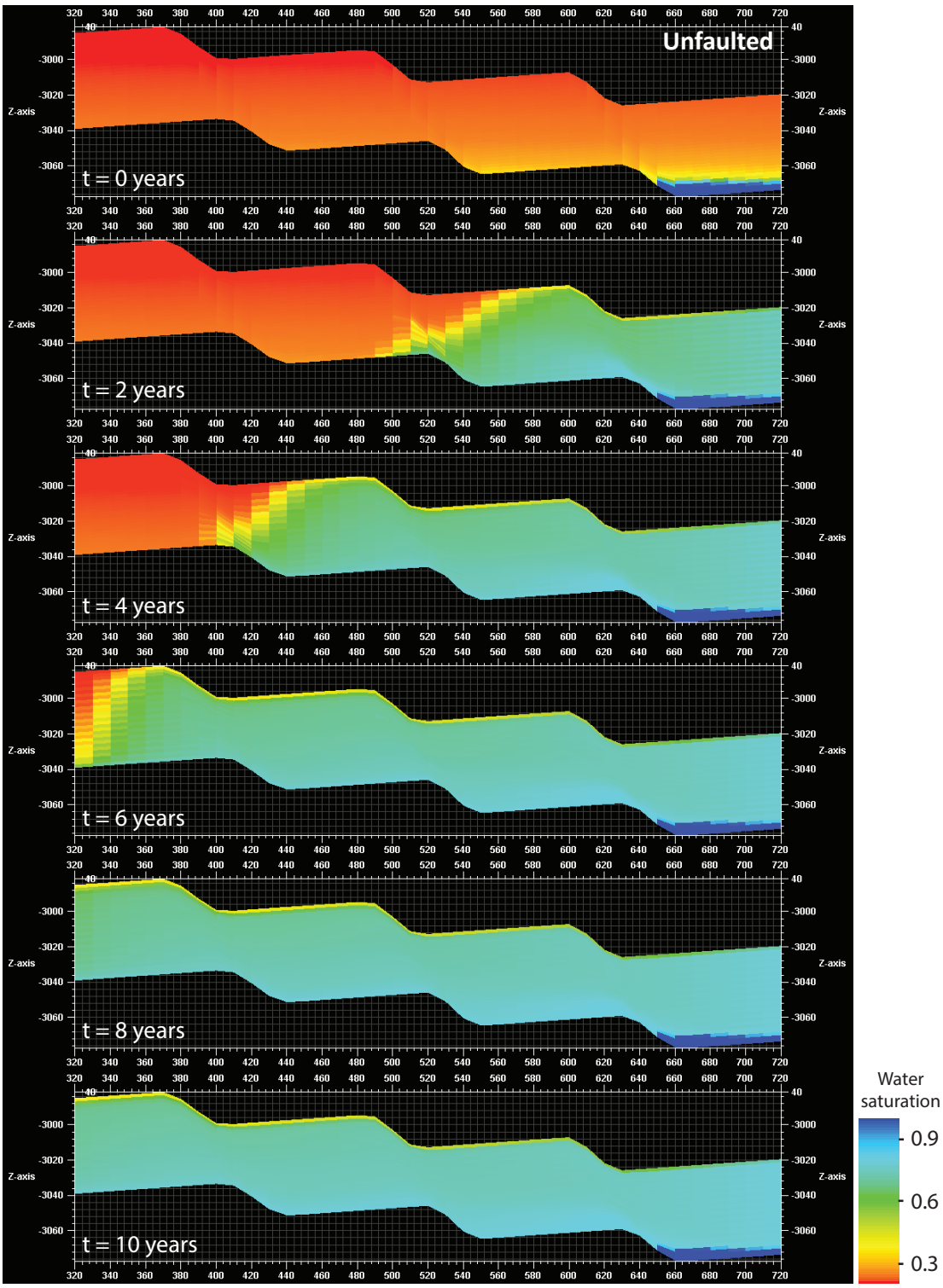

Figure 5.11: Simulated water saturation for the unfaulted model through time at 0, 2, 4, 6, 8 and 10 years of the 15 year long simulation, using the pressure control production strategy.

Strategy	Model	OIIP	EUR6	EUR12	RF
PCon	Faulted	108,192	44,036	64,337	59.5 %
PCon	Sim fault	108,558	55,765	68,636	63.2 %
PCon	Unfaulted	108,558	63,374	70,732	65.2 %
VCon	Faulted	108,192	34,944	64,014	59.2 %
VCon	Sim fault	108,558	34,957	65,596	60.4 %
VCon	Unfaulted	108,558	34,960	67,117	61.8 %

Table 5.5: Estimated ultimate production at 6 and 12 years and recovery factor, RF, calculated using the oil originally in place, OIIP All volumes are reported in Sm^3. See also Figure 5.5.

Considering the cumulative productivity of each of the cases, summarised in Table 5.5, there are significant differences in both the cumulative production at different timesteps and of the estimated recovery factors. In fact due to the early stage differences in production rates the three simulation strategies consistently diverge for the first 6 years, prior to converging again. However, despite some convergence, differences remain between all three of the models.

Normalising the production curves from each of the scenarios to the faulted model provides a means to compare the production forecasts across the full simulation time. If the faulted case is treated as a truth case, this would indicate a 30 to 50 % overestimate of the production rate in the first six to seven years, and a 50 to 70 % underestimate in subsequent years (Fig. 5.12).

Continuing to consider the faulted case as the true geometry, other cases may be history matched to it, in order to understand the significance of the changes caused by the modelling strategy, as an equivalent geological variable. Calibrating only the bulk reservoir permeability, both the simulated fault and unfaulted models are matched based on cumulative production. This requires use of 70 % and 60 % bulk permeability multipliers, respectively (Fig. 5.13).

This degree of variation in permeability is broadly comparable with that which may be

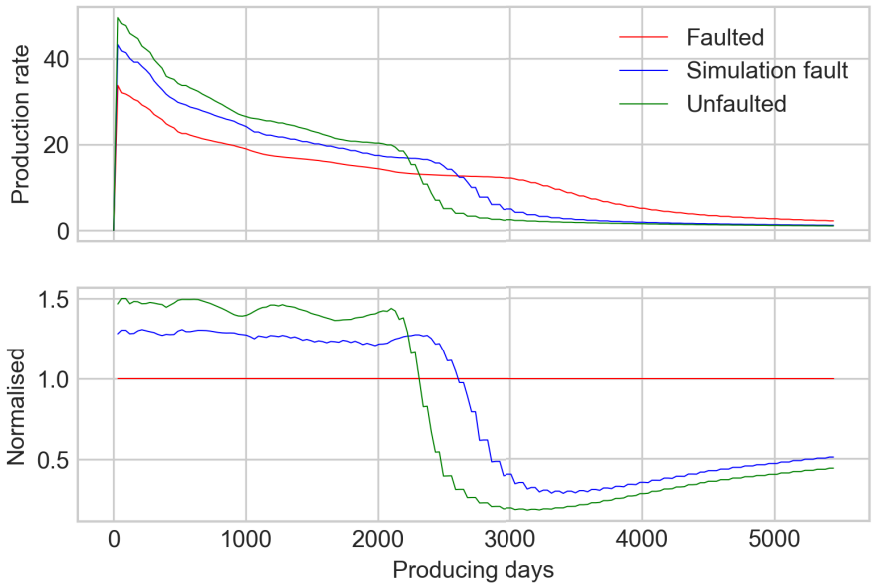

Figure 5.12: History matched normalised production rate of (a) simulation faulted and (b) unfaulted models to faulted model, using the pressure control production strategy.

expected in permeability from core analysis (Evans et al., 1997). Despite the use of gas in approximating permeability using these methods the literature suggests, for moderate permeability rocks, gas slippage effects would be minimal (Klinkenberg, 1941; Swanson, 1981), suggesting reaults may be comparable. If permeability is considered through a porosity-permeability transform, such as range would be broadly equivalent to a 20 % change in observed porosity (Evans et al., 1997).

Note that in both cases, production forecasts are reliably matched, however reservoir pressure features notable discrepancies. This supports the idea that for conventional reservoirs with moderate permeability, pressure data may provide a more sensitive discriminator for matching production forecasts to geological models (e.g. Irving et al., 2014).

a) History match of simulation fault model to faulted model

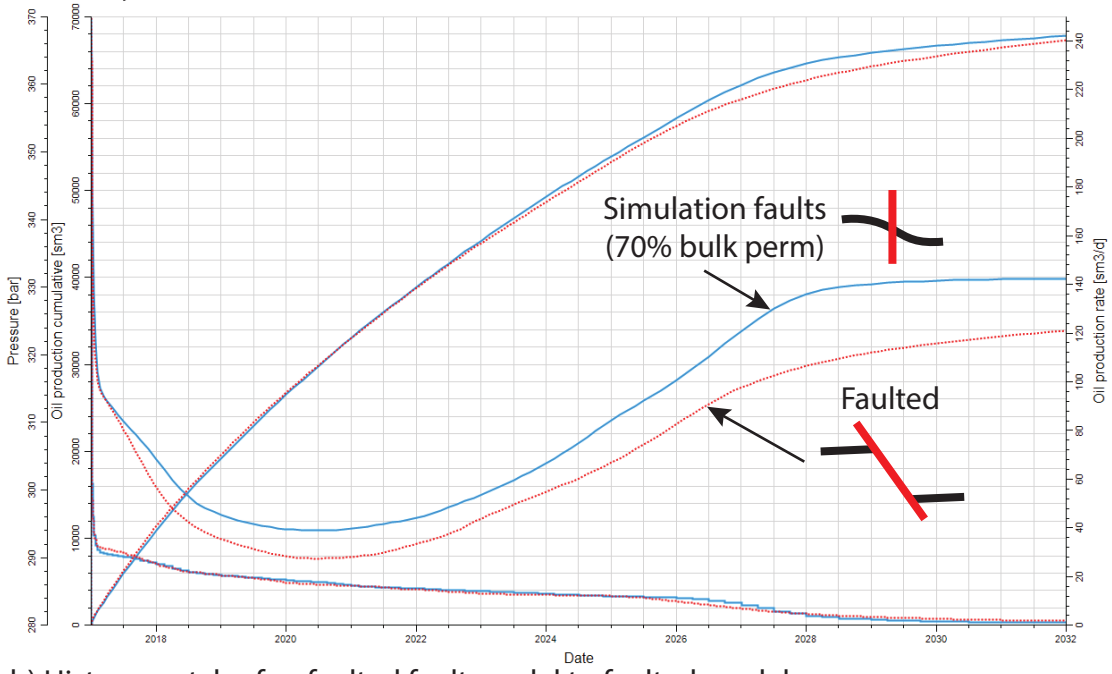

b) History match of unfaulted fault model to faulted model

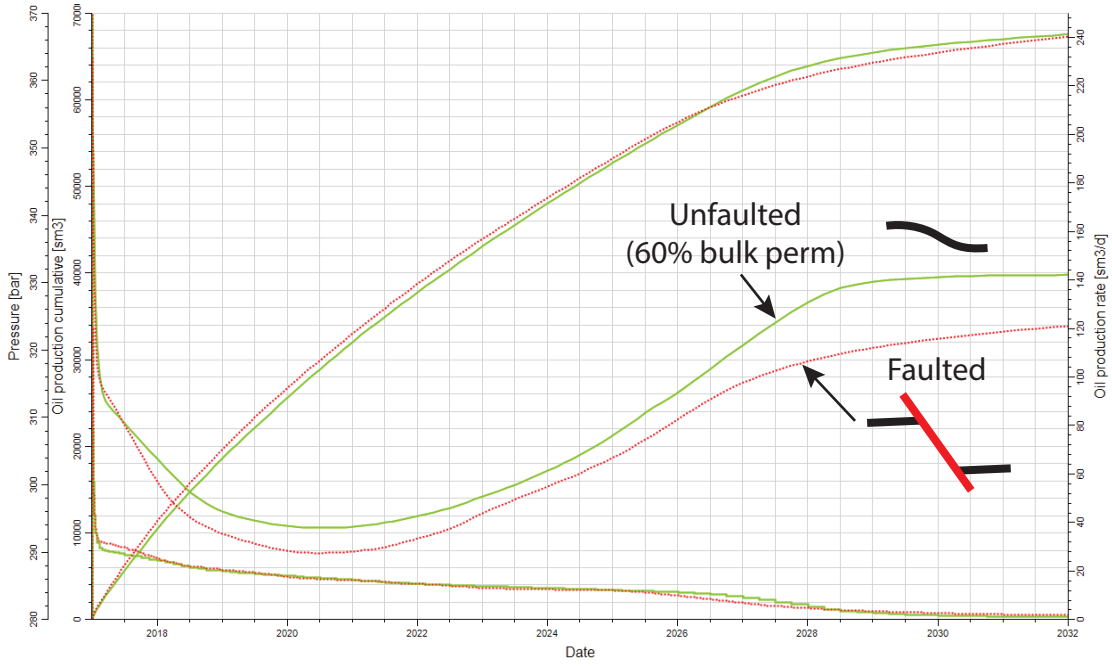

Figure 5.13: Oil production and reservoir pressure comparison for history matched simulation fault model. Oil production and reservoir pressure comparison for history matched unfaulted model.

5.5 Discussion & concluding remarks

Considering the scenario that new information suggests a subtle faulting in an existing reservoir, this chapter considered three strategies that are commonly employed to integrate new data into existing reservoir models. Using a single synthetic seismic images, I demonstrated that three fundamentally different geometries could reasonably be modelled.

The model geometries themselves incorporate a slight difference in pore volume (c. 1 %), with the faulted model being slightly smaller than the others. Comparison of cross-sections shows that this is due to the angular fault-horizon cut-offs, losing volume from additional areas that would be included in sweeping folded beds over the area of faulting.

Comparing pressure controlled modelling cases on the basis of 12 year recovery factors (Table 5.5) there is a 6 % difference between faulted and unfaulted cases for modelling, and a 4 % difference to the simulated fault model. This clearly suggests a greater difference than would be expected from the pore volume alone. Comparing production forecasts (Fig. 5.12), demonstrates a 40 % higher daily production rates for the first six year of production for the unfaulted case compared to the faulted case, and around 30 % for the simulated faults case.

The impact of this modelling outcome for decision-making would likely be significant as consideration of the time value of money, means that the early production and associated cash flow is more important for project economics than later production. This largely due to depreciation cash assets and the additional flexibility afforded by income (Bratvold and Begg, 2008; Allan, 2011).

Analysis of pressure plots and calculated derivative (Fig. 5.5b) show a number of pressure inflections (summarised in Table 5.4). Comparison to images of the waterflood captured as water saturation in the simulations (Figs. 5.6, 5.7 & 5.8) illustrates correlation to the front passing through areas of faulting and initiating vertical flow.

Despite the simplicity of the alternate models, there are significant differences in pressure

observations likely due to two separate key controls. In the faulted model, a reduced cross-sectional area is available for fluid flow across the fault zone, forming a baffle to flow. In both the unfaulted and simulation faulted models smoothing of the grid considers the fault-horizon intersections as smooth features with lateral connectivity through the faulted zones. This removes the need for fluid to move vertically through the stratigraphy, effectively increasing connectivity and bulk permeability by negating the K_v/K_h ratio.

To place this into context, geologically, the simulated and unfaulted models have subsequently been history matched to the faulted model. Using the faulted case as a truth case in this manner allows for consideration of the geological equivalence of the choice between modelling strategies. As observed, in this case varying the modelling strategy is equivalent to making a 60 to 70 % change in permeability.

The modelling case explored is very simple, using a black oil simulator with no dissolved gas avoids potential three-phase flow and detrimental affects on waterflooding (Archer and Wall, 1986). The stratigraphy is a simple series of high and medium flow lithologies, and the structure is formed by planar faults intersecting the reservoir orthogonally.

These factors could be interpreted to suggest that this would be a suitable reservoir for modelling using the simplest method possible, without need for developing a complex model. However, even in this case significant variation in production forecast is observed between the different cases.

Use of simple reservoir models, perhaps only using a bulk permeability multiplier to modify the flow tensor (Table 5.1) may provide a suitable and efficient way to represent many reservoirs when properly calibrated (Pickup et al., 1994; Ringrose and Bentley, 2015). However, it is suggested that these results demonstrate that care must be taken even in the case of simple geological models. Coupling modelling approaches to physical processes (Manzocchi et al., 1999), may be a more effective way of maintaining simplicity, rather than making numerically simple models.

This is likely not to always be the case, for example Main et al. (2007) discussed the 'statistical' reservoir model in the case of the Gullfaks field, were abundant production

data is available for comparison and tuning a statistical model. In such a case where the production well constrained, such a numerically simply approach is likely to provide an optimal approach. However, particularly in the case of exploration and appraisal stages projects, it is suggested that a simplistic geologically-based model using sensible values for unknown parameter may outperform more elegant solutions.

The only line that is true is the one you're from.

Israel Nebeker

Chapter 6

Prospect interpretation uncertainty

Chapter structure:

6.1 Abstract

Sub-thrust plays and complex compressional geometries present valuable global exploration opportunities. However, poor quality seismic imaging is characteristic of these areas due to the presence of steeply dipping strata and lateral velocity variations. Interpreting data under these constraints results in non-unique and model-driven geometric predictions.

Seismic forward modelling provides a means to generate synthetic seismic data from potential interpretations, providing an additional point of comparison and validation. In this chapter, I develop three potential interpretations of an area of complex geometry and use synthetic models from each interpretation for comparison to the original data.

This provides insight to specific zones of the interpretation that vary most between the models, providing insight as to the likelihood of each model. Calculating resource in-place for each potential reservoir geometry provides a means to quantitatively analyse the impact of interpretation choice on the resource estimation.

This work illustrates significant variation of resource estimations dependent on the selection of interpretation. Use of a Bayesian approach to conduct a probabilistic, multi-scenario, assessment better illustrates the way in which spatially-variable uncertainty impacts resource estimation.

Comparison of deterministic and probabilistic workflows, demonstrates the importance of using consistent workflows across assets when managing portfolios. Using a multi-scenario interpretation approach combined with probabilistic resource modelling provides a visual cue for teams to consider alternate interpretations and a quantitative dataset better capturing the range of potential outcomes.

6.2 Introduction

In this chapter, I continue to expand the spatial scale of focus, to investigate application of seismic forward modelling to an entire prospect. Having considered the impact of subtle geometric changes on local seismic response (Ch. 4) and the influence larger scale variations on production forecasts (Ch. 5). This chapter aims to quantify the uncertainty introduced when multiple valid geometric interpretations exist for a single dataset.

To provide a realistic scenario where multiple geometries are feasible this chapter focusses on the structural setting of a sub-thrust play. I consider alternate geometries each plausible in the geological setting and within constraint of the available data. The range of volumes of these alternate prospects are then considered as a whole to quantify the related range of uncertainty.

Initially, I complete a proof of concept exercise to test and illustrate the workflow, and then, using data from the frontal ranges of the Eastern Cordillera, Colombia (Fig. 1.1), a full example is provided and impact of the geometric variations considered in terms of estimated resource potential.

While the primary focus is on the interpretation uncertainty and potential to use seismic forward modelling to constrain potential interpretation outcomes, this also provides an opportunity to consider the relative merits of utilising stochastic and multi-deterministic modelling approaches for reserves calculation.

6.3 Proof of concept

In this section a simple thrust geometry will be used to establish a proof of concept for the remainder of the chapter. This being that multiple interpretation may be drawn from a single seismic image, and that these interpretations themselves may be used to generate subsequent synthetic seismic images for comparison.

The thrust fault geometry is generated using a trishear fault-propagation model populated with elastic properties. These represent a simple stratigraphy of alternating sand and shale (§ 3.3.1), from which the seismic image is simulated for interpretation (Fig. 6.1a).

This image was shared with nine structural geologists, who were asked to interpret the main thrust fault from detachment to the fault-tip. Once complete these interpretations are collated and overlain on the original synthetic image. Each interpretation is represented by a single dark red line, where multiple interpretations overlap the line colour is gradually brightened to yellow.

Three dominant trends are evident (Fig. 6.1b), representing low, medium and high angle thrust ramp interpretations. Imaging quality is spatially variable, with greater uncertainty in the regions of the forelimb and backlimb folds, challenging identification of continuity through these areas. While, flat-lying areas are better imaged ahead of the propagating thrust, behind the backlimb fold and within the ramp flat, providing constraint on the relatively undeformed areas of the section.

Information from areas of better quality imaging is used to constrain the input geometry for kinematic modelling. In this case, using the interpreted horizon geometries, leaves the fault position as the key element controlling the geometric expression of a kinematic model (Fig. 6.1c, e, & g).

These geometries are populated with simple elastic properties representing a stratigraphy of alternating sand and shale (§ 3.3.1). Seismic forward modelling these models provides a synthetic seismic image of that interpretation for direct comparison back to the original image (6.1d, f & h).

Modelling is achieved using an interface based model (§ 3.2.1) and elastic properties of sand and shale (Sand and Shale1 of Table 3.1). This impedance contrast and the resulting reflectivity is convolved with a Ricker wavelet of 30 Hz (§ 3.4.1). This is a normal incidence survey with a source and receiver spacing of 20m (§ 3.4.2), acquired with all receivers active throughout the survey duration.

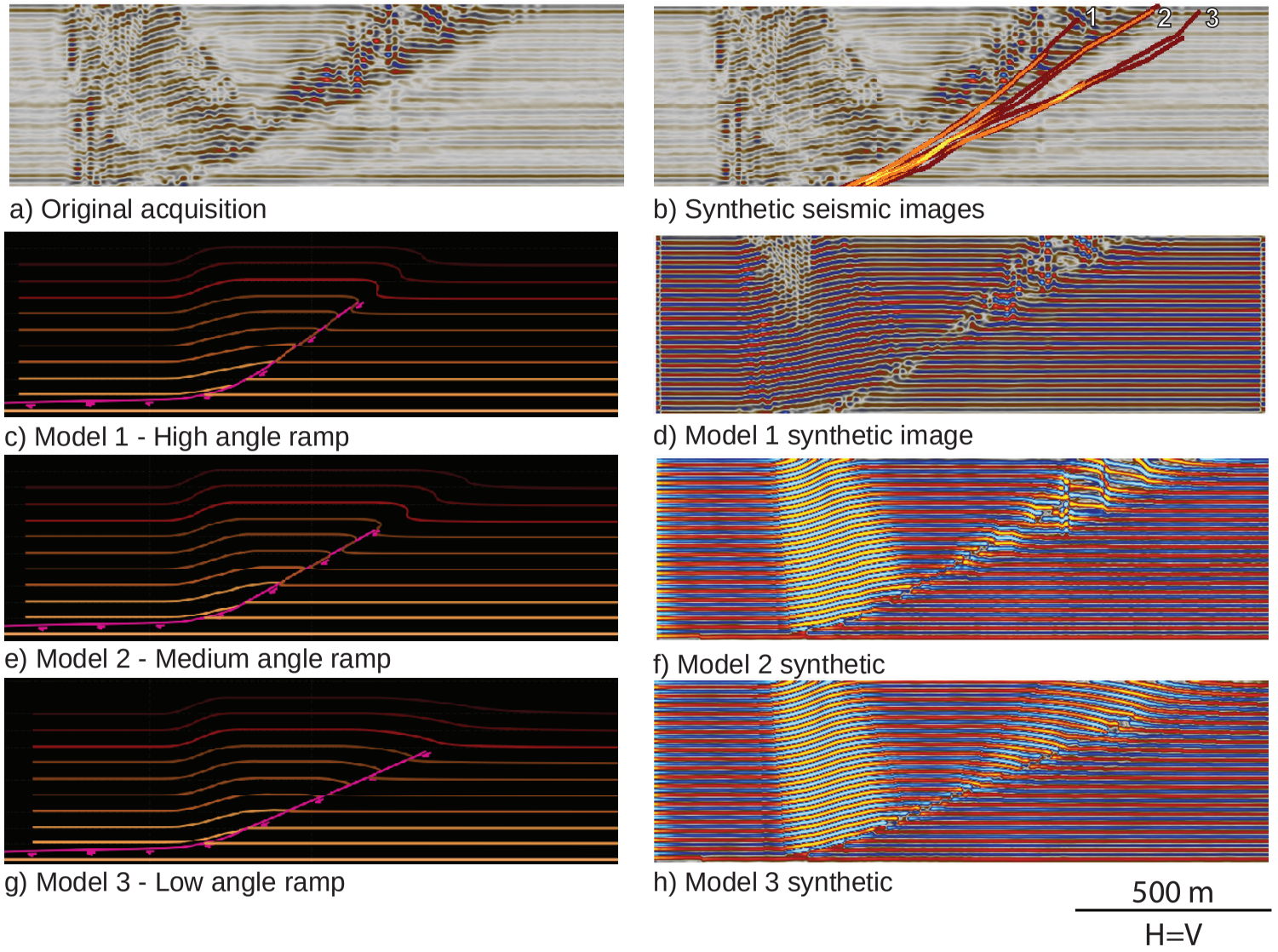

Figure 6.1: Example of multiple interpretation concepts used to generate alternate kinematic geometries and synthetic seismic images.

Comparison of the output synthetic images back to the original image illustrates a qualitative best fit with the highest angle thrust ramp model (Model 1). This qualitative conclusion is principally achieved by comparing the distribution of fault-related noise. This is consistent with observations made in Chapter 4, steeper faults are associated with wider and more complex seismic response, related to the the geometry of the Fresnel zone. This expresses a much poorer lateral resolution than vertical.

This workflow demonstrates the potential strength of seismic forward modelling for assisting interpretation in complex settings. As in Figure 6.2, incoming seismic data may be assessed to ascertain likely areas of divergence in interpretation, where multiple valid alternate models are more likely. Having selected an area of interest multiple interpretations may be gathered by conferring with other interpreters and used to generate the synthetic seismic images that may be used as an input for the next iteration of the cycle. Once multiple valid interpretations are available they may be risked, evaluated and considered as targets.

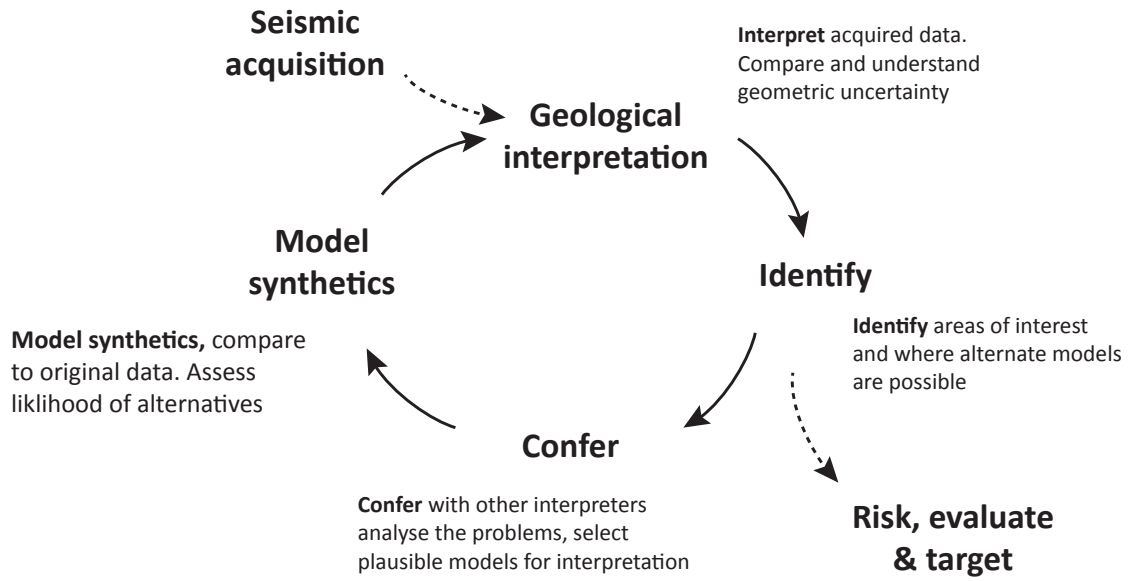

Figure 6.2: Suggested iterative interpretation workflow integrating seismic forward modelling to iterate interpretations.

6.4 Field example

Using the iterative interpretation workflow (Fig. 6.2), I will now apply it to an anonymised onshore seismic volume from the foothills of the Eastern Cordillera, Colombia (Fig. 6.3). Data access was kindly provided by Ecopetrol during a visit to the Instituto Colombiano del Petróleo, Colombia under the guidance of Andrés Mora. Initial interpretation was completed during this visit, I was subsequently allowed access to selected two dimensional sections for further analysis remotely.

The area is a prolific hydrocarbon province hosting some of the largest global discoveries in history (Cazier et al., 1995; Egbue and Kellogg, 2012). Since early recognition as a region of economic interest (Hettner, 1892), study of the foothills and western edge of the Llanos Basin have led to an understanding of the local geology. Along trend many indications of structural inversion have been identified (Cooper et al., 1995; Bayona et al., 2013), including significant harpoon structures (McClay, 1995).

However, the area local to the seismic volume studied below does not feature clear indications of structural inversion, despite reasonable seismic imaging quality (Fig. 6.3). Locally, published geological interpretations are constrained by good surface exposure, structural restorations calibrated by thermochronology and an extensive database of seismic data, covering much of the foothills and nearby Llanos Basin.

Surface mapping presents a repeated stratigraphic sequence associated with large anticlinal antiforms forming fault-propagation folds, likely controlled by a deeper detachment. The seismic volume lies between two of these fault-propagation folds in gently inclined strata, dipping to wards the orogenic axis. The gently inclined parallel reflectors of the upper section of the seismic image are interpreted to be a continuation of this strata, forming part of a ramp-flat.

On this initial presentation of the seismic image, minimal interpretation markings are made. Red arrows indicate the zones through which major thrust faults are interpreted, while a green arrow indicates the top of the hypothetical reservoir target to be discussed.

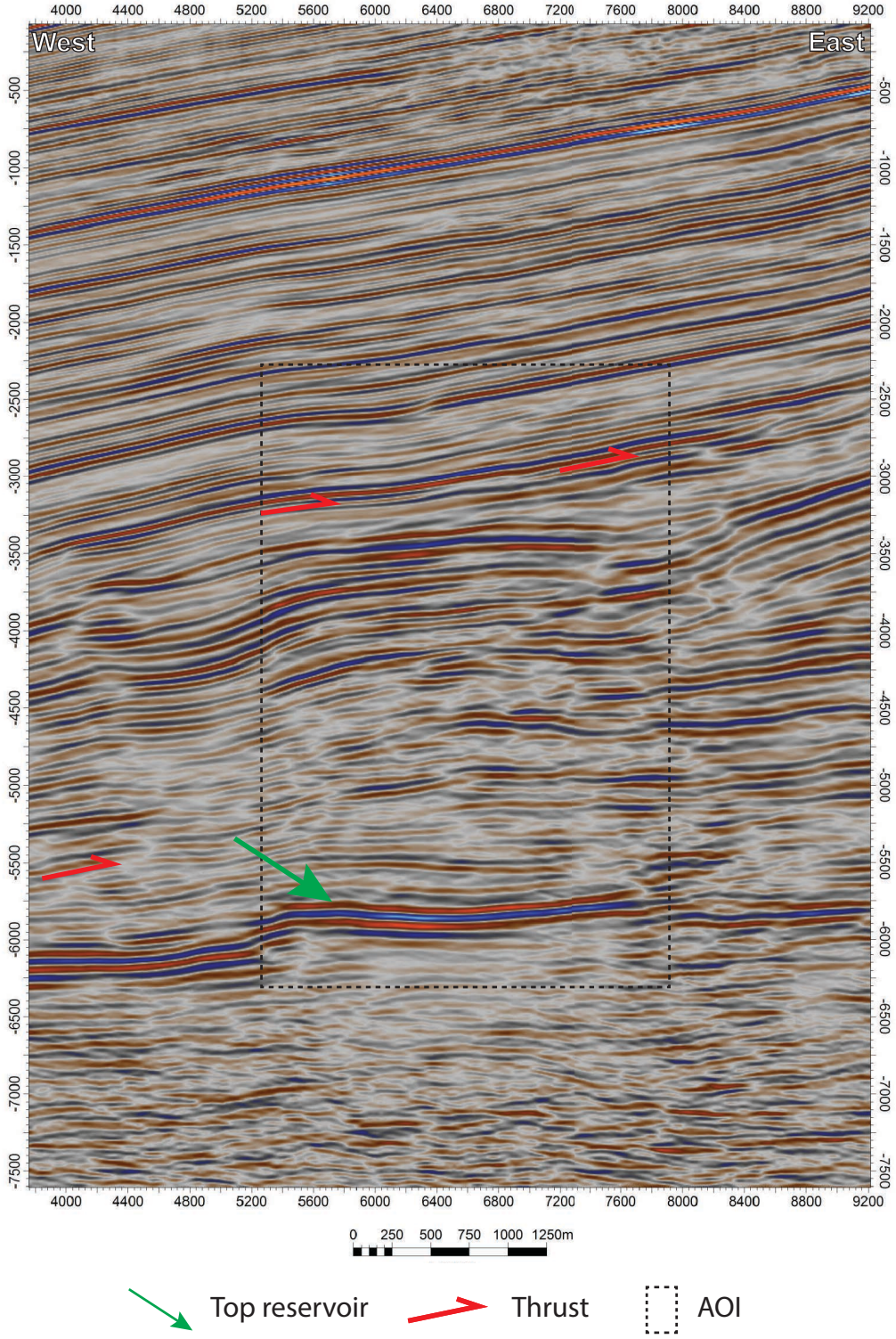

Figure 6.3: Original seismic data with annotations of key features

The upper package of reflections are generally continuous in nature, gently dipping towards the southwest.

Reflections are observed to terminate laterally along a gently dipping trend from -3800 m to the left of the image to -2700 m to the right. Beneath this, reflections become more undulating and less continuous, with a reduction in perceived signal quality. Sporadic trends of lateral termination of reflections are observed, cross-cutting reflections at various angles of dip. These dips form a number of populations, some steeply dipping at 70° towards either direction, some dipping at 30 to 50° typically towards the west and others gently dipping at 0 to 20° in either direction. These trends of reflection truncation are interpreted as duplexes caused by a buttressing effect of packages to the east.

Around -5700 m, a series of higher amplitude reflectors form a potential hydrocarbon prospect. These reflections form a generally continuous band, offset by faulting in two locations. Immediately below this prospect, amplitude is substantially reduced, which could be consistent with attenuation associated with a compositional variation, such as the presence of low impedance fluids.

Beneath -6500 m, the seismic signal becomes weak and discontinuous. The seismic texture appears to be sub-horizontal, however it is unclear as to whether this is representative of the underlying geology. Intermittent trends exist within the seismic response forming trends of discontinuous response, potentially related faulting.

In this volume there are no clear indications of syn-kinematic thickening or inversion structures. A regional strike-slip fault is identified in surface mapping cross-cutting the margin oblique to structural trend. It is suggested that this could result in the feature not being optimally oriented for reactivation effectively forming a stress bridge around the area.

6.4.1 Seismic interpretation

Lack of constraint on the tectonic style in the immediate vicinity of the prospect provides scope for multiple valid interpretations. Using a range of analogue models to bias my view of the data, I interpreted the data three times, each time applying a different model, representative of an; extensional, compressional or reactivated style (Fig, 6.4). This approach provides an opportunity to apply the iterative synthetic modelling approach (Fig. 6.2) to investigate the relative likelihood of occurrence for each interpretation style.

Recent work has demonstrated that alternate models are commonly generated by different interpreters, influenced by their past experience (Bond et al., 2007; Alcalde et al., 2017a). In an unconstrained situation, such as that presented, this approach provides a view into how the dataset may be interpreted differently (Fig. 6.5).

All interpretations feature a common interpretation of data to around -5700 m (§ 6.4), in that they underlie a mechanical detachment formed by the the floor thrust of the overlying duplexes. As such the style of deformation may be vertically segmented.

The reactivated case (6.4a) presents a single reservoir compartment hosted within a tilted fault block that has been subsequently reactivated with a through-cutting back-thrust and associated left-dipping fault that may be interpreted as an antithetic fault to the back-thrust or a footwall short-cut to the basement step.

The extensional case (6.4b) represents a raised horst play with primary normal faults dipping outwards. On the left hand side, a number of faults act together to accommodate extensional strain. These are cross-cut by the floor thrust, while the fault to the right features an upper termination into an unconformity immediately overlying the horst. In this case fault segmentation along the left hand side leads to the potential compartmentalisation of an area to the west.

The compressional case (6.4c) features left-verging thrust propagation, with slight fault-propagation folding forming gentle antiforms above the faults cross-cutting the target. The main reservoir is formed by two thrust nappes, with the main thrust bisected by the

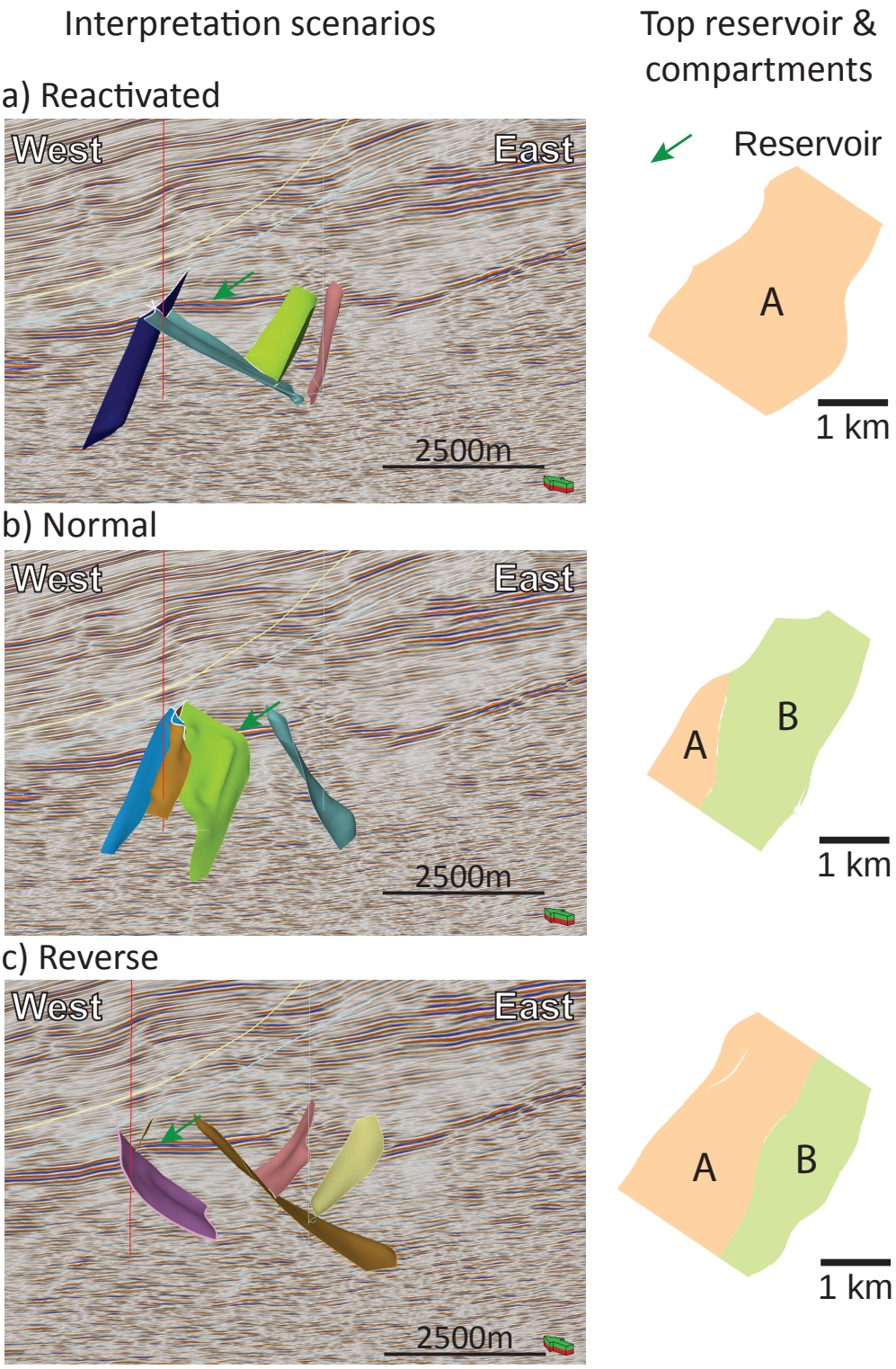

Figure 6.4: Alternate interpretations of seismic data, illustrating the 3D models on the left and the top reservoir footprint on the right.

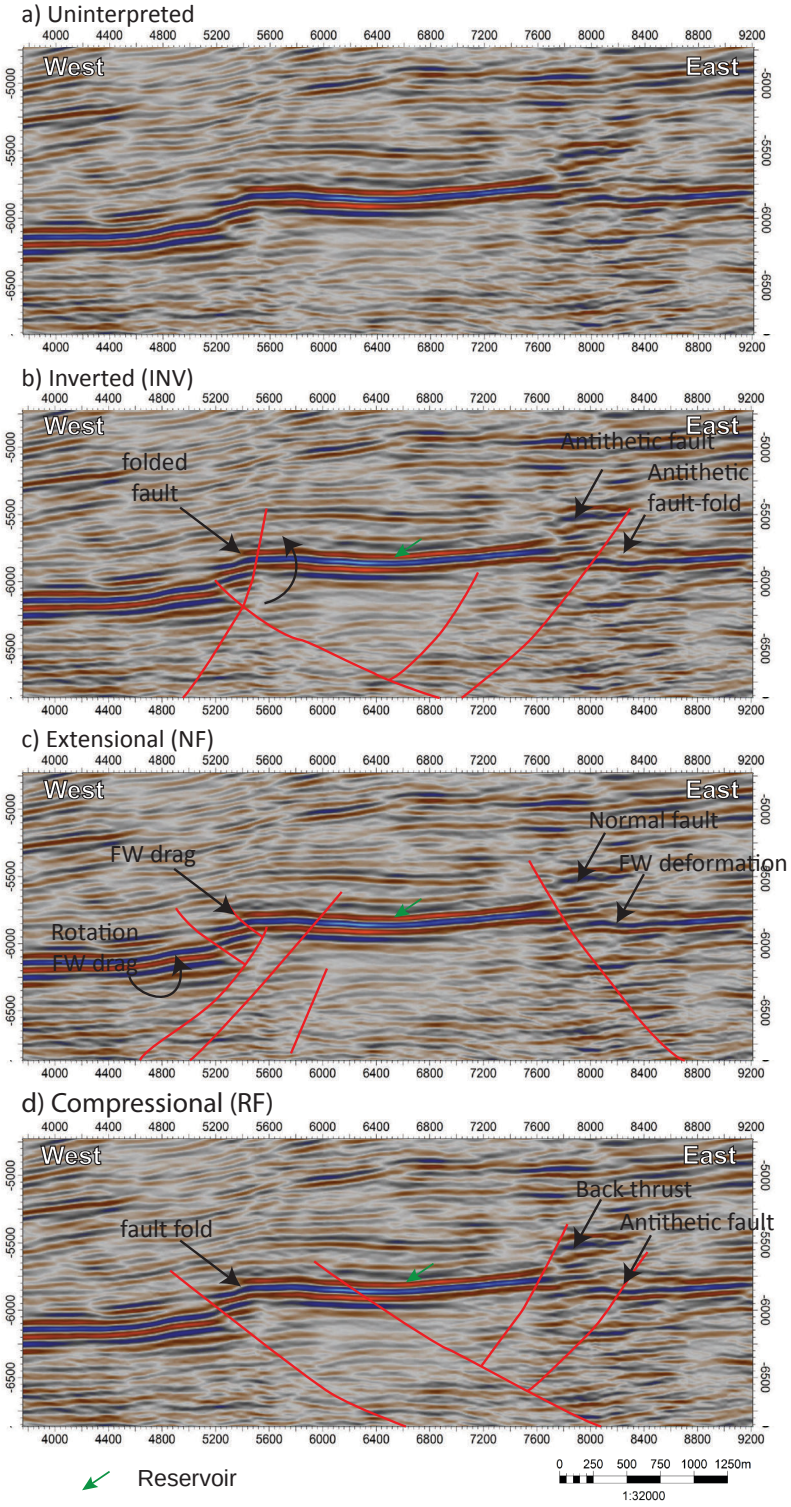

Figure 6.5: Close-up of alternate seismic interpretations

second thrust and limited by an antithetic back-thrust to that feature to the right hand side. This results in a reservoir approximately bisected by the fault.

6.4.2 Synthetic seismic image

Each interpreted case is developed into a synthetic seismic volume. Horizons picked during geometric interpretation, are used to define packages that are then populated with intermediary layers spaced proportionally around the existing horizons. Generating a geocellular grid from this structure elastic properties are populated (Table 3.1), representing an alternating sand and shale stratigraphy in the manner previously discussed (§ 3.3.1).

The workflow established in Chapter 3 is then applied (Fig. 3.1) using a volume-based model. A 30 Hz Ricker wavelet is used (§ 3.4.1), with sources and receivers spaced at 60 and 20 m, respectively (§ 3.4.2). Twelve survey lines are oriented parallel to the structural vergence, spaced at 200 m. These acquisition survey parameters have been selected to best emulate the survey of the real data to which the synthetic images are compared. The Zoeppritz equations are used to calculate the amplutude response with an angle dependency (§ 3.4.3). Amplitudes are then calibrated as described previously (§ 3.4.3).

Figure 6.6 illustrates the geological model (left), input elastic property models (centre) and the output synthetic seismic images (right). Comparing the output synthetic models key differences are observed in the manner in which input model geometries are exhibited in the output synthetic images (Fig. 6.7).

6.4.3 Relative likelihood of interpretations

After forward modelling each of the interpretation cases, they are compared both to their original geometric interpretations and each other to understand their relative likelihood of

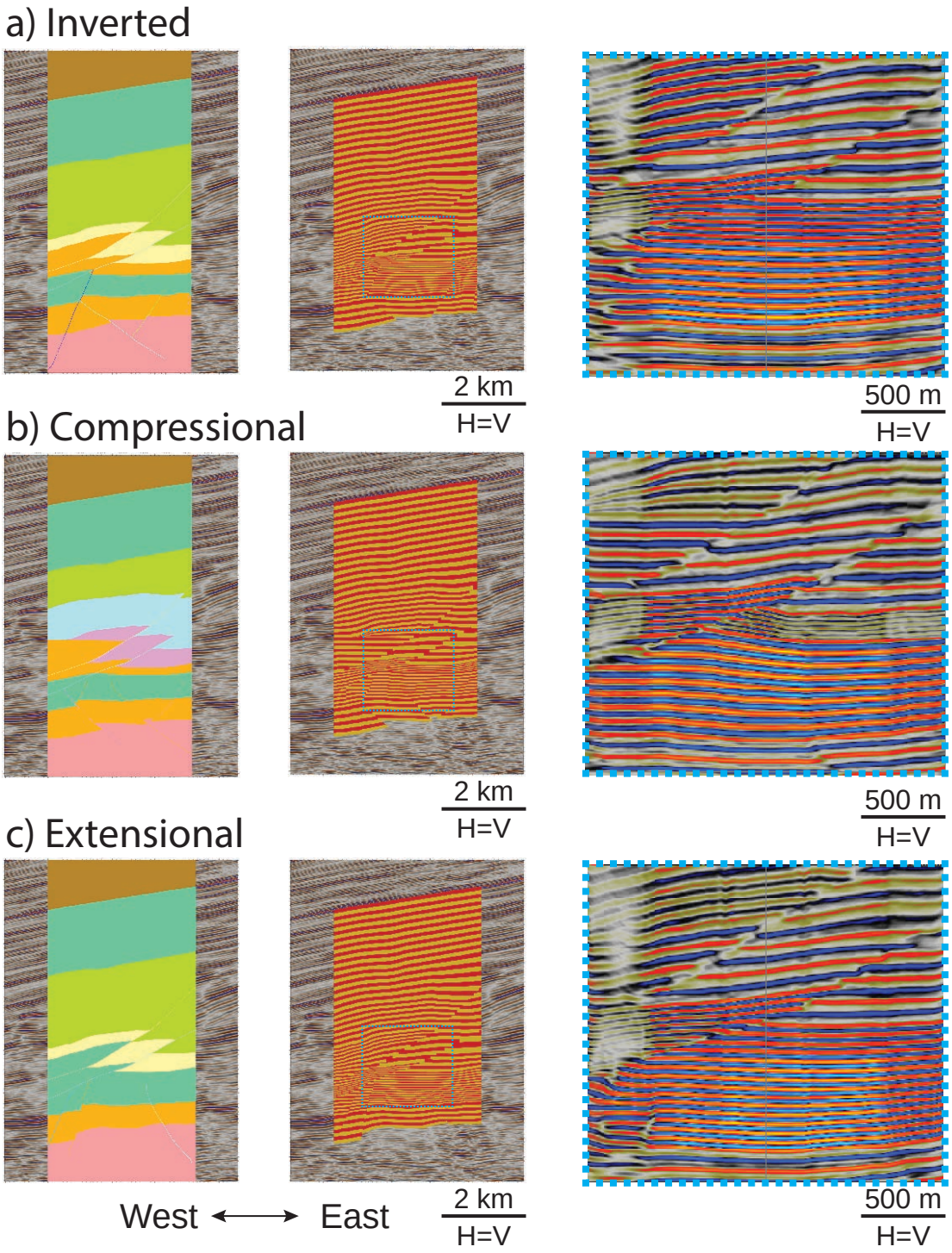

Figure 6.6: The geological model (left), elastic property model (centre) and output synthetic seismic image (right) of each alternate interpretations.

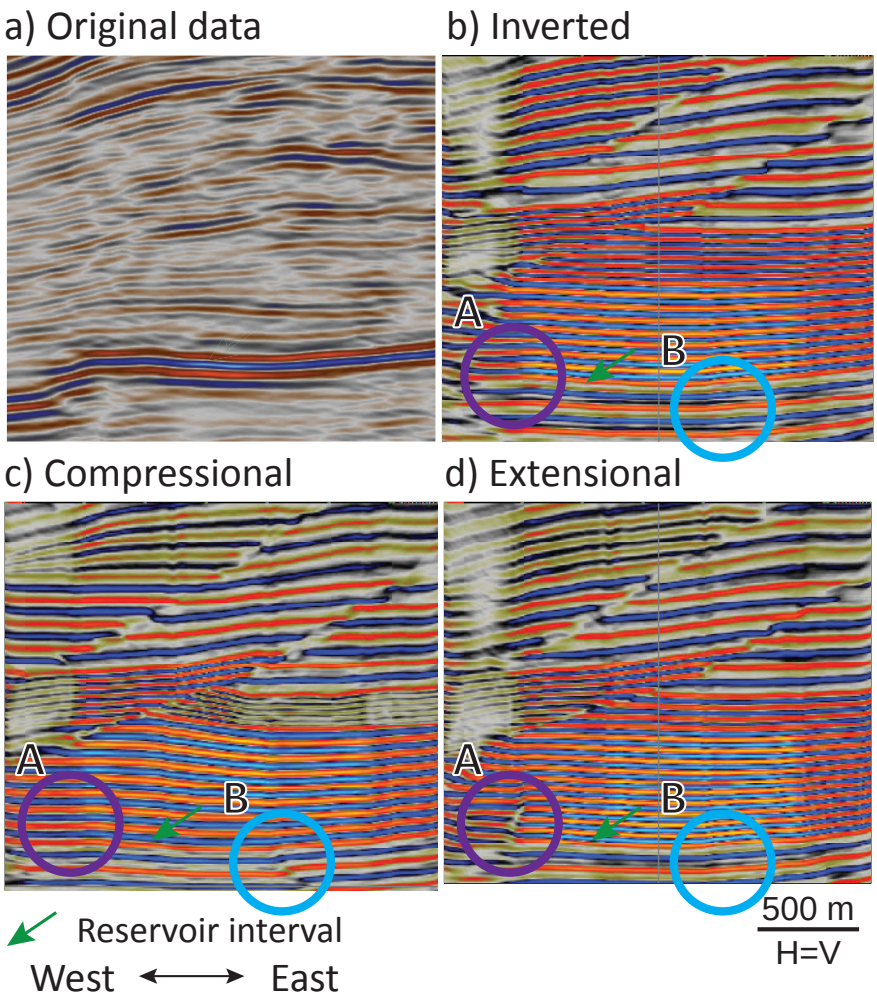

Figure 6.7: Synthetic models of alternate interpretations.

occurrence. Despite simulation of the same acquisition survey in each case, differences in subsurface geometry result in variations in the quality of imaging of structures. This may be attributed to variations in illumination, causing varying detectability, dependent on the orientation of faults, consistent with the reviewed controls of seismic imaging quality (§ 2.3).

In Figure 6.7, circles A and B are placed to highlight two particular areas of uncertainty where the reservoir terminates to either side. These cut-offs form one of the main discrepancies between the alternate interpretations (Fig. 6.5). Simulating the geometries therefore provides an insight to their expression and detectability in a real acquisition.

Considering the area of Circle A, in real data a significant offset of the reservoir is observed and reflections appear to drape over the area of potential faulting, with two areas of decreased amplitude, which have been interpreted to be synthetic, antithetic or anomalous in the interpretation cases. The amplitude anomaly is not expected within synthetic models due to the simple stratigraphic model. However, there are still amplitude anomalies present along the trends of the interpreted faults for the inverted and normal faulting cases, while there is no indication of a fault in the reverse case.

All models feature a left dipping fault at that location, removing the chance of this being a result of background illumination. However, the geometry of the reverse model and spacing of faults means that throw is stepped between two nearby faults. This appears to form a sloped contact rather than an abrupt lateral contact. Comparing these observations to the real data, a change in amplitude is observed, this may indicate a reduced likelihood of the reverse faulting model.

Considering the area of Circle B, in real data an intra-reservoir fault appears to be present by the offset of amplitudes, however is very poorly imaged at the location of the fault. In the inverted and compressional interpretations this is a left dipping synthetic reverse fault, while in the extensional case this is a right dipping normal fault. In the synthetic seismic, the reverse faulting model shows this fault clearly, whereas the inverted and extensional models show that this is a more subtle feature, as observed in the real data.

From these observations, it is suggested that the extensional or inverted interpretation cases may be more consistent with the observed seismic response, once the likely expression of faulting in seismic has been considered. Though the evidence is far from conclusive, this results in the suggestion that the extensional case or inverted case may be equally likely and the reverse case less so. This is illustrated in terms of likelihoods presented in Table 6.1.

While determination of these likelihoods is somewhat arbitrary, it is in-line with current practice (White, 1993; Peel and White, 2015; Suslick and Schiozer, 2004; Milkov, 2015; Yoe, 2011). This approach clearly lacks some degree of repeatability and robustness and

Case	Likelihood	Justification
Extensional	0.4	Passive margin history, normal offsets visible
Compressional	0.2	Features visible in synthetic, not in actual data
Reactivated	0.4	Passive margin history, normal offsets visible

Table 6.1: Weighting of alternate interpretation scenarios, illustrated in Figure 6.4.

improve the definition of rationale bounds within which the real solution is likely to be found (Kahneman, 2003; Curtis and Wood, 2004).

6.5 Resource uncertainty

Calculating hydrocarbon initially in place is fundamentally a very simple task, however in reality data availability and practical constraints make this very challenging. The purpose of such work is ultimately to inform a series of business decisions, requiring a numerical representation of the range of likely possibilities in a format that may be direct compared with other business opportunities.

In order to make decisions about design, strategy or investment, an understanding of both likely outcomes and associated risks are required. In this section, I use the geometries interpreted previously with information gleaned from synthetic modelling to demonstrate the sensitivity of economic appraisals to variations in structural interpretation.

Hydrocarbon volume estimates are typically initially explored as deterministic models, where depending on the mechanism of formation a single outcome may be expected. Where alternate scenarios of development may be expected, or a range of high to low cases are desired, individual changes may be made to the model in order to vary the result.

Stochastic calculations assume the same fundamental relationships between inputs and outputs, however instead of using single values inputs, distributions of possible inputs are

utilised to generate a range of potential input cases, all of which may be ran through those fundamental relations to determine the the range of potential outputs. An important aspect of this type of analysis is the randomisation of input cases, so that the full uncertainty range may be sampled more accurately (§ 2.2.3).

This concept has been explored more thoroughly in the field of sedimentology, where the classification of deposits lends itself to application of distributed property values (e.g. Baas et al., 2005; Colombera et al., 2012a; Vakarelov and Ainsworth, 2013; Adelinet and Le Ravalec, 2015). These may in turn be used to infer likely distributions of porosity, net:gross and other parameters. The common use of a porosity cut-off for determination of net to gross ratios, symbolises well the mutual dependency on these factors, in which the stratigraphic element within an environment of deposition effectively define the probability distribution of porosity.

Similarly, in a structural sense, determination of the geometry of the reservoir container is significantly controlled by the interpretation of structural geometry and trapping mechanism. Mistaken categorisation of the nature of a structural geometry may lead to dramatic misstatement of reserves.

6.5.1 Deterministic volume estimation

The reservoir interpretations made above provide the basic inputs required for a deterministic volumes calculation. Intra-reservoir faulting is used to divide the reservoirs into separate but dependent risk segments (Stabell, 2000), where appropriate (Fig. 6.8).

For each segment, a standard calculation of hydrocarbon initially in place using equation (6.1) is used to determine the in-place volume (Ahmed, 2010; Dake, 2001).

$$V_o = N = \frac{V\phi(1 - S_w)}{B_o} \tag{6.1}$$

Where; V is net rock volume, that is the gross rock volume minus any volume that does

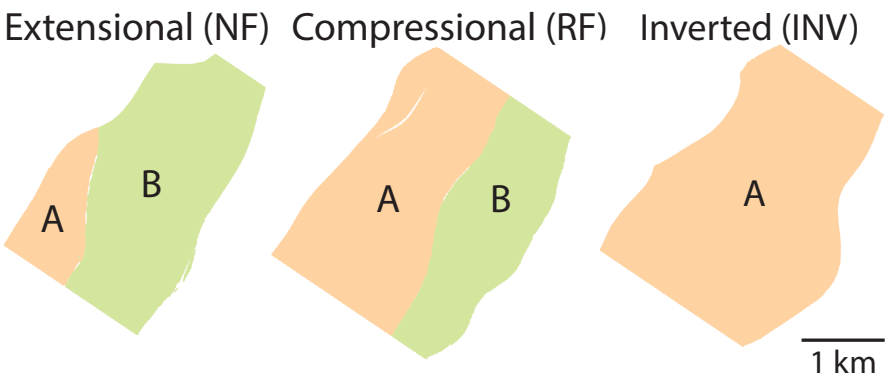

Figure 6.8: Interpreted segments and related labelling.

not contribute to flow within the volume; ϕ is the average porosity of that net reservoir rock; S_w is the average water saturation of the reservoir and B_o is the formation volume factor, that is the ratio of the volume of oil under reservoir condition relative to those under stock tank conditions.

Porosity and water saturation are assumed as 22 and 30 %, respectively, and results are presented in Table 6.2. The inverted interpretation consists of a single compartment with a volume greater than the total volumes for either of the other two interpretations. For the normal fault model segment B of the model is considerably larger than segment A, whereas for the reverse fault model, the two segments are of roughly equal size.

Although not calculated here, this indicates that in a scenario where the reverse fault interpretation was accurate fault seal could be a more significant issue in determining the viability of the prospect, whereas for the normal model, in which the smaller compartment is a relative small contribution to the overall volume this would be expected to be less of a concern.

6.5.2 Stochastic volume estimation

Stochastic modelling is implemented using custom scripts that implement the global sensitivity analysis approaches of Saltelli et al. (2008). Probability distributions

Segment	**Area** (m^2)	**GRV** (m^3)	ϕ	S_w	**HCIIP** (m^3)
RF UCret A	4.57×10^6	292×10^6	0.22	0.3	$37,425,822$
RF UCret B	2.95×10^6	285×10^6	0.22	0.3	$36,545,778$
NF UCret A	1.07×10^6	59.6×10^6	0.22	0.3	$7,653,076$
NF UCret B	4.42×10^6	320×10^6	0.22	0.3	$41,090,938$
INV UCret	6.52×10^6	494×10^6	0.22	0.3	$63,410,860$

Table 6.2: Volumetric calculation using deterministic models.

representing the parameters of HCIIP are outlines in Table 6.3. These apply uniform distributions defined by a minimum and maximum for area, height, formation factor and water saturation, while applying a normal distribution for porosity. Using such inputs the output reserves would be expected to form a log-normal distribution (Rose, 1992a).

A stochastic model has been generated for each of the reservoir segments addressed as deterministic cases (§ 6.5.1). Only the definitions of the distributions for reservoir area and thickness vary between models (Table 6.3).

Model		**RF UCret A**	**RF UCret B**	**NF UCret A**	**NF UCret B**	**INV UCret**
Area	max	4,794,290	3,099,201	1,118,744	4,641,704	6,842,735
	min	4,337,691	2,804,039	1,012,197	4,199,637	6,191,046
Height	max	74	106	66	82	86
	min	54	86	46	62	66
Porosity	mean	0.22	0.22	0.22	0.22	0.22
	sd	0.03	0.03	0.03	0.03	0.03
S_w	max	0.35	0.35	0.35	0.35	0.35
	min	0.25	0.25	0.25	0.25	0.25
B_o	max	1.25	1.25	1.25	1.25	1.25
	min	1.15	1.15	1.15	1.15	1.15

Table 6.3: Inputs used for stochastic modelling. Porosity is modelled using a normal probability distribution function, while all other properties are modelled as uniform functions.

The stochastic modelling itself is achieved using custom scripts, twelve thousand model runs are generated using random variants sampled from these probability distributions (Morris, 1991; Campolongo et al., 2007). Sampling is conducted randomly, applying Latin Hypercube sampling to ensure coverage of samples across the probability space, avoiding clustering of results (Usher et al., 2016). Both inputs and results are compiled in Figures 6.9 to 6.11. A cross-plot of each input with the iteration number is also included, confirming that the random sampling is evenly spread across the distribution with no undue trends.

Once the multiple cases have been ran and an output distribution for the calculated resource is available, comparison to deterministic cases requires consideration of the likelihood of occurrence for reference volumes. This is addressed by compiling the results as a survival function (Yoe, 2010), using this representation reading the resource associated with a given percentile indicates the probability with which you expect to exceed that resource, i.e. the chance of occurrence.

It is typical to use selected percentiles to illustrate the distribution of modelled outcomes (Table 6.4). Comparing the P50 (50^{th} percentile), the statistical expectation, with the deterministic volumes for each compartment of each interpretation, it is clear that the deterministic consistently estimates a larger expectation of resources.

6.5.3 Risking volume estimates

Applying either deterministic or stochastic methods assumes a certain level of viability. In a deterministic case it is essentially assumed that the actual result will be near to the expectation, or in probabilistic models it is assumed that the outcome will lie somewhere in the range of estimated likelihoods. These approaches assume a level of success in their implementation. This chance of success (COS) is calculated using an accepted industry methodology (Milkov, 2015; White, 1993) in which individual aspects of risk that could affect the overall probability of source, trapping and storage of hydrocarbons in the prospect is presented in Table 6.5.

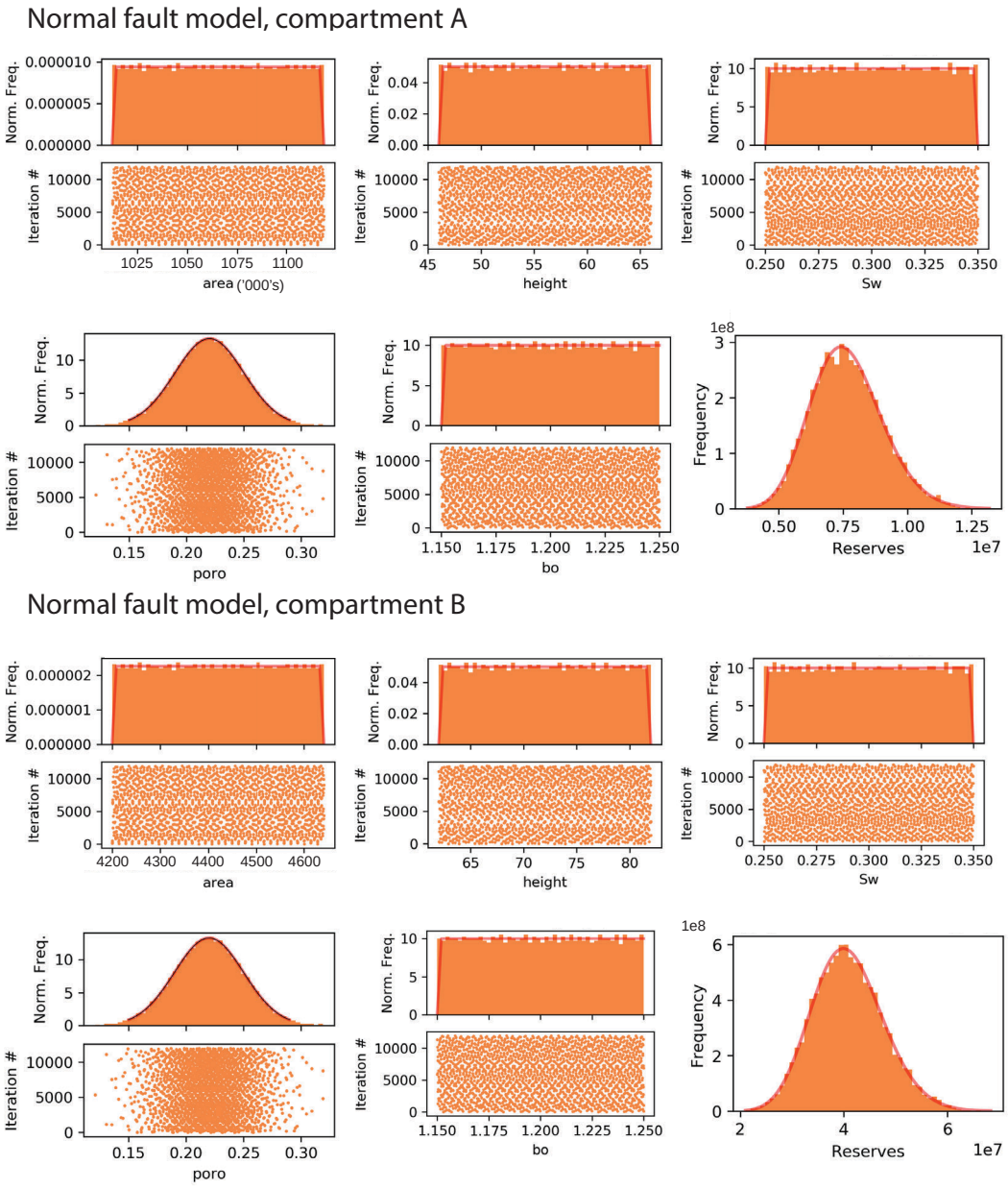

Figure 6.9: Input property distributions for the probabilistic reserves estimates of normal faulted compartments A & B.

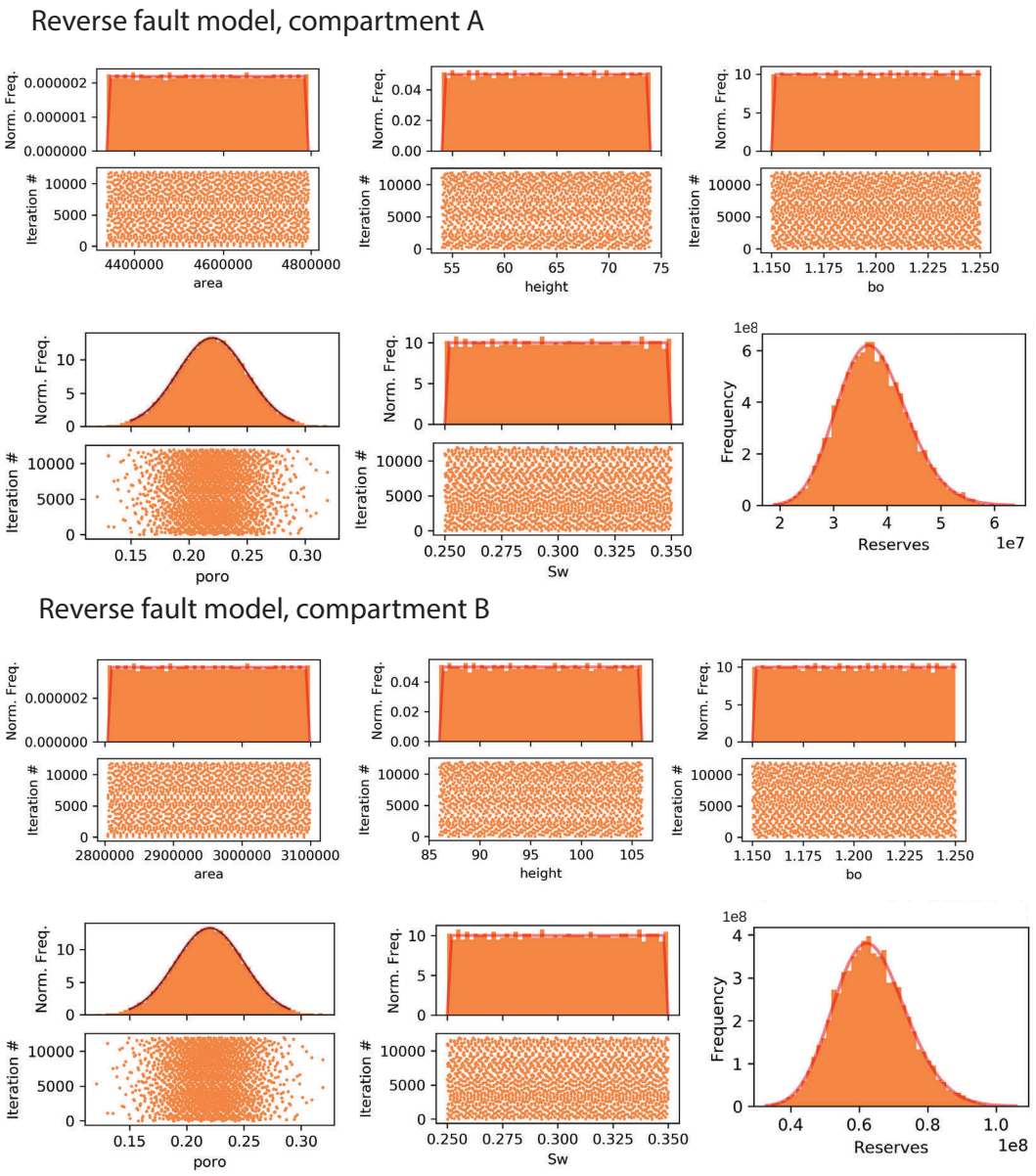

Figure 6.10: Input property distributions for the probabilistic reserves estimates of reverse faulted compartments A & B.

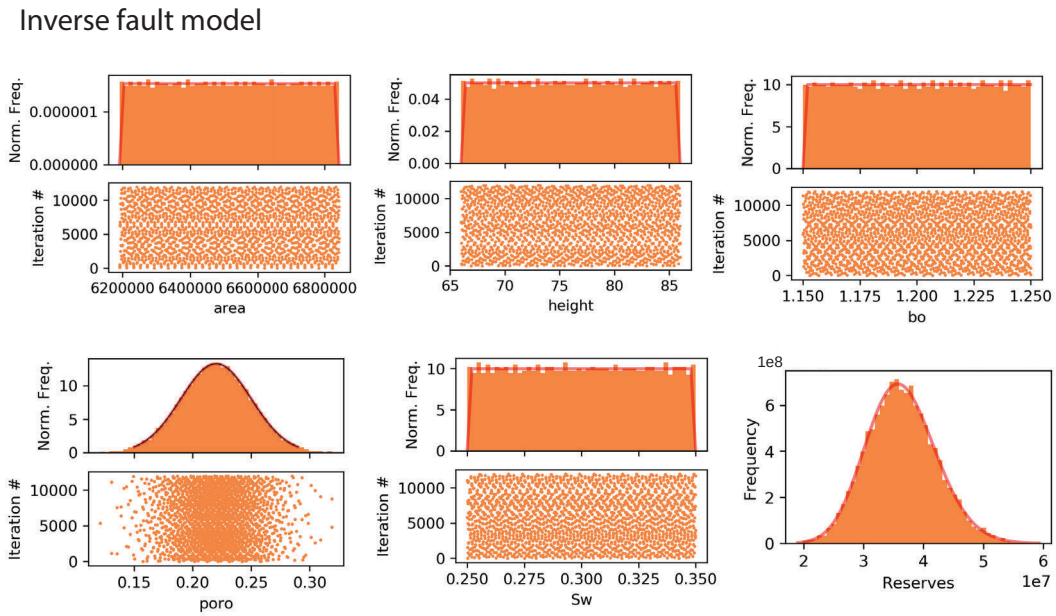

Figure 6.11: Input property distributions for the probabilistic reserves estimate of the inverted scenario.

Segment	**P90,** Sm^3	**P50,** Sm^3	**P10,** Sm^3	**Deterministic**
RF UCret A	29,440,173	37,194,981	46,046,526	37,425,822
RF UCret B	29,115,043	36,171,144	43,945,645	36,545,778
NF UCret A	5,948,689	7,583,362	9,478,585	7,653,076
NF UCret B	32,301,758	40,555,272	49,862,920	41,090,938
INV UCret	50,408,470	63,133,913	77,412,656	63,410,860

Table 6.4: Cumulatives density function used to illustrate the stochastic volume estimates for probability of exceedance of 90%, 50% and 10%, in cubic metres in stock tank conditions. Deterministic volume from Table 6.2 included for comparison.

Risk element	Risk
Trap	0.75
Source	0.7
Reservoir	0.8
COS	0.42

Table 6.5: Chance of success calculation.

This COS may then be used as a scalar multiplier in order to adjust the resource estimate for the degree of risk associated with it (Puga et al., 2015). In a situation where the risks are mutually independent, multiple risks may be considered through multiplication. Here I consider each of the interpretation scenarios as independent, using the estimated probabilities discussed previously (Table 6.1). For each of these scenarios the chance of success is then considered, along with a 50 % chance of fault seal along intra-reservoir faults.

This fault seal risk makes the approach equivalent to a single well analysis, in which a prospect is considered only successful if it may be economically viable targeted by a single well. This process is represented as a decision tree (Fig. 6.12) with probabilities further outlined in Table 6.6 for clarity (e.g. Smalley et al., 2008; Bratvold and Begg, 2008; Krzywinski and Altman, 2017).

Once the relative probability of different scenarios has been defined in this way, calculated volumes may be multiplied by these probabilities to provide a measure of risked volumes. This provides a single metric which, if applied consistently, should be comparable between different assets within a company's portfolio.

Table 6.7 and Figure 6.13 present these as a set of violin plots highlighting the range of likely outcomes of unrisked volumes for each segment and risked volumes for each outcome. The 50^{th} percentile (P50) of the stochastic approach forms the statistically expected value (Rose, 1992b; Peel, 2016), providing a useful point of comparison against deterministic results.

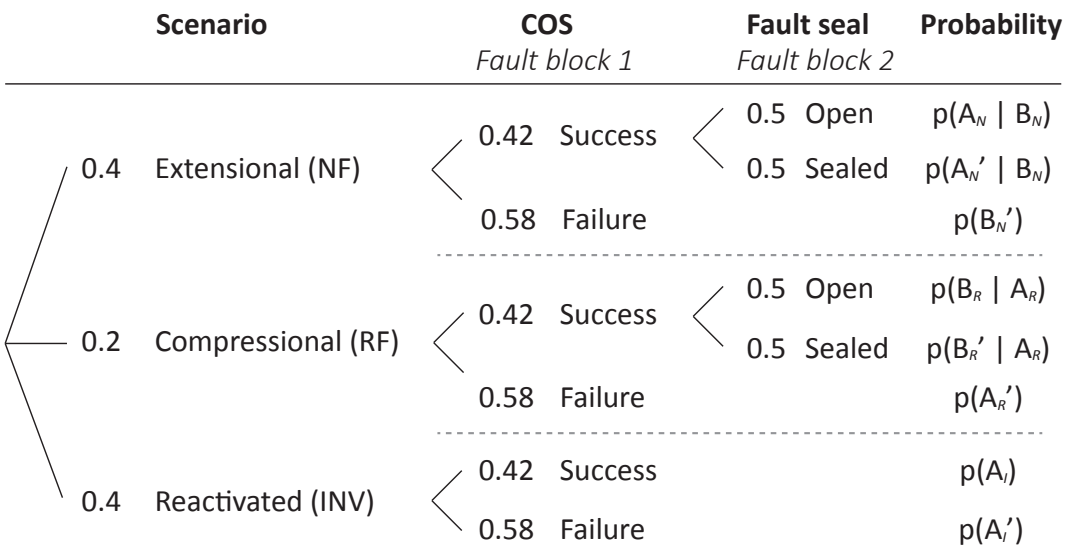

Figure 6.12: Risk analysis decision tree.

Element	Chance	COS	Fault seal	Probability
$p(A_N\|B_N)$	0.4	0.42	0.5	0.084
$p(A'_N\|B_N)$	0.4	0.42	0.5	0.084
$p(B'_N)$	0.4	0.58	-	0.232
$p(B_R\|A_R)$	0.2	0.42	0.5	0.042
$p(B'_R\|A_R)$	0.2	0.42	0.5	0.042
$p(A'_R)$	0.2	0.58	-	0.116
$p(A_I)$	0.4	0.42	-	0.168
$p(A'_I)$	0.4	0.58	-	0.232
Sum:	-	-	-	1.0

Table 6.6: Calculation of probability for each volumetric scenario. Subscript letters refer to normal, reverse or inverted interpretation cases. A and B refer to the prospect compartments.

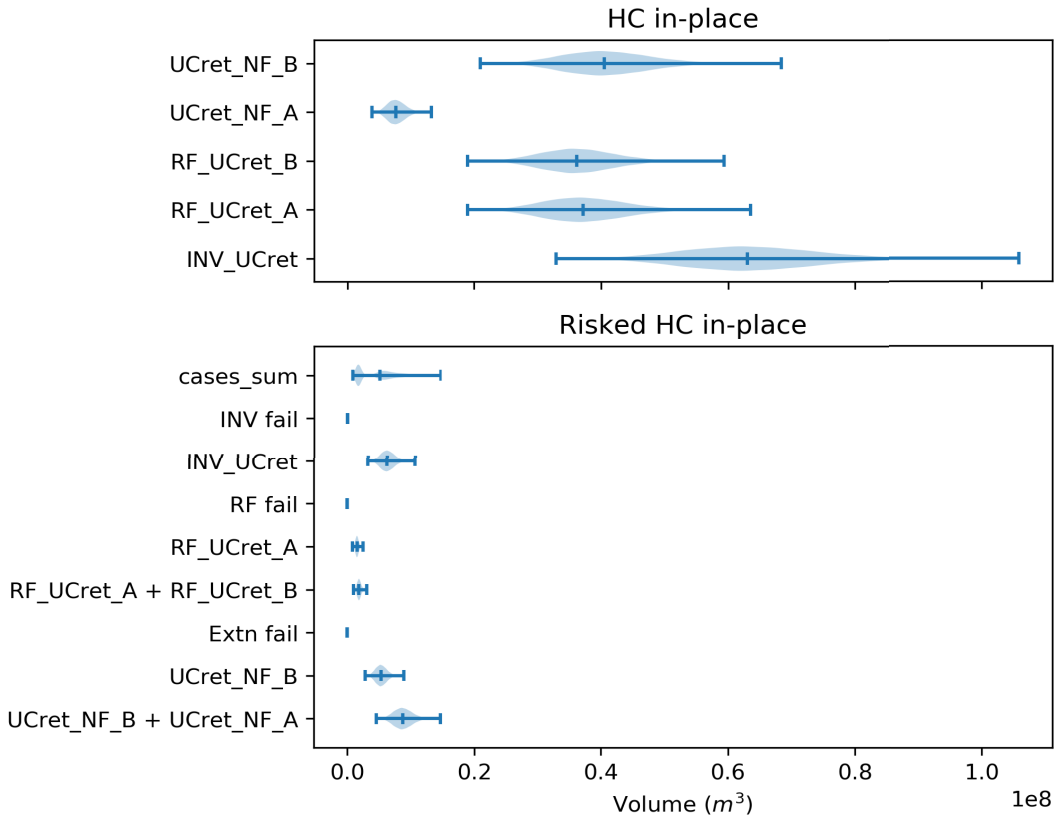

Figure 6.13: Histogram plots of unrisked and risked reserves calculated using the multi-stochastic approach.

The deterministic cases consistently estimate a larger expected value than the stochastic cases. Additionally, they do not capture the range of likely outcomes. If the lower limit of expected outcomes is below the threshold for economic viability, these outcomes may be considered as economic failures. Use of a deterministic approach would not capture these outcomes and so would overestimate the potential rate of success.

6.6 Discussion & concluding remarks

This chapter set out to investigate the potential to use seismic forward modelling to improve contemporary exploration workflows and the way they address subsurface uncertainty. Using real data to target a hypothetical exploration target, three alternate

Element	Chance	P50	P50 Risked	Det	Det Risked
$p(A_N\|B_N)$	0.084	302.8	25.4	306.6	25.8
$p(A'_N\|B_N)$	0.084	255.1	21.4	258.5	21.7
$p(B'_N)$	0.232	-	-	-	-
$p(B_R\|A_R)$	0.042	461.5	19.4	465.3	19.5
$p(B'_R\|A_R)$	0.042	233.9	9.8	235.4	9.9
$p(A'_R)$	0.116	-	-	-	-
$p(A_I)$	0.168	397.1	66.7	398.8	67.0
$p(A'_I)$	0.232	-	-	-	-

Table 6.7: Comparison of risked volumetrics using different risk models. Risks presented as - / best guess / -, high / medium / low, or P90 / P50 / P10. MMbbls.

interpretations were proposed. It is widely recognised that while there are many factors that influence the quality of a seismic interpretation (Macrae et al., 2016), it is easier to address fundamental issues in the process of interpretation. Multiple interpreters typically produce a range a different interpretations (§ 6.3), likely due to in part to differences in experience and personal bias (Polson and Curtis, 2010). However, it is also recognised that consideration of multiple interpretations offers an improved capacity to explore the full range of valid interpretation outcomes (Bond, 2015; Alcalde et al., 2017a).

The seismic forward modelling workflow encourages application of multiple hypotheses to sample the available probability space (Chamberlin, 1965; Frodeman, 1995). Aspects of the presentation of both seismic imaging quality (Alcalde et al., 2017b) and seismic interpretations (Alcalde et al., 2017c) are known to affect out perception of their quality and veracity. It is logical that using the contemporary system relative arbitrary selection of risk multipliers, this is likely to result in spurious estimates due to a lack of connection to the underlying conceptual uncertainty (Bond et al., 2008).

Using synthetic seismic images aids interpretation on this front to some extent by

providing some constraint on the relative likelihood of different elements of a section to be successfully imaged. This allows consideration of how well different interpretation concepts fit the available data.

Quantifying this effect is difficult as the range of alternate interpretations is largely open-ended and mainly constrained by time availability. In the case presented, three end-member interpretations have been modelled partly to exemplify the significant variation in interpretations that is possible. Within any one of these interpretations the locations of specific faults and horizons could be altered, generating new interpretation cases. However, it is considered likely that perturbating the existing interpretation will result in changes in predicted volumes that are less significant than a change between the style of interpretation.

As a result it is suggested that the use of multiple interpretation cases is a significant step in sampling the range of possible outcomes. Using synthetic modelling and cross-comparing subtle differences between models offer a route to a more tractable estimate of interpretation reliability. However, the approach remains qualitative at present.

Using the volume calculations considered earlier, the data may be collated in a variety of manners to represent likely approaches in considering the would-be prospect (Table 6.8). Best guess (deterministic), multi-deterministic, stochastic or multi-stochastic approaches may be represented with the collected data (Ringrose and Bentley, 2015).

Deterministic estimates of the risked volumes are c. 16 % higher than equivalent estimates using stochastic methods (Table 6.7). This demonstrates consistent overestimation when applying deterministic approaches, combined with a failure of such approaches to provide an indication of range of potential outcomes around the expected value. Variation on this scale means that results from the two modelling strategies are not directly comparable, raising the importance of comparing assets within a single portfolio on the same basis, using a uniform approach.

Here, the use of alternate modelled geometries provides an insight to the way in which different cases may be weighted during consideration of multiple scenarios. Utilising

Risk model	Interpretation	Risked expected volume
Best guess	Inverted	167.5
Single stochastic	Inverted	166.8
Multi-deterministic	Multiple	143.9
Multi-stochastic	Multiple	142.7

Table 6.8: Comparison of risked volumetrics using different risk modelling strategies. Volumes presented at MMbbls.

knowledge of which directions would be likely to be well illuminated improves constraint on the manner with which different models fits the constraint of the available data.

While we are unable verify the interpretations in this context, using a stochastic approach alternate models may be constrained. I demonstrate that the uncertainty range of a multi-scenario model are significantly broader than that of single models. As such the probability of the truth-case lying within the estimated range is significantly increased.

The presented seismic imaging quality is far better than is representative for many foothills areas (e.g. Fig. 1.1). When data constraint is limited in this manner interpretations are commonly more model-driven (e.g. Ferrill et al., 2016). However, while many such models are well supported by field analogies (Schmidt et al., 1993), kinematic (Almendral et al., 2015) or mechanical (Zhang et al., 2013) concepts, sparse datasets remain a challenge to modern interpretation.

Application of stochastic techniques in the field of sedimentology (e.g. Colombera et al., 2012b) is more advanced than equivalent methods in structural geology (e.g. Holden et al., 2003). While application has been acheived, they are challenged by the difficulty of programming structural interpretation. In sedimentology, the uncertainty represented by these models is in the representative properties to be allocated to a given unit. In this manner once each cell is categorised to a given facies application of uncertainty parameters may be mapped to the cells in the same manner as the facies labelling itself.

However, in structural geology the uncertainty regards the grid geometry itself. This

presents a challenge to our technical ability to generate multiple realisations of geometric grids and continue to build dependent variables (e.g. facies mapping) in a manner that is robust and repeatable.

The nature of a structural interpretation is part categorical and part natural variability. Typically the potential error involved in a mistaken categorisation of a structural geometry is significantly larger than that related to expected variability related to the picks of individual faults and horizons. That is to say that the range of resource estimations provided by a multi-scenario approach may frequently be much larger than the range presented by a single interpretation considering variability and basic error.

It is easy to obtain confirmations, or verifications, for nearly every theory – if we look for confirmations.

K.R. Popper

Chapter 7

Mechanically constrained interpretation

Chapter structure:

7.1 Abstract

Seismic images are often characterised by a small number of strong reflections forming geometries that reveal the local geological history. The higher reflectivity of these layers, as a result of increased contrast in elastic properties, provides greater constraint during interpretation. Between such reflections there is increased uncertainty, challenging interpreters to better represent local geometries and extrapolate into areas of limited constraint.

This chapter attempts to provide proof of concept that mechanical modelling could be used to offer potential interpretation solutions in such poorly imaged areas. Using the dataset from Chapter 6, I have extracted the prominent deeper reflection with the morphology of a rifted margin. Assuming that this has not been inverted, I have used this as a passive non-deforming basal element for mechanical modelling in order to consider the influence on geometry developed in overlying strata.

Three testing scenarios were used to consider the sensitivity of the model to material fill, presence of strength anisotropy and the location of anisotropy. Results from these models confirm the methods realistic behaviour and assist in interpretation of subsequent testing.

The method is then applied to a series of models representing the lateral interaction of two faults forming a relay ramp geometry. Compiling two dimensional displays from various times throughout the model run provides an insight into processes of strain localisation and how these are guided by the nature of underlying geometries.

These models demonstrate that the distribution of rigid non-deforming basal elements significantly influences the nature of subsequent thrusting. The basal detachment of thrusting is guided by variations in the mechanical strength of the underlying stratigraphy, influencing the ratio of horizontal to vertical displacement. Broader evidence of inversion is indisputable, however this may suggest a mixed mode of development in some structures observed in the area.

7.2 Introduction

Considering the data used in Chapter 6, the sub-thrust play is located beneath an area of great interpretation uncertainty and poor seismic image quality. Regionally passive roof duplexes are observed (Mora et al., 2014), however this area lacks any indication of a foreland dipping roof thrust. Elsewhere, there is significant evidence of reactivation in the form of harpoon structures (McClay, 1995), again this is not consistent with seismic observations. At surface significant fault-related folds crop out and at depth seismic images show a strong reflection consistent with a fully extensional or incompletely reactivated terrane (Fig. 6.3). Evidence indicates a likelihood of duplexing, however the internal structure of these packages are highly ambiguous.

As discussed in Chapters 4 & 6, seismic interpretation uncertainty is spatially variable (e.g. § 3.5.3, 4.6 & 6.4.3). In a single seismic image some aspects are more certain than others, requiring interpreters to apply their intuition (Alcalde et al., 2017c). In this context, reductions in imaging quality are often due to steeply dipping strata and lateral variation of seismic velocities (Gray et al., 2001).

The geometry and nature of disturbances to the seismic signal may have interpretive value (Iacopini and Butler, 2011), however these observations are unlikely to be prescriptive without further validation. As such, seismic interpretation of subsurface geometry often require a more model-driven approach when constrained by seismic imaging quality (e.g. Ferrill et al., 2016).

Additional information may be sourced from field analogues (Schmidt et al., 1993), kinematic models (Carrillo et al., 2016), laboratory analyses (Almendral et al., 2015), physical analogues (Bonini et al., 2012) and mechanical modelling (Zhang et al., 2013). Using a variety of techniques with complimentary sensitivities provides a means to deal with the specific challenges of temporally and spatially sparse datasets presented by an area.

In this chapter, I use mechanical modelling to investigate the relationship between the

better imaged and non-deforming basement and overlying, poorly imaged, compressional deformation. It has long been recognised that pre-existing extensional morphologies can guide subsequent compressional reactivation, by reactivating themselves (Jackson, 1980; Hayward and Graham, 1989), nucleating new faults (Davies, 1982) or controlling the distribution of actively deforming lower competency intervals (Underhill and Paterson, 1998; Paton et al., 2006).

While logic dictates that mechanisms involved in the case of a passive basal morphology should be similar (e.g. Butler et al., 2006), it has been less comprehensively investigated. Early physical analogue experiments considered analogous geometries (McClay, 1995), demonstrating a link in two-dimensions. Based on these experiments, it was suggested that material strength and basement morphology may combine to guide deformation (Fig. 7.1). Considering these controls it may be possible to use knowledge of the mechanical properties of stratigraphy, the basement morphology and surface outcrop to predict the behaviour in the poorly imaged interval.

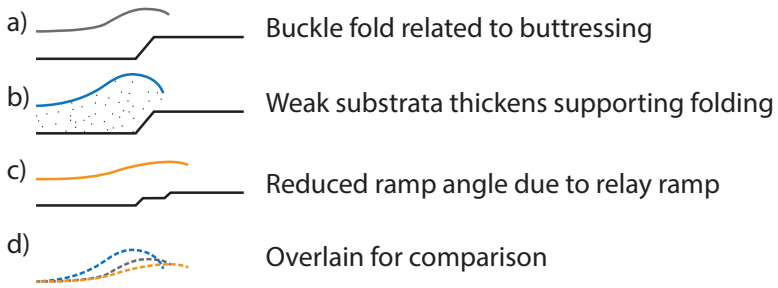

Figure 7.1: Three hypothetical thrust geometries that may be caused by reactivation above a passive basement. In each case three is a different dominant control on the geometric formation; (a) buttressing, (b) strength anisotropy and (c) ramp angle. Overlying the three (d), illustrates differences in the degree of shortening and style of strain accommodation in each.

7.3 Mechanical modelling

In structural geology mechanical modelling is currently applied using two principle methods, considering either a collection of discrete elements (Cundall and Strack, 1979) or a single finite element (Jongmans et al., 1998; Moresi et al., 2003). Discrete element modelling (DEM) represents the subsurface as a granular media of discrete, interacting particles. Finite element modelling (FEM) uses a continuous media, representing deformation as localised strain within a viscous media.

Various authors have compared and contrasted their application (e.g. Zhang et al., 2013; Gray et al., 2014). Overall, FEM models are significantly more computationally efficient allowing modelling of larger models, however they require a predetermined nucleation, or 'seed' point to be placed by the modeller to initiate deformation. DEM models will nucleate more naturally, self-seeding, but are more computationally demanding due to the significantly higher number of particle-particle interactions and neighbourhood search operations required.

Recent advances in the field of soil mechanics have begun to implement the two in tandem, using the ability DEMs to represent strain localisation and control viscous properties applied in a larger, more computationally efficient FEM (Guo and Zhao, 2013) . Currently applied at small scales this technology has not yet been expanded for use at the scale of full seismic acquisitions (Guo and Zhao, 2014; Zhao and Guo, 2014).

Here, I apply a DEM code provided by Emma Finch (University of Manchester), detailed in Finch (1999) and Finch et al. (2003). This is a lattice solid model adapted from the work of Mora and Place (1993, 1994) and originally based upon the discrete element method proposed by Cundall and Strack (1979). This approach has previously been used to investigate the impact of an actively deforming basement on overlying extensional (Finch et al., 2003; Hardy and Allmendinger, 2011; Pichel et al., 2017) and compressional (Finch et al., 2004; Hardy and Finch, 2006) faulting.

In this case, mechanical modelling has been applied to two sets of models, both are aimed

at investigating the impact of the geometry of a passive, non-deforming, basement on an active compressive deformation in the overburden. The first set of models investigates the sensitivity of mechanical modelling to a selection of basic geometric and strength parameters. Having selected a broadly representative set of parameters, the second set of models test a variety of geometries emulating those potentially present in a field example.

7.3.1 Modelling method

The method is described in detail in Finch et al. (2003), here I outline a summary, with description of elements specific to this study. In order to avoid potential pitfalls this code is ran as a serial process (Hardy, 2015), limiting the number of models due to runtime. This precludes use of the method in a probabilistic approach (Finch, 2018, *pers. comm.*). A small number of key geometries have been developed, varying only the strength of material and geometry of a passive (non-deforming) basement.

Each model is initiated as a rectangle measuring 300 units in width and 30 units tall, containing identical randomly populated grain-packs of 20,664 circular elements. The elements themselves are defined with a selection of radii, measuring 0.5, 0.4, 0.3 or 0.2 units. This random arrangement combined with a mixture of grain sizes prevents the imposition of geometric trends on the modelling outputs.

Models are ran using local units, however elements are provided density and a scaling factor for the models height is applied, providing a total height of 1,500 m. In turn this means that a model unit is 50 m. No vertical exaggeration is applied, resulting im model dimensions of 1,500 m high by 15,000 m wide.

The input grain packs used in this experimentation were prepared by Finch (2017, *pers. comm.*), once fully populated with elements they are allowed to reach a state of equilibrium within the mechanical simulation. At this point the distance between each neighbouring element is measured, providing the equilibrium distance, that is used as a

reference for calculation of strain using equation (7.1).

$$F_s = \begin{cases} K(r-R), & r < r_0 \text{ intact bond,} \\ K(r-R), & r < R \text{ broken bond,} \\ 0 & r >= R \text{ broken bond.} \end{cases} \tag{7.1}$$

Where; F_s is the resultant force of repulsive and attractive forces interacting between element; K, is the elastic constant, R is the reference distance between elements at equilibrium; r is the distance between elements at the time of observation; and, r_0 is the distance between initially neighbouring elements at which their bond will break, representing their cohesion (Finch et al., 2003).

The distance at which failure will occur has been set in line with grain pack experiments of Botter et al. (2014) conducted using the same code. These experiments conducted angle of repose and triaxial strength simulations, which were then compared to published experimental results to verify that the parameters were representative of the facies sandstone and shale (Fig. 7.2a & b, respectively). I assume a confining pressure of 40 MPa for these models. Intergranular friction is not considered in these models.

For presentation, elements are coloured by a layer number, this does not imply variation of mechanical properties. All sensitivity testing models utilise homogeneous background breaking strains, with strong layers represented as sandstone with a breaking strain of 0.05, and weak layers with a shale breaking strain of 0.02. In cases featuring alternating stratigraphy, sandstone layers are interbedded with shale, each represented as discussed above.

During the experiments, the left-hand wall of the original rectangle is progressively moved from left to right acting as a vertical planar impactor on all deformable elements. Boundaries towards the base and right-hand side are fixed and non-deformable. Movement of the impactor occurs at a rate of 0.00005 units (0.0025 m) per iteration with 3,000,000 iterations occurring throughout runtime of a single model, equating to a movement of 150 units (50% shortening). Time is not implicitly modelled in

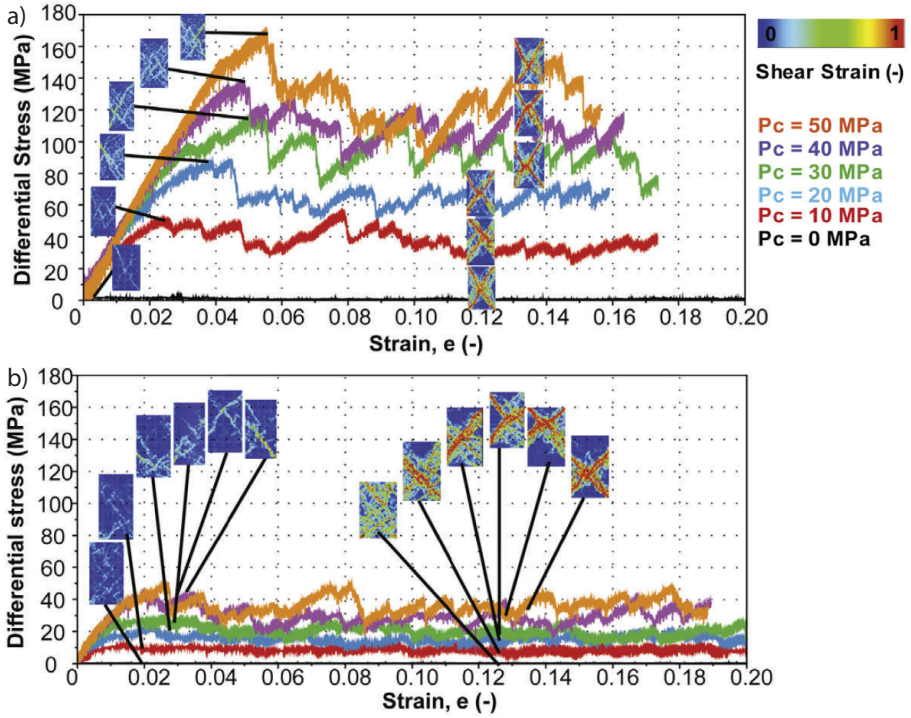

Figure 7.2: Axial strain versus differential stress curves for the bulk response of (a) sandstone and (b) shale to simulated triaxial strength tests (Botter et al., 2014). Coloured by confining pressure.

this approach, a timestep of 0.04 per iteration is applied, which may be scaled for consideration at appropriate timescales (Hardy, 2018a).

The basal geometry is horizontal with one or two steps representing basement faulting dipping at 60° towards the impactor (left). The impactor is initially located at $x = 20$ units and the left-hand fault intersects with the horizontal axis at $x = 220$ units in all models. The right-hand fault intersects at $225 \leqslant x \leqslant 260$, varying between different model geometries.

All sensitivity testing simulations use only the left fault ($x = 220$). In latter experiments, the throw on both faults is varied (Table 7.1). These geometries are used to represent the fundamental two-dimensional geometry across a pair of parallel faults forming a relay-ramp (§ 7.4).

Scenario	Throw on left fault	Throw on right fault
Footwall fault	6 units (300 m)	0
Relay ramp	3 units (150 m)	3 units (150 m)
Hangingwall fault	0	6 units (300 m)

Table 7.1: Geometric parameters used for DEM sensitivity testing.

Modelling results are visualised as a pseudo-geological section as is common. I also introduce a custom script to extract an individual layers profile at each timestep of the simulation, and display these with time and vertical position sharing the y-axis. This forms a geometry reminiscent of what may be expected to be related three-dimensional variation of geometry along a structure. The lower left hand side of each of these images forms an undeformed triangle, representing the forward propagation of deformation away from the impactor. These images provide a useful mechanism to investigate the temporal evolution of the accommodation of vertical strain.

7.3.2 Sensitivity testing

The purpose of this section is to provide a basic sensitivity test of some of the factors controlling deformation during inversion (e.g. Fig. 7.1). Three scenarios are used to provide a background for discussion of the subsequent models specifically aimed at the field area. These are:

- Homogeneous fill - strong versus weak;
- Single contrasting layer - strong versus weak; and,
- Free surface proximity to a single strong layer - high, medium & low.

In homogeneous models, the basement is fixed at x = 220 terminating with a fault dipping at 60° towards the left and a height of 300m. Comparing the strong and weak fill (representing sand and shale), the most prominent difference appears to be in vergence direction. In the weak model a preferred vergence direction fails to develop, whereas in

the strong model, thrusts take on a predominantly right verging pattern, dipping to the left, forming a series of distinct thrust ramps.

In both, cases a décollement has nucleated in the area of the upper fault tip in the basement morphology. Visually considering restoration of the section, deformation along this fault looks to restore to the location of the basement step. This may represent basement control on the nucleation point of the ramp as strain localised onto a discrete fault plane.

In the single contrasting layer models, the background material is given a strength of 0.035, so as to be half way between the strong and weak layers. A single layer (8th from the bottom) in the centre of the model is then allocated the shale or sand property, to represent a weak or strong layer, respectively.

In the free surface proximity test, a single more competent layer, 2 units (100 m) thick is placed below, level with and above the top of the horst geometry (Fig. 7.3). The purpose of this test is to observe the implications of placing the more competent layer where it will interact with the basement geometry.

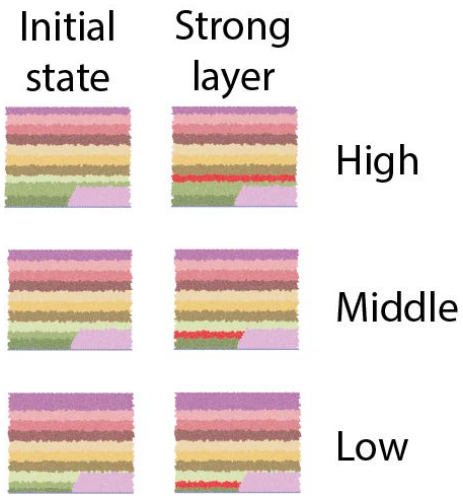

Figure 7.3: Initial state of the free surface proximity DEM experiment with a single 100 m thick layer of stronger elements highlighted in red. The location of this strength heterogeneity is adjusted to sit below, level and just above the basement fault.

7.3.3 Results

Differences in the modelling results are primarily described in terms of their vergence directions and a wavelength of deformation. Here, I consider these to be the direction in which a thrust is propagating and a general descriptor of the length of initially neighbouring elements that maintain continuity throughout deformation, similar to a thrust nappe in field geometries.

In the *homogeneous weak versus strong fill* models (Fig. 7.4), the final geometries reflect a difference in the manner of accommodation of vertical thickening. In the weak model faulting is both synthetic and antithetic, and in areas of intensified shortening accommodation, this is achieved by both with total strain spread across a greater number of faults. The strong model however accumulates thickening through the formation of discrete thrust nappes overlying detachments that have accumulated significant displacement. The weak fill model shows a greater degree of antithetic faulting and increased boundary effects at the edges of the model.

Both models feature displacement of layer 1 and much of layer 2, from the lowest fill of the horst, to overlying the basement block. Comparing the two models the weak model features greater intra-bed thickening and more frequent high angle faults. Whereas strain accumulation in the strong model is dominated by fewer, more significant low angle thrusts. Vertical thickening in this model is achieved through stacking of discrete thrust nappes. This is reflected in the plots of vertical strain against time, that illustrate early localisation of the faults that go on to form the most significant faults later on.

The *single contrasting layer* models (Fig. 7.5) demonstrate that the strength of layer 8 influences the overall final geometry of the sections. In both models, layer 1 (dark green), which is initially only present left of the basement fault, has been pushed up and over the basement. Layers immediately above have been rotated anticlockwise as they have entered the lower portion of the modelling space, formerly occupied by layer 1 and 2.

Both models feature a mixture of synthetic and antithetic faults. In the case of a weak

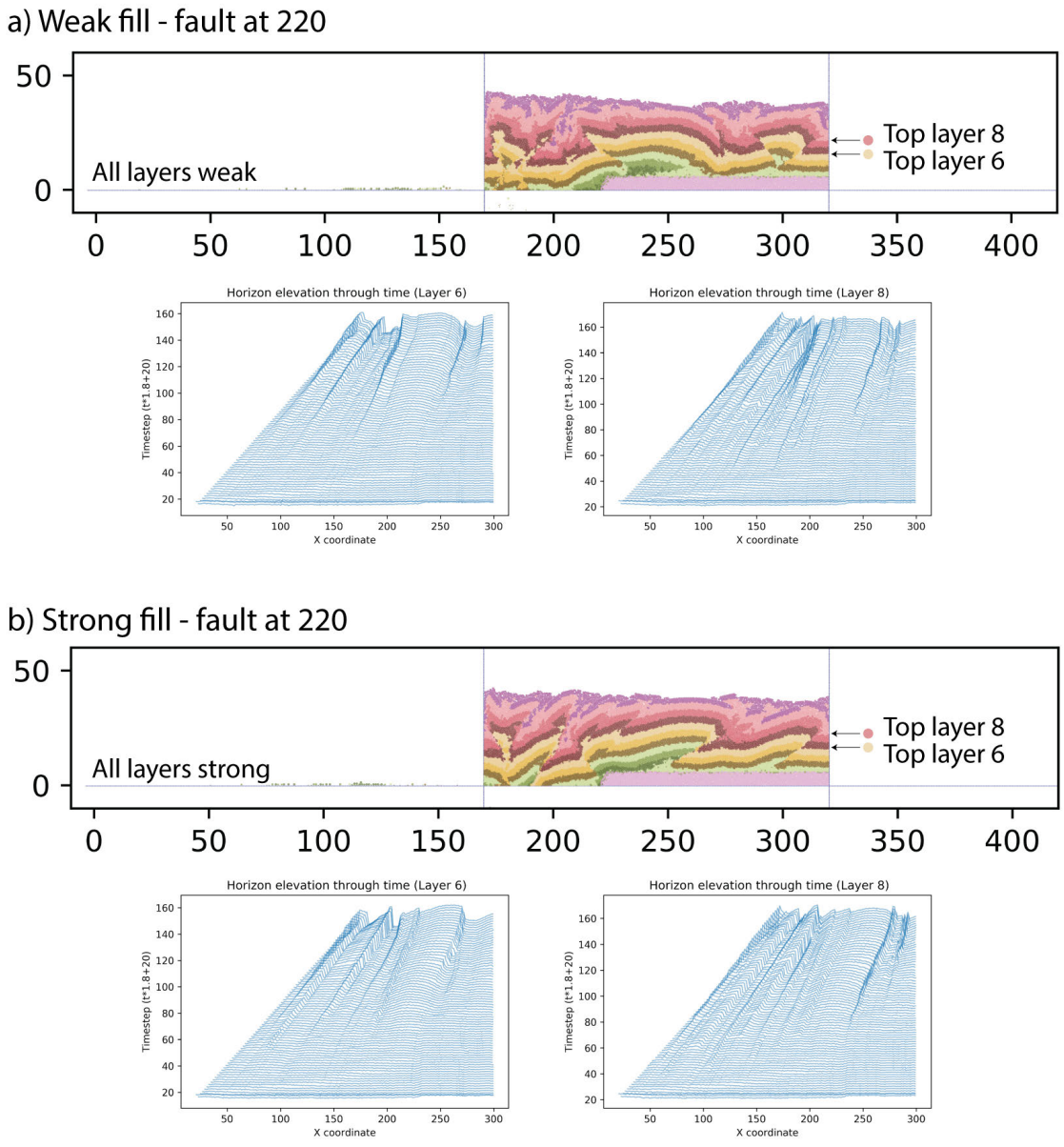

Figure 7.4: DEM result of homogeneous strength models with (a) weak and (b) strong fill. Beneath each profile is a graph of horizon elevation of the top of layer 6 and 8 for each timestep during the experiment.

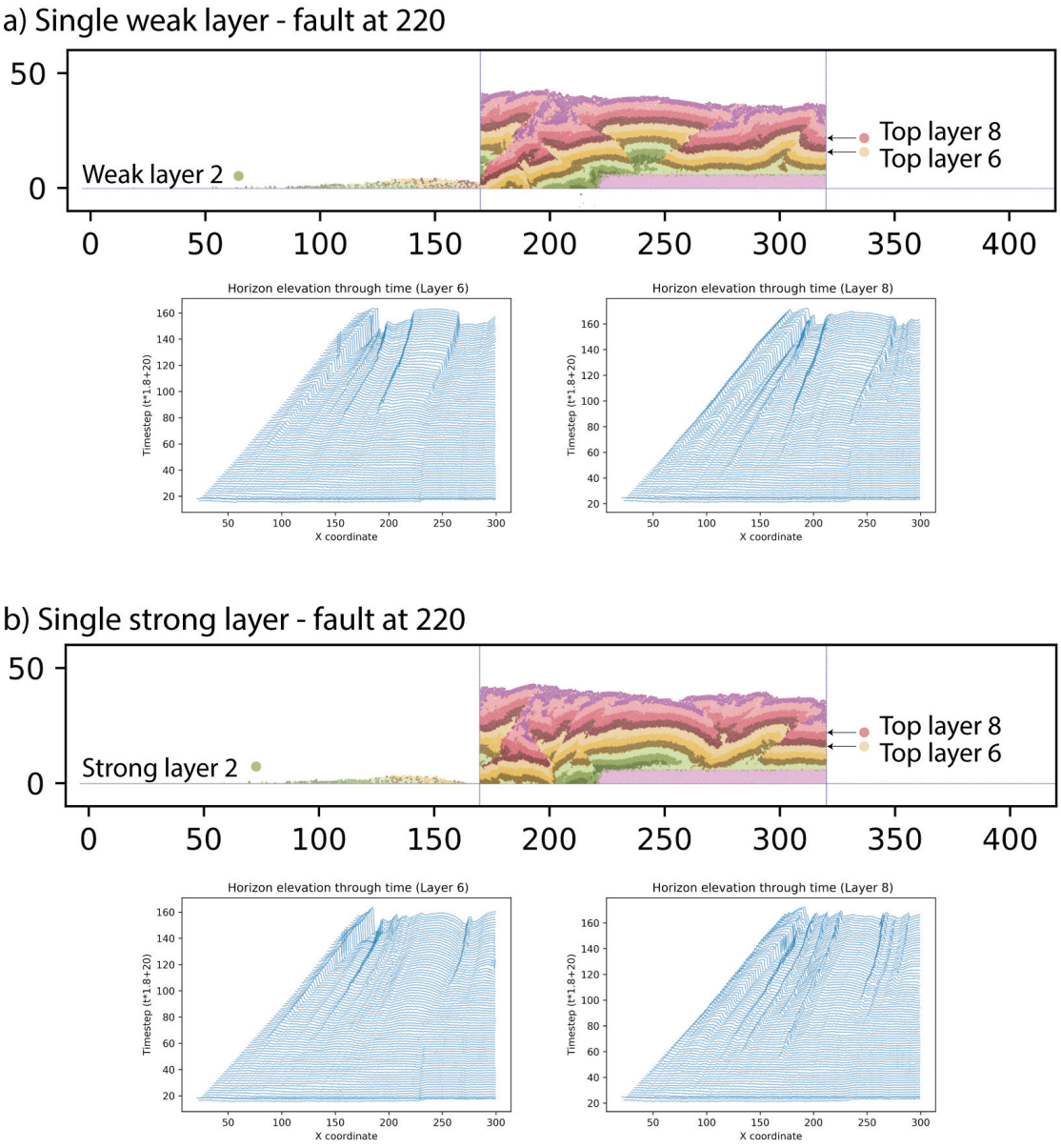

Figure 7.5: DEM result of models with a single (a) weak or (b) strong heterogeneous layer. Beneath each profile is a graph of horizon elevation of the top of layer 6 and 8 for each timestep during the experiment.

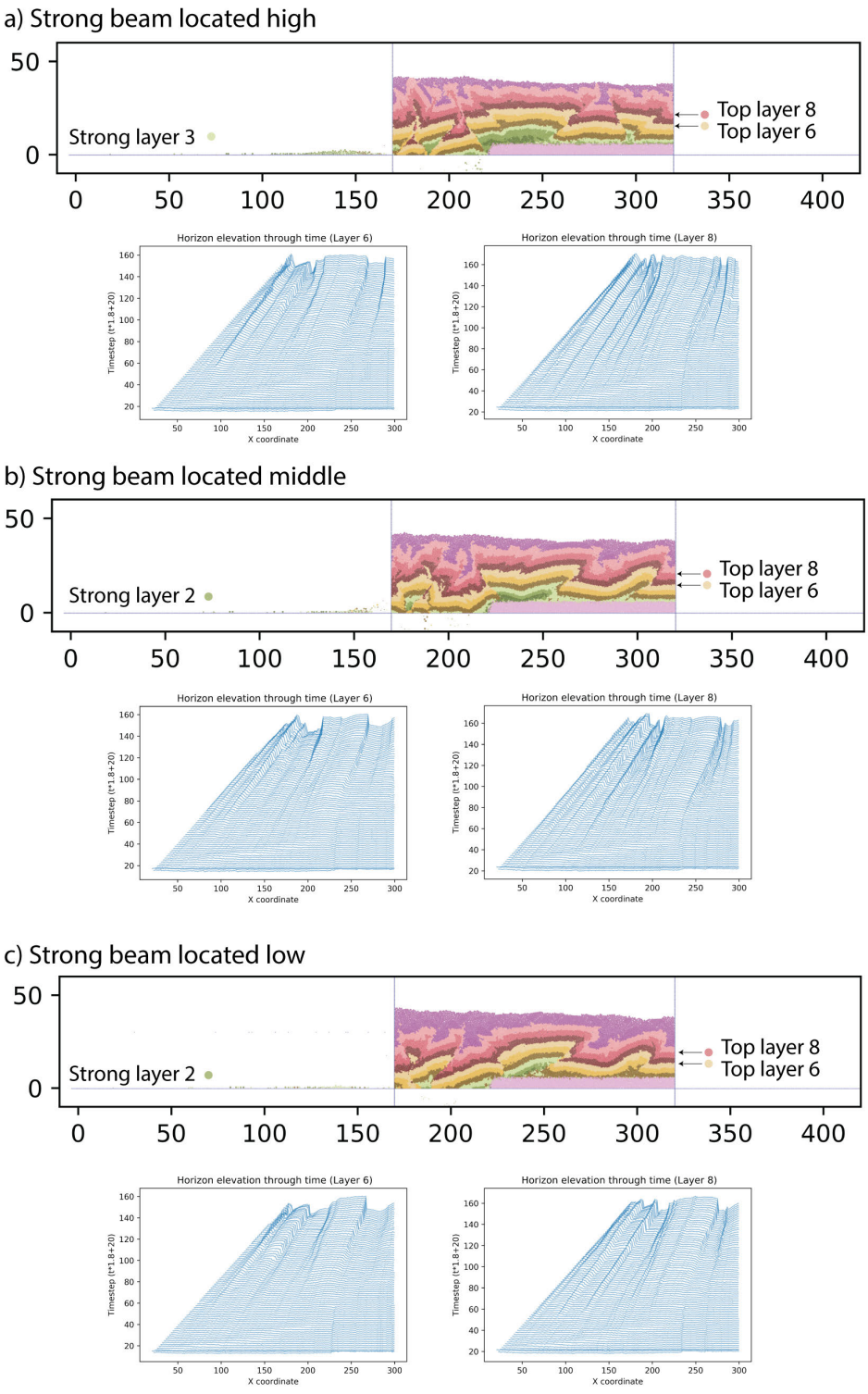

Figure 7.6: DEM result of models with a single strong layer inserted (a) high, (b) medium or (c) low relative to the basement fault. Beneath each profile is a graph of horizon elevation of the top of layer 6 and 8 for each timestep during the experiment.

intermediary layer, mechanical decoupling may be observed between the upper and lower elements of the stratigraphy. Minor thrusts in the overburden may be observed to sole out onto the weak layer. By comparison, the strong layer features an increased number of small-scale offsets across it, which may indicate that it is acting as a nucleation point for localisation of deformation.

In both models visual restoration of the layers and replaying previous timesteps of the model shows that major thrust localise above the basement fault position. In the vicinity of the basement fault, the single strong layer appears to lead to the generating of a series of stacked fault propagation folds, while the weak layer results in faulting more representative of a push-up geometry similar to that of a box-fold.

In this manner the final geometry of the stronger model appears to be more dominated by the forward motion of the impactor, while in the case of the weaker formation, geometries reflect buttressing by the basement. This results in a pop-up style structure in the weak layer, with faulting the left of the mode dominated by antithetic faults.

The *free surface proximity* models (Fig. 7.6) show more minor differences than the previous models, reflecting the subtle differences in input models (Fig. 7.3). The accumulation of vertical strain with time is illustrated to feature much earlier onset of strain localisation in the distal portions of the model with higher placement of the beam. Higher placement also appears to result in increasing back-thrusts associated with the basement fault, while lower placement leads to the development of a series of thrust nappes to the left hand side of the model.

In the case of the high placement of the strong beam, it is noted that significant thickening of layer two occurs, along with its displacement to above the basement block. This appears to be associated to the interaction of the stronger beam with the thrust to its right, forming a broad fold in response to buttressing to the right and support from the strata of background strength beneath. Such buttressing is also noted in physical analogue modelling (Fig. 7, McClay, 1995).

7.4 Field example

Using the same prospect example as introduced in Chapter 6 (§ 6.4), a deep, coherent, reflection is observed throughout the volume, likely to form an upper surface to pre-rift strata (Campos and Mann, 2015). As previously discussed, it is not clear whether these structures have remained in their original geometry or been partly reactivated.

In these models, the basement will be considered as a passive, non-deforming unit. Seismic interpretation reveals normal fault offset that may form part of a relay ramp geometry. In order to investigate variation in deformation along the front a series of models are generated that represent different elements of deformation along the trend of a relay ramp structure.

In this section I present a summary of seismic interpretation findings, describing the field association, before then conducting a series of DEM experiments to investigate potential relationships. The aim of this discussion is to consider the use of discrete element modelling as a supplementary tool in the seismic interpretation and possibly seismic forward modelling workflows.

7.4.1 Seismic interpretation

The prominent reflection has been interpreted throughout the three dimensional seismic volume (Fig. 7.7). This reveals a series of normal offset faults forming the style of a rifted basin with series of normal fault geometries with relay ramps forming at points of interaction. These minor faults, occurring northeast-southwest, are cross-cut by a significant offset approximately east-west with an intersection angle of 25°.

The orogenic trend is north-northeast (Delgado et al., 2012), sub-parallel to the minor faulting trend. This leads to the interpretation that the larger cross-cutting feature is part of a strike-slip system intersecting the orogenic front, or a relay between two trends of the extensional system. This cross-cutting fault, becomes the focus of the following enquiry.

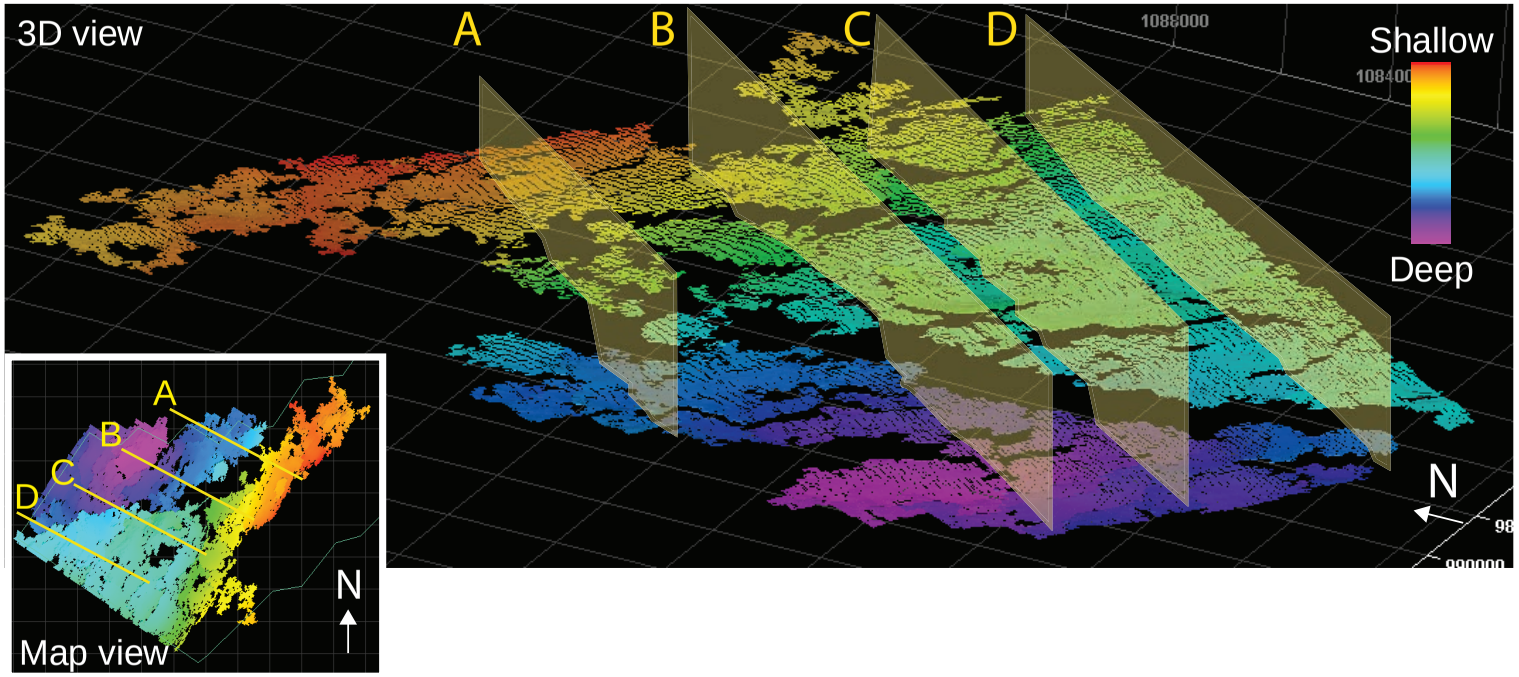

Figure 7.7: Seismic data from Colombia, with two dimensional yellow lines highlighted from Figure 7.8.

The feature has a dominant normal offset, with no direct evidence of strike-slip motion.

Four two-dimensional seismic lines are extracted across the area, along section lines presented in Figure 7.7 and presented in Figure 7.8. These section line are approximately parallel to the vergence direction of the foothills which matches that of the thrust nappe in the upper half of the sections.

These sections have been selected to demonstrate a pervasive and continuous trend, whereby the cumulative normal fault offset in the basement forms an increasing trend towards the north. Overlying this structure, compressional geometries also vary along trend.

In section D (Fig. 7.8d), the detachment of the overlying compressional system is a smooth and gently inclined floor thrust overlain by parallel continuous reflections forming a ramp structure. While some deformation is observed beneath the floor thrust, in a broadly sigmoidal pattern, this forms the principle plane of displacement. In comparison section D and C present ramp thrust geometries with increasing ramp angle. This is associated with folding of the overlying beds, that are known to outcrop as a antiform at surface.

In these sections, the height and length of the duplexed area increases, with the height and angle of the ramp. These changes are coincident with increasing cumulative throw on the basement faults. In section A, interpretation is uncertain, partly due to proximity to the edge of the survey and a related loss of imaging quality. However the loss of imaging at the edge of the section appears to be related to folding in the overlying horizons. It is suggested that the geometry of the principle detachment may be controlled by the buttressing effect of an otherwise passive substrata.

7.4.2 Mechanical modelling

To investigate the possible influence that a passive, non-deforming, basement may have on the compressional deformation of the overburden a set of six sets of models have been

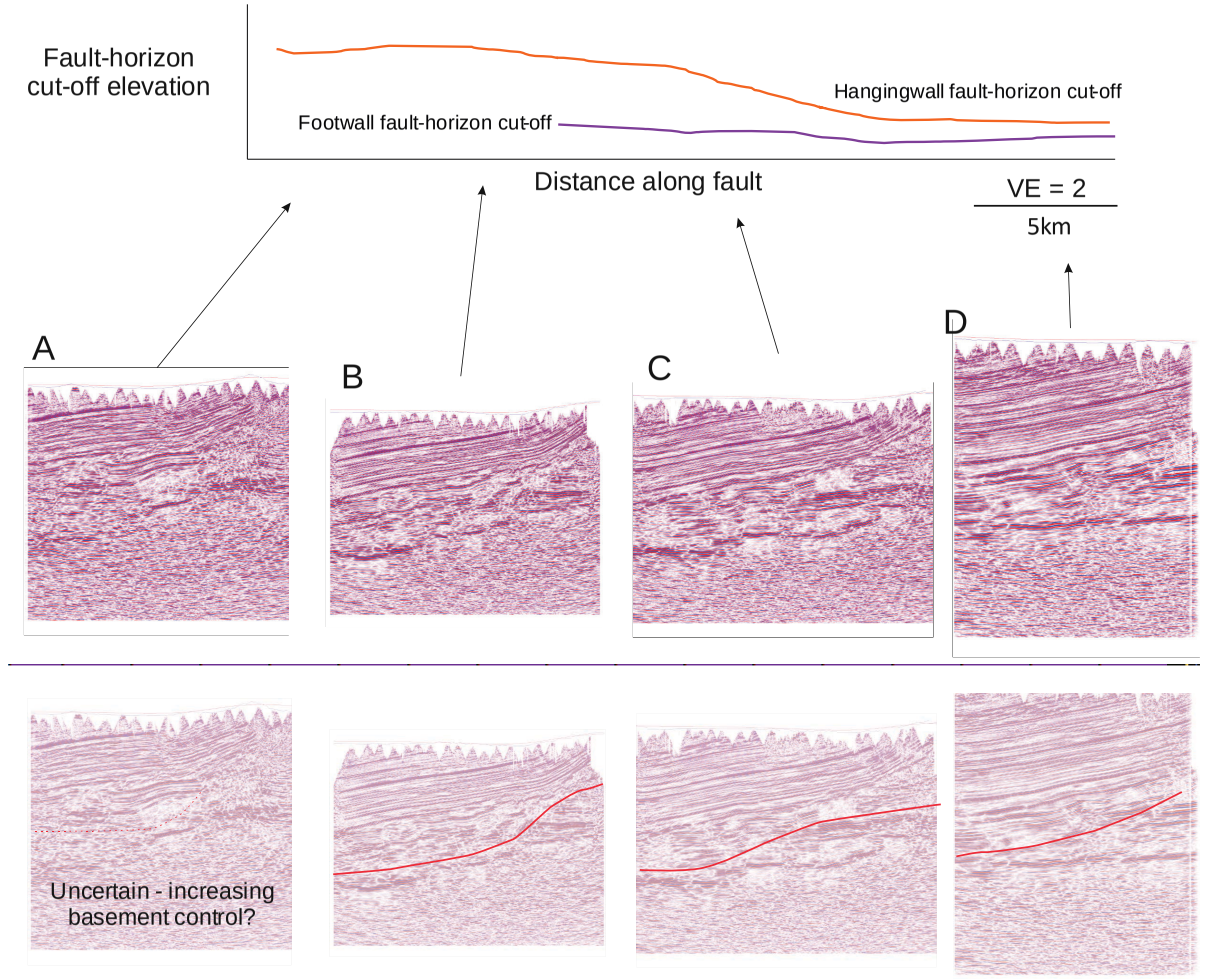

Figure 7.8: Compressional structural related to basement geometry control. Number refer to cross-section line illustrated in Figure 7.7.

generated. Each set represents a basement morphology of a relay ramp with differing fault separations. Each set is composed of a model with maximum displacement on the footwall fault, one with maximum displacement on the hangingwall fault and one with displacement split evenly between the two, simulating a relay ramp and deformation laterally along fault strike in either direction (detailed in Table 7.2).

Modelling of the range of geometries requires thirteen model runs, two individual models for each set plus the common hangingwall geometry (Fig. 7.9a). All models share the same initial state with ten horizontal layers, the lowest two of which are only found in the hangingwall. All share a common strength profile, representing alternating layers of sand and shale as previously introduced (§ 7.3.1).

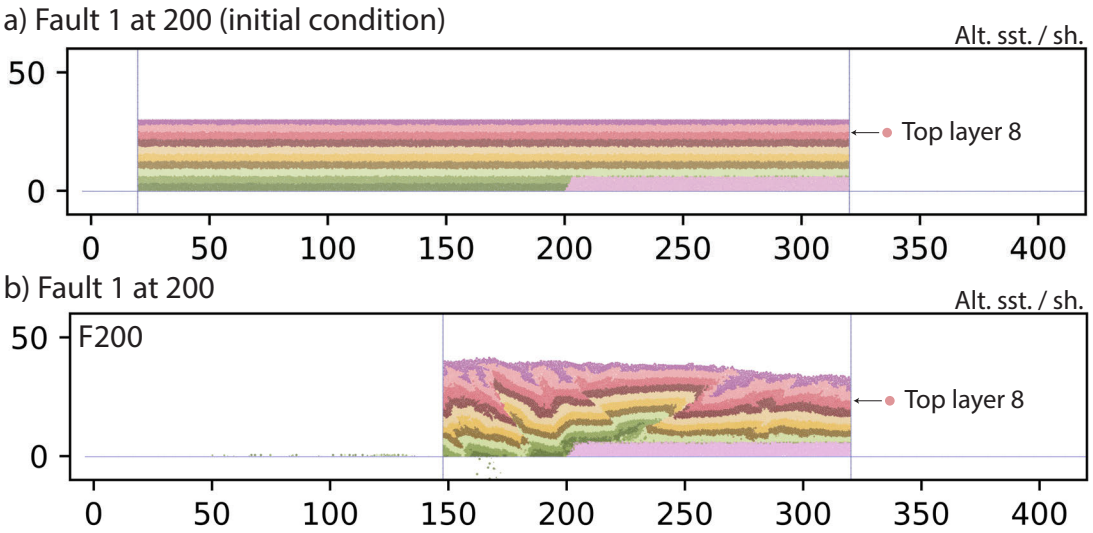

Figure 7.9: DEM model of hanging wall fault at 200; (a) initial conditions and (b) result.

Models of footwall fault and relay ramp geometries are illustrated in Figures 7.10 and 7.11 respectively. All final geometries represent a shortening of approximately 43 %. Vertical strain with time as observed in layer 8 is illustrated in Figure 7.12 for the relay ramp geometries of each model set.

All fault separations share a common simulation for the hangingwall fault (Fault 1) at 200 units (Fig. 7.9b). In this model, faults nucleating to the right of the basement fault are right-verging (synthetic), while those to the left are antithetic. Deeper structures form

Fault separation	Model	Fault 1		Fault 2	
		Location	Throw	Location	Throw
5 (250 m)	F200	200	300 m	-	-
	R205	200	150 m	205	150 m
	F205	-	-	205	300 m
10 (500 m)	F200	200	300 m	-	-
	R210	200	150 m	210	150 m
	F210	-	-	210	300 m
15 (750 m)	F200	200	300 m	-	-
	R215	200	150 m	215	150 m
	F215	-	-	215	300 m
20 (1000 m)	F200	200	300 m	-	-
	R220	200	150 m	220	150 m
	F220	-	-	220	300 m
30 1500 m)	F200	200	300 m	-	-
	R230	200	150 m	230	150 m
	F230	-	-	230	300 m
40 (2000 m)	F200	200	300 m	-	-
	R240	200	150 m	240	150 m
	F240	-	-	240	300 m

Table 7.2: Geometric modelling parameters for each experimental DEM model, detailing the location of faults at their intersection with the x axis and their throw.

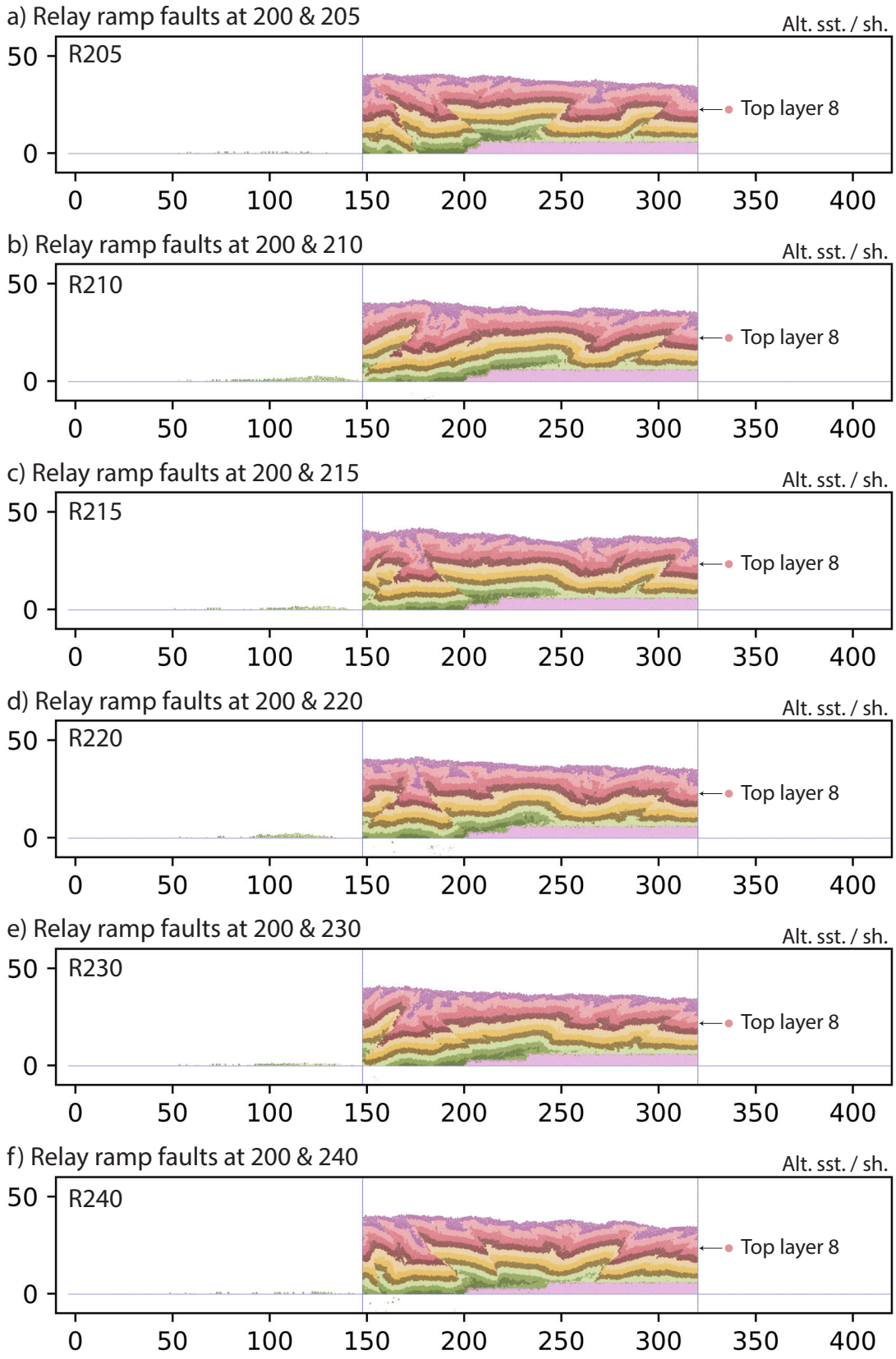

Figure 7.10: DEM modelling results of relay ramp geometries (a-f) with fault separation of between 5 and 40 units (250 and 2000 m).

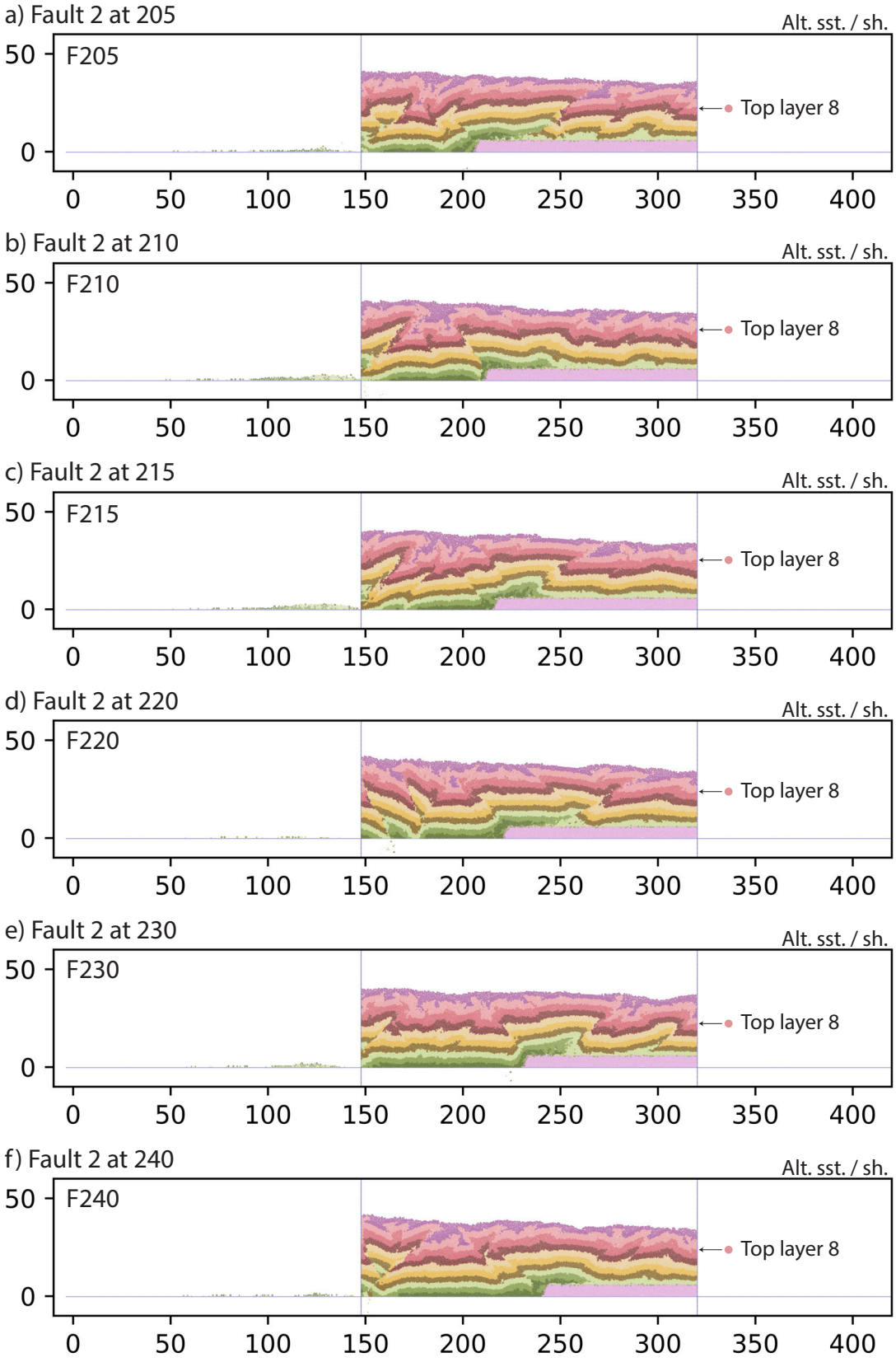

Figure 7.11: DEM modelling results of footwall fault geometries (a-f) at between 205 and 240 units on the x axis.

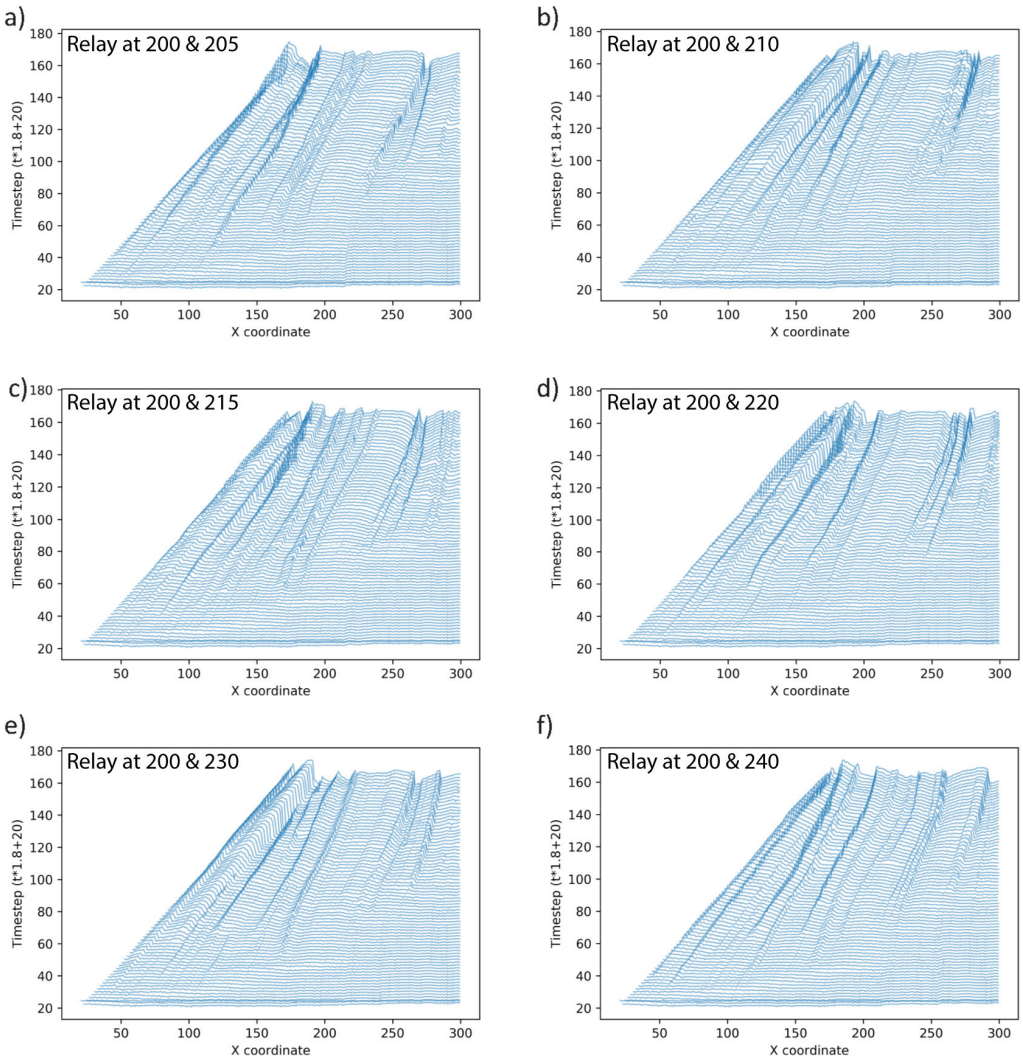

Figure 7.12: Horizon elevation with time for each relay ramp geometry model (a-f).

single localised planes upon which strain accumulates, while at shallower depths strain is more broadly accommodated between multiple structures.

Considering the relay geometry models (Fig. 7.10), the shortest fault separation features split vergence of thrusting across the location of the basement fault in the same manner as the F200 model. However, as the relay zone fault separation increases to 10 units (500 m), the vergence of the entire model becomes towards the right. At larger separations, the vergence returns to being split between towards to the right, right of the basement fault and towards the left, left of the basement fault.

At fault separations of 20 units (1 km) and greater, the multiple faults become related to the relay zone. Reviewing previous timesteps and elements of the final geometry, this appears to be due to the two faults causing separate structures. This is interpreted to indicate that the separation of the faults is now sufficient that the areas of influence of the two features are distinct, resulting in nucleation of discretely different structures.

Although proximity to the impactor may cause boundary effects in the models, it is noted that the lower element of the stratigraphy are buried towards the left. Depending on the separation of faults in the relay zone, these buried areas may or may not retain connection to up-dip elements of the stratigraphy.

In the Fault 2 models (Fig. 7.11), only the lateral location of the hangingwall fault varies. In all models the deformation to the right of the basement fault is dominantly verging towards the right. While that to the left of the basement fault is of mixed vergence, typically with antithetic faults originating from close to the basement fault and eastwards verging structures originating from the impactor. Interactions between faults with these opposing vergence directions are dependent on the spacing between their occurrence.

Typically the wavelength of deformation in these models appears to be shorter than in the relay ramp models, with an increased occurrence of layers vertically offset by their own thickness or more by faulting. As the fault moves backwards towards 230 and 240 units, the right verging faults occur near the boundary. While this appears to be due to boundary conditions they form an interesting observation, as this could be observed in real examples should it be more energetically efficient to nucleate new faults than to overcome the frictional resistance of material towards the foreland.

Analysis of the relative timing of structures (Fig. 7.12), shows that all models feature a forward propagation of deformation over time. These illustrations show that while strain localises onto discrete fault planes at varying times throughout the models, once established those faults typically continue to accumulate strain.

Models with lower fault separation, appear to feature a greater interaction between faults, this is also displayed through the greater intensity of deformation in the final

geometries. In these cases, some early faults can be seen to join or converge. At larger fault separations, such convergence is less regular. Instead a persistent wavelength of deformation appears to be established that then persists throughout the modelling duration.

7.5 Discussion & concluding remarks

Along the Eastern edge of the Eastern Cordillera, many areas feature clear signs of inversion, such as significant harpoon structures clear both in seismic and outcrop (Mora et al., 2013). However, in the study area, no such evidence presents itself. Instead, a deep, strong, reflection is observed with an extensional pattern of deformation (Fig. 7.7). Overlying this is a sequence of thrust nappes, cropping out at surface as large fault-propagation folds.

Locally a west-southwest trend of faulting exists oriented oblique to the compressional margin with potential for a strike-slip component of displacement. Due to the lack of evidence for reactivation of these deeper structures, it is suggested that the obliquity of this feature relative to the margin may preclude reactivation due to sub-optimal orientation. An alternative interpretation could be that the large fault is actually part of a relay zone between two trends outside of the seismic dataset.

It is suggested that knowledge of the geometry of the passive basement could provide insight into the interpretation of the overburden. In the setting of a reactivated extensional basement, correlation has been demonstrated between original normal fault displacement profiles and subsequent compressional fault displacement profiles (Reilly et al., 2017). Although this is for an actively deforming basement, it is thought that some of the mechanisms will be common. For example, in the presence of a relay ramp within the extensional system, this geometry may provide a low angle, relatively low friction basal surface for thrust propagation, or it may act as a area along which thrust may shear forming a lateral ramp (e.g. Fig. 7.13).

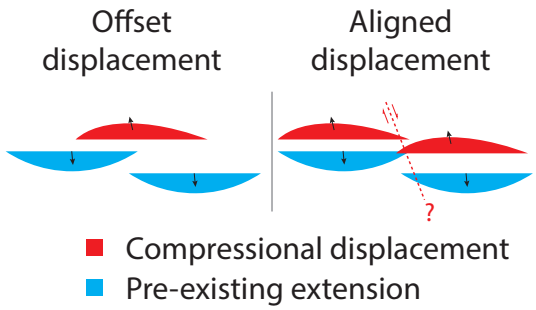

Figure 7.13: Illustration of two potential hypotheses of how displacement may align between a passive extensional basement and subsequent overlying thrust nappes.

The DEM modelling presented demonstrates a clear link between basement morphology and deformation of overlying strata. The sensitivity testing geometries demonstrated a clear control of mechanical stratigraphy, with weaker beds supporting broader more symmetrical deformation, while stronger layers took on a style more similar to ramp-flat thrusting, propagating forward with the vergence direction.

The role of mechanical stratigraphy is broadly recognised and has been discussed with relevance to outcrop (Peacock and Sanderson, 1992; Cardozo et al., 2005; Dalton et al., 2016), laboratory (Bonanno et al., 2017) and numerical studies (Hardy, 2018b; Schöpfer et al., 2009; Welch et al., 2009). However, models from the field example all feature identical input material.

In these examples relay ramp models feature longer wavelength thrust nappes. This may be comparable with Figure 7.8d, in which the lowest angle ramp is associated with the furtherest fault propagation. This could be interpreted to be due to the reduction in ramp angle. Further work is required to understand the significance of these results.

The location of nearby plays, suggests that these observations could have significant exploration potential, as basement morphology could be used to predict the nature of shallower structures. Furthermore, if the suspected patterns of broadening folds above relay ramps are correct, these can be observed to form larger trapping geometries than equivalent structures from these models.

A further consideration of the models illustrates the downwards movement to strata towards the impactor; this provides a potential mechanism for lowering source rock to depths of greater temperature for maturation. Considering the modelling results in this context, it may be observed that dependent on the separation of relay zone faults, the hinterland side of the model that is buried may remain in continuous connection with up-dip elements or become cut-off, influencing potential migration pathways.

Use of two-dimensional sections to represent the three-dimensional problem of thrust nappes passing over passive basement morphologies is insufficient to fully understand the relationship between the two. Chattopadhyay et al. (2014) demonstrated that lateral variations in floor thrust geometry lead to increased uplift of fault-propagation folds up-dip from areas with focussing of strain. This is supported by field observations that suggest an association of ramp initiation with basement morphology (Schmidt et al., 1993).

Work using finite element models has identifed stratified layers of deformation in compressional zones (Ellis et al., 2004). In homogeneous models, strain was described as stratified. Higher in the models deformation occurred in the frictional-viscous domain, while at the base of the model units remained relatively static, locking-up with only frictional deformation. Pop-up structures were noted to occur, originating at the boundary between the two, as observed in Figures 7.9, 7.10 and 7.11.

Mechanical modelling, and discrete element modelling in particular, are computationally intense, limiting their application. However some authors have coupled DEM and FEM to make more efficient and accurate models (Guo and Zhao, 2014). In the mean time however, recent work has illustrated that the parameter space of kinematic approaches (Pei et al., 2014) may be linked to mechanical properties (Cardozo et al., 2002). This could provide a method to understand and apply some mechanical controls without the necessity of full mechanical modelling.

A final observation from discrete element modelling is the continued application of 'force chains' to geological problems. Perhaps best illustrated in using photoelasticity

(Fig. 7.14), the approach identifies elements within a model that are in some way coupled to to pass on energy (Teshima, 1953; Geng et al., 2001).

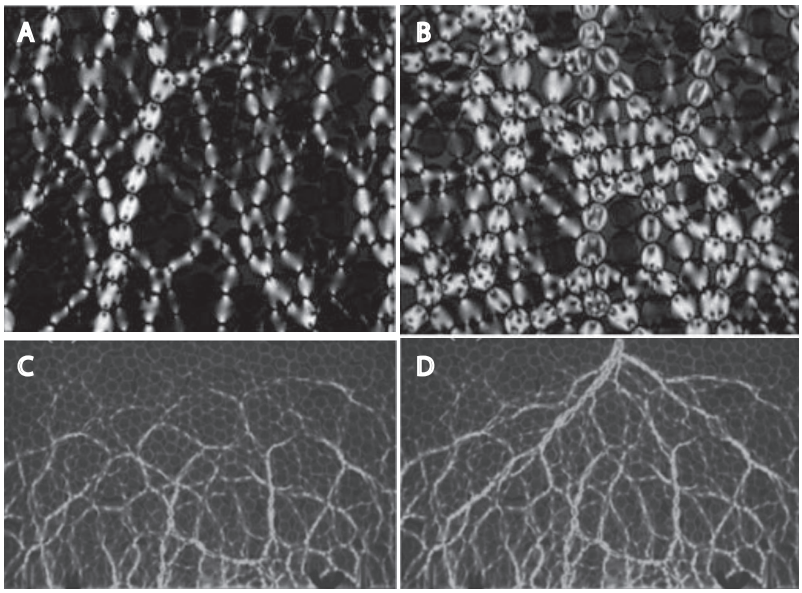

Figure 7.14: Experimental images of the photoelastic response to (a) low-force sheared state and (b) high-stress isotropically compressed state, from Majmudar and Behringer (2005); and, (c) force due to hydrostatic head and (d) combined response from gravity and a point source, from Geng et al. (2001).

Such experiments demonstrate granular materials do not compact homogeneously, rather stress anisotropies develop (Majmudar and Behringer, 2005). These anisotropies are formed by interaction of particles, passing forces from one to another, where a string of these connected by the stress that they pass on may be referred to as a force chain. Analysis of force chains has been directly related to deformation at small scales in crack developed and confirmed through comparison to lab experiments (Ord and Hobbs, 2010). Combining these observations with holistic approaches to interpretation (e.g. Chapman and Decelles, 2015) could provide interesting exploration insights, assisting in geometric problems in the absence of data constraint.

Virtue is more to be feared than vice, because its excesses are not subject to the regulation of conscience.

Adam Smith

Chapter 8

Discussion & concluding remarks

Chapter structure:

8.1 Introduction

This thesis set out to address uncertainty in the interpretation of geological structures through the application of seismic forward modelling. Seismic modelling is a mature technology broadly applied in the field of geophysics. It has been used to great effect in improving seismic processing efficacy and investigating the way in which seismic surveys capture information on the subsurface (Carcione et al., 2002). This research has influenced common interpretation workflows leading to the regular analysis of amplitude versus offset (Castagna et al., 1998; Russell et al., 2001; Foster et al., 2010) and tuning anomalies (Robertson and Nogami, 1984; Zeng and Marfurt, 2015).

These workflows have been demonstrated to have significant potential for application in the understanding of fluid and rock (Avseth et al., 2001) properties (§ 2.4.2), directly influencing the perceived risking of hydrocarbon plays (e.g. Roden et al., 2014) and providing evidence of fluid motion potentially related to fault seal (e.g. White et al., 2015). In these applications, the technology may be considered proven (Technology readiness level 9 of Mankins, 1995, 2009a), however simulation of complete seismic images and usage of these synthetic images in interpretation is very much in its infancy. In this field the technology requires proof of application to demonstrate its proficiency and positive contribution to value (Mankins, 2009b).

While the majority of work in this thesis has been in developing workflows to enable seismic forward modelling in a geologically realistic fashion, the primary scientific contribution is the proof of concept that seismic forward modelling may be applied at various scales. This represents progress in the readiness of the technology for application in practice.

Two workflows are developed joining contemporary methods of reservoir modelling and structural restoration with those of seismic modelling. The interface-based method combines structural restoration techniques with seismic image simulation to quickly iterate modelling of multiple methods (§ 3.2.1). This approach is limited to modelling

a single impedance contrast for each interface, but allows fast iteration of subtly different models. The volume-based method, utilises reservoir modelling approaches to build complex geological models featuring lateral variation of compositional and elastic properties, constrained by interpreted or modelled geometries (§ 3.2.2).

The methods lend themselves to different studies, volume based approaches provide accurate subsurface models, capable of high degrees of compositional or structural complexity. They facilitate detailed studies with subtle differences in response (e.g. Ch. 4), while interface based approaches lend themselves to fast, approximate model builds investigating interpretation dependants (e.g. Ch. 5) and studies utilising multiple modelling iterations (e.g. Ch. 6).

Using these approaches three themes of research are to be considered in this discussion: understanding image constraint, validating analytical methods and comparing alternate interpretations (§ 1.2).

8.2 Understanding image constraint

Seismic imaging quality is commonly referred to interchangeably with the term resolution, despite a specific definition of the latter (§ 2.2.3), limited to discriminating between different signals in a wavelet. Much of the perceived seismic image quality (Bond et al., 2015) is due to specific aspects of acquisition and processing that determine the detectability of a dataset. Similarly elements that are considerably below conventional estimates of resolution may be detectable in low noise settings such as the sphere resolution test (Fig. 3.12).

Experiments using the Marmousi data set (Brougois et al., 1990; Versteeg, 1994) show that even large bodies with significant changes in elastic properties due to compositional variation may also present an imaging challenge (Coleman et al., 2000). Ambiguity in aspects of their geometry are not caused by resolution and limited elastic contrast, but instead by survey illumination and migration (Gjøystdal et al., 2007). While migration

issues have been a focus of research for some time (Bee Bednar, 2005; Jones, 2014), with some levels of success, notably from application of reverse time migration (e.g. Zhou et al., 2018), illumination issues are yet to be fully considered. Minor overbank deposits can cause notable variation in modelled reserves (Alpak et al., 2013), migration and illumination issues may render entire prospects invisible.

Although dip, curvature, depth and thinning all affect seismic response, sometimes detrimentally (e.g. Fig. 3.11), aspects of the geometry are typically visible (e.g. Fig. 3.13) allowing supposition of the actual subsurface geometry. Energy from a single location may be spread considerably across the stacked data (e.g. Fig. 3.14).

Using point spread functions (§ 3.5.3), it is possible to see that the structure of a section dramatically changes the illumination of areas beneath it. This concept is known and widely considered during interpretation of salt (Jones and Davison, 2014), sills (Eide et al., 2018) an gas chimneys (Arntsen et al., 2007), however the effects of variation in the overburden are less well explored, even in the significant case of sub-thrust settings (e.g. Fig. 3.16).

The contemporary literature focusses primarily on consideration of composition in controlling seismic response. This aspects of the seismic response is very well understood and guidance from this field of work may be applied more generally across different acquisition surveys. However, especially in the case of compressional geometries, it would appear that illumination may be a key consideration.

Illumination is primarily a product of acquisition survey, geometry and composition, making it difficult to develop rules or guidelines for interpretation that are cross-applicable between difference scenarios. This could be the reason for the perceived lack of consideration given to this potential significant control in the published literature.

Recent advances in imaging compressional areas, have been gained through application of improved stacking patterns (Heilmann, 2007), survey design (Meunier, 2011) and selective use of post-stack structurally oriented filters (Höcker and Fehmers, 2003). This may suggest that at least part of the issue remains practical, and leads the author to suspect

that care should be taken before attributing all loss of signal associated with complex structures to migration issues.

Once the illumination and noise of real seismic data is considered, it is suggested that such issues may be more common as the inverse problem provide non-unique results, meaning the synthetic forward-problem discussed here may be representative of a greater range of real situations than is represented within my results.

Such issues are critical to geologically interpreting seismic data, as the association between reflections and chronostratigraphic surfaces has been shown to be at least partly dependent on imaging quality (Johansen et al., 2007). In areas of lower imaging quality, variability associated with the uncertainty of a horizon pick may be increased, reducing the accuracy of the calculation or extraction of attribute data using that surface subsequently (Rankey and Mitchell, 2003).

8.3 Validating analytical methods

Many seismic attributes have been developed, however there are a limited number of truly distinct attributes (Barnes, 2006) derived from complex trace analysis (Taner, 1979). A significant step forward came with the implementation of geometric attributes that locally compare the magnitudes and trends of seismic responses from individual traces within a local neighbourhood (Chopra and Marfurt, 2005), which have been employed to great effect in the field of structural geology (e.g. Hesthammer and Fossen, 1997a).

There are many pitfalls in applying these types of analysis, often related to inherent uncertainty of the dataset and artefacts that should be commonly expected (Marfurt and Alves, 2015). This emphasises the importance of validating observed signals as geological (e.g. Hart, 2002; Verma et al., 2015), while considering the expected limitations on visualisation (e.g. Fig. 8.1).

Using a single simple normal fault, with a Gaussian fault displacement profile, related

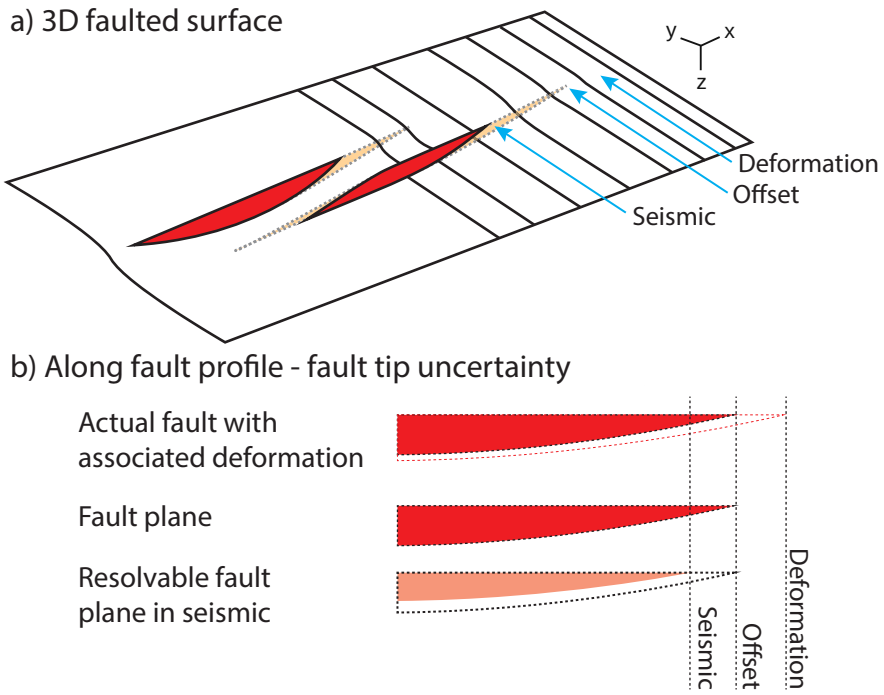

Figure 8.1: Illustration of different limits on the observation of faulting and fault related deformation in the subsurface; (a) three-dimensional illustration of fault displacement pattern along a horizon, indicating the expected ambiguity in fault length, also (b) shown in cross-section.

juxtaposition and no variation in elastic properties away from a simple alternating stratigraphy and sand and shale (Ch. 4), I demonstrated that significant trace anomalies should be expected (e.g. Fig. 4.15).

Significantly this implies that such anomalies are possible without the need for variation of elastic properties through the presence if complex fault facies, fault-related deformation or exotic pore fluids. Pore fluids, deformation and other causes are possible however not required for such anomalies (e.g. Fig. 4.24).

This is a key observation with regards to structural uncertainty. Assuming such anomalies are associated with along fault fluid movement is sometimes used to imply hydraulic conductivity, directly impacting an interpreters perception of trap effectiveness (e.g. Wiprut and Zoback, 2002), this is not necessarily the case.

The association of these anomalies with across-fault juxtaposition and repeat at each juxtaposition suggests that anomalies only vary slightly with dip. It is suggested that further models varying elastic properties may demonstrate a means to constrain elastic properties and impedance contrasts in the region of faulting.

Across-fault affects imply that both sides of the fault are sampled, and thus begin to illustrate that additional phenomena may be associated with sampling of the fault zones within a Fresnel zone than have yet been considered within the field of structural interpretation. I suspect, that following further investigation this may be an area that has been neglected due to its presence between geology and geophysics.

Along-fault identification of fault tip locations has been shown to be both under- and over-estimated. Conventional wisdom is that fault lengths are always under-estimated due to limits on seismic detectability. Further work is required to test this rather unintuitive finding in more complex settings.

Recent work has modelled fault facies distributions (Qu et al., 2015) and shown that they may be seismically resolvable by industry surveys (Botter et al., 2017; Kolyukhin et al., 2017). Although these studies have not demonstrated that this signal would be detectable with a representative overburden, they have inspired further interest through demonstration of significance to reservoir simulation of fluid flow (Qu and Tveranger, 2017).

My findings suggest that where complex fault fill may be present and detectable, across-fault juxtaposition effects are also likely. This may necessitate removal of the fault geometry effects prior to the consideration of fault fill effects. It is considered likely that in order to use either of these approaches in application to real data, both will require combined consideration. Consideration of more complex stratigraphic sequences is required prior to transitioning to application to real data.

Observations of spatial variation in fault response investigated in this thesis, suggest that models of spatial uncertainty based on symmetrical envelopes within which the faults is expected to occur are unrealistic. Instead, uncertainty envelopes should vary along the

fault strike, varying constraint of location across the fault surface (Fig. 8.2).

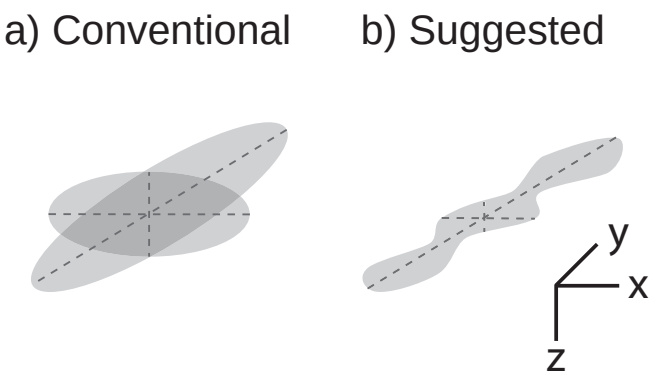

Figure 8.2: Illustration of fault interpretation uncertainty envelope as (a) conventionally described and as (b) suggested by this work.

8.4 Comparing alternate interpretations

Once an individual feature is identified, it is possible to consider the variability with which that feature could be interpreted. However, at times features are not discernible, or may be so ambiguous that multiple different features could be interpreted, all consistent with the available evidence (Bond et al., 2007; Polson and Curtis, 2010).

While typical in geoscience applications (Frodeman, 1995), this challenges contemporary approaches to representing subsurface uncertainty. Active debates in the fields of risk engineering, economics and behavioural psychology point to various methods for handing risk and uncertainty.

Two terms regarding types of uncertainty are usefully applied. Aleatory uncertainty, sometimes referred to as natural variability, is the uncertainty surrounding a quantifiable parameter related to aspects such as instrumental error. In application this type of uncertainty refers to a situation whereby there is an expected value associated with a range of potential values. Should the result occur within that range, the prediction may be considered valid. Alternatively, epistemic uncertainty is a fundamental lack of

understanding of what the value may be, in some cases this is a categorical uncertainty, where an interpretation may be one thing or another (Begg et al., 2014; Bratvold and Begg, 2008).

In application to the subsurface, these two are typically related, with the expectation and range of an aleatory uncertainty being dependent on the categorical description of the setting (Aven, 2010). For example, the likely distribution of porosity will vary about expectations differently for alternative categories of depositional environment. Continuing this example, some would argue that it is mathematically incorrect to consider these as separate uncertainties, as should the environment of deposition be unknown the situation could be represented by an expected value with a broader range. As such, these two types of uncertainty cannot be considered to be mutually independent (Winkler, 1996; Nilsen and Aven, 2003).

As this discussion considers the application of uncertainty, I will use the terms aleatory and epistemic to refer to the methods that are commonly used to address these uncertainties. Namely stochastic simulation for aleatory uncertainty and scenario-based probabilities for epistemic uncertainties (Smalley et al., 2008).

My results demonstrate a 16 % difference in the expected resource using different analysis strategies. It is suggested that a variation of this magnitude would be likely to affect decisions regarding investment, highlighting the importance of comparing appropriately derived values. A key aspect to ensuring use of comparable approaches is employing appropriate means to elicit expert opinion (Aspinall, 2010; Yoe, 2011; Usher and Strachan, 2013). In the case of calculating risks or chance of occurrence of multi-parameter problems with complex interdependencies, risk tables and formalised approaches may be applied (White, 1993; Milkov, 2015).

In cases of geometric interpretation uncertainty such approaches are very difficult to standardise due to the level of inter-dependency between different aspects of the interpretations. Comparison of the different geometries in this work (§ 4.6, 5.4, 3.5.3 & 6.4.3), indicate that there are distinct areas of the seismic section that are more or less

certain than others.

Using mechanical modelling (Ch. 7), I have demonstrated more certain elements of an interpretation can be assimilated into alternative analyses, such as mechanical modelling (§ 7.4).

Synthetic seismic data presents a means to allow direct comparison of an interpretation in the form of a seismic image to the original seismic data. Although, not currently quantified, this presents a means to qualitatively compare the output a given interpretation against the original input considering the effects of survey illumination and potentially overburden effects.

Current methods of modelling structural uncertainty (e.g. Røe et al., 2014) assume an aleatory variation around an interpretation. This generally assumes that the uncertainty of a fault may be represented by a three-dimensional tensor, with consistent distributions of likelihood along a given axis across the whole fault surface (Julio et al., 2015; Botter, 2016). Work presented in this thesis demonstrates that faults are not imaged evenly across their surfaces. As a result, uncertainty in their position should also be expected to be spatially variable.

8.5 Concluding remarks

Two seismic forward modelling workflows have been developed, the volume-based method, suitable for detailed models with complex variation of elastic properties; and, the interface-based method, suitable for quick iteration of compositionally simple but structurally complex models. These methods have been successfully applied to illustrate the uncertainty of interpreting geological structures at various scales.

In application a series of typical oil and gas workflows, significant uncertainty was calculated, including:

- Resource in-place estimates varies by 16 % using different appraisal methods,

- Daily production rates are overestimated by over 40 % dependent on modelling style, and;
- Fault lengths are underestimated by up to 100 m, or overestimated by up to 120 m using different seismic attributes.

Assessing the accuracy of seismic attributes in determining the known location of a fault tip in two different simple fault geometries demonstrated that both magnitude and rank of accuracy varied significantly between geometries. Trace attributes and in particular frequency offer one of the most robust estimates in this low noise dataset.

Further investigation of the frequency attributes identified a new mechanism to cause variation of seismic response along a fault trend. Crossovers in fault-horizon intersections demonstrate that the contrast in elastic properties across a fault may be detected in the seismic response. Significant amplitude and frequency anomalies may occur along faults without any change in fluid or rock composition, or deformation.

Recent attempts to extract fault facies data from seismic volumes are likely to be obstructed by the presence of these anomalies. Attempts to extract fault facies properties without removing the effects of these anomalies are unlikely to provide valid results.

Simulating flow in a simple faulted reservoir demonstrated that unintended smoothing of structure in seismic interpretation affects fluid flow by changing the cross-sectional area available for flow. Selecting from three common strategies to represent such near detectable scale faulting leads to a variation in production rates of over 40 %.

Simulating seismic images from different potential interpretations provides a means to encourage the use of multiple potential interpretation scenarios. The manner in which such interpretations are analysed to calculate resource in place affects the estimated volume by up to 16 %.

Mechanical modelling suggests that a passive basement guides deformation in overlying compressional systems. However three-dimensional modelling is required for further analysis.

8.6 Future development

In this thesis, I have demonstrated that contemporary reservoir modelling approaches may be used to great effect when combined with recent advances in seismic image simulation. However, a current limitation is the use of structured grids in reservoir modelling, as used to in volume-based methods. These may soon be surpassed by the use of unstructured grids (e.g. Prevost et al., 2005) and pluri-Gaussian approaches (e.g. Farrashkhalvat and Miles, 2003; Zagayevskiy and Deutsch, 2016) that utilise a cloud of data rather than uniform tabulation.

These changes would essentially merge the benefits of the volume-based method with those of the interface-based method (defined in § 3.2). Integration of these approaches with stochastic kinematic modelling (e.g. Moretti et al., 2006; Wellmann et al., 2016); topological approaches (Sanderson and Nixon, 2015; Thiele et al., 2016; Duffy et al., 2017); and modern geometric uncertainty analysis (e.g. Wellmann et al., 2014; de la Varga and Wellmann, 2016), could allow truly probabilistic modelling.

Efficiency gains in seismic modelling discussed in this thesis (after Lecomte et al., 2004) could be used to develop a stochastic seismic image simulator. This would improve the range of potential images that could be compared, potential providing a tractable route to probabilistic modelling and application of stochastic inversion procedures as has become typical in seismic inversion for rock physics properties (Spikes et al., 2007; Grana, 2014).

Mechanical modelling remains computationally expensive and requires additional levels of expertise for application. As a result it is not suitable for many industry applications. However efficiency gains in this field through the development of new methods (e.g. McBeck et al., 2016). There remains in issue in predicting potential geometries that may inform interpretation from modelling. Mechanical modelling provides a means to do this, however a greater level of detail in models is required to develop this into a useful tool for interpretation.

Further research is required to understand the relative sensitivity of seismic images to

composition and geometry. Application of detailed facies modelling results in realistic looking seismic images so that detection may be better understood (Fig. 8.3).

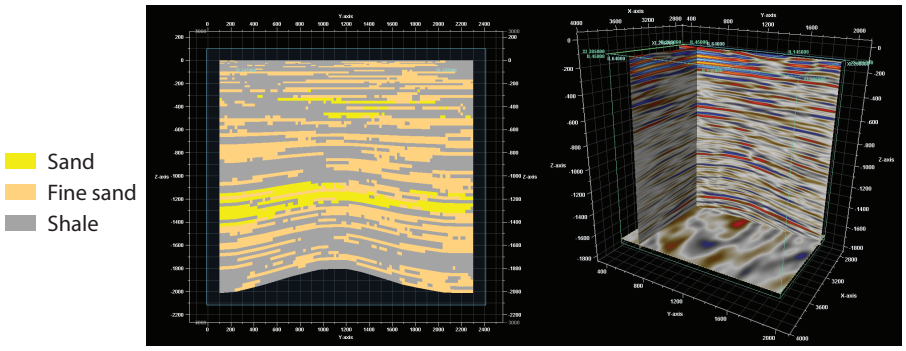

Figure 8.3: Example synthetic data based on a more complex facies model.

Uncertainty in geoscience is challenged by the variety of observations and parameters that may exist to describe a given situation. Sensitivity analysis (e.g. Saltelli et al., 2000) and measures of information entropy (Wellmann and Regenauer-Lieb, 2012) provides a means to better quantify this. Coupling these approaches with seismic forward modelling could allow for an improved understanding of the inherent uncertainty of complex seismic images.

References

Adelinet, M. and Le Ravalec, M. 2015. Effective medium modeling: How to efficiently infer porosity from seismic data? *Interpretation*, 3(4):SAC1–SAC7. doi: 10.1190/INT-2015-0065.1.

Ahmed, T., 2010. *Reservoir Engineering Handbook*. Elsevier, 4th edition. ISBN 978-1-85617-803-7.

Aki, K. and Richards, P. G., 2002. *Quantitative Seismology*. University Science Books, second edition. ISBN 0-935702-96-2.

Alaei, B. and Petersen, S. 2007. Geological modelling and finite difference forward realization of a regional section from the Zagros fold-and-thrust belt. *Petroleum Geoscience*, 13:241–251. doi: 10.1144/1354-079306-730.

Alaei, B. 2005. Seismic forward modelling of two fault- related folds from the Dezful Embayment of the Iranian Zagros Mountains. *Journal of Seismic Exploration*, 30:13–30.

Alcalde, J., Bond, C. E., Johnson, G., Butler, R. W., Cooper, M. A., and Ellis, J. F. 2017a. The importance of structural model availability on seismic interpretation. *Journal of Structural Geology*, 97:161–171. doi: 10.1016/j.jsg.2017.03.003.

Alcalde, J., Bond, C. E., Johnson, G., Ellis, J. F., and Butler, R. W. 2017b. Impact of seismic image quality on fault interpretation uncertainty. *GSA Today*, 27(2):4–10. doi: 10.1130/GSATG282A.1.

Alcalde, J., Bond, C. E., and Randle, C. H. 2017c. Framing bias: The effect of figure presentation on seismic interpretation. *Interpretation*, 5(4):T591–T605. doi: 10.1190/INT-2017-0083.1.

Aldridge, D. F. 1990. The Berlage wavelet. *Geophysics*, 55(11):1508–1511.

Allan, P. D. 2011. Stochastic analysis of resource plays: Maximizing portfolio value and mitigating risks. *SPE Economics & Management*, 3(03):141–148. doi: 10.2118/134811-PA.

Almendral, A., Robles, W., Parra, M., Mora, A., Ketcham, R., and Raghib, M. 2015. FetKin: Coupling kinematic restorations and temperature to predict thrusting, exhumation histories, and thermochronometric ages. *AAPG Bulletin*, 99(08):1557–1573. doi: 10.1306/07071411112.

Alpak, F. O., Barton, M. D., and Naruk, S. J. 2013. The impact of fine-scale turbidite channel architecture on deep-water reservoir performance. *AAPG Bulletin*, 97(2):251–284. doi: 10.1306/04021211067.

Anell, I., Lecomte, I., Braathen, A., and Buckley, S. J. 2016. Synthetic seismic illumination of small-scale growth faults, paralic deposits and low-angle clinoforms: A case study of the Triassic successions on Edgeøya, NW Barents Shelf. *Marine and Petroleum Geology*, 77:625–639. doi: 10.1016/j.marpetgeo.2016.07.005.

Archer, J. S. and Wall, C. G. 1986. Secondary recovery and pressure maintenance. In *Petroleum Engineering*, pages 173–190. Springer Netherlands, Dordrecht, 1986.

Arkes, H. R. 2001. Overconfidence in judgmental forecasting. In *Principles of Forecasting*, pages 495–515. Springer US, 2001.

Arntsen, B., Wensaas, L., Løseth, H., and Hermanrud, C. 2007. Seismic modeling of gas chimneys. *Geophysics*, 72(5):SM251–SM259. doi: 10.1190/1.2749570.

Aspinall, W. 2010. A route to more tractable expert advice. *Nature*, 463(January):294–295. doi: 10.1038/463294a.

Athy, L. F. 1930. Compaction and oil migration. *AAPG Bulletin*, 14(1):25–35. doi: 10.1306/3D93289F-16B1-11D7-8645000102C1865D.

Aven, T. 2010. On the need for restricting the probabilistic analysis in risk assessments to variability: Perspective. *Risk Analysis*, 30(3):354–360. doi: 10.1111/j.1539-6924.2009.01314.x.

Avseth, P., Mukerji, T., Jørstad, A., Mavko, G., and Veggeland, T. 2001. Seismic reservoir mapping from 3D AVO in a North Sea turbidite system. *Geophysics*, 66(4):1157–1176. doi: 10.1190/1.1487063.

Avseth, P., Mukerji, T., and Mavko, G., 2005. *Quantitative Seismic Interpretation: Applying Rock Physics Tools to Reduce Interpretation Risk*. Cambridge University Press, Cambridge. ISBN 9780521151351.

Baas, J. H., McCaffrey, W. D., and Knipe, R. J. 2005. The deep-water architecture knowledge base: towards an objective comparison of deep-marine sedimentary systems. *Petroleum Geoscience*, 11(4):309–320. doi: 10.1144/1354-079304-642.

Bacon, F., 1878. *Novum Organum*. Clarendon Press.

Badley, M. E., 1985. *Practical Seismic Interpretation*. Prentice Hall. ISBN 9780136922377.

Bakke, K., Agerlin Petersen, S., Martinsen, O. J., Johansen, T. A., Lien, T., and Thurmond, J. 2011. Seismic Modeling of Outcrop Analogues: Techniques and Applications. In Martinsen, O. J., Pulham, A. J., Haughton, P. D., and Sullivan, M. D., editors, *Outcrops Revitalized*, chapter 6, pages 69–86. SEPM (Society for Sedimentary Geology), 1st edition, 2011. ISBN 9781565763067. doi: 10.2110/sepmcsp.10.069.

Barnes, A. 2006. Too many seismic attributes? *CSEG Recorder*, 31(March):41–46.

Barnes, A. E. 1996. Theory of 2-D complex seismic trace analysis. *Geophysics*, 61(1): 264–272. doi: 10.1190/1.1443947.

Bayona, G., Cardona, A., Jaramillo, C., Mora, A., Montes, C., Caballero, V., Mahecha, H., Lamus, F., Montenegro, O., Jimenez, G., Mesa, A., and Valencia, V. A. 2013. Onset of fault reactivation in the Eastern Cordillera of Colombia and proximal Llanos Basin; response to Caribbean-South American convergence in early Palaeogene time. *Thick-Skin-Dominated Orogens: From Initial Inversion to Full Accretion*, 377(1):285–314. doi: 10.1144/SP377.5.

Beckwith, J., Clark, R., and Hodgson, L. 2017. Estimating frequency-dependent attenuation quality factor values from prestack surface seismic data. *Geophysics*, 82 (1):O11–O22. doi: 10.1190/geo2016-0169.1.

Bee Bednar, J. 2005. A brief history of seismic migration. *Geophysics*, 70(3):3MJ–20MJ. doi: 10.1190/1.1926579.

Begg, S. H., Welsh, M. B., and Bratvold, R. B. 2014. Uncertainty vs. variability: What's the difference and why is it important? In *SPE Hydrocarbon Economics and Evaluation Symposium*, Houston, Texas, 2014. Society of Petroleum Engineers. ISBN 9781632665904. doi: 10.2118/169850-MS.

Bentley, M. and Smith, S. 2008. Scenario-based reservoir modelling: the need for more determinism and less anchoring. *Geological Society, London, Special Publications*, 309(1):145–159. doi: 10.1144/SP309.11.

Berlage, H. 1932. Seismometer. In B. Gutenberg, editor, *Handbuch der Geophysik*, chapter 4, pages 299–526. Gebrueder Borntraeger Verlag, Berlin, 1932.

Bonanno, E., Bonini, L., Basili, R., Toscani, G., and Seno, S. 2017. How do horizontal, frictional discontinuities affect reverse fault-propagation folding? *Journal of Structural Geology*, 102:147–167. doi: 10.1016/j.jsg.2017.08.001.

Bond, C. E., Johnson, G., and Ellis, J. F. 2015. Structural model creation: the impact of data type and creative space on geological reasoning and interpretation. *Geological Society of London, Special Publication*, 421:83–97. doi: 10.1144/SP421.4.

Bond, C. E., Gibbs, A. D., Shipton, Z. K., and Jones, S. 2007. What do you think this is? "Conceptual uncertainty" in geoscience interpretation. *GSA Today*, 17(11):4. doi: 10.1130/GSAT01711A.1.

Bond, C. E., Shipton, Z. K., Gibbs, A. D., and Jones, S. 2008. Structural models: optimizing risk analysis by understanding conceptual uncertainty. *First Break*, 26(6): 65–71.

Bond, C. E. 2015. Uncertainty in structural interpretation: Lessons to be learnt. *Journal of Structural Geology*, 74:185–200. doi: 10.1016/j.jsg.2015.03.003.

Boneh, Y. and Reches, Z. 2017. Geotribology - Friction, wear, and lubrication of faults. *Tectonophysics*. doi: 10.1016/j.tecto.2017.11.022.

Bonini, M., Sani, F., and Antonielli, B. 2012. Basin inversion and contractional reactivation of inherited normal faults: A review based on previous and new experimental models. *Tectonophysics*, 522-523:55–88. doi: 10.1016/j.tecto.2011.11.014.

Bosch, M. 2004. The optimization approach to lithological tomography: Combining seismic data and petrophysics for porosity prediction. *Geophysics*, 69(5):1272–1282. doi: 10.1190/1.1801944.

Botter, C., Cardozo, N., Hardy, S., Lecomte, I., and Escalona, A. 2014. From mechanical modeling to seismic imaging of faults: A synthetic workflow to study the impact of faults on seismic. *Marine and Petroleum Geology*, 57:187–207. doi: 10.1016/j.marpetgeo.2014.05.013.

Botter, C., Cardozo, N., Qu, D., Tveranger, J., and Kolyukhin, D. 2017. Seismic characterization of fault facies models. *Interpretation*, 5(4):SP9–SP26. doi: 10.1190/INT-2016-0226.1.

Botter, C. D. 2016. *Seismic Imaging of Fault Zones*. PhD thesis, University of Stavanger.

Brandes, C. and Tanner, D. C. 2014. Fault-related folding: A review of kinematic models and their application. *Earth-Science Reviews*, 138:352–370. doi: 10.1016/j.earscirev.2014.06.008.

Bratvold, R. B. and Begg, S. H. 2008. I would rather be vaguely right than precisely wrong: A new approach to decision making in the petroleum exploration and production industry. *AAPG Bulletin*, 92(10):1373–1392. doi: 10.1306/06040808070.

Bredesen, K., Jensen, E. H., Johansen, T. A., and Avseth, P. 2015. Quantitative seismic interpretation using inverse rock physics modelling. *Petroleum Geoscience*, 21(4):271–284. doi: 10.1144/petgeo2015-006.

Brougois, A., Bourget, M., Lailly, P., Poulet, M., Ricarte, P., and Versteeg, R. 1990. Marmousi, model and data. In *EAGE Workshop - Practical Aspects of Seismic Data Inversion*, pages 5–16. doi: 10.3997/2214-4609.201411190.

Brown, A. R., 2011. *Interpretation of Three-Dimensional Seismic Data*. Society of Exploration Geophysicists and American Association of Petroleum Geologists. ISBN 978-0-89181-374-3. doi: 10.1190/1.9781560802884.

Butler, R. W. H., Tavarnelli, E., and Grasso, M. 2006. Structural inheritance in mountain belts: An Alpine-Apennine perspective. *Journal of Structural Geology*, 28(11):1893–1908. doi: 10.1016/j.jsg.2006.09.006.

Campolongo, F., Cariboni, J., and Saltelli, A. 2007. An effective screening design for sensitivity analysis of large models. *Environmental Modelling and Software*, 22(10):1509–1518. doi: 10.1016/j.envsoft.2006.10.004.

Campos, H. and Mann, P. 2015. Tectonostratigraphic evolution of the Northern Llanos foreland basin of Colombia and implications for its hydrocarbon potential. In *AAPG Memoir: Petroleum Geology and Potential of the Colombian Caribbean Margin*, volume 108, pages 517–546. AAPG, 2015. doi: 10.1306/13531948M1083651.

Carcione, J. M., Herman, G. C., and ten Kroode, A. P. E. 2002. Seismic modeling. *Geophysics*, 67(4):1304. doi: 10.1190/1.1500393.

Cardozo, N., Bhalla, K., Zehnder, A. T., and Allmendinger, R. W. 2002. Mechanical models of fault propagation folds and comparison to the trishear kinematic model. *Journal of Structural Geology*, 25(1):1–18. doi: 10.1016/S0191-8141(02)00013-5.

Cardozo, N., Allmendinger, R. W., and Morgan, J. K. 2005. Influence of mechanical stratigraphy and initial stress state on the formation of two fault propagation folds. *Journal of Structural Geology*, 27(11):1954–1972. doi: 10.1016/j.jsg.2005.06.003.

Carrillo, E., Mora, A., Ketcham, R. A., Amorocho, R., Parra, M., Costantino, D., Robles, W., Avellaneda, W., Carvajal, J. S., Corcione, M. F., Bello, W., Figueroa, J. D., Gómez, J. F., González, J. L., Quandt, D., Reyes, M., Rangel, A. M., Román, I., Pelayo, Y., and Porras, J. 2016. Movement vectors and deformation mechanisms in kinematic restorations: A case study from the Colombian Eastern Cordillera. *Interpretation*, 4 (1):T31–T48. doi: 10.1190/INT-2015-0049.1.

Cartwright, J. and Huuse, M. 2005. 3D seismic technology: The geological 'Hubble'. *Basin Research*, 17(1):1–20. doi: 10.1111/j.1365-2117.2005.00252.x.

Castagna, J. P., Swan, H. W., and Foster, D. J. 1998. Framework for AVO gradient and intercept interpretation. *Geophysics*, 63(3):948–956. doi: 10.1190/1.1444406.

Castagna, J. P. and Sun, S. 2006. Comparison of spectral decomposition methods. *First Break*, 24(March):75–79.

Cazier, E. C., Hayward, A. B., Espinosa, G., Velandia, J., Mugniot, J. F., and Leel, W. G. 1995. Petroleum geology of the Cusiana Field, Llanos Basin foothills, Colombia. *American Association of Petroleum Geologists Bulletin*, 79(10):1444–1463. doi: 10.1306/7834D9FE-1721-11D7-8645000102C1865D.

Cerveny, V. and Brown, M. G. 2003. Seismic ray theory. *The Journal of the Acoustical Society of America*, 113(1):14–14. doi: 10.1121/1.1523385.

Chamberlin, R. T. 1910. The Appalachian folds of central Pennsylvania. *The Journal of Geology*, 18(3):228–251. doi: 10.1086/621722.

Chamberlin, T. C. 1965. The method of multiple working hypotheses: With this method the dangers of parental affection for a favorite theory can be circumvented. *Science*, 148(3671):754–759. doi: 10.1126/science.148.3671.754.

Chapman, J. B. and Decelles, P. G. 2015. Foreland basin stratigraphic control on thrust belt evolution. *Geology*, 43(7):579–582. doi: 10.1130/G36597.1.

Chattopadhyay, A., Jain, M., and Bhattacharjee, D. 2014. Three-dimensional geometry of thrust surfaces and the origin of sinuous thrust traces in orogenic belts: Insights from scaled sandbox experiments. *Journal of Structural Geology*, 69:122–137. doi: 10.1016/j.jsg.2014.09.020.

Chellingsworth, L., Bentley, M., and Wynn, T. 2015. Human factors in seismic uncertainty - Restoring a realistic uncertainty range. *Interpretation*, 3(2):SQ21–SQ32. doi: 10.1190/INT-2014-0203.1.

Chen, J. and Schuster, G. T. 1999. Resolution limits of migrated images. *Geophysics*, 64 (4):1046–1053. doi: 10.1190/1.1444612.

Childs, C., Manzocchi, T., Walsh, J. J., Bonson, C. G., Nicol, A., and Schöpfer, M. P. J. 2009. A geometric model of fault zone and fault rock thickness variations. *Journal of Structural Geology*, 31(2):117–127. doi: 10.1016/j.jsg.2008.08.009.

Chopra, S. and Marfurt, K. J. 2005. Seismic attributes - A historical perspective. *Geophysics*, 70(5):3SO. doi: 10.1190/1.2098670.

Coleman, J., Sheppard, F. I., and Jones, T. 2000. Seismic resolution of submarine channel architecture as indicated by outcrop analogs. *Fine-Grained Turbidite Systems*, 72:119–126.

Colombera, L., Mountney, N. P., and McCaffrey, W. D. 2012a. A relational database for the digitization of fluvial architecture: concepts and example applications. *Petroleum Geoscience*, 18(1):129–140. doi: 10.1144/1354-079311-021.

Colombera, L., Felletti, F., Mountney, N. P., and McCaffrey, W. D. 2012b. A database approach for constraining stochastic simulations of the sedimentary heterogeneity of fluvial reservoirs. *AAPG Bulletin*, 96(11):2143–2166. doi: 10.1306/04211211179.

Cooley, J. W. and Tukey, J. W. 1965. An algorithm for the machine calculation of complex Fourier series. *Mathematics of Computation*, 19(90):297. doi: 10.2307/2003354.

Cooper, M. A., Addison, F. T., and Alvarez, R. 1995. Basin development and tectonic history of the Llanos Basin, Eastern Cordillera, and middle Magdalena Valley, Colombia. *AAPG Bulletin*, 10(10):1421–1443.

Corre, B., Thore, P., de Feraudy, V., and Vincent, G. 2000. Integrated uncertainty assessment for project evaluation and risk analysis. In *SPE European Petroleum Conference*. Society of Petroleum Engineers. ISBN 9781555639129. doi: 10.2118/65205-MS.

Couples, G., Ma, J., Lewis, H., Olden, P., and Quijano, J. 2007. Geomechanics of faults: impacts on seismic imaging. *First Break*, 25(October):83–90.

Cundall, P. A. and Strack, O. D. L. 1979. A discrete numerical model for granular assemblies. *Géotechnique*, 29(1):47–65. doi: 10.1680/geot.1979.29.1.47.

Curtis, A. 2012. The science of subjectivity. *Geology*, 40(1):95–96. doi: 10.1130/focus012012.1.

Curtis, A. and Wood, R. 2004. Optimal elicitation of probabilistic information from experts. *Geological Society, London, Special Publications*, 239(1):127–145. doi: 10.1144/gsl.sp.2004.239.01.09.

Curtis, J. 1975. A multi-trace synthetic seismogram generator. *Exploration Geophysics*, 6(4):91. doi: 10.1071/EG975091.

Dahlen, F. A. 1988. Mechanical energy budget of a fold-and-thrust belt. *Nature*, 331: 335–337. doi: 10.1038/331335a0.

Dahlstrom, C. D. A. 1970. Structural geology in the Eastern Margin of the Canadian Rocky Mountains. *Bulletin of Canadian Petroleum Geology*, 18(3):332–406.

Dake, L. 2001. The appraisal of oil and gas fields. In Dake, L., editor, *Practice of Reservoir Engineering*, pages 29–50. Elsevier, 2001. ISBN 978-0-444-50670-2.

Dalton, T. J. S., Paton, D. A., and Needham, D. T. 2016. Influence of mechanical stratigraphy on multi-layer gravity collapse structures: insights from the Orange Basin, South Africa. *Geological Society, London, Special Publications*, 438. doi: 10.1144/SP438.4.

Davies, V. M. 1982. Interaction of thrusts and basement faults in the French external Alps. *Tectonophysics*, 88(3-4):325–331. doi: 10.1016/0040-1951(82)90244-X.

de Groot, P., Qayyum, F., Brouwer, F., Liu, Y., and Hemstra, N. 2016. New methods for slicing and dicing seismic volumes. *First Break*, 34(March):51–55.

de la Varga, M. and Wellmann, J. F. 2016. Structural geologic modeling as an inference problem: A Bayesian perspective. *Interpretation*, 4(3):SM1–SM16. doi: 10.1190/INT-2015-0188.1.

Delaunay, B. 1934. Sur la sphère vide. *Izvestia Akademia Nauk SSSR*, 7(7):793–800.

Delgado, A., Mora, A., and Reyes-Harker, A. 2012. Deformation partitioning in the Llanos foreland basin during the Cenozoic and its correlation with mountain building in the hinterland. *Journal of South American Earth Sciences*, 39:228–244. doi: 10.1016/j.jsames.2012.04.011.

Deregowski, S., Bloor, R., and Koeninger, C. 1997. Increasing lateral resolution. In *EAGE 59th Conference and Technical Exhibition*, pages 1–2. EAGE.

Dragoset, B. 2005. A historical reflection on reflections. *The Leading Edge*, 24(s1): s46–s70. doi: 10.1190/1.2112392.

Drottning, Å. and Branston, M. 2009. Value of illumination-consistent modelling in time-lapse seismic analysis. *First Break*, 27(10):75–83.

Duchesne, M. J. and Gaillot, P. 2011. Did you smooth your well logs the right way for seismic interpretation? *Journal of Geophysics and Engineering*, 8(4):514–523. doi: 10.1088/1742-2132/8/4/004.

Duffy, O. B., Nixon, C. W., Bell, R. E., Jackson, C. A.-L., Gawthorpe, R. L., Sanderson, D. J., and Whipp, P. S. 2017. The topology of evolving rift fault networks: Single-phase vs multi-phase rifts. *Journal of Structural Geology*, 96(May):192–202. doi: 10.1016/j.jsg.2017.02.001.

Dvorkin, J. and Nur, A. 1996. Elasticity of high-porosity sandstones: Theory for two North Sea data sets. *Geophysics*, 61(5):890–893. doi: 10.1190/1.1444059.

Edgar, J. A. and van der Baan, M. 2011. How reliable is statistical wavelet estimation? *Geophysics*, 76(4):V59–V68. doi: 10.1190/1.3587220.

Egbue, O. and Kellogg, J. 2012. Three-dimensional structural evolution and kinematics of the Piedemonte Llanero, Central Llanos foothills, Eastern Cordillera, Colombia. *Journal of South American Earth Sciences*, 39:216–227. doi: 10.1016/j.jsames.2012.04.012.

Egeland, T., Holden, L., and Larsen, E. A. 1992. Designing better decisions. *European Petroleum Computer Conference*. doi: 10.2118/24275-MS.

Eichert, S. 2006. *Including Noise in the Simulated Migration Amplitude method*. Diplôme d'ingenieur, Universite Louis Pasteur, Strasbourg, Oslo, Norway.

Eide, C. H., Schofield, N., Lecomte, I., Buckley, S. J., and Howell, J. A. 2018. Seismic interpretation of sill complexes in sedimentary basins: implications for the

sub-sill imaging problem. *Journal of the Geological Society*, 175(2):193–209. doi: 10.1144/jgs2017-096.

Elliott, D. 1976. The energy balance and deformation mechanisms of thrust sheets. *Philosophical Transactions of the Royal Society*, 283:289–312.

Ellis, S., Schreurs, G., and Panien, M. 2004. Comparisons between analogue and numerical models of thrust wedge development. *Journal of Structural Geology*, 26: 1659–1675. doi: 10.1016/j.jsg.2004.02.012.

Epard, J.-L. and Groshong, R. 1995. Kinematic model of detachment folding including limb rotation, fixed hinges and layer-parallel strain. *Tectonophysics*, 247(1-4):85–103. doi: 10.1016/0040-1951(94)00266-C.

Erslev, E. A. 1991. Trishear fault-propagation folding. *Geology*, 19(6):617–620. doi: 10.1130/0091-7613(1991).

Evans, J., Cade, C. A., and Bryant, S. 1997. A geological approach to permeability prediction in clastic reservoirs. *AAPG Memoir*, 69:91–101.

Fagin, S. 1996. The fault shadow problem: Its nature and elimination. *The Leading Edge*, 15(9):1005–1013. doi: 10.1190/1.1437403.

Fagin, S. W., 1991. *Seismic Modeling of Geologic Structures*. Society of Exploration Geophysicists, Tulsa, USA. ISBN 978-1-56080-050-7. doi: 10.1190/1.9781560802754.

Farrashkhalvat, M. and Miles, J. 2003. Unstructured grid generation. In *Basic Structured Grid Generation*, chapter 8, pages 190–226. Elsevier, 2003. ISBN 9780511780066. doi: 10.1016/B978-075065058-8/50008-3.

Ferrill, D. A., Morris, A. P., Wigginton, S. S., Smart, K. J., McGinnis, R. N., and Lehrmann, D. 2016. Deciphering thrust fault nucleation and propagation and the importance of footwall synclines. *Journal of Structural Geology*, 85:1–11. doi: 10.1016/j.jsg.2016.01.009.

Finch, E. 1999. *A Lattice Solid Model for Crustal Extension*. PhD thesis, University of Ulster, Coleraine.

Finch, E., Hardy, S., and Gawthorpe, R. 2003. Discrete element modelling of contractional fault-propagation folding above rigid basement fault blocks. *Journal of Structural Geology*, 25(4):515–528. doi: 10.1016/S0191-8141(02)00053-6.

Finch, E., Hardy, S., and Gawthorpe, R. 2004. Discrete-element modelling of extensional fault-propagation folding above rigid basement fault blocks. *Basin Research*, 16(4): 467–488. doi: 10.1111/j.1365-2117.2004.00241.x.

Fisher, Q. J. and Jolley, S. J. 2007. Treatment of faults in production simulation models. *Geological Society, London, Special Publications*, 292:219–233. doi: 10.1144/SP292.13.

Foster, D. J., Keys, R. G., and Lane, F. D. 2010. Interpretation of AVO anomalies. *Geophysics*, 75(5):75A3–75A13. doi: 10.1190/1.3467825.

Frodeman, R. 1995. Geological reasoning: geology as an interpretive and historical science. *Geological Society of America Bulletin*, 107(8):960–968. doi: 10.1130/0016-7606(1995)107<0960:GRGAAI>2.3.CO.

Geng, J., Howell, D., Longhi, E., Behringer, R. P., Reydellet, G., Vanel, L., Clément, E., and Luding, S. 2001. Footprints in sand: the response of a granular material to local perturbations. *Physical Review Letters*, 87(3):035506. doi: 10.1103/PhysRevLett.87.035506.

Gholamy, A. and Kreinovich, V. 2014. Why Ricker wavelets are successful in processing seismic data: Towards a theoretical explanation. In *IEEE Symposium on Computational Intelligence for Engineering Solutions (CIES)*, pages 11–16. IEEE. ISBN 978-1-4799-4509-2. doi: 10.1109/CIES.2014.7011824.

Gibbs, A. 1983. Balanced cross-section construction from seismic sections in

areas of extensional tectonics. *Journal of Structural Geology*, 5(2):153–160. doi: 10.1016/0191-8141(83)90040-8.

Gjøystdal, H., Iversen, E., Laurain, R., Lecomte, I., Vinje, V., and Åstebøl, K. 2002. Review of ray theory applications in modelling and imaging of seismic data. *Studia Geophysica et Geodaetica*, 46:113–164. doi: 10.1023/A:1019893701439.

Gjøystdal, H., Iversen, E., Lecomte, I., Kaschwich, T., Drottning, Å., and Mispel, J. 2007. Improved applicability of ray tracing in seismic acquisition, imaging, and interpretation. *Geophysics*, 72(5):SM261–SM271. doi: 10.1190/1.2736515.

Görz, I., Herbst, M., Börner, J. H., and Zehner, B. 2017. Workflow for the integration of a realistic 3D geomodel in process simulations using different cell types and advanced scientific visualization: Variations on a synthetic salt diapir. *Tectonophysics*, 699:42–60. doi: 10.1016/j.tecto.2017.01.011.

Grabau, A. W. 1906. Types of sedimentary overlap. *Geological Society of America Bulletin*, 17(1):567–636. doi: 10.1130/GSAB-17-567.

Grana, D. 2014. Probabilistic approach to rock physics modeling. *Geophysics*, 79(2): D123–D143. doi: 10.1190/geo2013-0333.1.

Gray, G. G., Morgan, J. K., and Sanz, P. F. 2014. Overview of continuum and particle dynamics methods for mechanical modeling of contractional geologic structures. *Journal of Structural Geology*, 59:19–36. doi: 10.1016/j.jsg.2013.11.009.

Gray, S. H. 2013. Spatial sampling, migration aliasing, and migrated amplitudes. *Geophysics*, 78(3):S157—-S164. doi: 10.1190/geo2012-0451.1.

Gray, S. H., Etgen, J., Dellinger, J., and Whitmore, D. 2001. Seismic migration problems and solutions. *Geophysics*, 66(5):1622. doi: 10.1190/1.1487107.

Groshong, R. H. and Epard, J. L. 1994. Role of strain in area-constant detachment folding. *Journal of Structural Geology*, 16(5):613–615. doi: 10.1016/0191-8141(94)90113-9.

Guo, N. and Zhao, J. 2013. A hierarchical model for cross-scale simulation of granular media. *AIP Conference Proceedings*, 1542(2013):1222–1225. doi: 10.1063/1.4812158.

Guo, N. and Zhao, J. 2014. A coupled FEM/DEM approach for hierarchical multiscale modelling of granular media. *International Journal for Numerical Methods in Engineering*, 99(11):789–818. doi: 10.1002/nme.4702.

Guo, Y. and Morgan, J. K. 2008. Fault gouge evolution and its dependence on normal stress and rock strength - Results of discrete element simulations: Gouge zone micromechanics. *Journal of Geophysical Research: Solid Earth*, 113:1–19. doi: 10.1029/2006JB004525.

Hall, M. 2006a. Predicting bed thickness with cepstral decomposition. *The Leading Edge*, 25(2):199–204. doi: 10.1190/1.2172313.

Hall, M. 2006b. Resolution and uncertainty in spectral decomposition. *First Break*, 24 (December):43–47.

Han, D., Nur, A., and Morgan, D. 1986. Effects of porosity and clay content on wave velocities in sandstones. *Geophysics*, 51(11):2093–2107. doi: 10.1190/1.1442062.

Hardage, B. A. 2015. Pitfall experiences when interpreting complex structure with low-quality seismic images. *Interpretation*, 3(1):SB29–SB37. doi: 10.1190/INT-2014-0118.1.

Hardy, S. 2015. The Devil truly is in the detail. A cautionary note on computational determinism: Implications for structural geology numerical codes and interpretation of their results. *Interpretation*, 3(4):SAA29–SAA35. doi: 10.1190/INT-2015-0052.1.

Hardy, S. 2018a. Novel discrete element modelling of Gilbert-type delta formation in an active tectonic setting-first results. *Basin Research*, 00:1–15. doi: 10.1111/bre.12309.

Hardy, S. 2018b. Coupling a frictional-cohesive cover and a viscous substrate in a discrete element model: First results of application to thick- and thin-skinned

extensional tectonics. *Marine and Petroleum Geology*, 97(November 2017):32–44. doi: 10.1016/j.marpetgeo.2018.06.026.

Hardy, S. and Allmendinger, R. W. 2011. Trishear: A review of kinematics, mechanics, and applications. *AAPG Memoir*, 94:96–119. doi: 10.1306/13251334M943429.

Hardy, S. and Finch, E. 2006. Discrete element modelling of the influence of cover strength on basement-involved fault-propagation folding. *Tectonophysics*, 415(1-4): 225–238. doi: 10.1016/j.tecto.2006.01.002.

Hart, B. S. 2002. Validating seismic attribute studies: Beyond statistics. *The Leading Edge*, 21(10):1016–1021. doi: 10.1190/1.1518439.

Hart, B. 2008. Stratigraphically significant attributes. *The Leading Edge*, 27(3):320. doi: 10.1190/1.2896621.

Hauge, P. S. 1981. Measurements of attenuation from vertical seismic profiles. *Geophysics*, 46(11):1548–1558. doi: 10.1190/1.1441161.

Hayward, A. B. and Graham, R. H. 1989. Some geometrical characteristics of inversion. *Geological Society, London, Special Publications*, 44(1):17–39. doi: 10.1144/GSL.SP.1989.044.01.03.

Hedberg, H. D. 1936. Gravitational compaction of clays and shales. *American Journal of Science*, s5-31(184):241–287. doi: 10.2475/ajs.s5-31.184.241.

Heilmann, Z. 2007. *CRS-stack-based seismic reflection imaging for land data in time and depth domains*. PhD thesis, Universität (TH) Karlsruhe.

Hesthammer, J. 1998. Evaluation of the timedip, correlation and coherence maps for structural interpretation of seismic data. *First Break*, 16(5):151–167. doi: 10.1046/j.1365-2397.1998.00690.x.

Hesthammer, J. and Fossen, H. 1997a. Seismic attribute analysis in structural interpretation of the Gullfaks Field, northern North Sea. *Petroleum Geoscience*, 3(1): 13–26. doi: 10.1144/petgeo.3.1.13.

Hesthammer, J. and Fossen, H. 1997b. Research article: The influence of seismic noise in structural interpretation of seismic attribute maps. *First Break*, 15(1024):209–219. doi: 10.3997/1365-2397.1997007.

Hesthammer, J. and Henden, J. O. 2000. Closing the gap between theory and practice in seismic interpretation of small-scale faults. *Petroleum Geoscience*, 6(2):107–111. doi: 10.1144/petgeo.6.2.107.

Hettner, A., 1892. *Die Kordillere von Bogotá: Ergebnisse von Reisen und Studien*. Perthes.

Hill, R. 1952. The elastic behaviour of a crystalline aggregate. *Proceedings of the Physical Society. Section A*, 65(5):349–354. doi: 10.1088/0370-1298/65/5/307.

Hilterman, F. J. 1970. Three-dimensional seismic modelling. *Geophysics*, 35(6):1020–1037. doi: 10.1190/1.1440140.

Höcker, C. F. W. and Fehmers, G. C. 2003. Fast structural interpretation with structure-oriented filtering. *Geophysics*, 68(4):1286–1293. doi: 10.1190/1.1598121.

Hodgetts, D. and Howell, J. A. 2000. Synthetic seismic modelling of a large-scale geological cross-section from the Book Cliffs, Utah, USA. *Petroleum Geoscience*, 6(3):221–229. doi: 10.1144/petgeo.6.3.221.

Holden, L., Mostad, P., Nielsen, B. F., Gjerde, J., Townsend, C., and Ottesen, S. 2003. Stochastic structural modeling. *Mathematical Geology*, 35(8):899–914. doi: 10.1023/B:MATG.0000011584.51162.69.

Hosken, J. W. J. 1988. Ricker wavelets in their various guises. *First Break*, 6(1):24–33. doi: 10.3997/1365-2397.1988002.

Hossack, J. R. 1979. The use of balanced cross-sections in the calculation of orogenic contraction: A review. *Journal of the Geological Society*, 136(6):705–711. doi: 10.1144/gsjgs.136.6.0705.

Hubral, P., Schleicher, J., and Tygel, M. 1996. A unified approach to 3-D seismic reflection imaging, Part I: Basic concepts. *Geophysics*, 61(3):742–758. doi: 10.1190/1.1444001.

Hunter, J. D. 2007. Matplotlib: A 2D Graphics Environment. *Computing in Science & Engineering*, 9(3):90–95. doi: 10.1109/MCSE.2007.55.

Iacopini, D., Butler, R. W. H., Purves, S., McArdle, N., and De Freslon, N. 2016. Exploring the seismic expression of fault zones in 3D seismic volumes. *Journal of Structural Geology*, 89:54–73. doi: 10.1016/j.jsg.2016.05.005.

Iacopini, D. and Butler, R. W. H. 2011. Imaging deformation in submarine thrust belts using seismic attributes. *Earth and Planetary Science Letters*, 302(3-4):414–422. doi: 10.1016/j.epsl.2010.12.041.

Irving, A. D., Kuznetsov, D., Robert, E., Manzocchi, T., and Childs, C. 2014. Optimization of uncertain structural parameters with production and observation well data. *SPE Reservoir Evaluation & Engineering*, 17(04):547–558. doi: 10.2118/171558-PA.

Jackson, J. A. 1980. Reactivation of basement faults and crustal shortening in orogenic belts. *Nature*, 283(5745):343–346. doi: 10.1038/283343a0.

Janson, X. and Fomel, S. 2011. 3-D forward seismic model of an outcrop-based geocellular model. In Martinsen, O. J., Pulham, A. J., Haughton, P. D., and Sullivan, M. D., editors, *Outcrops Revitalized*, volume 10, chapter 7, pages 87–106. SEPM (Society for Sedimentary Geology), 1st edition, 2011. ISBN 9781565763067. doi: 10.2110/sepmcsp.10.087.

Johansen, S., Granberg, E., Mellere, D., Arntsen, B., and Olsen, T. 2007. Decoupling of seismic reflectors and stratigraphic timelines: A modeling study of Tertiary strata from Svalbard. *Geophysics*, 72(5):SM273–SM280. doi: 10.1190/1.2759479.

Jones, A. D. W., Denelle, F. R., Lee, W. J., MacDonald, D., and Seiller, B. J. 2016. The use of reservoir simulation in deterministic proved-reserves estimation. *SPE Reservoir Evaluation & Engineering*, 19(03):358–366. doi: 10.2118/170669-PA.

Jones, G. and Knipe, R. J. 1996. Seismic attribute maps; application to structural interpretation and fault seal analysis in the North Sea Basin. *First Break*, 14(12):449–461.

Jones, I. 2014. Tutorial: migration imaging conditions. *First Break*, 32(December): 45–55.

Jones, I. F. and Davison, I. 2014. Seismic imaging in and around salt bodies. *Interpretation*, 2(4):SL1–SL20. doi: 10.1190/INT-2014-0033.1.

Jongmans, D., Charlier, R., Cescotto, S., Cosgrove, J., Darve, F., Fourmaintraux, D., and Sassi, W. 1998. *Finite Element Modelling in Structural and Petroleum Geology*. PhD thesis, Université de Liège.

Julio, C., Caumon, G., and Ford, M. 2015. Sampling the uncertainty associated with segmented normal fault interpretation using a stochastic downscaling method. *Tectonophysics*, 639:56–67. doi: 10.1016/j.tecto.2014.11.013.

Kahneman, D. 2003. Maps of bounded rationality: Psychology for behavioral economics. *American Economic Review*, 93(5):1449–1475. doi: 10.1257/000282803322655392.

Kahneman, D. and Klein, G. 2009. Conditions for intuitive expertise: a failure to disagree. *The American psychologist*, 64(6):515–526. doi: 10.1037/a0016755.

Kahneman, D. and Tversky, A. 1972. Subjective probability: A judgment of representativeness. *Cognitive Psychology*, 3(3):430–454. doi: 10.1016/0010-0285(72)90016-3.

Kallweit, R. S. and Wood, L. C. 1982. The limits of resolution of zero-phase wavelets. *Geophysics*, 47(7):1035–1046. doi: 10.1190/1.1441367.

Kim, Y. S. and Sanderson, D. J. 2005. The relationship between displacement and length of faults: A review. *Earth-Science Reviews*, 68(3-4):317–334. doi: 10.1016/j.earscirev.2004.06.003.

Klinkenberg, L. 1941. The permeability of porous media to liquids and gases. *API Drilling and Production Practice*, pages 200–2013. doi: 10.5510/OGP20120200114.

Kolyukhin, D. R., Lisitsa, V. V., Protasov, M. I., Qu, D., Reshetova, G. V., Tveranger, J., Tcheverda, V. A., and Vishnevsky, D. M. 2017. Seismic imaging and statistical analysis of fault facies models. *Interpretation*, 5(4):SP71–SP82. doi: 10.1190/INT-2016-0202.1.

Krzywinski, M. and Altman, N. 2017. Points of significance: Classification and regression trees. *Nature Methods*, 14(8):757–758. doi: 10.1038/nmeth.4370.

Laurain, R., Geluis, L. J., Vinje, V., and Lecomte, I. 2004. A review of 3D illumination studies. *Journal of Seismic Exploration*, 13:17–37.

Lecomte, I., Gjøystdal, H., and Drottning, Å. 2003. Simulated prestack local imaging: A robust and efficient interpretation tool to control illumination, resolution, and time-lapse properties of reservoirs. In *73rd Annual International Meeting, SEG*, pages 1525–1528.

Lecomte, I. 1999. Local and controlled prestack depth migration in complex areas. *Geophysical Prospecting*, 47(6):799–818. doi: 10.1046/j.1365-2478.1999.00164.x.

Lecomte, I. 2004. Simulating prestack depth migrated sections. In *EAGE 66th Conference & Exhibition*, pages 1–2, Paris, France, 2004. EAGE.

Lecomte, I. 2008. Resolution and illumination analyses in PSDM: A ray-based approach. *The Leading Edge*, 27(5):650–663. doi: 10.1190/1.2919584.

Lecomte, I., Maao, F. A., Johansen, T. A., and Bakke, R. 2004. Interpreter's corner: Efficient and flexible seismic modeling of reservoirs : A hybrid approach. *The Leading Edge*, 23(5):432–437.

Lecomte, I., Lavadera, P. L., Anell, I., Buckley, S. J., Schmid, D. W., and Heeremans, M. 2015. Ray-based seismic modeling of geologic models: Understanding and analyzing seismic images efficiently. *Interpretation*, 3(4):SAC71–SAC89. doi: 10.1190/INT-2015-0061.1.

Lever, J., Krzywinski, M., and Altman, N. 2016. Points of significance: Classification evaluation. *Nature Methods*, 13(8):603–604. doi: 10.1038/nmeth.3945.

Lindsey, J. P. 1989. The Fresnel zone and its interpetive significance. *The Leading Edge*, 8(10):33–39. doi: 10.1190/1.1439575.

Lomask, J., Guitton, A., Fomel, S., Claerbout, J., and Valenciano, A. A. 2006. Flattening without picking. *Geophysics*, 71(4):P13. doi: 10.1190/1.2210848.

Long, J. J. and Imber, J. 2010. Geometrically coherent continuous deformation in the volume surrounding a seismically imaged normal fault-array. *Journal of Structural Geology*, 32:222–234. doi: 10.1016/j.jsg.2009.11.009.

Macrae, E. J., Bond, C. E., Shipton, Z. K., and Lunn, R. J. 2016. Increasing the quality of seismic interpretation. *Interpretation*, 4(3):T395—-T402. doi: 10.1190/INT-2015-0218.1.

Main, I. G., Li, L., Heffer, K. J., Papasouliotis, O., Leonard, T., Koutsabeloulis, N. C., and Zhang, X. 2007. The statistical reservoir model: calibrating faults and fractures, and predicting reservoir response to water flood. *Geological Society, London, Special Publications*, 292:469–482. doi: 10.1144/SP292.25.

Majmudar, T. S. and Behringer, R. P. 2005. Contact force measurements and stress-induced anisotropy in granular materials. *Nature*, 435(7045):1079–1082. doi: 10.1038/nature03805.

Mankins, J. C. 1995. Technology readiness levels. *White Paper*, page 5. doi: 10.1080/08956308.2010.11657640.

Mankins, J. C. 2009a. Technology readiness assessments: A retrospective. *Acta Astronautica*, 65(9-10):1216–1223. doi: 10.1016/j.actaastro.2009.03.058.

Mankins, J. C. 2009b. Technology readiness and risk assessments: A new approach. *Acta Astronautica*, 65(9-10):1208–1215. doi: 10.1016/j.actaastro.2009.03.059.

Manzocchi, T., Walsh, J. J., Nell, P., and Yielding, G. 1999. Fault transmissibility multipliers for flow simulation models. *Petroleum Geoscience*, 5(1):53–63. doi: 10.1144/petgeo.5.1.53.

Marfurt, K. J. 2015. Techniques and best practices in multiattribute display. *Interpretation*, 3(1):B1–B23. doi: 10.1190/INT-2014-0133.1.

Marfurt, K. J. and Alves, T. M. 2015. Pitfalls and limitations in seismic attribute interpretation of tectonic features. *Interpretation*, 3(1):SB5–SB15. doi: 10.1190/INT-2014-0122.1.

Marfurt, K. J. and Kirlin, R. L. 2001. Narrow-band spectral analysis and thin-bed tuning. *Geophysics*, 66(4):1274–1283. doi: 10.1190/1.1487075.

Marfurt, K. J., Kirlin, R. L., Farmer, S. L., and Bahorich, M. S. 1998. 3-D seismic attributes using a semblance-based coherency algorithm. *Geophysics*, 63(4):1150–1165. doi: 10.1190/1.1444415.

Marfurt, K. J., Sudhaker, V., Gersztenkorn, A., Crawford, K. D., and Nissen, S. E. 1999. Coherency calculations in the presence of structural dip. *Geophysics*, 64(1):104. doi: 10.1190/1.1444508.

Martin, G. S., Wiley, R., and Marfurt, K. J. 2006. Marmousi2: An elastic upgrade for Marmousi. *The Leading Edge*, 25(2):156–166. doi: 10.1190/1.2172306.

Martin, K. and Wood, W. 2017. A new model of marine sediment compression. *Earth and Planetary Science Letters*, 477:21–26. doi: 10.1016/j.epsl.2017.08.008.

Mavko, G., Mukerji, T., and Dvorkin, J., 1998. *The Rock Physics Handbook: Tools for Seismic Analysis in Porous Media*. Cambridge University Press, Cambridge. ISBN 9780521861366.

Mavriplis, D. J. 1996. Mesh generation and adaptivity for complex geometries and flows. In *Handbook of Computational Fluid Mechanics*, pages 417–459. Elsevier, 1996. ISBN 9780125530101. doi: 10.1016/B978-012553010-1/50008-6.

Mayne, W. H. 1962. Common reflection point horizontal data stacking techniques. *Geophysics*, 27(6):927–938. doi: 10.1190/1.1439118.

McBeck, J. A., Madden, E. H., and Cooke, M. L. 2016. Growth by Optimization of Work (GROW): A new modeling tool that predicts fault growth through work minimization. *Computers & Geosciences*, 88:142–151. doi: 10.1016/j.cageo.2015.12.019.

McClay, K. R. 1995. The geometries and kinematics of inverted fault systems: a review of analogue model studies. *Geological Society, London, Special Publications*, 88(1): 97–118. doi: 10.1144/GSL.SP.1995.088.01.07.

McDermott, K. and Reston, T. 2015. To see, or not to see? Rifted margin extension. *Geology*, 43(11):G36982.1. doi: 10.1130/G36982.1.

Merrow, E. W., McDonnel, L., and Argüden, R. Y. 1988. Understanding the outcomes of megaprojects: a quantitative analysis of very large civilian projects. Technical report, RAND.

Meunier, J., 2011. *Seismic Acquisition from Yesterday to Tomorrow*. Society of Exploration Geophysicists. ISBN 978-1-56080-281-5. doi: 10.1190/1.9781560802853.

Milkov, A. V. 2015. Risk tables for less biased and more consistent estimation of probability of geological success (PoS) for segments with conventional oil

and gas prospective resources. *Earth-Science Reviews*, 150:453–476. doi: 10.1016/j.earscirev.2015.08.006.

Mora, A., Ketcham, R. A., Higuera-Diaz, I. C., Bookhagen, B., Jimenez, L., and Rubiano, J. 2014. Formation of passive-roof duplexes in the Colombian Subandes and Peru. *Lithosphere*, 6(5):1–17. doi: 10.1130/L340.1.

Mora, A., Blanco, V., Naranjo, J., Sanchez, N., Ketcham, R. A., Rubiano, J., Stockli, D. F., Quintero, I., Nemčok, M., Horton, B. K., and Davila, H. 2013. On the lag time between internal strain and basement involved thrust induced exhumation: The case of the Colombian Eastern Cordillera. *Journal of Structural Geology*, 52:96–118. doi: 10.1016/j.jsg.2013.04.001.

Mora, P. and Place, D. 1993. A lattice solid model for the nonlinear dynamics of earthquakes. *International Journal of Modern Physics C*, 04(06):1059–1074. doi: 10.1142/S0129183193000823.

Mora, P. and Place, D. 1994. Simulation of the frictional stick-slip instability. *Pure and Applied Geophysics*, 143(1-3):61–87. doi: 10.1007/BF00874324.

Moresi, L., Dufour, F., and Mühlhaus, H.-B. 2003. A Lagrangian integration point finite element method for large deformation modeling of viscoelastic geomaterials. *Journal of Computational Physics*, 184(2):476–497. doi: 10.1016/S0021-9991(02)00031-1.

Moretti, I., Lepage, F., and Guiton, M. 2006. KINE3D: A new 3D restoration method bsed on a mixed approach linking geometry and geomechanics. *Oil & Gas Science and Technology*, 61(2):277–289. doi: 10.2516/ogst:2006021.

Morgan, M. G. 2014. Use (and abuse) of expert elicitation in support of decision making for public policy. *Proceedings of the National Academy of Sciences of the United States of America*, 111(20):7176–7184. doi: 10.1073/pnas.1319946111.

Morris, M. D. 1991. Factorial sampling plans for preliminary computational experiments. *Technometrics*, 33(2):161–174. doi: 10.2307/1269043.

Nilsen, T. and Aven, T. 2003. Models and model uncertainty in the context of risk analysis. *Reliability Engineering & System Safety*, 79(3):309–317. doi: 10.1016/S0951-8320(02)00239-9.

Nur, A., Mavko, G., Dvorkin, J., and Galmudi, D. 1998. Critical porosity: A key to relating physical properties to porosity in rocks. *The Leading Edge*, 17(3):357–362. doi: 10.1190/1.1437977.

O'Brien, J. and Lercue, I. 1988. Seismic imaging of deep hydrocarbon reservoirs. *Pure and Applied Geophysics*, 127(1):33–61.

Okaya, D. A. 1995. Spectral properties of the Earth's contribution to seismic resolution. *Geophysics*, 60(I):241–251.

Oliphant, T. E. 2007. Python for scientific computing. *Computing in Science & Engineering*, 9(3):10–20. doi: 10.1109/MCSE.2007.58.

Ord, A. and Hobbs, B. E. 2010. Fracture pattern formation in frictional, cohesive, granular material. *Philosophical Transactions. Series A, Mathematical, Physical, and Engineering Sciences*, 368(1910):95–118. doi: 10.1098/rsta.2009.0199.

Partyka, G., Gridley, J., and Lopez, J. 1999. Interpretational applications of spectral decomposition in reservoir characterization. *The Leading Edge*, 18:353. doi: 10.1190/1.1438295.

Paton, D. A., Macdonald, D. I. M. M., and Underhill, J. R. 2006. Applicability of thin or thick skinned structural models in a region of multiple inversion episodes; southern South Africa. *Journal of Structural Geology*, 28(11):1933–1947. doi: 10.1016/j.jsg.2006.07.002.

Peacock, D. C. P. and Sanderson, D. J. 1992. Effects of layering and anisotropy on fault geometry. *Journal of the Geological Society*, 149(5):793–802. doi: 10.1144/gsjgs.149.5.0793.

Peel, F. J. 2016. Prospect risk, pot odds , and efficient drill or no-drill decision making: What the exploration business can learn from high- stakes poker. *AAPG Bulletin*, 4(4): 525–535. doi: 10.1306/10191515063.

Peel, F. J. and White, J. 2015. Do technical studies reduce subsurface risk in hydrocarbon exploration: and if not, how do they add value? *Geological Society, London, Special Publications*, 436. doi: 10.1144/SP436.4.

Pei, Y., Paton, D. A., and Knipe, R. J. 2014. Defining a 3-dimensional trishear parameter space to understand the temporal evolution of fault propagation folds. *Journal of Structural Geology*, 66:284–297. doi: 10.1016/j.jsg.2014.05.018.

Pichel, L. M., Finch, E., Huuse, M., and Redfern, J. 2017. The influence of shortening and sedimentation on rejuvenation of salt diapirs: A new discrete-element modelling approach. *Journal of Structural Geology*, 104:61–79. doi: 10.1016/j.jsg.2017.09.016.

Pickup, G., Ringrose, P., Corbett, P., Jensen, J., and Sorbie, K. 1994. Geology, geometry and effective flow. In *SPE Annual Technical Conference and Exhibition*, volume 1, pages 37–42. Society of Petroleum Engineers. doi: 10.2118/28374-MS.

Platt, J. R. 1964. Strong Inference: Certain systematic methods of scientific thinking may produce much more rapid progress than others. *Science*, 146(3642):347–353. doi: 10.1126/science.146.3642.347.

Poblet, J. and McClay, K. 1996. Geometry and kinematics of single-layer detachment folds. *AAPG Bulletin*, 80(7):1085–1109. doi: 10.1306/64ED8CA0-1724-11D7-8645000102C1865D.

Polson, D. and Curtis, A. 2010. Dynamics of uncertainty in geological interpretation. *Journal of the Geological Society*, 167(1):5–10. doi: 10.1144/0016-76492009-055.

Prevost, M., Lepage, F., Durlofsky, L. J., and Mallet, J.-L. 2005. Unstructured 3D gridding and upscaling for coarse modelling of geometrically complex reservoirs. *Petroleum Geoscience*, 11(4):339–345. doi: 10.1144/1354-079304-657.

Price, D., Angus, D., Garcia, A., and Fisher, Q. 2017. Probabilistic analysis and comparison of stress-dependent rock physics models. *Geophysical Journal International*, 210(1):196–209. doi: 10.1093/gji/ggx151.

Pshenichny, C. A. 2004. Classical logic and the problem of uncertainty. *Geological Society, London, Special Publications*, 239(1):111–126. doi: 10.1144/GSL.SP.2004.239.01.08.

Puga, J. L., Krzywinski, M., and Altman, N. 2015. Points of significance: Bayes' theorem. *Nature Methods*, 12(4):277–278. doi: 10.1038/nmeth.3335.

Qayyum, F., Betzler, C., and Catuneanu, O. 2017. The Wheeler diagram, flattening theory, and time. *Marine and Petroleum Geology*, 86:1417–1430. doi: 10.1016/j.marpetgeo.2017.07.034.

Qu, D. and Tveranger, J. 2017. Incorporation of deformation band fault damage zones in reservoir models. *AAPG Bulletin*, 101(8):423–443. doi: 10.1306/12111514166.

Qu, D., Røe, P., and Tveranger, J. 2015. A method for generating volumetric fault zone grids for pillar gridded reservoir models. *Computers and Geosciences*, 81:28–37. doi: 10.1016/j.cageo.2015.04.009.

Ram, S., Ward, E. S., and Ober, R. J. 2006. Beyond Rayleigh's criterion: a resolution measure with application to single-molecule microscopy. *Proceedings of the National Academy of Sciences of the United States of America*, 103(12):4457–4462. doi: 10.1073/pnas.0508047103.

Ramsay, J. G. and Wood, D. S. 1973. The geometric effects of volume change during deformation processes. *Tectonophysics*, 16:263–277.

Rankey, E. C. and Mitchell, J. C. 2003. That's why it's called interpretation: Impact of horizon uncertainty. *The Leading Edge*, 22(1994):820–828. doi: 10.1190/1.1614152.

Rayleigh. 1879. Investigations in optics, with special reference to the spectroscope. *The London, Edinburgh, and Dublin Philosophical Magazine and Journal of Science*, 8 (49):261–274. doi: 10.1080/14786447908639684.

Reilly, C., Nicol, A., and Walsh, J. 2017. Importance of pre-existing fault size for the evolution of an inverted fault system. *Geological Society, London, Special Publications*, 439(1):447–463. doi: 10.1144/SP439.2.

Reston, T. J. 2009. The extension discrepancy and syn-rift subsidence deficit at rifted margins. *Petroleum Geoscience*, 15(3):217–237. doi: 10.1144/1354-079309-845.

Reuss, A. 1929. Berechnung der fließgrenze von mischkristallen auf grund der plastizitätsbedingung für einkristalle . *ZAMM - Zeitschrift für Angewandte Mathematik und Mechanik*, 9(1):49–58. doi: 10.1002/zamm.19290090104.

Ricker, N. 1943. Further developments in the wavelet theory of seismogram structure. *Bulletin of the Seismological Society of America*, 33(3):197–228.

Ricker, N. 1953a. Wavelet contraction, expansion and the control of seismic resolution. *Geophysics*, 18(4):769–792. doi: 10.1190/1.1437927.

Ricker, N. 1953b. The form and laws of propagation of seismic wavelets. *Geophysics*, 18(1):10–40. doi: 10.1190/1.1437843.

Ringrose, P. and Bentley, M. 2015. The rock model. In *Reservoir Model Design*, pages 13–59. Springer Netherlands, Dordrecht, 2015. ISBN 978-94-007-5496-6.

Robertson, J. D. and Nogami, H. 1984. Complex seismic trace analysis of thin beds. *Geophysics*, 49(4):344. doi: 10.1190/1.1441670.

Roden, R., Forrest, M., and Holeywell, R. 2014. The role of AVO in prospect risk assessment. *Interpretation*, 2(2):61–76.

Røe, P., Georgsen, F., and Abrahamsen, P. 2014. An uncertainty model for fault shape and location. *Mathematical Geosciences*, 46(123):957–969. doi: 10.1007/s11004-014-9536-z.

Rose, P. R. 1992a. Uncertainties impacting reserves, revenue, and costs. In *ME 10: Development Geology Reference Manual*, chapter 10, pages 25–29. AAPG, 1992a.

Rose, P. R. 1992b. Chance of success and its use in petroleum exploration. In *The Business of Petroleum Exploration*, chapter 7, pages 71–86. AAPG, 1992b.

Rotevatn, A., Tveranger, J., Howell, J. A., and Fossen, H. 2009. Dynamic investigation of the effect of a relay ramp on simulated fluid flow: geocellular modelling of the Delicate Arch Ramp, Utah. *Petroleum Geoscience*, 15:45–58. doi: 10.1144/1354-079309-779.

Ruffo, P., Bazzana, L., Consonni, A., Corradi, A., Saltelli, A., and Tarantola, S. 2006. Hydrocarbon exploration risk evaluation through uncertainty and sensitivity analyses techniques. *Reliability Engineering & System Safety*, 91(10-11):1155–1162. doi: 10.1016/j.ress.2005.11.056.

Russell, B., Lines, L., Hirsche, K., Peron, J., and Hampson, D. 2001. The AVO modelling volume. *Exploration Geophysics*, 32(4):264. doi: 10.1071/EG01264.

Ryan, H. 1994. Ricker, Ormsby; Klander, Butterworth - A choice of wavelets. *CSEG Recorder*, September:24–25. doi: 209.91.124.56.

Saenger, E. H., Ciz, R., Krüger, O. S., Schmalholz, S. M., Gurevich, B., and Shapiro, S. A. 2007. Finite-difference modeling of wave propagation on microscale: A snapshot of the work in progress. *Geophysics*, 72(5):SM293–SM300. doi: 10.1190/1.2753552.

Sæther, O.-P. 2013. *Seismic Forward Modeling of Deltaic Sequences*. Masters thesis, NTNU - Trondheim.

Saltelli, A., Chan, K., and Scott, E. M., 2000. *Sensitivity Analysis*. Wiley, 1st edition. ISBN 978-0471998921.

Saltelli, A., Ratto, M., Andres, T., Campolongo, F., Cariboni, J., Gatelli, D., Saisana, M., and Tarantola, S., 2008. *Global Sensitivity Analysis: The Primer*. Wiley. ISBN 0470059974.

Samson, S., Reneke, J. A., and Wiecek, M. M. 2009. A review of different perspectives on uncertainty and risk and an alternative modeling paradigm. *Reliability Engineering and System Safety*, 94(2):558–567. doi: 10.1016/j.ress.2008.06.004.

Sanderson, D. J. and Nixon, C. W. 2015. The use of topology in fracture network characterization. *Journal of Structural Geology*, 72:55–66. doi: 10.1016/j.jsg.2015.01.005.

Savage, H. M. and Cooke, M. L. 2010. Unlocking the effects of friction on fault damage zones. *Journal of Structural Geology*, 32(11):1732–1741. doi: 10.1016/j.jsg.2009.08.014.

Schmidt, C. J., Genovese, P. W., and Chase, R. B. 1993. Role of basement fabric and cover-rock lithology on the geometry and kinematics of twelve folds in the Rocky Mountain foreland. In Schmidt, C. J., Chase, R. B., and Erslev, E. A., editors, *Laramide Basement Deformation in the Rocky Mountain Foreland of the Western United States*, volume 280, pages 1–44. Geological Society of America, 1993. ISBN 9780813722801. doi: 10.1130/SPE280-p1.

Schöpfer, M. P. J., Childs, C., and Walsh, J. J. 2009. Two-dimensional Distinct Element Method (DEM) modeling of tectonic fault growth in mechanically layered sequences. *2009 Symposium on Mechanics of Natural Solids*, pages 127–146.

Sclater, J. G. and Christie, P. A. F. 1980. Continental stretching: An explanation of the post-Mid Cretaceous subsidence of the Central North Sea Basin. *Journal of Geophysical Research*, 85(B7):3711–3739.

Sheriff, R. E. 1977. Limitations on resolution of seismic reflections and geologic detail derivable from them: Section 1. Fundamentals of stratigraphic interpretation of seismic

data. *AAPG Memoir: Seismic Stratigraphy–Applications to Hydrocarbon Exploration*, 26:3–14.

Sheriff, R. E. and Geldart, L., 1995. *Exploration Seismology*. Cambridge University Press, Cambridge, 2nd edition. ISBN 9780521468268.

Sigernes, L.-T. W. 2004. *Rock Physics of Extensional Faults and their Seismic Imaging Properties*. PhD thesis, NTNU: Norwegian University of Science and Technology.

Sigernes, L.-T. W. and Morton, A. 2002. Seismic fault imaging. In *SEG International Exposition and 72nd Annual Meeting*, pages 1–4, Salt Lake City, Utah, 2002.

Simm, R. and Bacon, M., 2014. *Seismic Amplitude*. Cambridge University Press, Cambridge, 1st edition. ISBN 9781107011502. doi: 10.1017/CBO9780511984501.

Simm, R. and White, R. 2002. Phase, polarity and the interpreter's wavelet. *First Break*, 20(May):277–281.

Skauvold, J., Eidsvik, J., and Theune, U. 2016. A parametric model for seismic wavelets - with estimation and uncertainty quantification. *Geophysical Journal International*, 205(2):796–809. doi: 10.1093/gji/ggw029.

Smalley, P. C., Begg, S. H., Naylor, M., Johnsen, S., and Godi, A. 2008. Handling risk and uncertainty in petroleum exploration and asset management: An overview. *AAPG Bulletin*, 92(10):1251–1261. doi: 10.1306/06040808063.

Smith, W., 1815. *A Delineation of the Strata of England and Wales: with Part of Scotland.* John Cary.

Spikes, K., Mukerji, T., Dvorkin, J., and Mavko, G. 2007. Probabilistic seismic inversion based on rock-physics models. *Geophysics*, 72(5):R87–R97. doi: 10.1190/1.2760162.

Stabell, C. B. 2000. Alternative Approaches to Modeling Risks in Prospects with Dependent Layers. In *SPE Annual Technical Conference and Exhibition*. Society of Petroleum Engineers. doi: 10.2118/63204-MS.

Stark, T. J. 1996. Surface slice generation and interpretation: A review. *The Leading Edge*, 15(7):818–819. doi: 10.1190/1.1437369.

Stark, T. J. 2004. Relative geologic time (age) volumes - Relating every seismic sample to a geologically reasonable horizon. *The Leading Edge*, 23(9):928–932. doi: 10.1190/1.1803505.

Stark, T. J., Zeng, H., and Jackson, A. 2013. An introduction to this special section: Chronostratigraphy. *The Leading Edge*, 32(2):132–138. doi: 10.1190/tle32020132.1.

Suppe, J. 1983. Geometry and kinematics of fault-bend folding. *American Journal of Science*, 283(7):684–721. doi: 10.2475/ajs.283.7.684.

Suppe, J. 2011. Mass balance and thrusting in detachment folds. *AAPG Memoir*, 94: 21–37. doi: 10.1306/13251331M94389.

Suslick, S. B. and Schiozer, D. J. 2004. Risk analysis applied to petroleum exploration and production: An overview. *Journal of Petroleum Science and Engineering*, 44(1-2): 1–9. doi: 10.1016/j.petrol.2004.02.001.

Suslick, S. B., Schiozer, D., and Rodriguez, M. R. 2009. Uncertainty and risk analysis in petroleum exploration and production. *Terrae*, 6(1):30–41.

Swanson, B. 1981. A simple correlation between permeabilities and mercury capillary pressures. *Journal of Petroleum Technology*, 33(12):2498–2504. doi: 10.2118/8234-PA.

Tabti, H., Gelius, L., and Lecomte, I. 2001. On: 'Resolution limits of migrated images' (J. Chen and G. T. Schuster, Geophysics, 64, 1046-1053). *Geophysics*, 66(2):691–692. doi: 10.1190/1.1444958.

Taner, M. T. 1979. Complex seismic trace analysis. *Geophysics*, 44(6):1041. doi: 10.1190/1.1440994.

Tatham, R. H. 1982. Vp/Vs and lithology. *Geophysics*, 47(3):336–344. doi: 10.1190/1.1441339.

Teshima, Y. 1953. *Mechanical and Stress-Optical Properties*. Master of science, Oregon State College.

Thiele, S. T., Jessell, M. W., Lindsay, M., Wellmann, J. F., and Pakyuz-Charrier, E. 2016. The topology of geology 2: Topological uncertainty. *Journal of Structural Geology*, 91:74–87. doi: 10.1016/j.jsg.2016.08.010.

Thore, P., Shtuka, A., Lecour, M., Ait Ettajer, T., and Cognot, R. 2002. Structural uncertainties: Determination, management and applications. *Geophysics*, 67(3):840–852. doi: 10.1190/1.1484528.

Tomasso, M., Bouroullec, R., and Pyles, D. R. 2010. The use of spectral recomposition in tailored forward seismic modeling of outcrop analogs. *AAPG Bulletin*, 94(4):457–474. doi: 10.1306/08240909051.

Torabi, A. and Berg, S. S. 2011. Scaling of fault attributes: A review. *Marine and Petroleum Geology*, 28(8):1444–1460. doi: 10.1016/j.marpetgeo.2011.04.003.

Townsend, C., Firth, I. R., Westerman, R., Kirkevollen, L., Hårde, M., and Andersen, T. 1998. Small seismic-scale fault identification and mapping. *Geological Society, London, Special Publications*, 147(1):1–25. doi: 10.1144/GSL.SP.1998.147.01.02.

Tversky, A. and Kahneman, D. 1974. Judgment under uncertainty: Heuristics and biases. *Science*, 185(4157):1124–1131. doi: 10.1126/science.185.4157.1124.

Underhill, J. R. and Paterson, S. 1998. Genesis of tectonic inversion structures: seismic evidence for the development of key structures along the Purbeck-Isle of Wight Disturbance. *Journal of the Geological Society*, 155(6):975–992. doi: 10.1144/gsjgs.155.6.0975.

Usher, W. and Strachan, N. 2013. An expert elicitation of climate, energy and economic uncertainties. *Energy Policy*, 61:811–821. doi: 10.1016/j.enpol.2013.06.110.

Usher, W., Herman, J., Hadka, D., Xantares, Bernardoct, Rios, F., Mutel, C., and van Engelen, J. 2016. SALib: Improvements to Morris Sampling and Sobol Groups/Distributions.

Vail, P. R., Hardenbol, J., and Todd, R. G. 1984. Jurassic unconformities, chronostratigraphy and sea-level changes from seismic stratigraphy and biostratigraphy. *AAPG Memoir*, M 36:129–144.

Vakarelov, B. K. and Ainsworth, R. B. 2013. A hierarchical approach to architectural classification in marginal-marine systems: Bridging the gap between sedimentology and sequence stratigraphy. *AAPG Bulletin*, 97(7):1121–1161. doi: 10.1306/11011212024.

Van der Heijden, K. 1997. Scenarios, strategies and the strategy process. *Nyenrode Research Papers Series*, page 32.

Van der Heijden, K., 2011. *Scenarios: the art of strategic conversation*. Wiley. ISBN 1-119-99552-3.

van der Walt, S., Colbert, S. C., and Varoquaux, G. 2011. The NumPy Array: A structure for efficient numerical computation. *Computing in Science & Engineering*, 13(2):22–30. doi: 10.1109/MCSE.2011.37.

Verma, S., Mutlu, O., Ha, T., Bailey, W., and Marfurt, K. J. 2015. Calibration of attribute anomalies through prestack seismic modeling. *Interpretation*, 3(4):SAC55—-SAC70. doi: 10.1190/INT-2015-0072.1.

Versteeg, R. 1994. The Marmousi experience: Velocity model determination on a synthetic complex data set. *The Leading Edge*, 13(9):927–936. doi: 10.1190/1.1437051.

Voigt, W. 1890. Bestimmung der elasticitätsconstanten des brasilianischen turmalines. *Annalen der Physik und Chemie*, 277(12):712–724. doi: 10.1002/andp.18902771205.

Walden, A. T. and White, R. E. 1984. On errors of fit and accuracy in matching synthetic seismograms and seismic traces. *Geophysical Prospecting*, 32(5):871–891. doi: 10.1111/j.1365-2478.1984.tb00744.x.

Walden, A. T. and White, R. E. 1998. Seismic wavelet estimation: a frequency domain solution to a geophysical noisy input-output problem. *IEEE Transactions on Geoscience and Remote Sensing*, 36(1):287–297. doi: 10.1109/36.655337.

Walsh, J. J., Watterson, J., Heath, A. E., and Childs, C. 1998. Representation and scaling of faults in fluid flow models. *Petroleum Geoscience*, 4(3):241–251. doi: 10.1144/petgeo.4.3.241.

Wang, Z. Z. 2001. Fundamentals of seismic rock physics. *Geophysics*, 66(2):398–412. doi: 10.1190/1.1444931.

Welch, M. J., Davies, R. K., Knipe, R. J., and Tueckmantel, C. 2009. A dynamic model for fault nucleation and propagation in a mechanically layered section. *Tectonophysics*, 474(3-4):473–492. doi: 10.1016/j.tecto.2009.04.025.

Wellmann, F. J., Thiele, S. T., Lindsay, M. D., and Jessell, M. W. 2016. Pynoddy 1.0: An experimental platform for automated 3-D kinematic and potential field modelling. *Geoscientific Model Development*, 9(3):1019–1035. doi: 10.5194/gmd-9-1019-2016.

Wellmann, J. F. and Regenauer-Lieb, K. 2012. Uncertainties have a meaning: Information entropy as a quality measure for 3-D geological models. *Tectonophysics*, 526-529:207–216. doi: 10.1016/j.tecto.2011.05.001.

Wellmann, J. F., Finsterle, S., and Croucher, A. 2014. Integrating structural geological data into the inverse modelling framework of iTOUGH2. *Computers & Geosciences*, 65:95–109. doi: 10.1016/j.cageo.2013.10.014.

Wenzlau, F. and Müller, T. M. 2009. Finite-difference modeling of wave propagation and diffusion in poroelastic media. *Geophysics*, 74(4):T55–T66. doi: 10.1190/1.3122928.

Wheeler, H. E. 1959. Stratigraphic units in space and time. *American Journal of Science*, 257:692–706. doi: 10.2475/ajs.257.10.692.

White, D. A. 1993. Geologic risking guide for prospects and plays. *AAPG Bulletin*, 77 (12):2048–2061. doi: 10.1306/BDFF8FCE-1718-11D7-8645000102C1865D.

White, J. C., Williams, G. A., Grude, S., and Chadwick, R. A. 2015. Utilizing spectral decomposition to determine the distribution of injected CO2 at the Snøhvit Field. *Geophysical Prospecting*, 63(5):1213–1223. doi: 10.1111/1365-2478.12217.

White, R. E. and Simm, R. 2003. Tutorial: Good practice in well ties. *First Break*, 21 (October):75–83.

Whittle, T. M. and Gringarten, A. C. 2008. The determination of minimum tested volume from the deconvolution of well test pressure transients. In *SPE Annual Technical Conference and Exhibition*, volume 6, pages 4112–4120. Society of Petroleum Engineers. doi: 10.2118/116575-MS.

Widess, M. B. 1973. How thin is a thin bed? *Geophysics*, 38(6):1176–1180. doi: 10.1190/1.1440403.

Winkler, R. L. 1996. Uncertainty in probabilistic risk assessment. *Reliability Engineering & System Safety*, 54(2-3):127–132. doi: 10.1016/S0951-8320(96)00070-1.

Wiprut, D. and Zoback, M. D. 2002. Fault reactivation, leakage potential, and hydrocarbon column heights in the northern north sea. *Norwegian Petroleum Society Special Publications*, 11(C):203–219. doi: 10.1016/S0928-8937(02)80016-9.

Wood, A. M., Paton, D. A., and Collier, R. E. L. 2015. The missing complexity in seismically imaged normal faults: what are the implications for geometry and production response? *Geological Society, London, Special Publications*, 421(1):213–230. doi: 10.1144/SP421.12.

Wood, A. M. 2013. *The Influence of Fault Geometric Uncertainty on Hydrocarbon Reservoir and Simulation Models*. PhD thesis, University of Leeds.

Wu, X. and Hale, D. 2015. Horizon volumes with interpreted constraints. *Geophysics*, 80(2):IM21–IM33. doi: 10.1190/geo2014-0212.1.

Wyllie, M. R. J., Gregory, A. R., and Gardner, L. W. 1956. Elastic wave velocities in heterogeneous and porous media. *Geophysics*, 21(1):41–70. doi: 10.1190/1.1438217.

Yielding, G., Bretan, P., and Freeman, B. 2010. Fault seal calibration: a brief review. *Geological Society, London, Special Publications*, 347(1):243–255. doi: 10.1144/SP347.14.

Yilmaz, Ö., 2001. *Seismic Data Analysis*. Society of Exploration Geophysicists. ISBN 978-1-56080-094-1. doi: 10.1190/1.9781560801580.

Yoe, C. 2010. Choosing a probability distribution. In *Principles of Risk Analysis*, pages 1–30. CRC Press, 2010. ISBN 978-1-4398-5749-6. doi: 10.1201/b11256-13.

Yoe, C. 2011. Probability elicitation. In *Principles of Risk Analysis*, volume 85, pages 363–386. CRC Press, 2011. ISBN 9780444879523. doi: 10.1201/b11256-14.

Yousef, B. M. and Angus, D. A. 2016. When do fractured media become seismically anisotropic? Some implications on quantifying fracture properties. *Earth and Planetary Science Letters*, 444:150–159. doi: 10.1016/j.epsl.2016.03.040.

Zagayevskiy, Y. and Deutsch, C. V. 2016. Grid-free petroleum reservoir characterization with truncated pluri-Gaussian simulation: Hekla case study. *Petroleum Geoscience*, 22 (3):241–256. doi: 10.1144/petgeo2015-078.

Zamora-Valcarce, G. and Zapata, T. 2015. Building a valid structural model in a triangle zone: An example from the Neuquén fold and thrust belt, Argentina. *Interpretation*, 3 (4):SAA117–SAA131. doi: 10.1190/INT-2015-0014.1.

Zehner, B., Börner, J. H., Görz, I., and Spitzer, K. 2015. Workflows for generating tetrahedral meshes for finite element simulations on complex geological structures. *Computers and Geosciences*, 79:105–117. doi: 10.1016/j.cageo.2015.02.009.

Zeng, H. and Marfurt, K. J. 2015. Recent progress in analysis of seismically thin beds. *Interpretation*, 3(3):15–22. doi: 10.1190/INT-2014-0232.1.

Zeng, H., Backus, M. M., Barrow, K. T., and Tyler, N. 1998a. Stratal slicing, Part I: Realistic 3-D seismic model. *Geophysics*, 63(2):502–513. doi: 10.1190/1.1444351.

Zeng, H., Henry, S. C., and Riola, J. P. 1998b. Stratal slicing, Part II: Real 3-D seismic data. *Geophysics*, 63(2):514–522. doi: 10.1190/1.1444352.

Zhang, J., Morgan, J. K., Gray, G. G., Harkins, N. W., Sanz, P. F., and Chikichev, I. 2013. Comparative FEM and DEM modeling of basement-involved thrust structures, with application to Sheep Mountain, Greybull area, Wyoming. *Tectonophysics*, 608: 408–417. doi: 10.1016/j.tecto.2013.09.006.

Zhao, J. and Guo, N. 2014. Bridging the micro and macro for granular media: A computational multi-scale paradigm. *Geomechanics from Micro to Macro*, pages 747–752. doi: 10.1201/b17395-134.

Zhou, H. W., Hu, H., Zou, Z., Wo, Y., and Youn, O. 2018. Reverse time migration: A prospect of seismic imaging methodology. *Earth-Science Reviews*, 179(December 2017):207–227. doi: 10.1016/j.earscirev.2018.02.008.

Ziolkowski, A. 1991. Why don't we measure seismic signatures? *Geophysics*, 56(2): 190–201. doi: 10.1190/1.1443031.

Ziolkowski, A., Underhill, J. R., and Johnston, R. G. K. 1998. Wavelets, well ties, and the search for subtle stratigraphic traps. *Geophysics*, 63(1):297–313. doi: 10.1190/1.1444324.